Understanding the Mechanisms of Plasmon-Enhanced Phenomena in Mesoscopic Solar Cells

By

Holly Frances Zarick

Dissertation

Submitted to the Faculty of the

Graduate School of Vanderbilt University

in partial fulfillment of the requirements

for the degree of

DOCTOR OF PHILOSOPHY

in

Chemical Engineering

December 16, 2017

Nashville, Tennessee

Approved:

Rizia Bardhan, Ph.D.

Bridget Rogers, Ph.D.

Cary Pint, Ph.D.

Peter Cummings, Ph.D.

For Kobe, who helped me leave my comfort zone. I miss you, sweet girl.

ACKNOWLEDGMENTS

First and foremost, I would like to thank my advisor, Rizia Bardhan, for her guidance and mentorship throughout these past five years. I have had the unique opportunity of being one of her first students, and because of that she's helped me grow not just professionally but also personally. I am also thankful for the guidance of my dissertation committee members: Cary Pint, Bridget Rogers, and Peter Cummings. They have provided invaluable scientific insight and discussion during my graduate tenure and I am grateful for the time they have invested in helping me grow as a scientist.

I am grateful to all of those with whom I have had the pleasure to work during this time, especially the current and former members of the Bardhan Lab: William Erwin, Joseph Webb, May Ou, Eric Talbert, Naiya Soetan, and Eden Paul. I feel especially fortunate to have worked with such encouraging, bright, and supportive people. Thank you all for never hesitating to offer help or intellectual insight whenever possible, and I am thankful that I can consider you not just colleagues but friends as well.

I would also like to thank all the ChBE departmental staff for their invaluable assistance. In particular, I would like to thank Mary Gilleran, Rae Uson, Angie Pernell, Julie James, and Mark Holmes for their assistance in navigating my graduate student tenure, administrative issues, and the many basement repair challenges that arose over the course of my time in the department. Research in our department would not be possible without all of you.

My time in Nashville has been unforgettable. I am so thankful for the community of people I have met here that have made Nashville feel like a second home to me, including Danny and Melba Isom, the sweet Gann family, Bryce Foster, Aaron Bolton, Hannah Hogue, Nathalie Burack, and all of the members of the ILKB family. In particular I would like to say an extra special thank you to Ms. Barbara; your strength and pure heart are so inspiring. You have been my family here, and I don't know how to thank you for sharing

your home and all the stories from your fascinating life with me. I am a better person for knowing you.

I am very blessed to have met and befriended many wonderful women engineers during both my time in undergrad and graduate school. To my ChemE girls from undergrad, Kylen Johns, Amanda Mackey, and Marissa Conroy: you all are the most brilliant and supportive group of women I've ever had the pleasure to encounter and I am forever thankful to have made such amazing friends. It's been such an incredible comfort knowing that no matter how far apart we are, you are always still there for me. I would not have survived undergrad or grad school without you. And to my friends from graduate school, Sonia Brady, Ali Pereira, Lara Jazmin, Anne Talley, and Nikki Reinemann: I am so grateful to have gotten to know all of you. You've made my time at Vanderbilt so much brighter. I am also thankful for the support of my Albuquerque friends, Christyl Rosewater and Alyssa Dye, that have shown me what true life-long friendships looks like.

And finally, and most importantly, I am indebted to my family whose value only grows with age. To my parents: thank you for always believing in me, especially at the times when I most doubted myself. Your unwavering love and guidance has been priceless. To my brothers and sisters, Amy, Cory, Drew, and Tyler: thank you for being the stubborn, crazy, funny, driven, loving, and smart people that you are. Given a choice, I would still choose to be related to you. And to my person, my lobster, Logan. Thank you for keeping me well caffeinated, well fed, comforted, and sane through the most stressful points of grad school, for exploring Nashville with me, always making me laugh, being crazy supportive, being the best person I know, and for choosing to be my partner in all the new adventures to come.

TABLE OF CONTENTS

LIST OF TABLES

LIST OF FIGURES

CHAPTER 1

INTRODUCTION

Despite technological advances and extensive research efforts, the bulk of the world's energy is still being provided by petroleum, natural gas, and coal. The production and consumption of these fossil fuels is the leading source of CO_2 emissions, and mitigating greenhouse gas emissions is urgently needed to prevent global temperature rises that will become devastating to ecosystems, biodiversity, and society by 2100 if left unabated.[1] Besides harmful environmental impact, fossil fuels are finite resources and their reserves are steadily depleting as energy demands continue to rise, further driving the necessity to find clean, renewable, and reliable resources. Sunlight is arguably the most abundant clean source of energy with the highest theoretical potential; everyday, more energy from the sun reaches the earth's surface than is presently globally consumed in a year. Despite this potential, terrestrially installed PV only supplied 1.3% of global power in 2016.[2] In order to make solar conversion systems a competitive technology, it is essential to develop inexpensive, cost effective, and environmentally benign photovoltaics that have high stability and efficiency. Silicon-based photovoltaics, specifically crystalline silicon photovoltaics (c-Si PVs), are currently the most commercially available, with terrestrial single junction cells achieving power conversion efficiencies over 26%.[3] While significant improvements in device performance and reductions in construction costs have been made over the last 40 years, c-Si PVs still require thick (160-240 μm) layers of highly pure materials that are doped with toxic heavy metals that making disposal and recycling of panels at the end of their useful life (20-25 years)[4, 5, 6, 7] a challenging task.[8] Overall, the current costs and reliability of silicon-based devices put it at a disadvantage to other forms of electrical generation, so c-Si PVs are likely to remain a small slice of the energy matrix in their current state.

Great effort has been made to find promising alternatives for silicon solar cells to drive the widespread implementation of photovoltaic energy production forward. Over the last 10 years, third generation solar cells have attracted much attention due to their inexpensive and non-toxic constituents, and scalable manufacturing potential as a result of low cost solution processing. Here we will be focusing on two of these emerging technologies. The first are dye-sensitized solar cells (DSSCs). In addition to being comprised of low cost and widely available materials and offering the potential of roll to roll processing, DSSCs have favorable differential kinetics that allow them to work even in low light conditions, and possess a mechanical robustness that leads to higher efficiencies at higher temperatures instead of degradation. They also offer a multitude of design options, including transparency, color tunability, are lightweight, and can be deposited on flexible substrates, which makes them ideal candidates for building integrated photovoltaics (such as windows with a stained glass look, offering shade while generating electricity), and wearable and portable electronics for both civilian and military applications. Their biggest downfalls and obstructions to widespread commercialization are their use of a liquid electrolyte and the absorption limitation of the photosensitive dyes they employ. While a lot of progress has been made in finding solid state electrolytes,[9, 10, 11] the lack of photosensitive dyes with panchromatic absorption has limited device efficiencies to $\sim$12%.[3]

The second class of solar devices we will be studying are perovskite-sensitized solar cells (PSCs) based on organolead halide perovskites. Perovskites combine the advantages of high performance with inexpensive materials and low-cost scalable manufacturing potential, however stability is an issue. The most commonly studied perovskite, methylammonium lead triiodide ($MAPbI_3$) possess prominent broadband absorption in films less than 1 μm thick and devices based on this material are steadily reaching power conversion efficiencies competitive with c-Si PVs. However, stability is an issue with this material; the tetragonal crystal structure of $MAPbI_3$ leads to rapid degradation in the presence of moisture, and so would require expensive encapsulation for practical implementation. Br-based

perovskites, $MAPbBr_3$, have displayed much improved stability due to their pseudo-cubic crystal structure, but have been plagued by power conversion efficiency caps $\sim$10% as a result of the larger band gap that leads to poor light absorption beyond the 550 nm band edge.[12, 13, 14]

While there are many approaches being investigated to combat the poor absorption in these devices, in this dissertation we focus on the incorporation of plasmonic nanostructures to improve the light harvesting efficiency in these emerging solar technologies. Plasmonics provides the benefit of being a tunable, easy to incorporate, and universal method of enhancement that has minimal impact on construction costs and does not require any additional and complicated processing steps. The primary objective of this work was first to improve the light harvesting ability in 3rd generation mesoscopic solar cells by incorporating plasmonic metal nanostructures. Secondly, we wanted to further probe the mechanisms behind this plasmonic enhancement and ultimately further the development of superior performing devices

- In chapter 3, we first investigated the synthesis of bimetallic nanostructures with the intent of tuning superior optical properties for optimal plasmonic enhancements in our solar devices. We utilized a seed mediated growth process to first synthesize Au nanocubes and then coat them with a Ag outer layer to form Au/Ag core/shell nanaostructures (Au/Ag NSs). We systematically studied the impact of synthesis parameters on the morphological evolution, degree of polydispersity, and optical properties of the particles. To further explore the potential of these Au/Ag NSs in other applications, we tested their catalytic ability compared to commercially purchased Ag nanospheres using a model reaction, the reduction of 4-nitrophenol to 4-aminophenol.

- Before incorporating these structures into to devices, we first studied the excited state dynamics of Au/Ag NSs in aqueous solution using femtosecond transient absorption spectroscopy (TAS), as detailed in Chapter 4. We compared excited state lifetimes

as a function of both Ag layer thickness, excitation fluence of the pump, and nanostructure geometry.

- After observing the mostly monometallic and spherical studies reported in the literature, we attempted to decouple the impact of nanostructure shape and composition, by first looking at DSSCs enhanced with Au nanocubes in Chapter 5. Au nanocubes were coated with a thin layer of silica ($Au@SiO_2$ NCs) and then embedded in the TiO_2 mesoporous scaffold of the active layer. A range of concentrations were incorporated to find the optimum density of $Au@SiO_2$ NCs for maximum enhancements. Plasmon-enhanced active layers and full devices were characterized for optical property and performance comparison to reference, non-enhanced devices.

- Composition effects on plasmonic enhancement potential were then investigated by incorporating bimetallic silica-coated Au/Ag NSs into the TiO_2 mesoporous scaffold of the active layer of DSSCs. Similarly, a range of concentrations were incorporated to find the optimum density of nanostructure for maximum enhancements, and plasmon-enhanced active layers and full devices were characterized for optical property and performance comparison. The impact of the presence of the plasmonic particles on the carrier dynamics in the devices were probed using TAS.

- Chapter 7 investigates the impact of Au/Ag NS on the device performance and carrier dynamics in $MAPbBr_3$ mesoporous perovskite solar cells. In addition to TAS, another complimentary spectral technique, time-resolved photoluminescence (trPL), was utilized to help gain a mechanistic understanding of plasmon-enhancement processes.

- Finally, in Chapter 8 we investigate another strategy currently being studied to obtain high efficiency perovskites with high stability: the partial substitution of I^- ions with Br^- in the crystal lattice. The impact of Br content on the excited state dynamics was systematically studied up to 30% substation of I^- with Br^- using transient absorption

spectroscopy, and we compare the impact on carrier thermalization, recombination, and charge injection lifetimes.

1.1 Bibliography

[1] C. Mora, A. G. Frazier, R. J. Longman, R. S. Dacks, M. M. Walton, E. J. Tong, J. J. Sanchez, L. R. Kaiser, Y. O. Stender, J. M. Anderson, C. M. Ambrosino, I. Fernandez-Silva, L. M. Giuseffi, and T. W. Giambelluca. The projected timing of climate departure from recent variability. *Nature*, 502(7470):183–187, 2013.

[2] REN21. Renewables 2016 global status report. Technical Report ISBN 978-3-9818107-0-7, REN21 Secretariat, Paris, 2016.

[3] Martin A. Green, Yoshihiro Hishikawa, Wilhelm Warta, Ewan D. Dunlop, Dean H. Levi, Jochen Hohl-Ebinger, and Anita W. H. Ho-Baillie. Solar cell efficiency tables (version 50). *Prog. Photovolt: Res. Appl.*, 25(7):668–676, 2017.

[4] D. C. Jordan and S. R. Kurtz. Photovoltaic degradation rates-an analytical review. *Prog. Photovolt: Res. Appl.*, 21(1):12–29, 2013.

[5] Davide Polverini, Michael Field, Ewan Dunlop, and Willem Zaaiman. Polycrystalline silicon PV modules performance and degradation over 20years. *Prog. Photovolt: Res. Appl.*, 21:1004–1015, 2013.

[6] Ewan D. Dunlop and David Halton. The performance of crystalline silicon photovoltaic solar modules after 22 years of continuous outdoor exposure. *Prog. Photovolt: Res. Appl.*, 14(1):53–64, 2006.

[7] Alberto Pozza and Tony Sample. Crystalline silicon PV module degradation after 20years of field exposure studied by electrical tests, electroluminescence, and LBIC. *Prog. Photovolt: Res. Appl.*, 24(3):368–378, 2016.

[8] Hanning Chen, Martin G. Blaber, Stacey D. Standridge, Erica J. DeMarco, Joseph T. Hupp, Mark A. Ratner, and George C. Schatz. Computational modeling of plasmon-

enhanced light absorption in a multicomponent dye sensitized solar cell. *J. Phys. Chem. C*, 116(18):10215–10221, 2012.

[9] J. Wu, Z. Lan, J. Lin, M. Huang, Y. Huang, L. Fan, and G. Luo. Electrolytes in dye-sensitized solar cells. *Chem. Rev.*, 115(5):2136–2173, 2015.

[10] Li Tao, Zhipeng Huo, Yong Ding, Yi Li, Songyuan Dai, Lu Wang, Jun Zhu, Xu Pan, Bing Zhang, Jianxi Yao, Mohammad K. Nazeeruddin, and Michael Grtzel. High-efficiency and stable quasi-solid-state dye-sensitized solar cell based on low molecular mass organogelator electrolyte. *J. Mater. Chem. A*, 3(5):2344–2352, 2015.

[11] Jean-David Decoppet, Thomas Moehl, Saeed Salem Babkair, Raysah Ali Alzubaydi, Azhar Ahmad Ansari, Sami S. Habib, Shaik M. Zakeeruddin, Hans-Werner Schmidt, and Michael Grtzel. Molecular gelation of ionic liquidsulfolane mixtures, a solid electrolyte for high performance dye-sensitized solar cells. *J. Mater. Chem. A*, 2(38):15972–15977, 2014.

[12] Rui Sheng, Anita Ho-Baillie, Shujuan Huang, Sheng Chen, Xiaoming Wen, Xiaojing Hao, and Martin A. Green. Methylammonium lead bromide perovskite-based solar cells by vapor-assisted deposition. *J. Phys. Chem. C*, 119(7):3545–3549, 2015.

[13] M. Kulbak, S. Gupta, N. Kedem, I. Levine, T. Bendikov, G. Hodes, and D. Cahen. Cesium enhances long-term stability of lead bromide perovskite-based solar cells. *J. Phys. Chem. Lett.*, 7(1):167–172, 2016.

[14] Sawanta S. Mali, Chang Su Shim, and Chang Kook Hong. Highly stable and efficient solid-state solar cells based on methylammonium lead bromide ($CH_3NH_3PbBr_3$) perovskite quantum dots. *NPG Asia Mater.*, 7(8):e208, 2015.

CHAPTER 2

BACKGROUND

2.1 Third Generation Mesoscopic Photovoltaics

2.1.1 Dye-Sensitized Solar Cells

A dye-sensitized solar cell (DSSC), also known as a Grätzel cell, is a type of photoelectrochemical cell that stems from early biomimetic approaches aiming to simulate photosynthesis.[1] Co-invented by Brian O'Regan and Michael Grätzel in 1988, certified power conversion efficiencies for DSSCs have currently reached 11.9% since their first publication in 1991.[2, 3] Unlike conventional photovoltaics (PVs) where light absorption occurs in a low band gap semiconductor (E_g of crystalline silicon is 1.1 eV), DSSCs employ photosensitive dyes, such as a ruthenium-based or porphyrin dyes, that have large optical absorptivity cross sections and can couple absorbed light into a wide bandgap, semiconducting scaffold. In a typical DSSC architecture, these dye molecules are adsorbed in monolayer on top of the mesoporous, semiconducting backbone that acts as an electron accepting and transport layer. Anatase TiO_2, which has a bandgap of 3.2 eV and absorption out to $\sim$400 nm, is most often used in these devices because of its high stability even in corrosive environments, low cost, wide availability, and is non-toxic.[4] Because of the nanometer-size dimensions of the dye molecules, a conventional flat morphology does not allow for enough dye adsorption for efficient light absorption; what makes these devices possible is the mesoscopic nature of the TiO_2 scaffold. The scaffold, on the range of $\sim$10 μm thick is comprised of nanometer sized (2-50 nm) particles of the semiconductor which creates a mesoporous morphology that has a network of very high contact area, allowing for 1000$\times$ more dye adsorption than a flat morphology.[5, 6] The small size of the semiconductor particles (generally $\sim$20 for TiO_2) also makes it unnecessary to electronically dope

them as they exhibit photoinduced conductivity and allows for electron collection without significant Ohmic losses.[7] This dye-sensitized semiconducting active layer is deposited on a transparent conductive oxide, such as fluorine-doped or indium-doped tin oxide (FTO or ITO), with a glass support. An external circuit connects this anode to a noble metal (usually platinum) counter electrode deposited on FTO or ITO. A liquid electrolyte layer with a redox couple (such as I^-/I_3^-) lies between the counter electrode and the semiconducting active layer, completing the photoelectrochemical cell. Unlike a p-n junction found in tradition silicon PVs, charge separation occurs at the interfaces of the dye, semiconductor, and electrolyte. A schematic representation of a DSSC and its operation is shown in Figure 2.1.

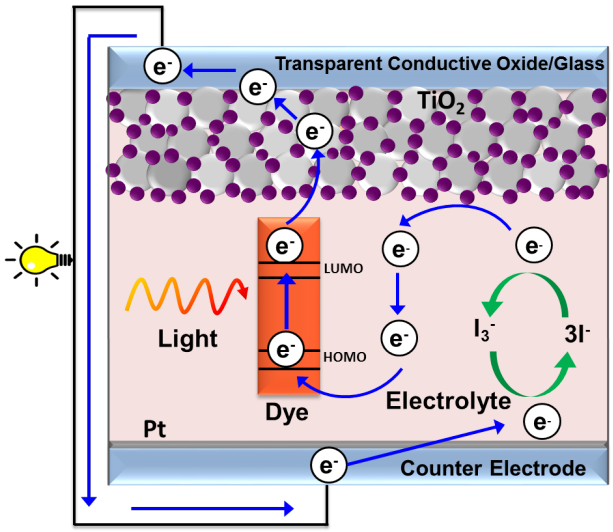

Figure 2.1: Schematic representation of components and electron transfer mechanism in a dye-sensitized solar cell.

The working mechanism of a DSSC is described in the list of reactions below:[8] (I) when light (*hv*) hits the photosensitive dye (D) absorbed on the surface of the TiO_2, the incident photon is absorbed by the dye complex, electrons (e-) are excited from the ground state (HOMO) to the excited state (LUMO, D^*) and then are injected into the conduction band of the TiO_2 (II), resulting in oxidation of the dye (D^+). The oxidized dye molecules are regenerated by an electron donor in the electrolyte (I^- of the redox mediator), which is

oxidized to the I_3^- state (III). Finally, the I_3^- diffuses towards the Pt counter electrode where it is reduced back to I^- (IV) by e^- that traveled through the mesoporous TiO_2 scaffold to the conductive oxide and then through the external circuit.

$$D_{adsorbed} \xrightarrow{h\nu} D^*_{adsorbed} \tag{I}$$

$$D^*_{adsorbed} \rightarrow D^+_{adsorbed} + e^-_{injected} \tag{II}$$

$$D^+_{adsorbed} + \frac{3}{2} I^- \rightarrow \frac{1}{2} I_3^- + D_{adsorbed} \tag{III}$$

$$I^-_{3(cathode)} + 2e^- \rightarrow 3I^-_{(cathode)} \tag{IV}$$

$$D^*_{adsorbed} \rightarrow D_{adsorbed} \tag{V}$$

$$D^+_{adsorbed} + e^-_{(TiO_2)} \rightarrow D^+_{adsorbed} \tag{VI}$$

$$I^-_{3(anode)} + 2e^-_{(TiO_2)} \rightarrow 3I^-_{(anode)} \tag{VII}$$

Reactions (V), (VI), and (VII) describe undesirable processes that can occur within in the cell to negatively impact device performance, including relaxation of the excited e^- in the dye molecules back to the ground state before it can inject into the conduction band of the TiO_2 and unwanted recombination at the interfaces. A variety of factors can impact the efficiency of these reactions, including the thickness of the mesoporous TiO_2 transport layer, concentration of species, thickness and viscosity of the electrolyte, diffusion coefficients of the redox mediators, the intensity of the incoming photon flux, and the density of charges flowing through the cell, as well as the alignment of the energy levels of the device components.[8]

2.1.2 Perovskite Solar Cells

Perovskite-based solar cells (PSCs) are the newest generation of PV devices and have already revolutionized the field; major developments are being made at an unprecedented

rate, with efficiency values more than doubling from 9.7% for the first high efficiency all solid-state PSC in 2012[9] to an NREL certified power conversion over 22% by 2017.[3, 10, 11, 12] The term perovskite, named in honor of Russian mineralogist Lev Perovksi, refers to a class of materials which have the same type of crystal structure as calcium titanate, and are described by the general formula AMX_3.[13, 14] This family of materials has long been studied and shown a wealth of useful and exciting functional properties, including superconducting, conducting, semiconducting, insulating, piezoelectric, thermoelectric, ferroelectric, ferromagnetic, and more.[14, 15] However, it is only recently that the organometal trihalide family of perovskites have been gaining attention as a promising absorber for light harvesting applications due to their excellent optical and electronic properties; they possess unique combination of strong broadband light absorption in submicron-thick films, efficient ambipolar charge transport, low exciton binding energies, and rapid charge extraction rates .[16, 17, 18, 19] In this category of perovskites, A is an organic monovalent cation (typically $CH_3NH_3^+$, $C_2H_5NH_3^+$, or $HC(NH_2)_2^+$), M is usually a divalent metal ion (Pb^{2+} is the most common; Sn^{2+} has been investigated, but is less stable), and X is a halide ion (I^-, Cl^-, or Br^-). A typical crystal structure for these perovskites is depicted in Figure 2.2a, where the halogen atoms occupy the vertices of an octahedron and the divalent metal atoms lie at the centers of the octahedra (MX_6).[20, 21, 22] The cavity formed by neighboring, corner-linked octahedra enclose the monovalent cation. The crystal lattice can be engineered to be pseudocubic, tetragonal, orthorhombic, trigonal, or monoclinic based on the identity and substitution of A^+, M^{2+}, or X^- components and its impact on the tilt and rotation of MX_6 polyhedra in the lattice.[23] Phase changes can also be caused by external stimuli, such as temperature and pressure, but are usually reversible. Chemical and structural variations allow for tuning of optoelectronic properties, including bandgap, exciton binding energy, and charge carrier diffusion lengths of the perovskite material.[17] To note, all inorganic perovskites for solar applications, such as where A is a cesium ion, are also being investigated with some success, though will not be discussed in this work.

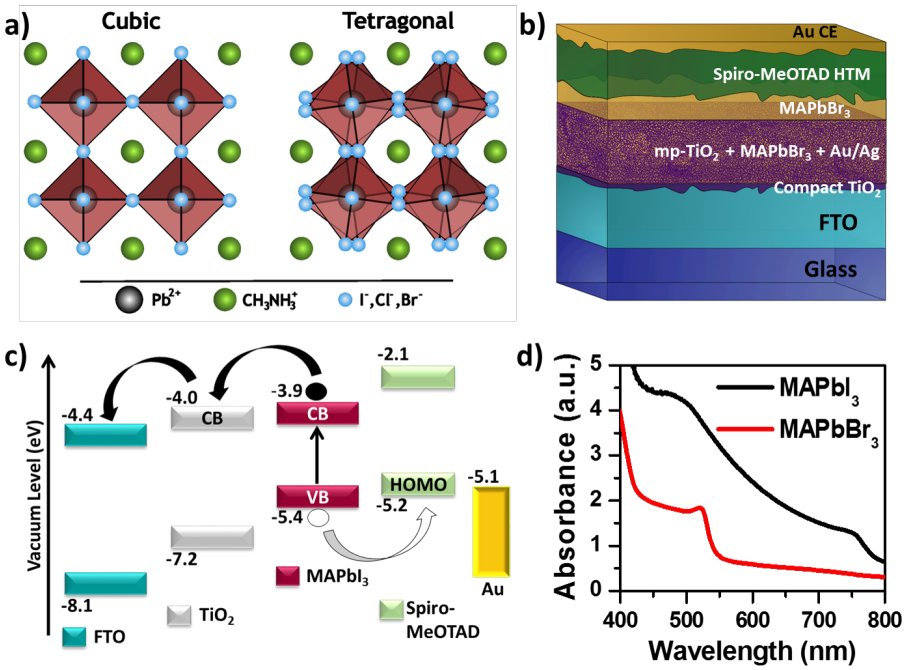

Figure 2.2: (a) Methylammonium lead halide perovskites with cubic (left) and tetragonal (right) crystal structures. Organometal halide perovskites have chemical formula of ABX_3, where organic or inorganic cations occupy position A (green), metal cations occupy B (black), and halide ions occupy X (blue). The lead halide octahedral (maroon) forms a corner linked network around methylammonium cations. (b) Schematic representation of an organometal trihalide ($MAPbBr_3$ shown) perovskite-sensitized solar cell, with a mesoporous architecture featuring a TiO_2 scaffold and bilayer configuration. (c) An energy level diagram depicting the basic working principle in a mesoporous perovskite sensitized solar cell with an active TiO_2 scaffold that acts as an electron transport material. (d) UV-vis absorption comparing the light harvesting capability of methylammonium lead triiodide vs tribromide perovskites.

Methylammonium lead tribromide ($MAPbBr_3$) perovskite nanoparticles were the first to be incorporated in a solar cell in 2006, and were used to replace the photosensitive dye in a dye-sensitized solar cell.[24]. A PCE of 2.2% was achieved, which was increased to 3.8% in 2009 by replacing the Br halogen ions with I^- ($MAPbI_3$).[25] While the perovskite nanoparticles exhibited better optical properties than standard dyes, displaying stronger and broader absorption, they could not withstand the presence of the liquid electrolyte and degraded quickly. This spurred the rapid finding of a of solid state hole transport material to replace the liquid electrolyte.[26] Since 2009, perovskites have evolved past DSSCs and into their own class of solar cell devices. In the process, they have overcome many of the downfalls that have plagued DSSCs, including a more stable absorber that does not photobleach under long periods of illumination, no corrosive liquid electrolyte that could dry up or decompose over time, and faster charge extraction rates that enable much higher open circuit voltages.[19] In this new generation of perovskite-based solar cells, high performance devices have been successfully observed in a variety of cell architectures, including mesoporous geometries, similar to that of their dye-sensitized predecessors, on both active (TiO_2) or passive scaffolds (such as Al_2O_3), and in thin film planar geometries with both regular (n-i-p) and inverted (p-i-n) configurations.[27, 28, 29, 30] This is largely made possible by the long carrier diffusion lengths ($\sim 1\mu$m for $MAPbI_3$) and ambipolar diffusion with balanced transport properties of electrons and holes and is an exciting prospect for future optimization potential.[31] Planar geometries are more suitable for tandem and flexible PVs[11, 30, 32, 33] and offer the benefit of low temperature fabrication, however film morphology and surface coverage are critical to device performance and are less tolerant to defects. Additionally, these devices generally exhibit a higher degree of J-V hysteresis.[34, 27] Mesoporous architectures, which we have focused on in this work, offer the benefit of more facile, uniform, and reproducible deposition as crystal growth and morphology are largely controlled by the underlying scaffold,[35, 36, 37] and usually demonstrate negligible amounts of hysteresis.[30] The highest certified efficiencies

of perovskite-based solar cells have been achieved with this configuration,[38, 10, 39, 40] the components of which and working principle are shown in Figure 2.2b and c. Similar to the DSSC, the perovskite absorber ($MAPbI_3$) is infiltrated throughout the mesoporous matrix; in our studies we have implemented the active, electron-transporting TiO_2 scaffold. Because absorption is so much stronger and broader in the perovskites than the standard organic dyes of DSSCs, films on the range of $\sim$500 nm or less are sufficient.[14, 41] A compact layer of rutile TiO_2 ($\sim$50 nm) lies between the mesoporous layer and the FTO glass in order to block contact between the both the perovskite and the hole transport material with the conductive oxide and prevent charge recombination at the interface. Mesoporous PSCs can take on a bilayer configuration, depending on deposition parameters, with an overlayer of perovskite crystals grown on top of the infiltrated scaffold. A hole transport material (HTM, usually spiro-MeOTAD) is deposited on top of the perovskite-sensitized TiO_2 layer. Finally, a thin metal film ($<$100 nm of gold or silver) is deposited on top of the HTM layer as the back contact.

As depicted in the energy level diagram in Figure 2.2c, upon illumination with photons with energy exceeding that of the band gap (1.5-1.6 eV for $MAPbI_3$) are absorbed by the perovskite, exciting an electron from the valence band to the conduction band, generating excitons. Due to the combination of high dielectric constant and low effective masses of the perovskite, which is considered to be a direct band gap semiconductor,[20, 9] the electron hole pairs formed are generally Wannier-Mott type excitons,[29, 42] which are characterized by low exciton binding energy (estimated in the range of 10-50 meV for $MAPbI_3$),[43, 44, 10, 45] and thus have a high likelihood of dissociating into free carriers even at room temperature, and the electrons and holes readily split and migrate toward their respective electrodes. The direction of electron and hole transport is dictated by the band and work function alignment of device components, controllable by selected electron- and hole-transport contacts. The device components shown in Figure 2.2c are those utilized in our studies, however Figure 2.3 illustrates some other commonly used charge extraction

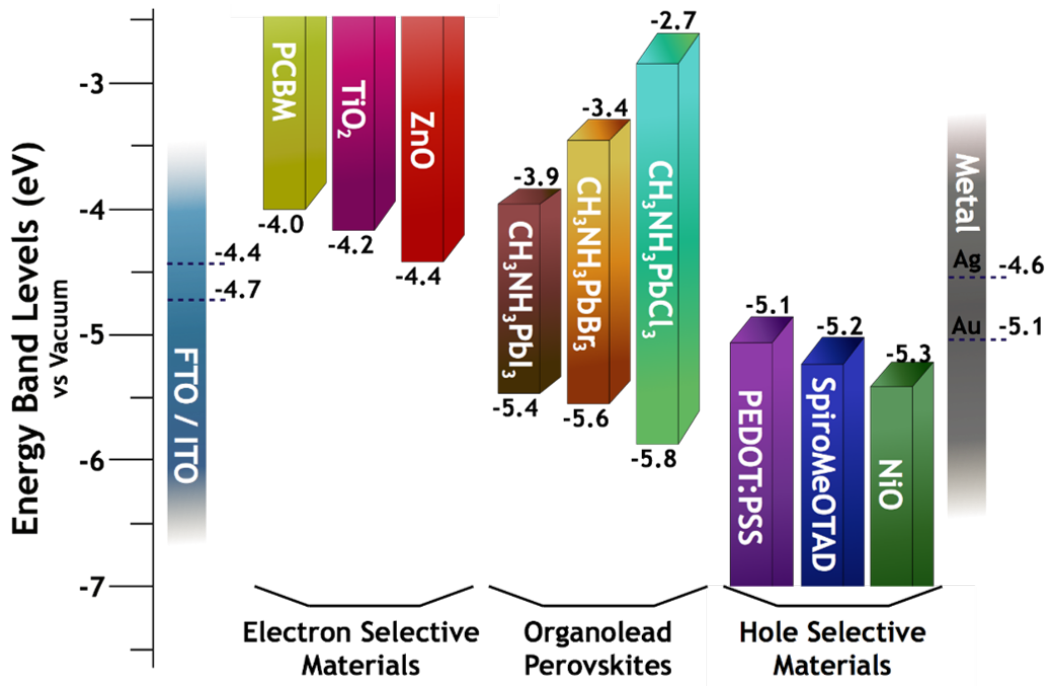

Figure 2.3: Band energy level diagram of organolead single halide perovskites and some common charge-extraction layers. The work function of given materials is represented by dotted lines.

layers.

Thus far, $MAPbI_3$ perovskites have remained the most widely studied for solar applications and devices with high efficiency. With a bandgap in the range of 1.5-1.6 eV, they display strong and broad absorption throughout most of the visible spectrum, with an absorption onset of $\sim$770 nm (Figure 2.2d). However, $MAPbI_3$ perovskites possess a tetragonal structure (Figure 2.1a, right) which is inherently unstable and contributes to their rapid degradation in ambient conditions.[10, 46, 47, 48, 27] When exposed to moisture, UV-light, and heat, $MAPbI_3$ reorganize from a black α-phase to a yellow δ-phase, due to material decomposition,[49] which has poor photovoltaic performance[50, 51, 52, 53] and also results in harmful byproducts such as HI and PbI_2.[54] Despite complex encapsulation techniques,[55, 56, 28, 57, 58] and application of UV filters[59, 60] the stability of $MAPbI_3$ is a major barrier to commercialization for utility-scale solar power. In contrast, $MAPbBr_3$ perovskites acquire a more stab;e pseudocubic crystal structure due to the smaller ionic

radius of Br^- (1.96 *Å vs* 2.2 *Å* for I^-); the larger iodide atoms cause a 15 offset of the PbX_6 octahedra in perovskites, and this angle of offset is reduced to nearly 0 when I^- is replaced with Br^-.[38] The smaller size of the Br ions reduces the lattice parameter of the perovskite, which restricts the diffusion of water into methylammonium vacancies and provides air and moisture stability, increasing its long term durability.[61, 62, 63] $MAPbBr_3$, has also piqued tremendous interest in PVs due to their high V_{oc} ($\sim$1.2-1.5 V) enabled by a large 2.2 eV bandgap, good charge transport facilitated by their long exciton diffusion length ($>$1.2 μm), and long-term stability.[64, 65] However, poor light absorption beyond the $\sim$550 nm band edge (Figure 2.2d) has limited device efficiencies to $<$10%.[61, 66, 37, 67, 68, 69]

2.2 Theory of Plasmon Enhancement Mechanisms in Solar Devices

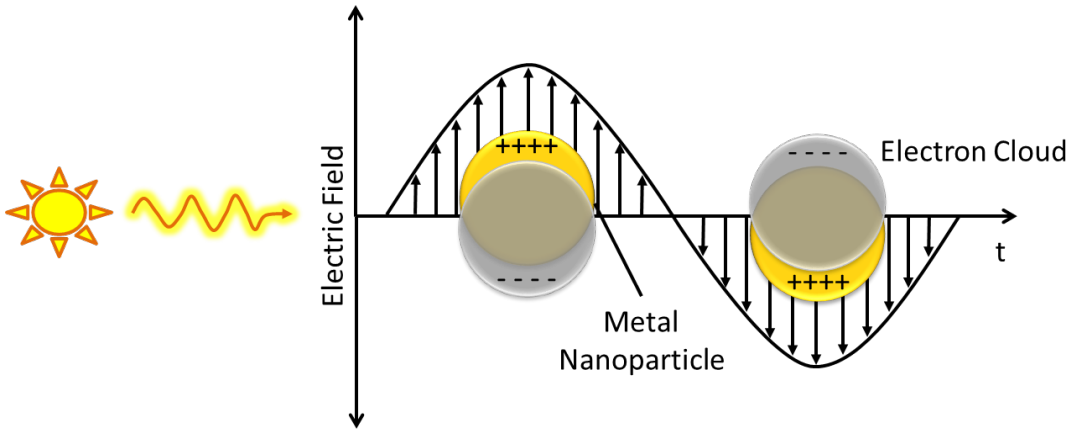

Figure 2.4: Diagram of the collective oscillation of conduction band electrons that occur in metal nanostructures resulting in plasmons upon irradiation.

2.2.1 Near Field Coupling

Incident light interacting with plasmonic nanostructures results in local enhancement of electromagnetic fields, defined as near fields. This strong electromagnetic near field generation close to the surface of the metal nanoparticle can be up to orders of magnitude greater than that of the incident light.[71] The surrounding absorber molecules couple with

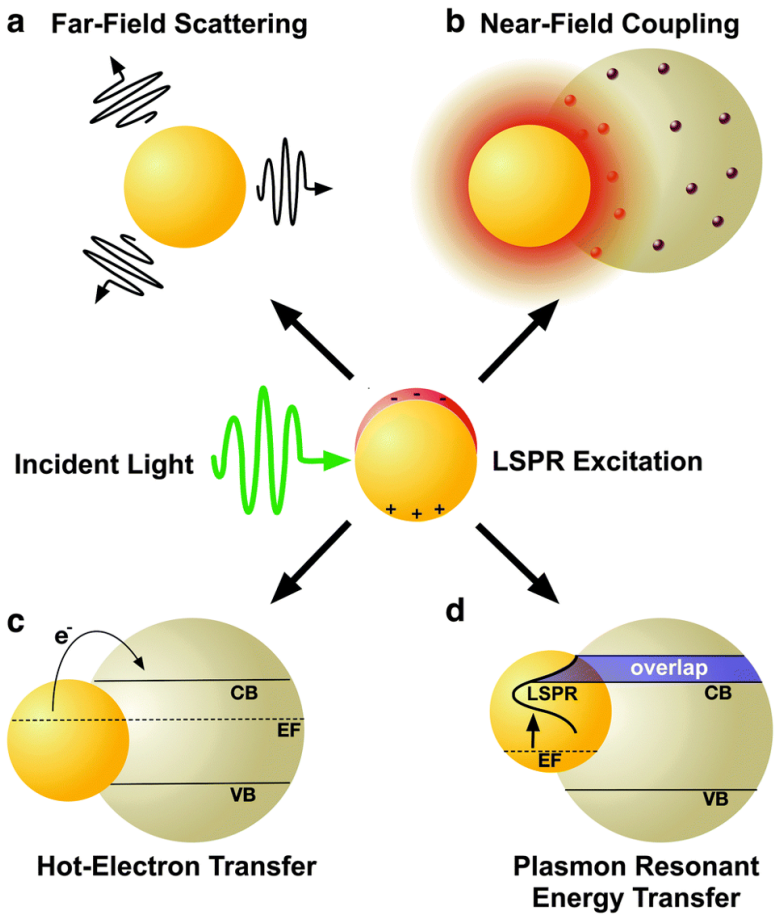

Figure 2.5: Schematic illustration of plasmon enhancement mechanisms including (a) far-field scattering, (b) near-field coupling, (c) hot-electron transfer, and (d) plasmon resonant energy transfer. Reproduced with permission from ref.[70]. Copyright Royal Society of Chemisty 2016.

the increased light intensity from these near fields, and so are exposed to an increased photon flux, resulting in greater generation of electron hole pairs,[72], and ultimately higher current generation and PCE. The strongest near field coupling is achieved when the optical absorption of the absorber overlaps with the LSPR of the nanostructure.[73, 74] Nanoparticles can be tuned for desired optical properties and spectral overlay by altering their size, geometry, and composition.[75]

Electromagnetic near fields at the plasmon resonance typically extend $<$50 nm from the surface of the nanoparticle, decaying at a rate proportional to r^{-6}, where r is the distance from the nanostructure.[70] The composition and the geometry of the nanostructure largely

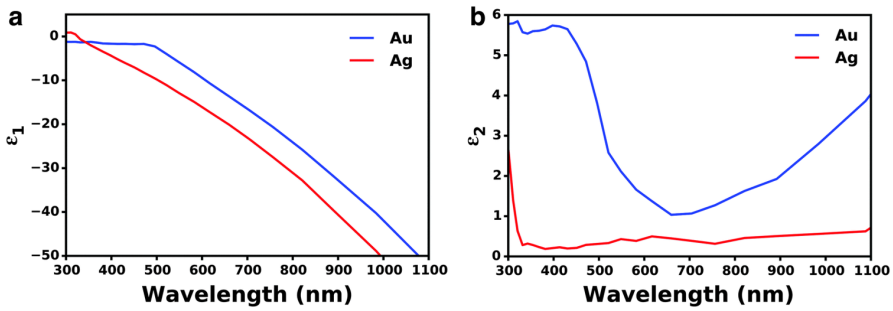

Figure 2.6: (a) Real and (b) imaginary parts of the dielectric function for Au and Ag. Data adapted from Ref. [81]. Reproduced with permission from Ref. [70]. Copyright Royal Society of Chemisty 2016.

govern the properties of the near field generated by the plasmon resonance.[76, 77, 78] Higher intensity near fields are generated by non-spherical particles with sharp features (edges and corners) attributable to the lightning rod effect, which describes how charges tend to accumulate in greater numbers at locations of greatest curvature.[79, 80] The electric field strength at these locations of greatest curvature is larger in magnitude, and will generally decay slower and extend longer than electromagnetic fields generated by spherical particles.

Near field effects are also inherently stronger in Ag than in Au. Ag has stronger radiative properties as a result of fewer Ohmic losses, which is illustrated by comparing the complex dielectric function of the two metals (Figure 2.6).[70, 81] The complex dielectric function describes the optical response of naturally occuring materials, and consists of both the real part (ε_1), which reflects the polarization response and the imaginary part, ε_2, which reflects the optical losses due to interband and intraband (Drude) transitions. As shown in Figure 2.6b, Au has high interband losses at shorter wavelengths and high Drude losses in the near infrared. Ag has a smaller dielectric function than Au across all wavelengths, indicating less optical losses, reflected by lower plasmon damping and higher absorption and scattering efficiency.

2.2.2 Far Field Scattering

When incident light hits a nanostructure with a sufciently high albedo (ratio of total scattered light to extinction), the resultant plasmon can decay radiatively into a photon. This photon can scatter off the surface of the nanoparticle, reaching distances up to 10 times the physical cross-section of the nanostructure; the exact distance it can reach dependsoncompositionandgeometryofthenanostructure.[82, 83, 84, 85] Photons scattered off a nanostructure can also be re-scattered multiple times if they encounter any proximal nanostructures prior to absorption by the sensitizer.[86, 87, 88] These scattering events significantly increase the optical path length of the active layer and ultimately increases the total light trapped within the solar cells; light not initially absorbed by the active layer can be absorbed and scattered off the nanostructures giving the sensitizer ample opportunity to absorb it.[84]

The light scattering ability of a nanostructure is most strongly related to its size, as described by Mie theory, a theory of absorption and scattering of plane electromagnetic waves by uniform, isotropic particles of the simplest form (spherical) in a uniform, isotropic dielectric medium. Mie theory is the simplest analytical solution of Maxwell's equations and can be used to describe the extinction behavior of a spherical metal nanoparticle when excited with an incident electric eld, where the extinction cross section is the sum of the scattering and absorption cross sections. The scattering cross section, σ_{scat}, is given by:

$$\sigma_{scatt} = \frac{8\pi}{3} k^4 a^6 \left| \frac{\varepsilon_{metal} - \varepsilon_{medium}}{\varepsilon_{metal} - 2\varepsilon_{medium}} \right|^2 \quad (1)$$

where $k = 2\pi/\lambda$, a is the radius of the spherical paricle, and ε_{metal} and ε_{medium} are the permittivity for the metal and medium, respectively. The scattering cross section scales with a^6, and thus increases rapidly with increasing size. Figure 2.7 illustrates the percent of scattered light compared to absorbed light for a spherical gold nanoparticle calculated as a function of diameter; Au nanospheres with a>30 nm begin to have good light scat-

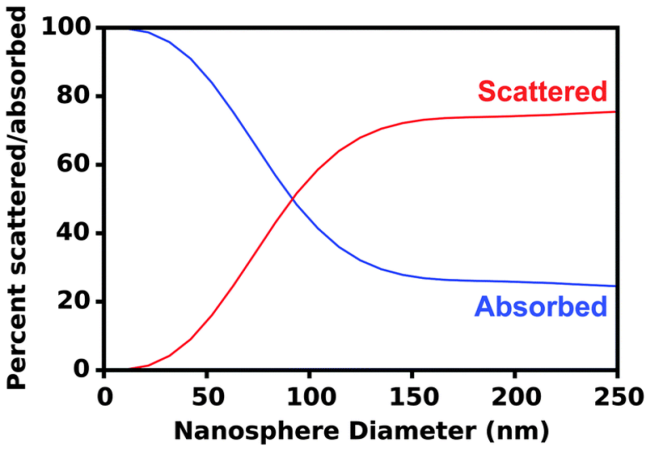

Figure 2.7: Percent of light scattered and absorbed calculated as a function of Au nanosphere diameter integrated from 300-800 nm. Reproduced with permission from Ref. [70]. Copyright Royal Society of Chemisty 2016.

tering ability. In the 80-90 nm size regime, Au nanospheres predominately scatter light, minimizing near field effects.

Beyond size, shape and composition can also influence the scattering properties. Anisotropic shapes with sharp edges and corners have displayed enhanced polarizability; the higher a particles polarizability, the higher the magnitude of the dipole moment (or LSPR) induced by the incident electromagnetic field.[75, 89, 77, 78] In addition, as discussed in the previous section, Ag suffers from fewer Ohmic losses (Figure 2.6b), and so will have better scattering efficiency compared to similar Au nanostructures.

2.2.3 Hot Electron Transfer

The third mechanism of plasmon enhancement is direct energy transfer from the plasmons of the metal to the semiconductor via highly energetic, ”hot” electrons that are not in thermal equilibrium with the surrounding material.[90] The generation of hot electrons in Au or Ag nanostructures is driven by either intraband excitations within the conduction band or interband excitations resulting from transitions between d bands and the conduction band.[70, 91] When plasmons undergo nonradiative decay by energetic relaxation, they can

gain enough energy to overcome the Schottky barrier at the junction of the metal and semiconductor and inject electrons directly into the conduction band of the semiconductor (see Figure 3c), increasing the number of carriers and thus, photocurrent generation.[83, 92, 93] This injection happens in the range of picoseconds; if the injection is too slow, the electrons will recombine on the surface of the metal or will be released as a phonon and lost to heat generation.[90]

Hot electron transfer depends on the alignment of the semiconductor's band levels and the Fermi level of the plasmonic metal, and will only occur if they are matching and there is a clear path for electrons to travel between the two.[94, 95, 96] However, because the only requirement is that the electronic energy levels match, one of the benefits of this enhancement mechanism is that spectral overlap between the metal nanostructures and the semiconductor is not needed for energy transfer to occur, as the energy needed for hot electron transfer can be smaller than the band gap of the semiconductor.[94] However, engineering an environment where this enhancement mechanism is promoted is challenging. In plasmon-enhanced mesoscopic solar cell systems, the plasmonic nanoparticles incorporated are usually first coated in an insulating interlayer, such as SiO_2, in order to protect the integrity of the nanostructures during device processing. In order for hot electron transfer to occur, this insulating interlayer must be thinner than the electron tunneling barrier of the material; for SiO_2, this is $\sim$3 nm.[70]

2.2.4 Plasmon Resonant Energy Transfer

Another non-radiative enhancement mechanism is plasmon resonant energy transfer (PRET). While not as well understood as an enhancement mechanism in solar devices as the others discussed, it has been found to be analogous to the well known phenomenon, Förster resonant energy transfer (FRET).[70] In FRET, the energy a light sensitive molecule in an excited state can transfer to another light sensitive molecule non-radiatively through dipole-dipole coupling. Typically, this only allows for downward energy transfer to a red-

shift acceptor and prevents charge separation to a higher band gap material.[28] In a plasmon/semiconductor system, this would result in energy transfer from the semiconductor to the plasmon. However, energy transfer in the opposite direction, energy upconversion, has been shown possible via PRET, where the resonant energy from the LSPR of a metal nanostructure can transfer to adjacent semiconductor via dipole-dipole coupling.[28, 94] As a result, electron hole pairs are generated below and near the semiconductor band edge.[94, 97] The potential for this energy transfer is distant dependent, as well as dependent on their respective dipole moments and dephasing time of the LSPR. While distant dependent, the mechanism does not require direct contact and is not limited by Fermi level equilibration; energy transfer can occur as long as there is spectral overlap with the LSPR and semiconductor, and the semiconductor is within the near field of the nanostructure. Because direct contact is not required, the standard thin protective SiO_2 interlayers will not interfere with PRET processes. However, because spectral overlap is required, Ag nanoparticles have shown to induce much stronger PRET enhancements than Au, as there is significantly more spectral overlap between Ag and TiO_2.[97]

2.3 Spectroscopic Investigations of Carrier Dynamics

2.3.1 Time-Resolved Photoluminescence

Photoluminescence (PL) spectroscopy is a noncontact, nondestructive spectroscopy technique used to probe electronic structures of materials. A simplified illustration of photoluminescence in a direct band gap semiconductor is shown in Figure 2.8. Typically, a light source hits the sample with photons with energy exceeding that of the band gap. The incoming photons are absorbed by the semiconductor, raising electrons and holes with finite momenta, k, into the conduction and valence bands, respectively. Post excitation, there is energy and momentum relaxation of the charge carriers towards the band gap minimum; these relaxation processes are faster than radiative emission, so electrons will collect at the

bottom of the conduction band. Finally, photons are emitted when electrons at the bottom of the conduction band recombine with holes at the top of the valence band. When a sample absorbs photons at one energy and then emits them at another, the spectrum emitted can be dispersed and detected with a device (such as a CCD), and we can then acquire information about the sample, as the set of wavelengths can be corresponded to transition energies of the sample. Looking at these measurements as a function of time (time-resolved PL, trPL) provides us with a means to measure the transition energy and their lifetimes. The fundamental limitation of PL analysis, however, is its reliance on radiative events; PL is a very sensitive probe of radiative levels, but one must rely on indirect evidence or other spectroscopic techniques to states taht couple weakly with light or non-emissive dark states.

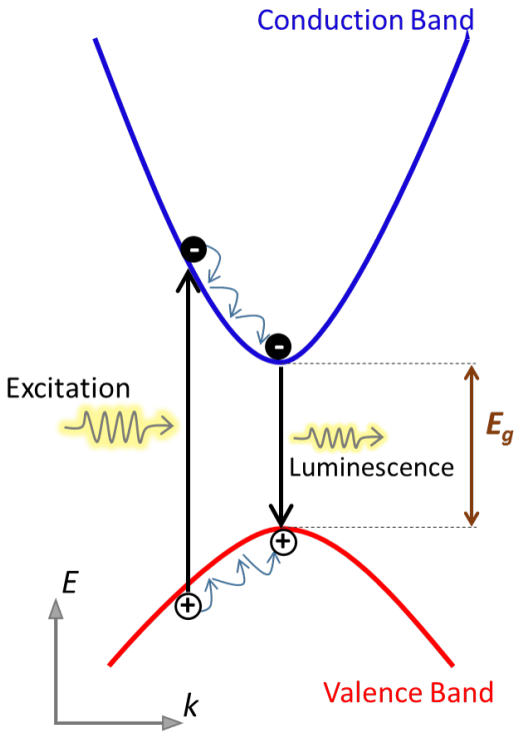

Figure 2.8: Schematic illustration of PL in a direct band gap semiconductor.

Time-resolved photoluminescence has been extensively used to examine the timescales of radiative decay of excited species in photoactive materials and has been a cornerstone to providing insight into carrier transport in perovskite solar cells.[63, 98, 99, 100, 101, 102,

103] A picosecond light pulse initiates electronic excitation and generates electron hole pairs, which are generally free carriers in perovskites due to their relatively low exciton binding energy. Carriers either recombine radiatively emitting a photon or non-radiatively by Auger processes, where the energy released from an electron recombining with a hole is instead transferred to another carrier, exciting it to a higher energy level without moving it to another energy band. The additional energy of this carrier can normally be expelled through a series of collisions with the llattice, thermalizing back to the band edge. In pristine perovskite films or when paired with passive scaffolds (such as Al_2O_3), longer radiative decay indicates slow recombination and long carrier diffusion lengths desirable for high performance devices. Perovskites paired with an electron- or hole-selective material often show shorter lifetimes suggesting improved charge injection.[104, 105, 106]

2.3.2 Femtosecond Transient Absorption Spectroscopy

Transient absorption spectroscopy (TAS) is a complementary spectroscopic technique to trPL spectroscopy, but offers the advantage of probing non-emissive and dark states, which play a critical role in PSCs. It is a pump probe technique where an ultrafast femtosecond pump pulse excites the sensitizer in the sample being investigated. A subsequent probe pulse is used to closely measure the absorbance of the system after a very well defined delay time (τ) between the two pulses. A standard TAS testing system is illustrated in Figure 2.9, where an input laser pulse is passed through a beam splitter and the two resultant beams then travel separate paths before being spatially overlapped at the sample. The pump probe travels down a path with a variable delay line to generate the controllable delay between the pump and probe, and the probe beam is focused through a sapphire window to generate a white light continuum so that samples can be monitored as a function of wavelength from 450-900 nm. After reaching the sample, the probe beam is routed to a detector (such as a CCD). The detector allows us to monitor the difference in absorption between the ground state and excited states after excitation (ΔOD) as a function of both τ and wave-

length. In these measurements, three fundamental contribution features can be observed in the spectra: ground state bleach (or photobleach, PB), stimulated emission (SE), and photo-induced absorptions (PIA). PBs and SEs usually manifest as negative signals, while PIA is positive. The PB occurs as the concentration of the ground state molecules decreases as the incoming pump pulse transfers molecules to the excited state. The corresponding negative signal will persist until all excited molecules return to the ground state. SE occurs when the probe pulse encounters some molecules in the excited state, and photons from the probe pulse stimulate emission from the sample molecules. PIA happens when molecules in the excited state absorb another photon and go to a higher excited state. Monitoring the nature, region, formation, and recovery of these signals can give us insight into the nature and lifetime of these excited states and the properties of the material. However, interpretation of spectral and kinetic information can be quite complex, as process that occur during decay, such as the excited molecules interacting with their surrounding matrix, will influence the difference absorption spectrum. Decoupling these processes is not always straightforward, especially if the signals from these processes overlap in the same region.

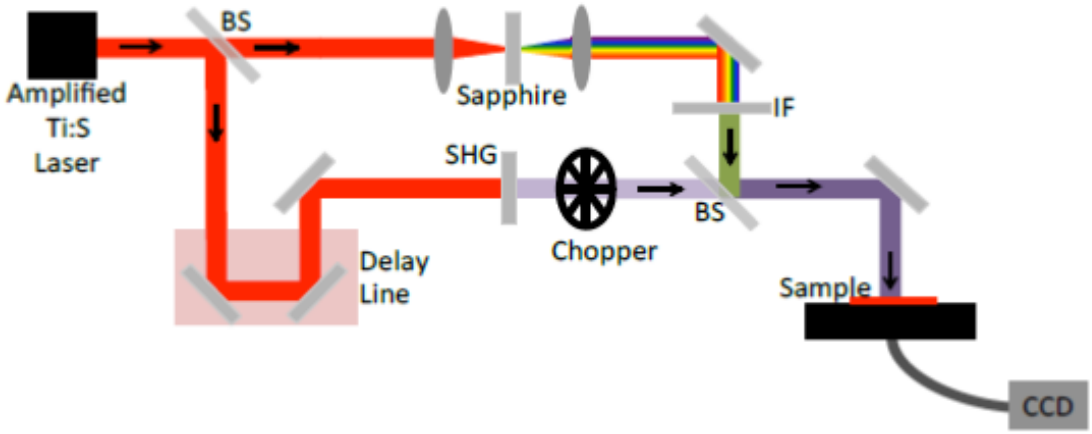

Figure 2.9: Schematic representation of an experimental ultrafast transient absorption set-up with a Ti:sapphire laser source and a CCD detector. For reference, BS: beam splitter; IF: interference filter.

For organometal trihalide perovskites, the pump pulse excites electrons from the valence band to the conduction band. The excited electrons thermalize to a nonequilib-

rium distribution in the conduction band, which is bound by a characteristic parabolic band shape. The carriers then cool within a few picoseconds via electron-phonon coupling to a stable energy distribution, which follows the parabolic band shape that is centered slightly above the absorption band edge. The optical transitions of the incoming white light probe are then either blocked or enhanced. Further excitation of carriers into the conduction band is blocked by the equilibrium distribution of filled electronic states; these blocked transitions manifest as a negative photobleach signal (PB) in the TA spectra, which corresponds to the bandgap energies with reference to the valence band.[107] Enhanced transitions (PIA) manifest as positive signals in the TA spectra. PIA bands have been correlated to both conduction band saturation which increases photoexcitation at off-peak wavelengths, and refractive index changes from the free carrier population as dielectric function of organometal trihalide perovskites will vary as a result of the photoexcited states.[108, 109] Decay of photoexcited states is studied by monitoring the recovery of PB and PIA in TA spectra where carriers can relax either via trap-assisted recombination at grain boundaries or via Auger recombination processes. Auger recombination typically dominates at high pump uences; increasing pump uence results in a higher initial density of excited carriers, and the greater proximity of charge carriers increases the liklihood of their ability to exchange energy.[109, 110, 111, 13] For both dye- and perovskite-sensitized systems, if the light harvesting sensitizer is paired with an electron transport layer, such as TiO_2, then electrons that do not recombine are injected into the electron-selective scaffold.

2.4 Bibliography

[1] H. Tributsch M. Calvin. Electrochemistry of excited molecules: Photoelectrochemical reactions of chlorophylls. *Photochem. Photobio.*, 14:95–112, 1971.

[2] Brian O'Regan and Michael Gratzel. A low-cost, high efficiency solar cell based on dye-sensitized colloidal TiO_2 films. *Nature*, 353:737–740, 1991.

[3] Martin A. Green, Yoshihiro Hishikawa, Wilhelm Warta, Ewan D. Dunlop, Dean H. Levi, Jochen Hohl-Ebinger, and Anita W. H. Ho-Baillie. Solar cell efficiency tables (version 50). *Prog. Photovolt: Res. Appl.*, 25(7):668–676, 2017.

[4] Michael Grtzel. Dye-sensitized solar cells. *J. Photochem. Photobiol.*, 4(2):145–153, 2003.

[5] Michael Gratzel. Photoelectrochemical cells. *Nature*, 414:338–344, 2001.

[6] Brian E. Hardin, Henry J. Snaith, and Michael D. McGehee. The renaissance of dye-sensitized solar cells. *Nat. Photon.*, 6(3):162–169, 2012.

[7] M. Gratzel. Photovoltaic and photoelectrochemical conversion of solar energy. *Philos. Trans. A Math. Phys. Eng. Sci.*, 365(1853):993–1005, 2007.

[8] G. Kalaignan and Y. Kang. A review on mass transport in dye-sensitized nanocrystalline solar cells. *J. Photochem. Photobiol.*, 7(1):17–22, 2006.

[9] H. S. Kim, C. R. Lee, J. H. Im, K. B. Lee, T. Moehl, A. Marchioro, S. J. Moon, R. Humphry-Baker, J. H. Yum, J. E. Moser, M. Gratzel, and N. G. Park. Lead iodide perovskite sensitized all-solid-state submicron thin film mesoscopic solar cell with efficiency exceeding 9%. *Sci. Rep.*, 2:591, 2012.

[10] Jinli Yang, Braden D. Siempelkamp, Dianyi Liu, and Timothy L. Kelly. Investigation of $CH_3NH_3PbI_3$ degradation rates and mechanisms in controlled humidity environments using in situ techniques. *ACS Nano*, 9(2):1955–1963, 2015.

[11] Hairen Tan, Ankit Jain, Oleksandr Voznyy, Xinzheng Lan, F. Pelayo Garca de Arquer, James Z. Fan, Rafael Quintero-Bermudez, Mingjian Yuan, Bo Zhang, Yicheng Zhao, Fengjia Fan, Peicheng Li, Li Na Quan, Yongbiao Zhao, Zheng-Hong Lu, Zhenyu Yang, Sjoerd Hoogland, and Edward H. Sargent. Efficient and stable solution-processed planar perovskite solar cells via contact passivation. *Science*, 355:722–726, 2017.

[12] T. Jesper Jacobsson, Juan-Pablo Correa-Baena, Meysam Pazoki, Michael Saliba, Kurt Schenk, Michael Grtzel, and Anders Hagfeldt. Exploration of the compositional space for mixed lead halogen perovskites for high efficiency solar cells. *Energy Environ. Sci.*, 9(5):1706–1724, 2016.

[13] Tze Chien Sum and Nripan Mathews. Advancements in perovskite solar cells: photophysics behind the photovoltaics. *Energy Environ. Sci.*, 7(8):2518–2534, 2014.

[14] Henry J. Snaith. Perovskites: The emergence of a new era for low-cost, high-efficiency solar cells. *J. Phys. Chem. Lett.*, 4(21):3623–3630, 2013.

[15] Zhen Fan, Kuan Sun, and John Wang. Perovskites for photovoltaics: a combined review of organicinorganic halide perovskites and ferroelectric oxide perovskites. *J. Mater. Chem. A*, 3(37):18809–18828, 2015.

[16] P. Qin, S. Tanaka, S. Ito, N. Tetreault, K. Manabe, H. Nishino, M. K. Nazeeruddin, and M. Gratzel. Inorganic hole conductor-based lead halide perovskite solar cells with 12.4% conversion efficiency. *Nat. Commun.*, 5:3834, 2014.

[17] S. Kazim, M. K. Nazeeruddin, M. Gratzel, and S. Ahmad. Perovskite as light harvester: a game changer in photovoltaics. *Angew. Chem. Int. Ed. Engl.*, 53(11):2812–2824, 2014.

[18] Luis M. Pazos-Outn, Monika Szumilo, Robin Lamboll, Johannes M. Richter, Micaela Crespo-Quesada, Mojtaba Abdi-Jalebi, Harry J. Beeson, Milan Vruini, Mejd

Alsari, Henry J. Snaith, Bruno Ehrler, Richard H. Friend, and Felix Deschler. Photon recycling in lead iodide perovskite solar cells. *Science*, 351:1430–1433, 2016.

[19] Guichuan Xing, Nripan Mathews, Shuangyong Sun, Swee Sien Lim, Yeng Ming Lam, Michael Grtzel, Subodh Mhaisalkar, and Tze Chien Sum. Electron-hole diffusion lengths exceeding 1 micrometer in an organometal trihalide perovskite absorber. *Science*, 342:341–344, 2013.

[20] Tom Baikie, Yanan Fang, Jeannette M. Kadro, Martin Schreyer, Fengxia Wei, Subodh G. Mhaisalkar, Michael Graetzel, and Tim J. White. Synthesis and crystal chemistry of the hybrid perovskite $CH_3NH_3PbI_3$ for solid-state sensitised solar cell applications. *J. Mater. Chem. A*, 1(18):5628–5641, 2013.

[21] Ziyong Cheng and Jun Lin. Layered organicinorganic hybrid perovskites: structure, optical properties, film preparation, patterning and templating engineering. *CrystEngComm*, 12(10):2646–2662, 2010.

[22] David B. Mitzi. Templating and structural engineering in organicinorganic perovskites. *J. Chem. Soc., Dalton Trans.*, (1):1–12, 2001.

[23] J. M. Frost, K. T. Butler, F. Brivio, C. H. Hendon, M. van Schilfgaarde, and A. Walsh. Atomistic origins of high-performance in hybrid halide perovskite solar cells. *Nano Lett.*, 14(5):2584–2590, 2014.

[24] Akihiro Kojima, Kenjiro Teshima, Tsutomu Miyasaka, and Yasuo Shirai. Novel photoelectrochemical cell with mesoscopic electrodes sensitized by lead-halide compounds (2). In *210th ECS Meeting*. ECS, 2006.

[25] Akihiro Kojima, Kenjiro Teshima, Yasuo Shirai, and Tsutomu Miyasaka. Organometal halide perovskites as visible-light sensitizers for photovoltaic cells. *J. Am. Chem. Soc.*, 131:60506051, 2009.

[26] Martin A. Green, Anita Ho-Baillie, and Henry J. Snaith. The emergence of perovskite solar cells. *Nat. Photon.*, 8(7):506–514, 2014.

[27] J. Zhao, B. Cai, Z. Luo, Y. Dong, Y. Zhang, H. Xu, B. Hong, Y. Yang, L. Li, W. Zhang, and C. Gao. Investigation of the hydrolysis of perovskite organometallic halide $CH_3NH_3PbI_3$ in humidity environment. *Sci. Rep.*, 6:21976, 2016.

[28] Jiangtian Li, Scott K. Cushing, Fanke Meng, Tess R. Senty, Alan D. Bristow, and Nianqiang Wu. Plasmon-induced resonance energy transfer for solar energy conversion. *Nat. Photon.*, 9(9):601–607, 2015.

[29] Teddy Salim, Shuangyong Sun, Yuichiro Abe, Anurag Krishna, Andrew C. Grimsdale, and Yeng Ming Lam. Perovskite-based solar cells: impact of morphology and device architecture on device performance. *J. Mater. Chem. A*, 3(17):8943–8969, 2015.

[30] H. S. Kim and N. G. Park. Parameters affecting I-V hysteresis of $CH_3NH_3PbI_3$ perovskite solar cells: Effects of perovskite crystal size and mesoporous TiO_2 layer. *J. Phys. Chem. Lett.*, 5(17):2927–34, 2014.

[31] V. Gonzalez-Pedro, E. J. Juarez-Perez, W. S. Arsyad, E. M. Barea, F. Fabregat-Santiago, I. Mora-Sero, and J. Bisquert. General working principles of $CH_3NH_3PbX_3$ perovskite solar cells. *Nano Lett.*, 14(2):888–893, 2014.

[32] Steve Albrecht, Michael Saliba, Juan Pablo Correa Baena, Felix Lang, Lukas Kegelmann, Mathias Mews, Ludmilla Steier, Antonio Abate, Jrg Rappich, Lars Korte, Rutger Schlatmann, Mohammad Khaja Nazeeruddin, Anders Hagfeldt, Michael Grtzel, and Bernd Rech. Monolithic perovskite/silicon-heterojunction tandem solar cells processed at low temperature. *Energy Environ. Sci.*, 9(1):81–88, 2016.

[33] Stefano Pisoni, Fan Fu, Thomas Feurer, Mohammed Makha, Benjamin Bissig, Shiro Nishiwaki, Ayodhya N. Tiwari, and Stephan Buecheler. Flexible NIR-transparent

perovskite solar cells for all-thin-film tandem photovoltaic devices. *J. Mater. Chem. A*, 5(26):13639–13647, 2017.

[34] Dong Yang, Xin Zhou, Ruixia Yang, Zhou Yang, Wei Yu, Xiuli Wang, Can Li, Shengzhong Liu, and Robert P. H. Chang. Surface optimization to eliminate hysteresis for record efficiency planar perovskite solar cells. *Energy Environ. Sci.*, 9(10):3071–3078, 2016.

[35] J. J. Choi, X. Yang, Z. M. Norman, S. J. Billinge, and J. S. Owen. Structure of methylammonium lead iodide within mesoporous titanium dioxide: active material in high-performance perovskite solar cells. *Nano Lett.*, 14(1):127–133, 2014.

[36] H. S. Kim, J. W. Lee, N. Yantara, P. P. Boix, S. A. Kulkarni, S. Mhaisalkar, M. Gratzel, and N. G. Park. High efficiency solid-state sensitized solar cell-based on submicrometer rutile TiO_2 nanorod and $CH_3NH_3PbI_3$ perovskite sensitizer. *Nano Lett.*, 13(6):2412–7, 2013.

[37] E. Edri, S. Kirmayer, M. Kulbak, G. Hodes, and D. Cahen. Chloride inclusion and hole transport material doping to improve methyl ammonium lead bromide perovskite-based high open-circuit voltage solar cells. *J. Phys. Chem. Lett.*, 5(3):429–433, 2014.

[38] N. J. Jeon, J. H. Noh, W. S. Yang, Y. C. Kim, S. Ryu, J. Seo, and S. I. Seok. Compositional engineering of perovskite materials for high-performance solar cells. *Nature*, 517(7535):476–480, 2015.

[39] Dongqin Bi, Wolfgang Tress, M. Ibrahim Dar, Peng Gao, Jingshan Luo, Clmentine Renevier, Kurt Schenk, Antonio Abate, Fabrizio Giordano, Juan-Pablo Correa Baena, Jean-David Decoppet, Shaik Mohammed Zakeeruddin, Mohammad Khaja Nazeeruddin, Michael Grtzel, and Anders Hagfeldt. Efficient luminescent solar cells based on tailored mixed-cation perovskites. *Sci. Adv.*, 2:e1501170, 2016.

[40] N. J. Jeon, J. H. Noh, Y. C. Kim, W. S. Yang, S. Ryu, and S. I. Seok. Solvent engineering for high-performance inorganic-organic hybrid perovskite solar cells. *Nat. Mater.*, 13(9):897–903, 2014.

[41] Nam-Gyu Park. Organometal perovskite light absorbers toward a 20% efficiency low-cost solid-state mesoscopic solar cell. *J. Phys. Chem. Lett.*, 4(15):2423–2429, 2013.

[42] Yu-Che Hsiao, Ting Wu, Mingxing Li, Qing Liu, Wei Qin, and Bin Hu. Fundamental physics behind high-efficiency organo-metal halide perovskite solar cells. *J. Mater. Chem. A*, 3(30):15372–15385, 2015.

[43] Atsuhiko Miyata, Anatolie Mitioglu, Paulina Plochocka, Oliver Portugall, Jacob Tse-Wei Wang, Samuel D. Stranks, Henry J. Snaith, and Robin J. Nicholas. Direct measurement of the exciton binding energy and effective masses for charge carriers in organicinorganic tri-halide perovskites. *Nat. Phys.*, 11(7):582–587, 2015.

[44] V. D'Innocenzo, G. Grancini, M. J. Alcocer, A. R. Kandada, S. D. Stranks, M. M. Lee, G. Lanzani, H. J. Snaith, and A. Petrozza. Excitons versus free charges in organo-lead tri-halide perovskites. *Nat. Commun.*, 5:3586, 2014.

[45] Krzysztof Galkowski, Anatolie Mitioglu, Atsuhiko Miyata, Paulina Plochocka, Oliver Portugall, Giles E. Eperon, Jacob Tse-Wei Wang, Thomas Stergiopoulos, Samuel D. Stranks, Henry J. Snaith, and Robin J. Nicholas. Determination of the exciton binding energy and effective masses for methylammonium and formamidinium lead tri-halide perovskite semiconductors. *Energy Environ. Sci.*, 9(3):962–970, 2016.

[46] J. A. Christians, P. A. Miranda Herrera, and P. V. Kamat. Transformation of the excited state and photovoltaic efficiency of $CH_3NH_3PbI_3$ perovskite upon controlled exposure to humidified air. *J. Am. Chem. Soc.*, 137(4):1530–1538, 2015.

[47] Weixin Huang, Joseph S. Manser, Prashant V. Kamat, and Sylwia Ptasinska. Evolution of chemical composition, morphology, and photovoltaic efficiency of $CH_3NH_3PbI_3$ perovskite under ambient conditions. *Chem. Mater.*, 28(1):303–311, 2016.

[48] Masaki Shirayama, Masato Kato, Tetsuhiko Miyadera, Takeshi Sugita, Takemasa Fujiseki, Shota Hara, Hideyuki Kadowaki, Daisuke Murata, Masayuki Chikamatsu, and Hiroyuki Fujiwara. Degradation mechanism of $CH_3NH_3PbI_3$ perovskite materials upon exposure to humid air. *J. Appl. Phys.*, 119(11):115501, 2016.

[49] Dan Li, Peizhe Liao, Xuxia Shai, Wenchao Huang, Shaungshuang Liu, Hao Li, Yan Shen, and Mingkui Wang. Recent progress on stability issues of organicinorganic hybrid lead perovskite-based solar cells. *RSC Adv.*, 6(92):89356–89366, 2016.

[50] Nan Li, Zonglong Zhu, Chu-Chen Chueh, Hongbin Liu, Bo Peng, Alessio Petrone, Xiaosong Li, Liduo Wang, and Alex K. Y. Jen. Mixed cation $FA_xPEA_{1-x}PbI_3$ with enhanced phase and ambient stability toward high-performance perovskite solar cells. *Adv. Energy Mater.*, 7(1):1601307, 2017.

[51] Chenyi Yi, Jingshan Luo, Simone Meloni, Ariadni Boziki, Negar Ashari-Astani, Carole Grtzel, Shaik M. Zakeeruddin, Ursula Rthlisberger, and Michael Grtzel. Entropic stabilization of mixed A-cation ABX_3 metal halide perovskites for high performance perovskite solar cells. *Energy Environ. Sci.*, 9(2):656–662, 2016.

[52] Wan-Jian Yin, Ji-Hui Yang, Joongoo Kang, Yanfa Yan, and Su-Huai Wei. Halide perovskite materials for solar cells: a theoretical review. *J. Mater. Chem. A*, 3(17):8926–8942, 2015.

[53] Ling-yi Huang and Walter R. L. Lambrecht. Electronic band structure trends of perovskite halides: Beyond Pb and Sn to Ge and Si. *Phys. Rev. B*, 93(19):195211, 2016.

[54] Dian Wang, Matthew Wright, Naveen Kumar Elumalai, and Ashraf Uddin. Stability of perovskite solar cells. *Sol. Energy Mater. Sol. Cells*, 147:255–275, 2016.

[55] Yu Han, Steffen Meyer, Yasmina Dkhissi, Karl Weber, Jennifer M. Pringle, Udo Bach, Leone Spiccia, and Yi-Bing Cheng. Degradation observations of encapsulated planar $CH_3NH_3PbI_3$ perovskite solar cells at high temperatures and humidity. *J. Mater. Chem. A*, 3(15):8139–8147, 2015.

[56] Seigo Ito, Soichiro Tanaka, Kyohei Manabe, and Hitoshi Nishino. Effects of surface blocking layer of Sb_2S_3 on nanocrystalline TiO_2 for $CH_3NH_3PbI_3$ perovskite solar cells. *J. Phys. Chem. C*, 118(30):16995–17000, 2014.

[57] M. Kaltenbrunner, G. Adam, E. D. Glowacki, M. Drack, R. Schwodiauer, L. Leonat, D. H. Apaydin, H. Groiss, M. C. Scharber, M. S. White, N. S. Sariciftci, and S. Bauer. Flexible high power-per-weight perovskite solar cells with chromium oxide-metal contacts for improved stability in air. *Nat. Mater.*, 14(10):1032–1039, 2015.

[58] I. C. Smith, E. T. Hoke, D. Solis-Ibarra, M. D. McGehee, and H. I. Karunadasa. A layered hybrid perovskite solar-cell absorber with enhanced moisture stability. *Angew. Chem. Int. Ed. Engl.*, 53(42):11232–11235, 2014.

[59] T. Leijtens, G. E. Eperon, S. Pathak, A. Abate, M. M. Lee, and H. J. Snaith. Overcoming ultraviolet light instability of sensitized TiO_2 with meso-superstructured organometal tri-halide perovskite solar cells. *Nat. Commun.*, 4:2885, 2013.

[60] Nikhil Chander, A. F. Khan, P. S. Chandrasekhar, Eshwar Thouti, Sanjay Kumar Swami, Viresh Dutta, and Vamsi K. Komarala. Reduced ultraviolet light induced degradation and enhanced light harvesting using $YVO_4:Eu^{3+}$ down-shifting nano-phosphor layer in organometal halide perovskite solar cells. *Appl. Phys. Lett.*, 105(3):033904, 2014.

[61] Rui Sheng, Anita Ho-Baillie, Shujuan Huang, Sheng Chen, Xiaoming Wen, Xiaojing Hao, and Martin A. Green. Methylammonium lead bromide perovskite-based solar cells by vapor-assisted deposition. *J. Phys. Chem. C*, 119(7):3545–3549, 2015.

[62] J. H. Noh, S. H. Im, J. H. Heo, T. N. Mandal, and S. I. Seok. Chemical management for colorful, efficient, and stable inorganic-organic hybrid nanostructured solar cells. *Nano Lett.*, 13(4):1764–1769, 2013.

[63] Eric M. Talbert, Holly F. Zarick, Noah J. Orfield, Wei Li, William R. Erwin, Zachary R. DeBra, Kemar R. Reid, Christopher P. McDonald, James R. McBride, Jason Valentine, Sandra J. Rosenthal, and Rizia Bardhan. Interplay of structural and compositional effects on carrier recombination in mixed-halide perovskites. *RSC Adv.*, 6(90):86947–86954, 2016.

[64] Sigalit Aharon, Bat El Cohen, and Lioz Etgar. Hybrid lead halide iodide and lead halide bromide in efficient hole conductor free perovskite solar cell. *J. Phys. Chem. C*, 118(30):17160–17165, 2014.

[65] Sneha A. Kulkarni, Tom Baikie, Pablo P. Boix, Natalia Yantara, Nripan Mathews, and Subodh Mhaisalkar. Band-gap tuning of lead halide perovskites using a sequential deposition process. *J. Mater. Chem. A*, 2(24):9221–9225, 2014.

[66] E. Edri, S. Kirmayer, D. Cahen, and G. Hodes. High open-circuit voltage solar cells based on organic-inorganic lead bromide perovskite. *J. Phys. Chem. Lett.*, 4(6):897–902, 2013.

[67] F. C. Hanusch, E. Wiesenmayer, E. Mankel, A. Binek, P. Angloher, C. Fraunhofer, N. Giesbrecht, J. M. Feckl, W. Jaegermann, D. Johrendt, T. Bein, and P. Docampo. Efficient planar heterojunction perovskite solar cells based on formamidinium lead bromide. *J. Phys. Chem. Lett.*, 5(16):2791–2795, 2014.

[68] M. Kulbak, S. Gupta, N. Kedem, I. Levine, T. Bendikov, G. Hodes, and D. Cahen. Cesium enhances long-term stability of lead bromide perovskite-based solar cells. *J. Phys. Chem. Lett.*, 7(1):167–172, 2016.

[69] Sawanta S. Mali, Chang Su Shim, and Chang Kook Hong. Highly stable and efficient solid-state solar cells based on methylammonium lead bromide $CH_3NH_3PbBr_3$ perovskite quantum dots. *NPG Asia Mater.*, 7(8):e208, 2015.

[70] William R. Erwin, Holly F. Zarick, Eric M. Talbert, and Rizia Bardhan. Light trapping in mesoporous solar cells with plasmonic nanostructures. *Energy Environ. Sci.*, 9(5):1577–1601, 2016.

[71] P. Spinelli and A. Polman. Prospects of near-field plasmonic absorption enhancement in semiconductor materials using embedded Ag nanoparticles. *Opt. Express*, 20(85):A641, 2012.

[72] X. Dang, J. Qi, M. T. Klug, P. Y. Chen, D. S. Yun, N. X. Fang, P. T. Hammond, and A. M. Belcher. Tunable localized surface plasmon-enabled broadband light-harvesting enhancement for high-efficiency panchromatic dye-sensitized solar cells. *Nano Lett.*, 13(2):637–642, 2013.

[73] Rizia Bardhan, Nathaniel K. Grady, Joseph R. Cole, Amit Joshi, and Naomi J. Halas. Fluorescence enhancement by Au nanostructures: Nanoshells and nanorods. *ACS Nano*, 3(3):744–752, 2009.

[74] H. Aouani, O. Mahboub, E. Devaux, H. Rigneault, T. W. Ebbesen, and J. Wenger. Plasmonic antennas for directional sorting of fluorescence emission. *Nano Lett.*, 11(6):2400–6, 2011.

[75] K. Lance Kelly, Eduardo Coronado, Lin Lin Zhao, and George C. Schatz. The optical properties of metal nanoparticles: The influence of size, shape, and dielectric environment. *J. Phys. Chem. B*, 107:668–677, 2003.

[76] C. Sonnichsen, T. Franzl, T. Wilk, G. von Plessen, and J. Feldmann. Plasmon resonances in large noble-metal clusters. *New J. Phys.*, 4(93.1-93.8), 2002.

[77] Encai Hao, George C. Schatz, and Joseph T. Hupp. Synthesis and optical properties of anisotropic metal nanoparticles. *J. Fluoresc.*, 14(4):331–341, 2004.

[78] I. O. Sosa, C. Noguez, and R. G. Barerra. Optical properties of metal nanoparticles with arbitrary shapes. *J. Phys. Chem. B*, 107:6269–6275, 2003.

[79] Mohamed Haggui, Montacer Dridi, Jerome Plain, Sylvie Marguet, Henri Perez, George C. Schatz, Gary P. Wiederrecht, Stephen K. Gray, and Renaud Bachelot. Spatial confinement of electromagnetic hot and cold spots in gold nanocubes. *ACS Nano*, 6(2):12991307, 2012.

[80] Matthew Rycenga, Moon Ho Kim, Pedro H. C. Camargo, Claire Cobley, Zhi-Yuan Li, and Younan Xia. Surface-enhanced Raman scattering: Comparison of three different molecules on single-crystal nanocubes and nanospheres of silver. *J. Phys. Chem. A*, 113,:39323939, 2009.

[81] P. B. Johnson and R. W. Christy. Optical constants of the noble metals. *Phys. Rev. B*, 6(12):4370–4379, 1972.

[82] H. A. Atwater and A. Polman. Plasmonics for improved photovoltaic devices. *Nat. Mater.*, 9(3):205–213, 2010.

[83] S. Mukherjee, F. Libisch, N. Large, O. Neumann, L. V. Brown, J. Cheng, J. B. Lassiter, E. A. Carter, P. Nordlander, and N. J. Halas. Hot electrons do the impossible: plasmon-induced dissociation of H_2 on Au. *Nano Lett.*, 13(1):240–247, 2013.

[84] Q. Gan, F. J. Bartoli, and Z. H. Kafafi. Plasmonic-enhanced organic photovoltaics: breaking the 10% efficiency barrier. *Adv. Mater.*, 25(17):2385–2396, 2013.

[85] Craig F. Borhen and Donald R. Huffman. *Absorption and Scattering of Light by Small Particles*. Wiley, 1983.

[86] W. S. Chang, B. A. Willingham, L. S. Slaughter, B. P. Khanal, L. Vigderman, E. R. Zubarev, and S. Link. Low absorption losses of strongly coupled surface plasmons in nanoparticle assemblies. *Proc. Natl. Acad. Sci. USA*, 108(50):19879–19884, 2011.

[87] Jonathan A. Fan, Chihhui Wu, Kui Bao, Jiming Bao, Rizia Bardhan, Naomi J. Halas, Vinothan N. Manoharan, Peter Nordlander, Gennady Shvets, and Federico Capasso. Self-assembled plasmonic nanoparticle clusters. *Science*, 328(5982):1135–1138, 2010.

[88] Andrea Tao, Prasert Sinsermsuksakul, and Peidong Yang. Tunable plasmonic lattices of silver nanocrystals. *Nat. Nanotechnol.*, 2(7):435–440, 2007.

[89] Kyeong-Seok Lee and Mostafa A. El-Sayed. Gold and silver nanoparticles in sensing and imaging: Sensitivity of plasmon response to size, shape, and metal composition. *J. Phys. Chem. B*, 110:19220–19225, 2006.

[90] Csar Clavero. Plasmon-induced hot-electron generation at nanoparticle/metal-oxide interfaces for photovoltaic and photocatalytic devices. *Nat. Photon.*, 8(2):95–103, 2014.

[91] Stefan A. Maier. *Plasmonics: Fundamentals and Applications*. Springer, 2007.

[92] P. James Schuck. Hot electrons go through the barrier. *Nat. Nanotech.*, 8:799–800, 2013.

[93] F. Wang and N. A. Melosh. Plasmonic energy collection through hot carrier extraction. *Nano Lett.*, 11(12):5426–5430, 2011.

[94] S. K. Cushing, J. Li, F. Meng, T. R. Senty, S. Suri, M. Zhi, M. Li, A. D. Bristow,

and N. Wu. Photocatalytic activity enhanced by plasmonic resonant energy transfer from metal to semiconductor. *J. Am. Chem. Soc.*, 134(36):15033–15041, 2012.

[95] Mark W. Knight, Heidar Sobhani, Peter Nordlander, and Naomi J. Halas. Photodetection with active optical antennas. *Science*, 332(6030):702–704, 2011.

[96] Alejandro Manjavacas, Jun G. Liu, Vikram Kulkarni, and Peter Nordlander. Plasmon-induced hot carriers in metallic nanoparticles. *ACS Nano*, 8(8):7630–7638, 2014.

[97] Scott K. Cushing, Jiangtian Li, Joeseph Bright, Brandon T. Yost, Peng Zheng, Alan D. Bristow, and Nianqiang Wu. Controlling plasmon-induced resonance energy transfer and hot electron injection processes in metal@TiO_2 core-shell nanoparticles. *J. Phys. Chem. C*, 119(28):16239–16244, 2015.

[98] Feng Xian Xie, Huimin Su, Jian Mao, Kam Sing Wong, and Wallace C. H. Choy. Evolution of diffusion length and trap state induced by chloride in perovskite solar cell. *J. Phys. Chem. C*, 120(38):21248–21253, 2016.

[99] Huanping Zhou, Qi Chen, Gang Li, Song Luo, Tze-bing Song, Hsin-Sheng Duan, Ziruo Hong, Jingbi You, Yongsheng Liu, and Yang Yang. Interface engineering of highly efficient perovskite solar cells. *Science*, 345(6196):542–546, 2014.

[100] Dane W. deQuilettes, Sarah M. Vorpahl, Samuel D. Stranks, Hirokazu Nagaoka, Giles E. Eperon, Mark E. Ziffer, Henry J. Snaith, and David S. Ginger. Impact of microstructure on local carrier lifetime in perovskite solar cells. *Science*, 348(6235):683–686, 2015.

[101] Po-Wei Liang, Chien-Yi Liao, Chu-Chen Chueh, Fan Zuo, Spencer T. Williams, Xu-Kai Xin, Jiangjen Lin, and Alex K. Y. Jen. Additive enhanced crystallization of solution-processed perovskite for highly efficient planar-heterojunction solar cells. *Adv. Mater.*, 26(22):3748–3754, 2014.

[102] Jin Hyuck Heo, Hye Ji Han, Dasom Kim, Tae Kyu Ahn, and Sang Hyuk Im. Hysteresis-less inverted $CH_3NH_3PbI_3$ planar perovskite hybrid solar cells with 18.1% power conversion efficiency. *Energy Environ. Sci.*, 8(5):1602–1608, 2015.

[103] Y. Yamada, T. Nakamura, M. Endo, A. Wakamiya, and Y. Kanemitsu. Photocarrier recombination dynamics in perovskite $CH_3NH_3PbI_3$ for solar cell applications. *J. Am. Chem. Soc.*, 136(33):11610–11613, 2014.

[104] Jingbi You, Ziruo Hong, Yang Yang, Qi Chen, Min Cai, Tze-Bin Song, Chun-Chao Chen, Shirong Lu, Yongsheng Liu, Huanping Zhou, and Yang Yang. Low-temperature solution-processed perovskite solar cells with high efficiency and flexibility. *ACS Nano*, 8(2):1674–1680, 2014.

[105] Giles E. Eperon, Samuel D. Stranks, Christopher Menelaou, Michael B. Johnston, Laura M. Herz, and Henry J. Snaith. Formamidinium lead trihalide: a broadly tunable perovskite for efficient planar heterojunction solar cells. *Energy Environ. Sci.*, 7(3):982–988, 2014.

[106] Yantao Shi, Yujin Xing, Yu Li, Qingshun Dong, Kai Wang, Yi Du, Xiaogong Bai, Shufeng Wang, Zhijian Chen, and Tingli Ma. $CH_3NH_3PbI_3$ and $CH_3NH_3PbI_{3-x}Cl_x$ in planar or mesoporous perovskite solar cells: Comprehensive insight into the dependence of performance on architecture. *J. Phys. Chem. C*, 119(28):15868–15873, 2015.

[107] Vinay sharma, Sigalit Aharon, Itay Gdor, Chunfan Yang, Lioz Etgar, and Sanford Ruhman. New insights into exciton binding and relaxation from high time resolution ultrafast spectroscopy of $CH_3NH_3PbI_3$ and $CH_3NH_3PbBr_3$ films. *J. Mater. Chem. A*, 4(9):3546–3553, 2016.

[108] P. Piatkowski, B. Cohen, F. Javier Ramos, M. Di Nunzio, M. K. Nazeeruddin, M. Gratzel, S. Ahmad, and A. Douhal. Direct monitoring of ultrafast electron and

hole dynamics in perovskite solar cells. *Phys. Chem. Chem. Phys.*, 17(22):14674–14684, 2015.

[109] T. C. Sum, N. Mathews, G. Xing, S. S. Lim, W. K. Chong, D. Giovanni, and H. A. Dewi. Spectral features and charge dynamics of lead halide perovskites: Origins and interpretations. *Acc. Chem. Res.*, 49(2):294–302, 2016.

[110] Xiaofan Deng, Xiaoming Wen, Shujuan Huang, Rui Sheng, Takaaki Harada, Tak W. Kee, Martin Green, and Anita Ho-Baillie. Ultrafast carrier dynamics in methylammonium lead bromide perovskite. *J. Phys. Chem. C*, 120(5):2542–2547, 2016.

[111] Lydia H. Manger, Matthew B. Rowley, Yongping Fu, Alexander K. Foote, Morgan T. Rea, Sharla L. Wood, Song Jin, John C. Wright, and Randall H. Goldsmith. Global analysis of perovskite photophysics reveals importance of geminate pathways. *J. Phys. Chem. C*, 121(2):1062–1071, 2017.

CHAPTER 3

MORPHOLOGICAL MODULATION OF BIMETALLIC NANOSTRUCTURES FOR ACCELERATED CATALYSIS

Adapted from H. F. Zarick, W. R. Erwin, J. Aufrecht, A. Coppola, B. R. Rogers, C. L. Pint, and R. Bardhan, *J. Mater. Chem. A*, **2014**, *2*, 7088 with permission from The Royal Society of Chemistry.

3.1 Summary

Bimetallic nanostructures are of significant technological interest due to their ability to uniformly combine properties of two distinct metals giving rise to multimodal characteristics with promising potential for in plasmonically enhanced PV systems. In this chapter, we have synthesized Au/Ag core/shell bimetallic nanostructures and investigated the role of temperature in controlling the morphological evolution. By increasing the reaction temperature from 35 °C to 80 °C, the edge morphologies of Au/Ag nanostructure evolved from rounded to sharp corners which directly impact the catalytic properties. The size of the bimetallic nanostructures also increased when the temperature was raised due to faster Ag^+ reduction along specific crystallographic planes, giving rise to red shifts in the plasmon resonance. The catalytic activity of Au/Ag nanostructures was compared to commercially purchased Ag nanospheres for the reduction of 4-nitrophenol to 4-aminophenol with $NaBH_4$. The reaction rate for 4-nitrophenol reduction was significantly higher on Au/Ag-NSs relative to the Ag nanospheres, while the induction time was lowest on the Ag nanospheres. These observations were attributed to the simultaneous effects of (i) surface area available for catalytic reaction, (ii) crystallographic facets supporting the nanostructures, (iii) surface ligands, and (iv) composition of the metal nanostructures.

3.2 Introduction

Heterogeneous catalysis is pivotal to many chemical transformations. Shape and size variable noble metal nanostructures have been extensively explored in catalysis, where the morphology of the nanostructure dominates the catalytic pathways, stability, selectivity, and reaction kinetics.[1, 2, 3] The surface structure of metal nanocatalysts is governed by the crystallographic facets that direct the shape of the nanostructure and the energetics of the catalytic reaction.[4, 5, 6] For example, Ag nanocubes bound by the $\{100\}$ facets have demonstrated higher catalytic activity and selectivity relative to spherical nanoparticles bound by $\{111\}$ facets for oxidation of styrene.[7] The catalytic reduction of aromatic nitro compounds, such as 4-nitrophenol (4-NP) to the corresponding amino derivative, 4-aminophenol (4-AP), using sodium borohydride ($NaBH_4$) has been well-studied as a model reaction as it selectively produces only one product.[2, 8, 9, 10] This pseudo first-order reaction is known to be catalyzed only in the presence of metal nanocatalysts since the metal surface relays electrons from the BH_4^- ions to 4-nitrophenolate ($4\text{-}NP^-$) ions.[11] In this reaction, BH_4^- ions react with the metal nanocatalyst surface and transfer a hydrogen species to the surface of the catalyst. Simultaneously $4\text{-}NP^-$ ions also adsorb on the nanocatalyst surface where it is reduced to 4-AP by the surface hydrogen species. This is essentially the rate-determining step. In the final step of the catalytic reaction 4-AP is detached from the surface. This entire catalytic reaction is studied by monitoring the change in the absorbance of the $4\text{-}NP^-$ ions at 400 nm. The catalytic reduction of 4-NP is highly dependent on the crystalline facets of the metal nanostructures, the ligands present on the surface, and the composition of the metal nanocatalyst. Cubic-shaped metal nanostructures bound by the [100] planes have been shown to rapidly catalyze 4-NP due to the high surface area of nanocubes and high surface energy of $\{100\}$ facets relative to other low-index facets $\{111\}$ and $\{110\}$.[12, 13] Surface ligands also play a key role in controlling the catalytic pathway; long-chain bulky ligands pose a greater diffusion barrier for the availability of active sites slowing the adsorption of BH_4^- and $4\text{-}NP^-$ ions. This gives rise to a long induction

time, t_0, which is the time needed for the catalytic reaction to initiate.[1, 3, 10] Removal of ligands may reduce t_0, but it also results in surface restructuring, degradation, and poor stability of the nanocatalysts.[1, 14, 15] Finally, the composition of the nanostructure also strongly influences the rate of catalysis where bimetallic nanocatalysts, either in core-shell or alloy form, have demonstrated higher catalytic rates and faster catalytic induction due to the synergistic electronic effects mediated by a combination of two metals.[2, 8, 16, 17] Additionally, for core-shell nanostructures, the lattice mismatch between the core and shell material may induce strain at the interface; interfacial strain has been shown to enhance catalytic rates in dual-metal systems.[18, 19] In this work, we discuss the synthesis and accelerated catalysis with bimetallic Au/Ag nanostructures.

Bimetallic nanostructures form an important class of nanomaterials linked by their ability to manipulate light in unique ways.[20] Such dual-metal nanostructures may either be arranged in a random alloy[21] or in a structured core/shell architecture where each constituent metal contributes to distinct spectral characteristics. These core/shell nanostructures can be engineered to exhibit hybrid catalytic, optical, and electronic properties not achievable in monometallic architectures.[1, 22, 23, 24, 25, 26, 27, 28, 29, 30, 31, 32, 33, 34, 35] For example, Au/Pd nanostructures were constructed and the H_2 uptake trajectories were studied by observing the shifts in the plasmon resonance of the Au core while the Pd shell adsorbed and released hydrogen.[36] Au/Pt core/shell nanoparticles enabled enhanced electrocatalysis for oxygen reduction reaction.[37] Among bimetallic systems, Au/Ag nanostructures have been extensively explored due to their enhanced optical characteristics attributed to hybridized electronic and lattice effects.[29] Au/Ag nanostructures offer several advantages including (*i*) multiple plasmon resonant peaks attributed to the presence of dual metals enabling multiplexed optical manipulation, (*ii*) enhanced electromagnetic near-fields, and far field properties of absorption and scattering facilitating superior light harvesting characteristics, (*iii*) stronger radiative properties since Ag is less lossy relative to Au in the visible region of the spectrum, (*iv*) enhanced catalytic abilities due to syner-

gistic electronic effects of the two metals, and (*v*) the ability to dynamically modulate properties by altering the Au/Ag core/shell ratio without modifying the overall dimensions.[23, 28, 35] The ability to controllably manipulate the plasmon resonances from the dipole up makes this class of nanostructures beneficial for a range of applications from catalysis,[2] to refractive index sensing,[33] to surface enhanced spectroscopies.[38] To successfully realize these technological applications, bimetallic nanostructures are being synthesized with increasingly complex geometries following a range of synthetic strategies including galvanic replacement reactions,[39, 40, 41, 42] seed-mediated growth processes,[23, 35, 43] simultaneous reduction of the metals,[25, 44, 45] and by thermal annealing processes.[34]

Here we have synthesized bimetallic Au/Ag nanostructures and studied the role of temperature in directing the morphological evolution and growth along different crystallographic planes. The effect of shape modulation of bimetallic nanostructures was investigated on the catalytic reduction of 4-NP to 4-AP with sodium borohydride $NaBH_4$). By increasing the reaction temperature from 35 °C to 80 °C, we observe three distinct effects: (*i*) the edge morphologies of Au/Ag nanostructure evolve from rounded to sharp corners which directly impacts the catalytic properties, (*ii*) the size of the bimetallic nanostructures increases due to rapid Ag^+ reduction along specific crystallographic planes giving rise to red shifts in the plasmon resonance, and (*iii*) spontaneous nucleation at high temperatures (80 °C) gives rise to a mixture of shapes and polydispersity. This suggests that a critical temperature exists where Au/Ag nanostructures should be synthesized to achieve the desired induction time and reaction rate for catalytic reduction of 4-nitrophenol. The catalytic reduction of 4-NP to 4-AP was significantly higher on Au/Ag-NSs relative to the commercially purchased Ag nanospheres. This observation was attributed to effects of (*i*) the available surface area, (*ii*) crystallographic facets, (*iii*) surface ligands, and (*iv*) metal composition; these factors are all discussed in details.

3.3 Results and Discussion

Bimetallic Au/Ag core/shell nanostructures were synthesized by a seed-mediated growth process. The gold nanocrystal (Au-NC) core was synthesized by utilizing CTAB ligands as a shape directing agent in aqueous media following a procedure previously described.[46, 47] The Au-NC reaction mixture consisted of both rounded corner nanocubes ($\sim$60%), and truncated nanocubes ($\sim$40%) of 44$\pm$3 nm edge length as shown in the transmission electron microscopy (TEM) image in Figure 3.1a. Truncated nanocubes have been observed previously in CTAB mediated Au-NC synthesis.[46, 48, 49] The Au-NC cores were then transferred to CTAC surfactant solution and Ag growth was promoted in the presence of Ag^{+} ions and ascorbic acid. The Ag growth resulted in bimetallic Au/Ag nanostructures (Au/Ag-NSs) consisting of cubic and pyramidal shape (Figure 3.1b). The dimensions of the Au/Ag-NSs are summarized in Table 3.1. It is evident that subtle changes in shape and corresponding crystal planes of the Au-NC core govern the final geometry of the Au/Ag-NSs. To assess the role of crystal planes in controlling Au/Ag-NSs morphology, we performed high-resolution TEM. The TEM images (Figure 3.1c-d) and corresponding FFT with their measured d-spacing demonstrate that the Au nanocube cores have a measured d-spacing corresponding to $\{100\}$ crystal facets as observed in previous studies.[46] The truncated nanocube cores have a measured d-spacing corresponding to $\{111\}$ crystal facets along the edges. Both shapes have rounded corners bound by the $\{110\}$ facets. The high resolution TEM images of the Au/Ag nanocubes (Figure 3.1e) and Au/Ag nanopyramids (Figure 3.1f) indicate that Ag growth occurs along the [100] plane of the Au nanocube cores giving rise to the Au/Ag nanocubes, while for the truncated Au cores growth occurs along the [111] crystal planes generating Au/Ag nanopyramids. The edge morphology of the bimetallic cubes and pyramids, straight vs. rounded, is driven by temperature, which will be discussed below.

The spectral characteristics of the Au/Ag nanostructures were measured to examine the impact of the two shapes, nanocubes and nanopyramids, on the plasmon resonance. Two

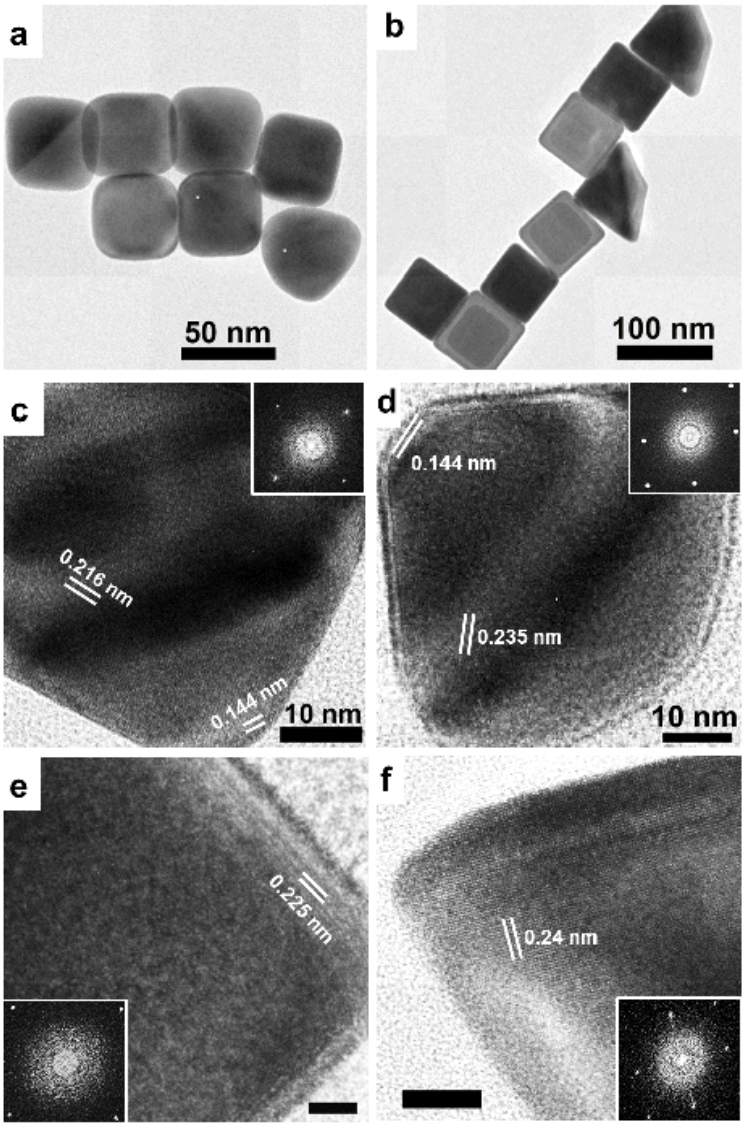

Figure 3.1: TEM images of (a) Au nanocubes, (b) Au/Ag core/shell bimetallic nanostructures. High magnification TEM image and corresponding FFT (inset) of (c) Au nanocube and d-spacing corresponding to $\{100\}$ crystal plane, rounded corners correspond to $\{110\}$ planes, (d) Au truncated nanocube and d-spacing corresponding to $\{111\}$ crystal plane, and rounded corner correspond to $\{110\}$, (e) Au/Ag nanocube, and (f) Au/Ag nanopyramid. The scale bar is 10 nm in e-f. The FFT and d-spacing in (e-f) clearly indicate that the Ag atoms grow along the same crystallographic planes as the Au core.

Table 3.1: The size of bimetallic nanocubes and nanopyramids is provided as a function of reaction temperature.

Temperature (°C)	**Size of Au/Ag Nanostructures (nm)**		
	Nanocube	Nanopyramid (base length)	Nanopyramid (side length)
28	61 ± 4	84 ± 5	66 ± 4
35	63 ± 5	88 ± 6	73 ± 5
55	65 ± 3	93 ± 4	80 ± 4
65	67 ± 3	98 ± 4	86 ± 4
80	70 ± 3	106 ± 5	95 ± 5

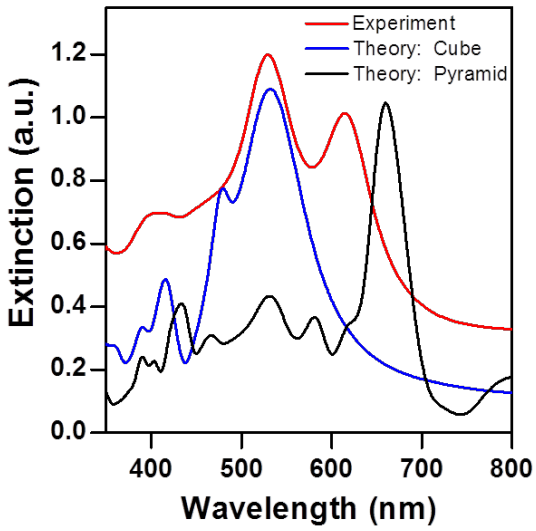

Figure 3.2: Experimental and theoretical extinction spectra of Au/Ag nanostructures. The red line corresponds to experimental spectrum. The blue line corresponds to FDTD simulated spectrum of bimetallic nanocube and black line corresponds to simulated spectrum of bimetallic nanopyramid.

prominent plasmon peaks are observed; one centered at 535 nm and another at 615 nm (Figure 3.2). To understand the observed resonances, we performed finite difference time domain (FDTD) simulations to assign the experimentally observed modes to the nanostructures present (Figure 3.2). Calculations were performed on single particles in water using a total-field scattered-field plane wave source. The details of the simulations are provided in the supporting information. Calculated spectrum of bimetallic nanocubes (Figure 3.2, blue spectrum) show a dipolar mode at 534 nm, a quadrupolar resonance at 480 nm, and other higher order multipole modes associated with the nanocube corners.[35] Bimetallic nanopyramids (Figure 3.2, black spectrum) have a dipolar resonance at 650 nm, a quadrupolar mode at 580 nm, a mode at 531 nm likely associated with the Au core, and other higher order multipolar modes associated with the corners. The peak positions observed experimentally match well with the theoretical dipole resonance of Au/Ag nanocubes, however, we note that the dipolar and quadrupolar resonance are overlapped in experiments. This may be attributable to (i) variations in nanocube size in the reaction mixture which gives rise to peak broadening and (ii) an offset of the Au core within the Ag shell which gives rise to symmetry breaking in these plasmonic nanostructures (Figure 3.3). Structural irregularities arising during the synthesis process break the cubic symmetry of the system, such as an outer shell of non-uniform thickness or a nonconcentric alignment of the core and shell. This promotes quadrupole modes to hybridize with dipolar modes, thus strongly enhancing their intensity. In the case of the Au/Ag nanopyramids, the experimental peaks are also blue-shifted relative to the calculated resonances. This is again attributed to variation in sizes in the reaction mixture and symmetry breaking in the pyramidal structures (Figure 3.3c), resulting in hybridized dipolar-quadrupolar modes.

To understand the growth process of the Ag shell around the Au core, high angle annular dark field (HAADF) TEM images was obtained and elemental mapping showing Au and Ag was performed at different time points of the reaction (Figure 3.4). Elemental mapping in TEM demonstrated that at 35 °C, the Ag growth is initiated within 2 minutes into the

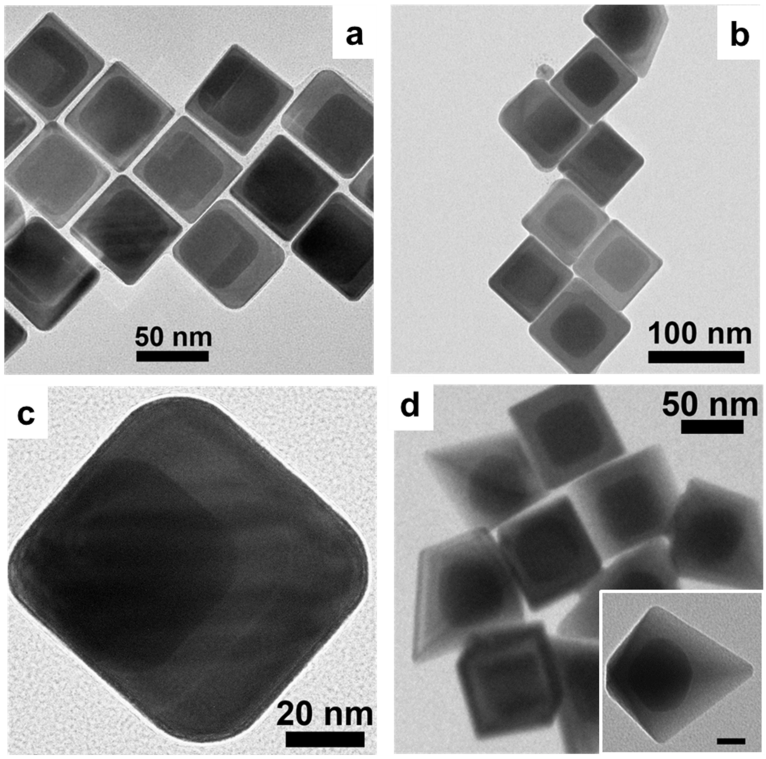

Figure 3.3: TEM images of Au/Ag nanostructures showing symmetry breaking in the nanocubes with an offset core (a, c) 35 °C Au/Ag-NSs, (b) 65 °C Au/Ag-NSs, and in the nanopyramids with an offset core (c).

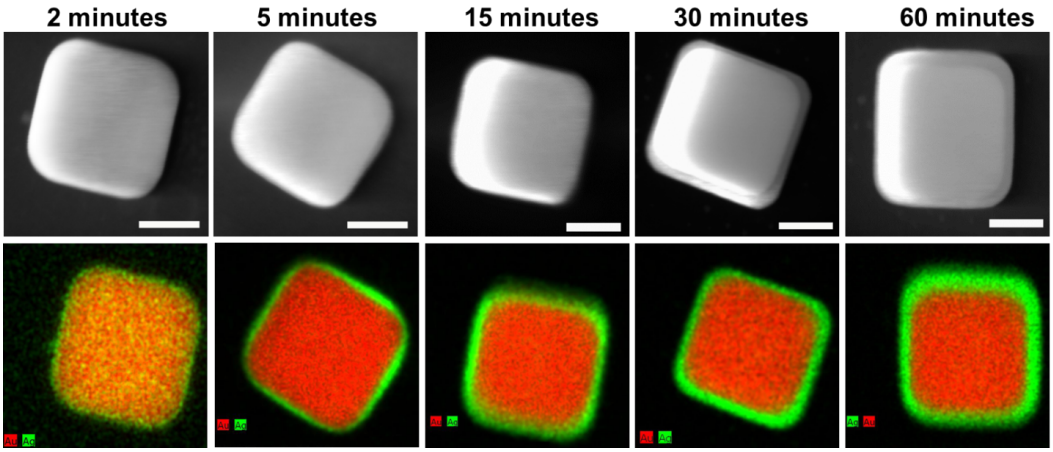

Figure 3.4: (Top row) HAADF TEM images and (bottom row) corresponding elemental map showing Au (red) and Ag (green) in STEM images demonstrating Ag growth on Au core at different time points of the reaction. The reaction time point is indicated on the top. The scale bar is 20 nm in all the panels.

reaction process and a uniform $\sim$1 nm Ag layer is formed around the Au core. Contrary to our expectation that nucleation of Ag atoms should start at the corners due to low steric hindrance, analysis of the elemental maps at the 2 and 5 minutes time points revealed that Ag shell growth occurred by a layer-by-layer assembly generating a smooth, uniform 10 nm shell within 60 minutes. The Au/Ag nanopyramids follow a similar trend of growth process where Ag shell grows on the truncated Au cores via layer by layer growth (Figure 3.5). The relatively slow growth kinetics at 35 °C is due to both the insufficient thermal energy resulting in slow nucleation of Ag^+ ions in solution, and also due to the presence of $\{110\}$ facets along the rounded corners and edges of the Au cores which has the lowest energy and is the least reactive crystallographic facet.[50]

Since the [110] planes are least reactive and catalytically less active, we modulated the reaction parameters to maximize the $\{100\}$ and $\{111\}$ facets and minimize the $\{110\}$ facets. Temperature induced changes in nanoparticle shape have been extensively studied in monometallic nanostructures, such as Au nanorods,[51, 52, 53, 54] but is poorly understood in bimetallic systems. We varied the reaction temperature of Ag growth between 35-80 °C and the shape modulation in the bimetallic nanostructures was examined

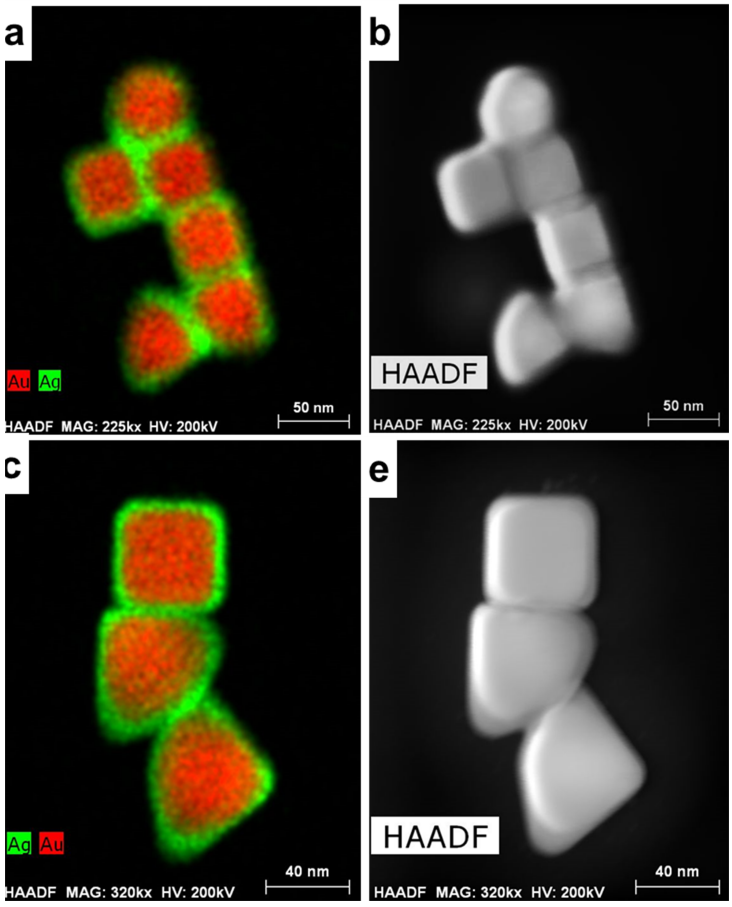

Figure 3.5: Elemental map showing Au and Ag in STEM images (left) and corresponding HAADF TEM images (right) of multiple particles at (a,b) 30 mins and (c,d) 45 mins post silver growth reaction.

by scanning electron microscopy (SEM). SEM images (Figure 3.6a-d) and size analysis (Table 3.1) show three different effects of temperature. First, at low temperature, 35 °C, Au/Ag nanocubes and Au/Ag nanopyramids show rounded corners. However, as the temperature is increased to 55 °C and 65 °C the morphology changes to sharp corners and edges. This clearly demonstrates that as more thermal energy is introduced into the system, the growth along the [100] and [111] planes progresses more rapidly relative to the less reactive [110] planes eliminating the rounded corners at higher temperatures (Figure 3.6e). Second, as the temperature is further increased to 80 °C, spontaneous nucleation occurs resulting in polydispersity and formation of 5-fold twinned Au/Ag nanorods (Figure

3.6d,e). In seed-mediated growth process, spontaneous nucleation occurs when metal salts spontaneously reduce in homogenous solution without the surface catalysis of the seeds present in solution.[55] At high temperature, growth dynamics increases and the reduction rate of Ag atoms is accelerated. This implies that the same amount of Au seed is not sufficient and cannot provide enough deposition sites for Ag atoms at a high generation rate.[55, 56] This gives rise to spontaneous nucleation where excess Ag is deposited on cubic Au cores resulting in the formation of rods. To confirm this analysis, we monitored the growth dynamics at different temperatures by examining the change in the extinction spectrum of Au/Ag nanostructures.

The time-dependent growth of Au/Ag-NSs was monitored and the spectral peak intensity of the dipole resonance of Au/Ag nanopyramids was evaluated at different time points (Figure 3.6f-g). Representative growth curves obtained at 65 °C is shown in Figure 3.6f. At low reaction temperatures (35 degree C) due to insufficient thermal energy, reaction processes are slow and growth dynamics follow a sigmoidal growth curve which was fit to a logistic function:

$$y = \frac{a}{1 + e^{-k(t-t_c)}} \tag{1}$$

where a is the amplitude, k is the exponential growth constant, and t_c is the growth time at half the amplitude. The logistic function fitted to the 35 °C growth dynamics is defined by four distinct parameters:[57] the lag phase characterizes the slow rate of reduction of Ag^+ ions [58] which is accompanied by a slow nucleation of Ag^0 atoms; this is followed by exponential growth phase which is dominated by a diffusion mechanism where Ag atoms rapidly diffuse in solution and locate deposition sites on the preferred Au crystal planes, and subsequently develop a uniform Ag layer; as the diffusion process slows down and most of the available Ag^+ ions have reduced and Ag atoms have already deposited, the formation rate diminishes which is characterized by the diminishing growth phase; and finally growth is completed and no change in the peak amplitude is observed which defines the saturation phase. At reaction temperatures $\geq$ 55 °C, burst nucleation followed by an

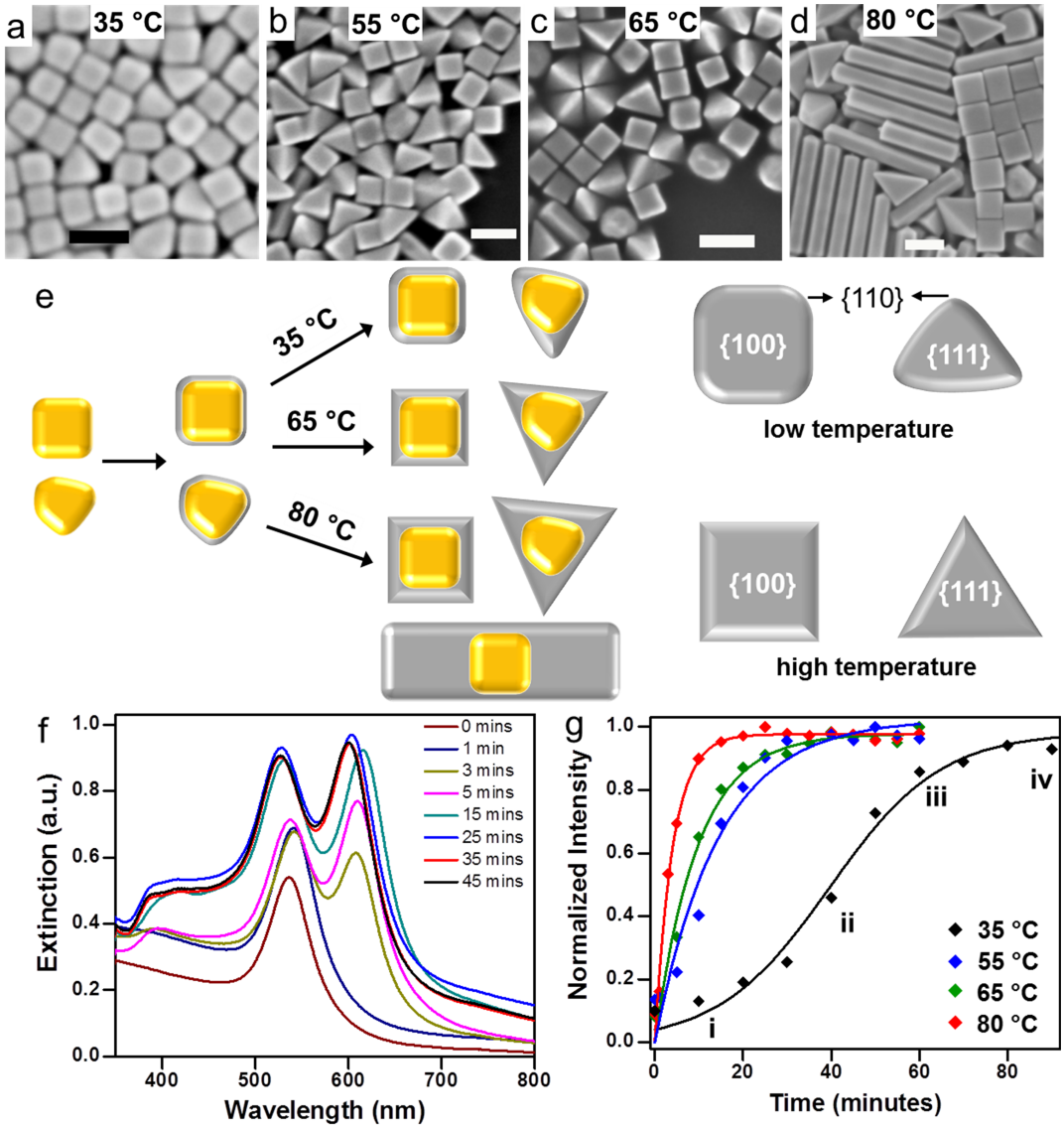

Figure 3.6: (a-d) SEM images of Au/Ag nanostructures generated at different temperatures. Scale bar is 100 nm in all images. (e) Left: Schematic representation of growth dynamics of Au/Ag nanostructures at different temperatures. Right: Schematic showing the crystal planes of Ag shell for nanocubes/nanopyramids with rounded corners generated at 35 °C and with sharp corners generated at 65 °C and above. (f) Plasmon peak evolution of Au/Ag nanostructures as a function of time synthesized at 65 °C. (g) Growth kinetics at various temperatures. Growth at 35 °C was fit to a sigmoidal logistic function (eq. 1). The different phases in a sigmoidal growth: lag phase (*i*), exponential phase (*ii*), diminishing growth phase (*iii*), and final saturation phase (*iv*), are indicated. Growth at higher temperatures were fit to an exponential growth function (eq. 2).

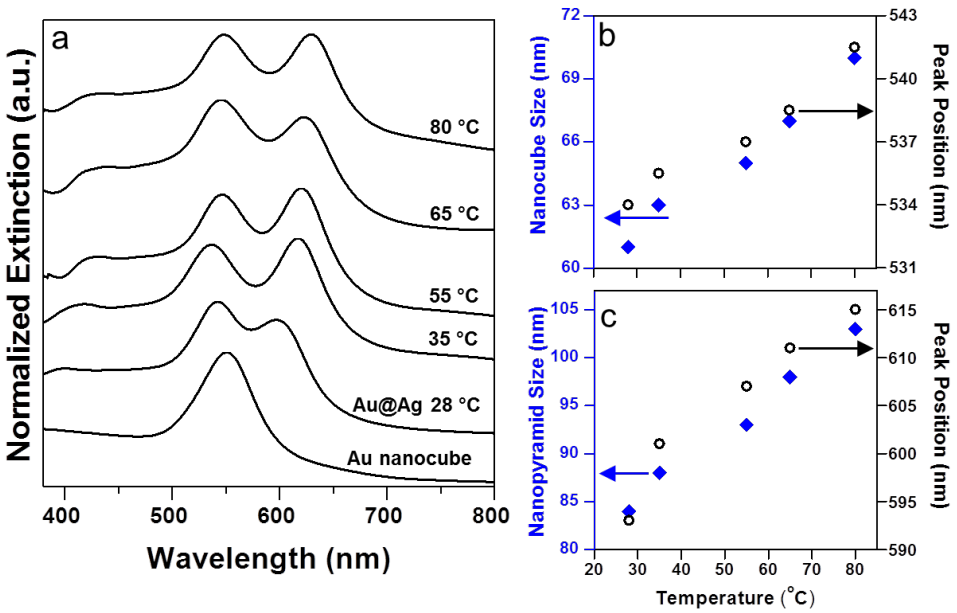

Figure 3.7: (a) Temperature dependent shifts in plasmon resonance of Au/Ag nanostructures. The plasmon resonance of Au nanocubes is also shown. Shifts in peak position and corresponding shift in nanostructure size as a function of temperature for (b) bimetallic nanocubes and (c) bimetallic nanopyramids. The base length of the pyramids is shown.

exponential growth occurs until growth terminates, which characterizes the completion of Ag shell on the Au core. The exponential growth curves were fit to a function given by:

$$y = a(1 - e^{-kt}) \tag{2}$$

where a is the amplitude and k is the rate constant. It is evident growth rate accelerates rapidly with increasing temperature. Due to the rapid exponential growth rate at 80 °C (Figure 3.6g), spontaneous nucleation is expected which confirms the polydispersity observed in the SEM image (Figure 3.6d).

Finally, raising the reaction temperature also results in an increase in the size of the bimetallic nanostructures (Table 3.1) and a red-shift in the plasmon resonance. The increase in the Au/Ag-NSs size is attributable to the faster reduction of Ag^{+} salts at higher temperatures. However, it is notable, the dimensions of Au/Ag nanocubes only incrementally increases while the size of Au/Ag nanopyramids rapidly increases with temperature.

This observed trend is due to two different phenomena: (i) The [100] crystalline plane of Au has higher energy relative to [111] plane which gives rise to a slower Ag reduction and growth along the $\{100\}$ facets.[59] Therefore as the temperature increases, the size of the nanopyramids bound by the [111] plane increases faster than the nanocubes bound by the [100] planes. (ii) CTAB and CTAC are known to bind strongly to the $\{100\}$ facet relative to other crystallographic planes of noble metals.[30, 46, 51] This consequently slows down the growth process on the crystal planes where CTAC is more tightly bound, resulting in a small change in size of Au/Ag nanocubes relative to faster increase in size of the nanopyramids.

The increase in size with increasing temperature is accompanied with a red-shift in the plasmon resonance (Figure 3.7a). The shift to longer wavelengths is attributed to phase-retardation effects which arise from the oscillations of the electron cloud around the Au/Ag-NSs.[60, 61] The amplitude of the electron oscillation increases with increasing particle size, which subsequently increases the period of each oscillation, defined as the plasmon lifetime. This increase in plasmon lifetime is accompanied with a decrease in the frequency of the waves, which red-shifts the plasmon wavelength. The increase in plasmon lifetime with increasing Au/Ag-NSs size also gives rise to broadening and damping of plasmon resonances as observed in Figure 3.7. The increase in particle dimensions and corresponding shifts in peak position of Au/Ag nanocubes (Figure 3.7b) and nanopyramids (Figure 3.7c) as a function of temperature are analogous supporting our above discussion on temperature mediated size-controlled plasmon shifts. Note stronger peak shifts are observed for bimetallic nanopyramids relative to the nanocubes which is directly associated with the very small change in nanocube size with temperature (Table 3.1).

In addition to temperature, we also varied the overall morphology of the Au/Ag-NSs by changing the geometry of the Au-NC core, as well as by increasing the concentration of Ag^+ salts. The dimensions of the Au-NC core were varied by mixing different amounts of seed in the growth solution while keeping all other reaction parameters constant (Figure

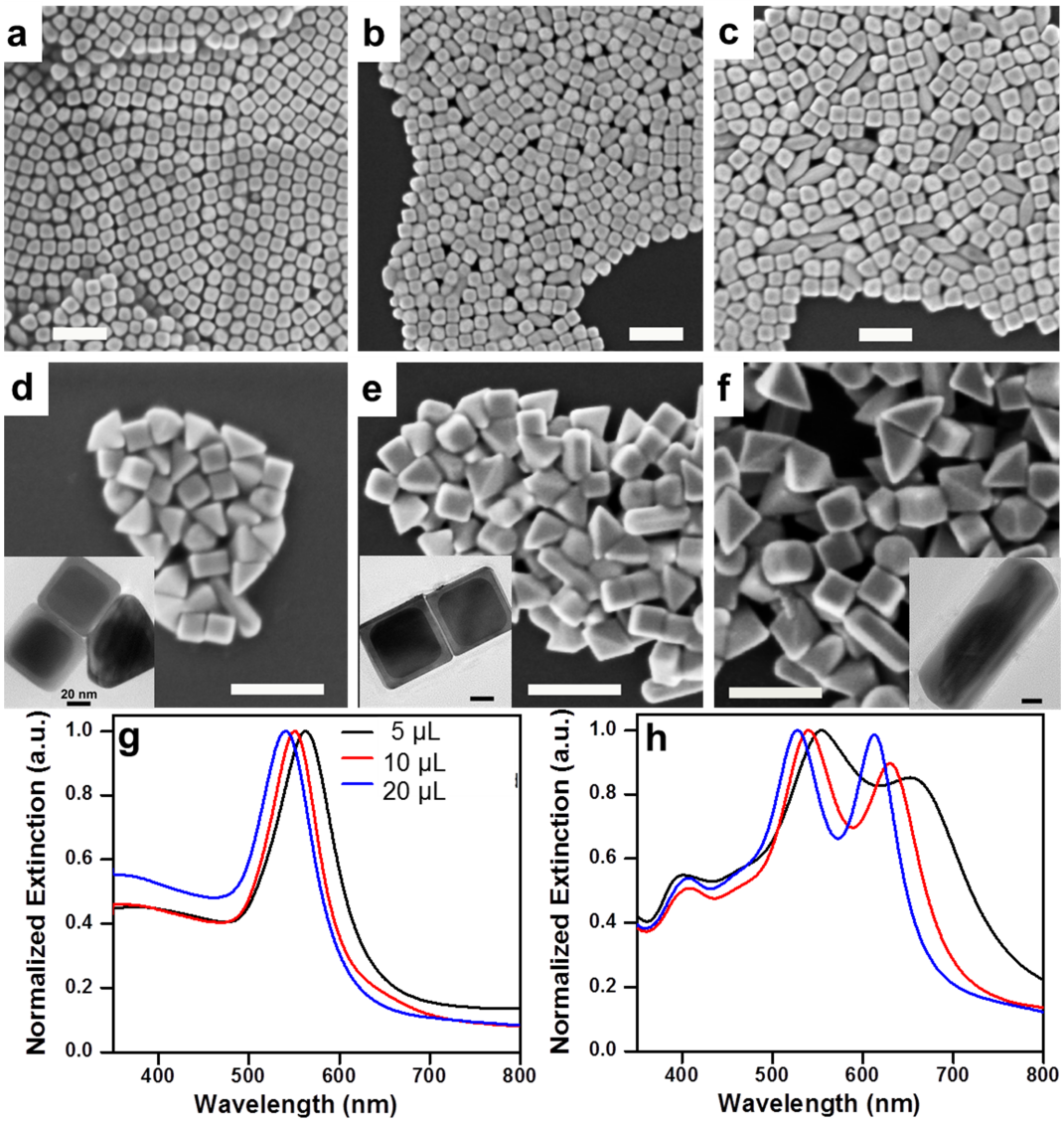

Figure 3.8: SEM images of Au nanocrystals of increasing sizes synthesized with different amounts of precursor. (a) 20 μL precursor, (b) 10 μL precursor, and (c) 5 μL precursor. (d-f) SEM images of Au/Ag nanostructures synthesized with Au nanocrystals shown in (c), (d) and (e). Corresponding TEM images are provided in inset. The scale bar is 200 nm in all SEM images and 20 nm in all TEM images. (g) Plasmon resonance of Au nanocrystals of different sizes synthesized by addition of different amounts of precursor. The precursor volumes are provided. (h) Au/Ag nanostructures synthesized with Au nanocrystals of different sizes. The spectra are color coded with (g).

Table 3.2: Size distribution of Au nanocrystals at different Au seed volume and corresponding size of Au/Ag nanostructures synthesized at 65 °C.

Au Seed Volume (μL)	**Size of Au Nanocrystals (nm)**		**Size of Au/Ag Nanostructures (nm)**		
	Cubes	Truncated Cubes	Cubes	Pyramids (base length)	Pyramids (side length)
20	45 ± 3	46 ± 5	67 ± 3	98 ± 4	86 ± 4
10	52 ± 4	55 ± 6	76 ± 4	110 ± 5	93 ± 5
5	63 ± 3	67 ± 4	87 ± 4	125 ± 7	100 ± 7

3.8). By altering the seed volume from 20 L (the standard reaction condition) to 10 μL and 5 μL respectively, the Au-NC edge length increased for all the particle shapes in the solution mixture (Figure 3.8a-c). The resulting edge lengths of the Au-NCs and corresponding dimensions of the Au/Ag-NSs are provided in Table 3.2. The increase is size gives rise to a red-shift in the plasmon resonance due to phase retardation effects (Figure 3.8g). The increase in size was also accompanied with a high degree of polydispersity and evolution of elongated rhombic prisms in the solution. The increase in nanocrystal size with reduction in seed volume is a typical characteristic of seed-mediated growth process; as the ratio of seed to growth solution volume decreases, the Au^{3+} ions have fewer nucleation sites to promote additional growth. This also results in spontaneous nucleation since the same amount of Au seed is not sufficient and cannot provide enough deposition sites for Ag atoms giving rise to polydispersity. This is an innate limitation of seed-mediated growth process. The different sized Au-NCs were coated with Ag at 65 °C, and the corresponding bimetallic nanostructures are shown in Figure 3.8d-f. The dimensions of the Au/Ag-NSs increased with increase in Au core size. A large density of Au/Ag nanorods was observed for the larger Au-NCs where the elongated rhombic prisms formed the core of the nanorods (Figure 3.8d-f). An increase in Au/Ag-NS size with increasing core size results in a red-shift in the plasmon resonance attributable to increased polarizability and phase retardation effects (Figure 3.8h). The increase in polydispersity with increasing Au-NC size also results in inhomogeneous broadening of both the plasmon peaks.

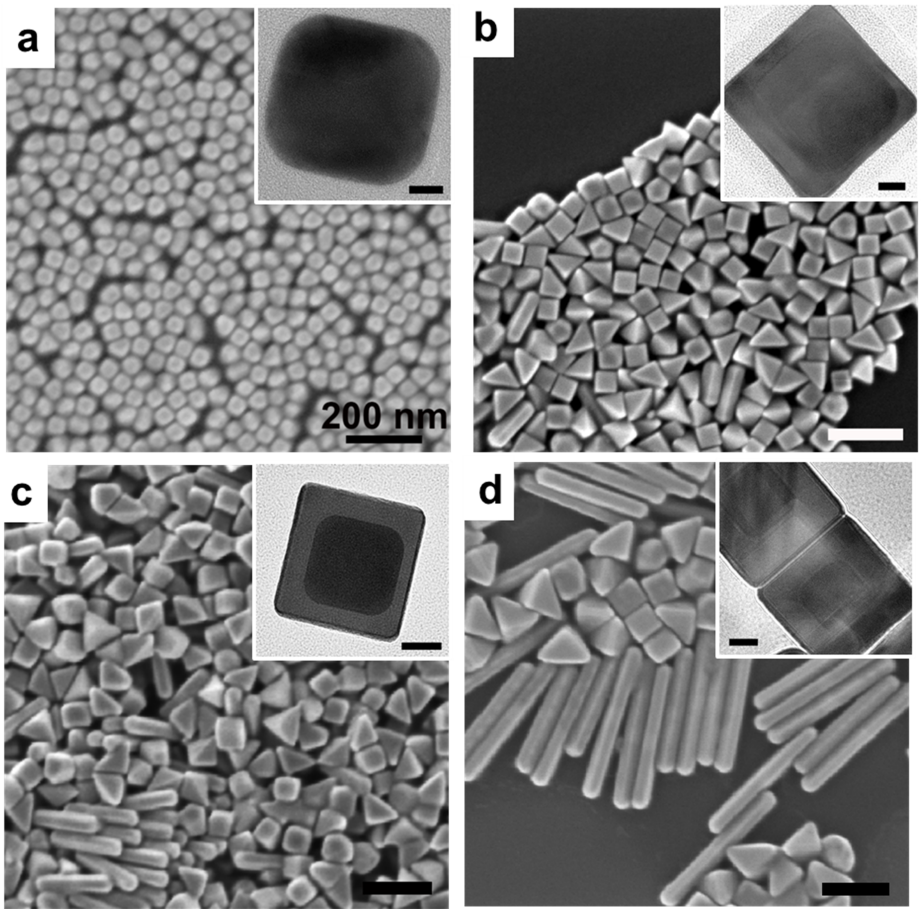

Figure 3.9: SEM images and TEM images provided in inset of Au/Ag nanostructures fabricated with different concentrations of $AgNO_3$ while keeping Au nanocube concentration constant. The $AgNO_3$ concentrations are (a) 0.2 μ mol, (b) 0.5 μmol, (c) 1 μmol, and (d) 2 μmol. The scale bar of SEM images is 200 nm in all images. The scale bar of TEM images in inset is 10 nm in (a,b) and 20 nm in (c, d).

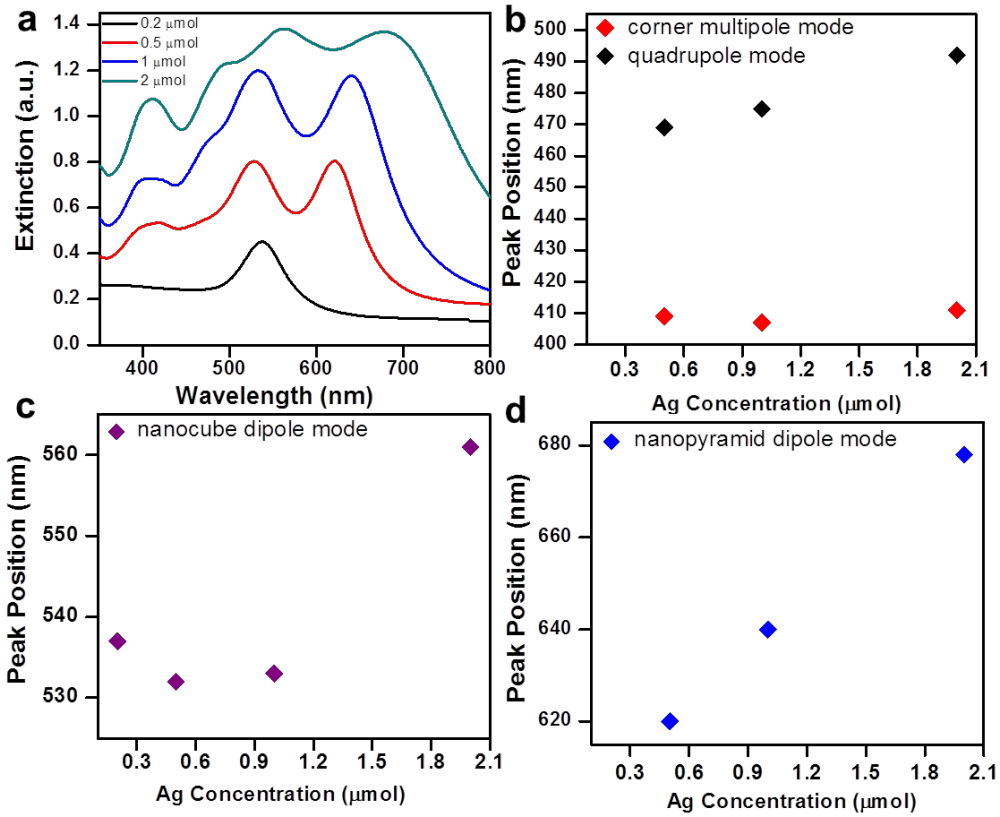

Figure 3.10: (a) Plasmon resonances of Au/Ag nanostructures fabricated with different concentrations of $AgNO_3$ while keeping Au nanocube concentration constant. The $AgNO_3$ concentrations are indicated on the left. Plasmon peak position as function of $AgNO_3$ concentration (b) corner multipole mode and quadrupole mode, (c) for the nanocube dipole mode, and (d) for the nanopyramid dipole mode.

Further, we also varied the $AgNO_3$ concentration to 0.2, 0.5, 1, and 2 μmoles while keeping all other reaction parameters constant to evaluate Ag^+ role in determining the growth. At low Ag^+ concentration (0.2 μmoles) a very thin Ag shell is formed around the Au core (Figure 3.9a inset); the thickness of the Ag shell is insufficient to appear in the optical spectra. The plasmon resonance does not have the characteristic Ag resonance peak at $\sim$410 nm for 0.2 μmoles of $AgNO_3$ (Figure 3.10a). With increasing Ag^+ concentration the Ag shell thickness increases resulting in an overall increase in size of the Au/Ag-NSs (Figure 3.9b-d). This is accompanied with a significant shift in the dipolar resonances (Figure 3.10a, c-d) of the Au/Ag nanocubes ($\sim$540 nm) and nanopyramids ($\sim$620 nm). The corner multipole ($\sim$411 nm) mode becomes stronger with increasing Ag shell thickness (Figure 3.10a-b). The quadruple mode of the nanocubes at 480 nm becomes stronger with increasing Ag shell thickness as well as red-shifts to longer wavelengths (Figure 3.10b). The red-shift in the plasmon resonance is attributable to phase retardation effects and an increase in polarizability of light with increasing size. The phase-retardation effects with increasing size also enables higher order modes to couple with dipole modes and increase in intensity which explains the enhancement in the corner multipole ($\sim$ 411 nm) and quadrupole ($\sim$480 nm) modes. Finally, at very high Ag^+ concentration spontaneous nucleation occurs resulting in the formation of Au/Ag nanorods (Figure 3.9d). This gives rise to multipolar modes in the extinction spectrum and strong red-shifts (Figure 3.10).

The Au/Ag-NSs synthesized at different temperatures were utilized for the catalytic reduction of 4-NP to 4-AP in the presence of $NaBH_4$. The alkaline environment created by the addition of BH_4^- ions to the 4-NP initiates the formation of 4-NP^-, which have a distinct absorption peak at 400 nm (Figure 3.11a, relevant peak shown in dashed box). The 400 nm absorbance peak does not overlap with plasmon resonances of Au/Ag-NSs enabling straightforward monitoring of the reduction in the absorbance of 4-NP^- over time. $NaBH_4$ reacts with water to evolve H_2 gas which aids in keeping the system well-mixed throughout the course of the reaction.[10, 16, 62] $NaBH_4$ is added in excess to the system;

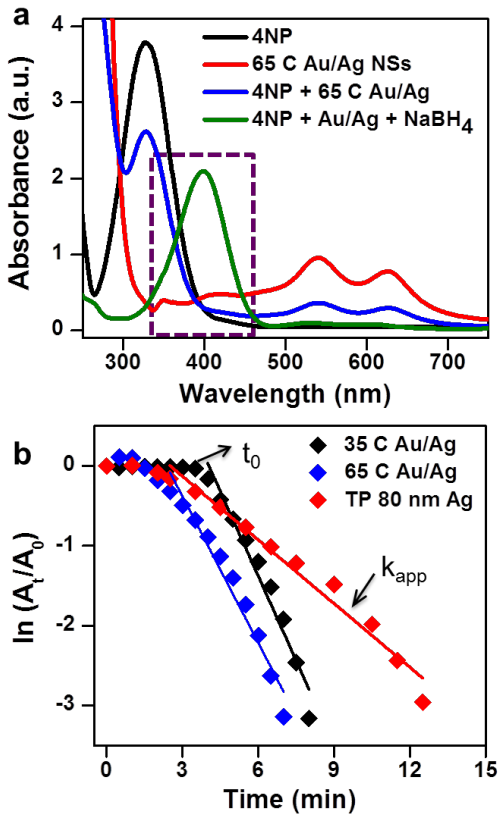

Figure 3.11: (a) UV-vis absorption spectra of a 4-NP solution, Au/Ag-NSs synthesized at 65 °C, 4-NP with the addition of Au/Ag-NSs, and 4-NP + Au/Ag-NSs immediately after the addition of $NaBH_4$, showing the formation of the characteristic 400 nm peak of the 4-NP- ions. This peak is highlighted with a dashed box around it, and the degradation of this peak was monitored to determine reaction kinetics. (b) Time dependence of the decrease in absorption of 4-NP- ions at 400 nm is shown for three different samples: commercially purchased (Ted Pella, TP) 80 nm Ag nanospheres, Au/Ag-NSs synthesized at 35 °C and 65 °C. The linear section from which k_{app} was derived is shown. The induction time, t_0, indicating the onset of the catalytic reduction is also shown.

Table 3.3: The rate constants (k_{app}) and induction time (t_0) of the catalytic reduction of 4-nitrophenol via $NaBH_4$ with the Au/Ag-NSs and Ag nanospheres.

Sample Name	**Rate Constant (k_{app}, minutes^{-1})**	**Induction Time (t_0, minutes)**
Au/Ag-NSs 35 °C	0.7	4
Au/Ag-NSs 65 °C	0.61	2
Ag Nanospheres	0.26	1

due to this high concentration of $NaBH_4$ it is reasonable to assume that it remains essentially constant during the reaction, allowing for pseudo first order reaction kinetics to be used with respect to 4-NP. The rate of catalysis and the induction time needed to initiate the catalytic reaction is dependent on the crystallographic facets, surface ligands, and metal composition of the nanocatalysts. To understand the role of each of these components, we compared the catalytic activity of Au/Ag-NSs with the rounded corners synthesized at 35 °C, Au/Ag-NSs with sharp corners synthesized at 65 °C, and commercially purchased 80 nm Ag nanospheres from Ted Pella Inc. A linear correlation between $ln(A_t/A_0)$ vs time, where A_0 is absorbance at $t = 0$, is observed as expected for a pseudo-first order reaction (Figure 3.11b). The apparent reaction rate, k_{app}, for each nanocatalyst was determined from the negative slope of the linear fits. While the reduction of 4-NP demonstrated the shortest induction time on the Ag nanospheres ($t_0^{Ag} = 1$ min, $t_0^{Au/Ag-35C} = 4$ mins, $t_0^{Au/Ag-65C} = 2$ mins), k_{app} was slowest on the Ag nanospheres ($k_{app}^{Ag} = 0.26 min^{-1}$) relative to the Au/Ag-NSs synthesized at 35 °C ($k_{app}^{Au/Ag-35C} = 0.7$ min^{-1}) and Au/Ag-NSs synthesized at 65 °C ($k_{app}^{Au/Ag-65C} = 0.61$ min^{-1}). It is notable, however, despite the difference in induction time, the Au/Ag-NSs synthesized at 35 °C and 65 °C have comparable reaction rates. The t_0 and k_{app} values are shown in Table 3.3. The observed differences in catalytic properties between the three samples are attributable to: (*i*) electronic effects due to presence of dual metals, (*ii*) the available surface area of the nanocatalyst, (*iii*) energies of different crystalline facets, and (*iv*) role of surface ligands.

To understand the mechanistic process that results in enhanced catalysis by the Au/Ag-NSs, X-ray photoelectron spectroscopy (XPS) was performed. XPS revealed the silver

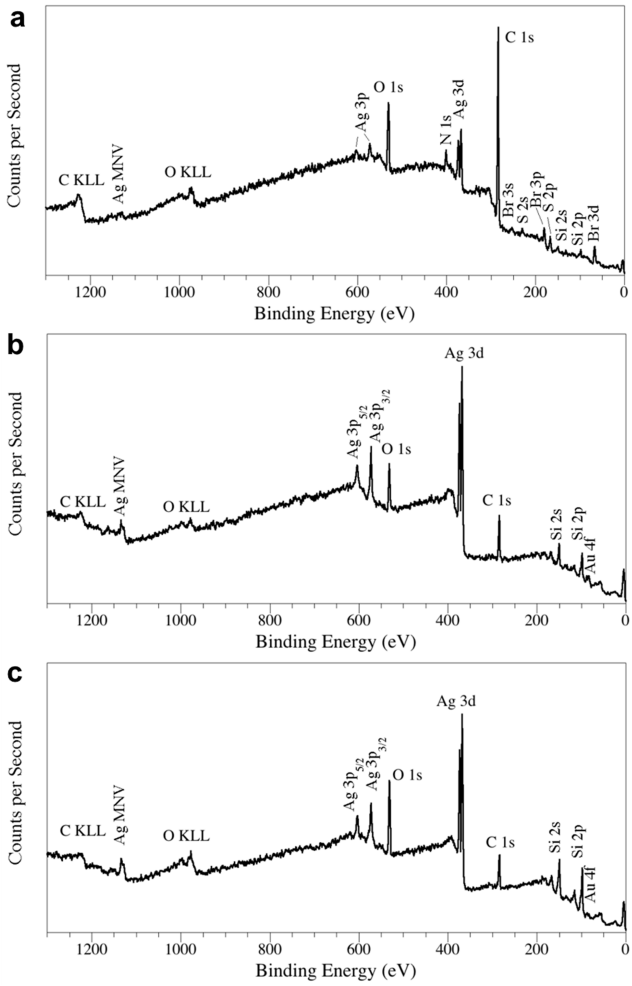

Figure 3.12: XPS survey spectra acquired from (a) commercially purchased Ag nanoparticles, (b) Au/Ag NSs synthesized at 35 °C, and (c) Au/Ag NSs synthesized at 65 °C.

binding states and the surface composition of the nanostructures. Samples of the Au/Ag NSs synthesized at 35 °C and 65 °C were dropcast onto clean silicon substrates and dried. A similarly prepared sample of the commercially purchased silver nanoparticles was included in the analysis for comparison. The survey spectra acquired on the three samples are shown in Figure 3.12. Note that gold peaks are present in both spectra acquired on the Au/Ag-NSs which can be attributed to photoelectrons produced in the Au core of these nanostructures. The Au 4f electrons produced from Al $K\alpha$ x-rays (1486.6 eV) have a kinetic energy of approximately 1400 eV. Based on the inelastic mean free path of 1400 eV electrons traveling through a Ag layer the Ag shell on these particles would have to be on the order of 12 nm thick for the Au 4f signal to be attenuated to the point that it would not be distinguished from the background. This suggests that the Ag shells are less than 12 nm thick. If the shells were indeed thick enough to attenuate the Au photoelectrons produced in the core, the Au signal present in the survey spectra would suggest that there are Au atoms present on the surface of or incorporated in the Ag capping layer. The ratio of silver to gold atoms present within the analysis volume of each sample was determined from high resolution spectra (Figure 3.13) using handbook sensitivity factors.[63] The Au/Ag ratios for the 35 °C and 65 °C synthesized nanostructures were 0.056 and 0.018, respectively. The higher Au/Ag ratio for the Au/Ag-NSs synthesized at 35 °C is due to the thinner Ag shell achieved at the lower temperature relative to the Au/Ag NSs synthesized at 65 °C (see Table 3.1). The higher Au/Ag ratio may also be contributed by the high degree of offset Au core observed in the Au/Ag-NSs synthesized at 35 °C resulting a thinner Ag shell ($<$5 nm) in one or more edges (Figure 3.3).

High resolution Ag 3d and Ag MNN spectra (Figure 3.13) were used to determine the bonding state of the Ag in the three samples analyzed. The bonding energy of Ag is relatively insensitive to its chemical environment. Therefore the Auger parameter was used to determine the Ag bonding states in these particles.[64] The Auger parameter is the sum of the binding energy of the photoelectron peak (Ag $3d_{5/2}$) and the kinetic energy of the Auger

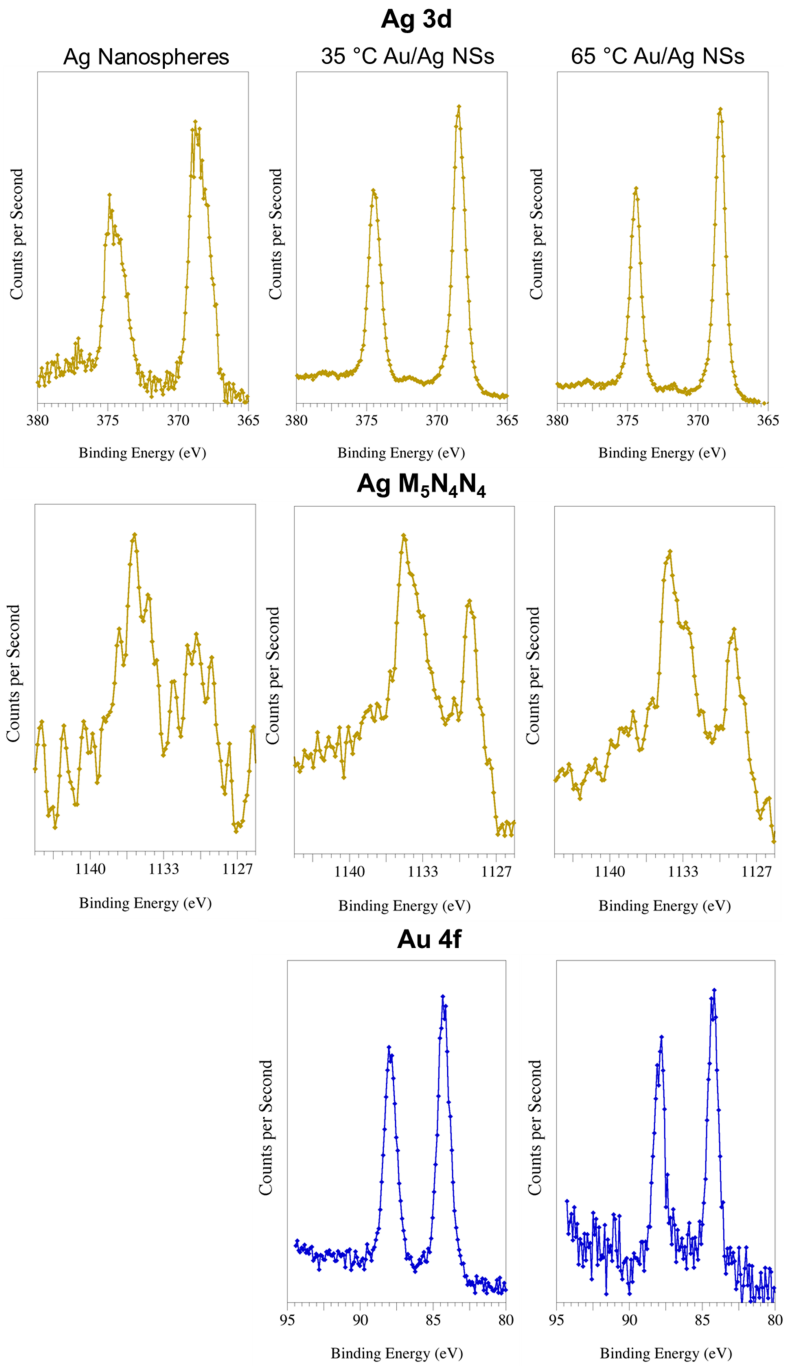

Figure 3.13: High-resolution XPS spectra of the Ag 3d, Ag $M_5N_4N_4$, and Au 4f transitions for the Ag nanospheres, Au/Ag-NSs synthesized at 35 °C, and Au/Ag-NSs synthesized at 65 °C.

peak (Ag $M_4N_5N_5$). The Auger parameters determined for both the Au/Ag nanoparticles synthesized at 35 °C and at 65 °C were 726.0 eV, which is consistent with that of metallic Ag. The Auger parameter determined for the commercially purchased Ag nanoparticles was 724.4 eV, which is consistent with Ag_2O. The results of XPs suggest the composition of metal nanostructure strongly influences their catalytic properties consistent with previous reports where bimetallic nanocatalysts have been shown to demonstrate superior catalytic activity relative to their monometallic counterparts.[8, 17, 50] The significantly higher k_{app} observed for the reduction of 4-NP by Au/Ag-NSs than the monometallic 80 nm Ag nanospheres is attributed to the enhanced electronic effects due to the presence of both metals. Au is more electronegative than Ag, while Ag has higher electron conductivity than Au. The synergistic combination of the two metals in core-shell geometry with a relatively thin Ag shell improves the relay of electrons at the surface, which consequently increases the k_{app}.[2, 8, 16, 17] The effect of composition is pictorially illustrated in Figure 3.14i. We do not believe strain effects at the interface of Au and Ag plays a role in the catalysis since the lattice spacing of Au (a = 4.08 Å) is nearly equivalent to Ag (a = 4.09 Å).

In addition to the nanostructure composition, the catalytic activity is also governed by its shape and the corresponding surface area available for catalytic transformations. In the case of a sphere with diameter equivalent to the edge length of a cube or pyramid, the surface-area-to-volume ratio is least for the sphere and highest for the pyramid. A large surface-area-to-volume ratio indicates higher number of surface sites available for catalytic reaction to proceed, which may contribute to the higher k_{app} observed for the Au/Ag-NSs relative to the Ag nanospheres. In addition to the surface area, the crystallographic planes constituting the nanostructure play a major role in catalytic rate due to the differences in binding energies of ions and molecules to different facets. Spherical nanoparticles are dominated by the $\{111\}$ facets on the surface and $\{100\}$ facets in the interior (Figure 3.14ii).[65] The nanocube faces are bound by $\{100\}$ facets and nanopyra-

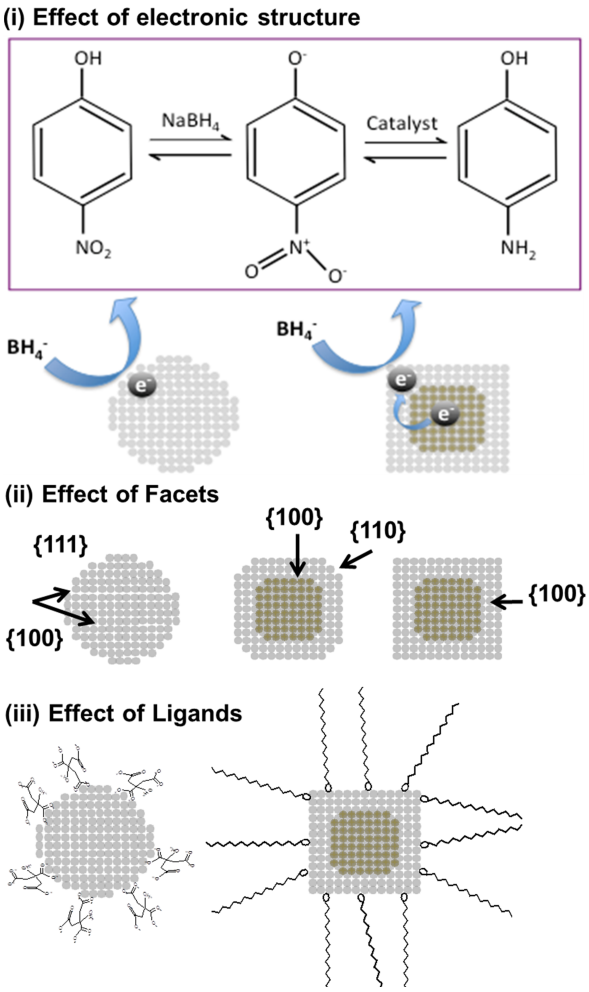

Figure 3.14: Schematic illustration of the effects that contribute to differences in k_{app} and t_0 between the commercially purchased Ag nanospheres and Au/Ag-NSs including (i) metal composition influencing the electronic structure, (ii) crystallographic facets, and (iii) surface ligands.

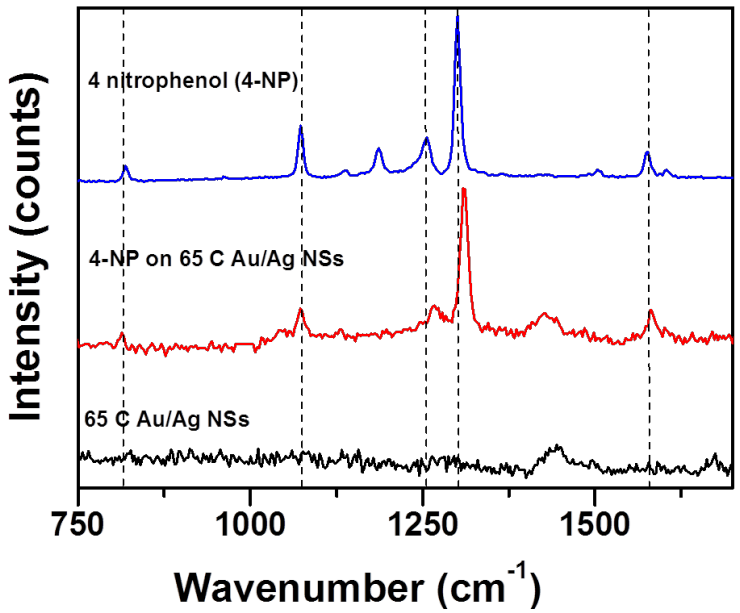

Figure 3.15: Raman spectra of solid 4-nitrophenol, 4-nitrophenol adsorbed on Au/Ag-NSs synthesized at 65 °C, and control spectrum of 65 °C Au/Ag-NSs. The NO_2 stretching mode at 1321 cm^{-1} blue shifts to 1330 cm^{-1}, while the C-NO_2 stretching mode at 1279 cm^{-1} blue shifts to 1289 cm^{-1}. This suggests that 4-NP adsorbs on Ag surface via the nitrogen of the NO_2 group. Note that the C-H bending mode at 1106 cm^{-1} and ring stretching mode at 1585 cm^{-1} do not shift at all strongly, supporting that 4-NP adsorbs on the Ag surface via the NO_2 group. Such large shifts are unlikely to be contributed by simple drying effects of the 4-NP on the Au/Ag-NSs surface.

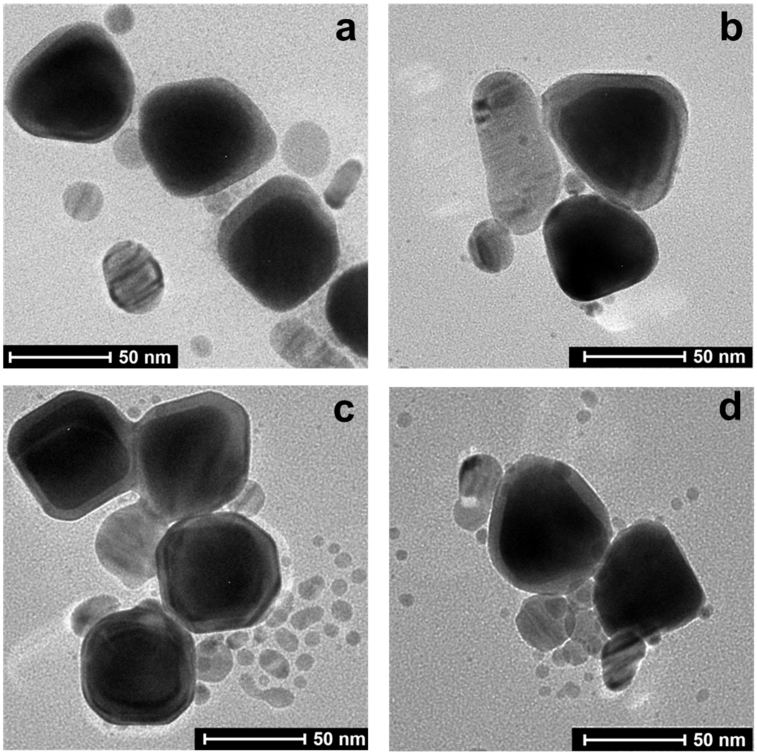

Figure 3.16: TEM images of nanostructures after catalytic reaction (a-b) 35 °C Au/Ag nanostructures, and (c-d) 65 °C Au/Ag nanostructures.

mids faces are dominated by $\{111\}$ facets. Since $\{100\}$ facets are most catalytically active to the reduction of 4-NP to 4-AP, Au/Ag-NSs have a higher reaction rate relative to the Ag nanospheres.[12, 13] To ensure 4-NP binds to the Au/Ag-NSs surface, we performed Raman spectroscopy (Figure 3.15) of solid 4-NP and 4-NP bound to Au/Ag-NSs. A 10 cm^{-1} shift in the NO_2 and C-NO_2 stretching modes of 4-nitrophenol was observed after binding to Au/Ag-NSs surface which suggests that 4-NP adsorbs on Ag surface via the nitrogen of the NO_2 group. Further, we also noted that the Au/Ag-NSs synthesized at 35 °C have $2\times$ longer induction time ($t_0^{Au/Ag-35C} = 4$ mins) than those synthesized at 65 °C ($t_0^{Au/Ag-65C} = 2$ mins). This is attributed to the rounded corners bound by the $\{110\}$ facets of the Au/Ag-NSs synthesized at 35 °C relative to the sharp corners implying the absence of $\{110\}$ facets for Au/Ag-NSs synthesized at 65 °C. The $\{110\}$ facet has lower energy and catalytically less active than $\{100\}$ and $\{111\}$ facets.

Finally the ligands on the surface of metal nanostructure also play a key role in catalytic reaction pathways. Contrary to the belief that ligands should be removed from the nanocatalyst surface to minimize blocking of the active sites, ligand removal often results in nanostructure destabilization, shape deformation, and aggregation, which are detrimental to catalytic performance.[1] Both citrate[66] and cetyltrimethylammonium salts[9] have demonstrated the ability to directly reduce 4-NP and assist in the electron transfer that occurs on the nanocatalyst surface. The Au/Ag-NSs synthesized in this work are capped with CTAC; the commercially purchased Ted Pella 80 nm Ag nanospheres are capped with citrate. Surface ligands not only control the accessibility of 4-NP^- ions to catalytically active sites, but also act as a diffusion barrier for the 4-NP^- ions to reach the surface.[67] This diffusion barrier mediated by the ligands results in the induction time related to the magnitude of the diffusion barrier.[3] Since CTAC is a long-chain bulky molecule (Figure 3.14iii) it would be expected to induce a longer diffusion time, and therefore a longer induction period than the citrate molecules. This explains the longer induction time for the Au/Ag-NSs relative to the Ag nanospheres.

We have also performed control experiments showing the interaction of Au/Ag nanostructures and Ag nanospheres with $NaBH_4$ only (without 4-nitrophenol). It is evident that upon addition of $NaBH_4$, the CTAC ligands are partially stripped from the Au/Ag nanostructures surface which partially compromises the structural integrity of the Ag layer (Figure 3.16). This results in a blue shift in the Au/Ag nanocubes (535 nm to 525 nm) and nanopyramids (620 nm to 600 nm) as well as decrease in the intensity of the nanopyramids resonance (Figure 3.17b). The blue shift also results from a change in the refractive index of the surrounding medium as previously suggested in ref. 11. The adsorption of BH_4^- ions decompose to give H_2 gas (consistent with previously proposed mechanism) lowering the dielectric constant of the surrounding media. The decrease in the intensity of the nanopyramids resonance may occur because CTAC is less strongly bound to the $\{111\}$ facets of nanopyramids (relative $\{100\}$ facets of nanocubes), which makes them more susceptible

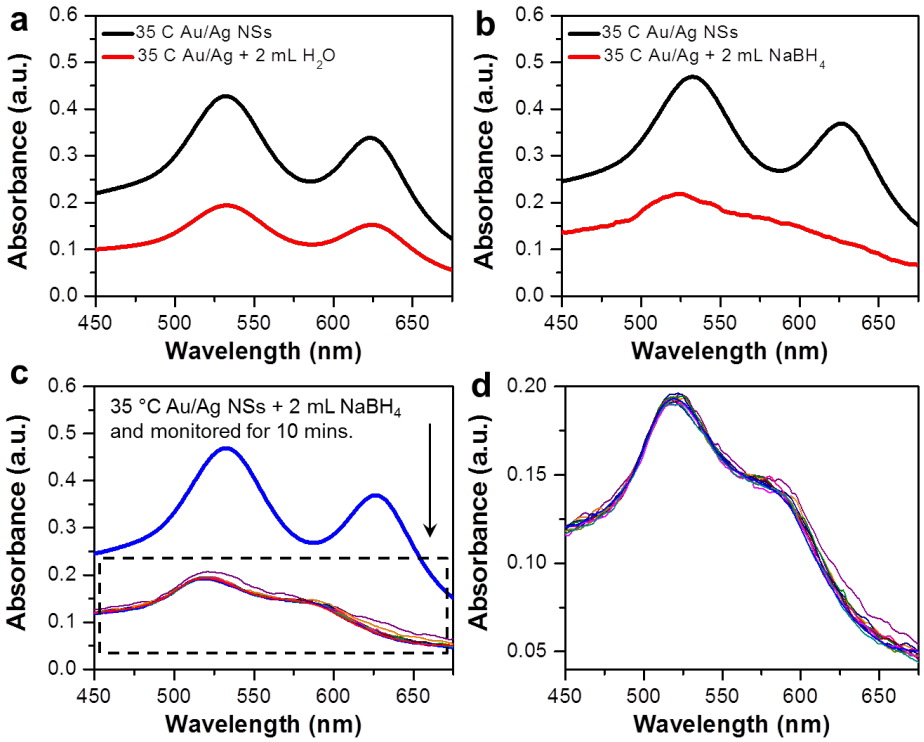

Figure 3.17: UV-vis absorption spectra of Au/Ag nanostructures synthesized at 35 °C (a) diluted with 2 mL H_2O, (b) diluted with 2 mL $NaBH_4$, (c) diluted with 2 mL $NaBH_4$ and monitored for 10 mins, i.e. the course of the catalytic reaction, and (d) zoomed in view of the spectra shown in dashed box from (c).

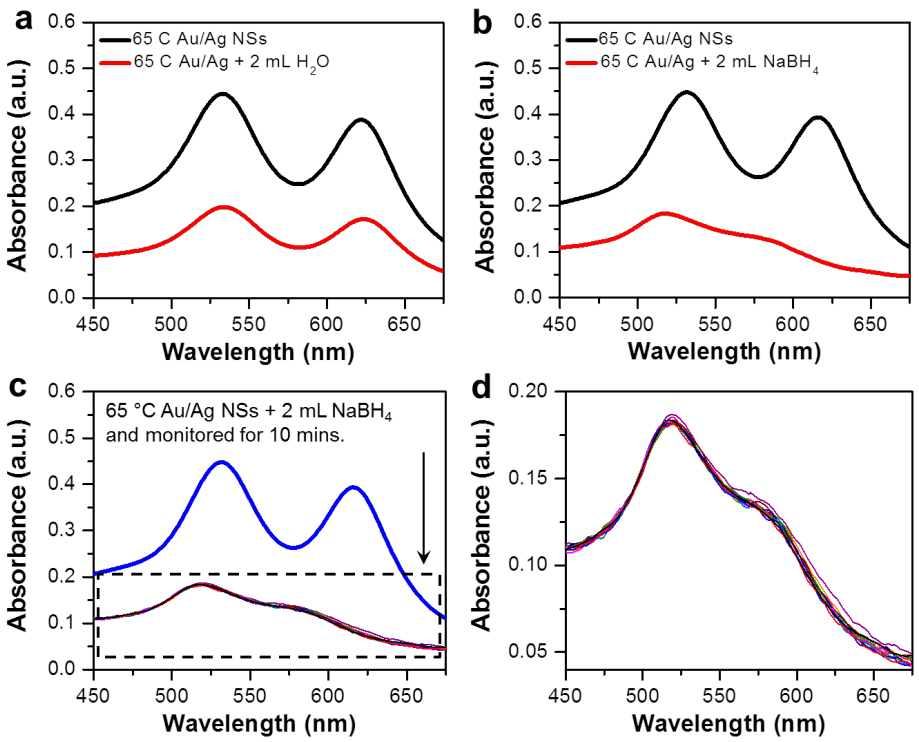

Figure 3.18: UV-vis absorption spectra of Au/Ag nanostructures synthesized at 65 °C (a) diluted with 2 mL H_2O, (b) diluted with 2 mL $NaBH_4$, (c) diluted with 2 mL $NaBH_4$ and monitored for 10 mins i.e. the course of the catalytic reaction, and (d) zoomed in view of the spectra shown in dashed box from (c).

to stripping by $NaBH_4$. We note however, the spectral characteristics of the Au/Ag nanostructures are stabilized after the first few seconds and do not change during the course of the catalytic reduction (Figure 3.17c-d). This indicates that the Ag layer is partly compromised within the first few seconds after adding the $NaBH_4$ but remains stable afterwards suggesting that a thin layer of Ag likely enhances the catalysis due to stronger electronic effects from the gold core and a thinner Ag layer is more desirable for 4-NP reduction.

The degradation of the Ag layer is not ideal for long term stability of the catalysts and can be minimized by ameliorating the synthesis process and adding a protective polymer layer, such as poly(vinyl pyrrolidone). However, the thickness of the polymer layer will likely impact the rate of the catalytic reduction, as thick layer will slow down the pathways for the nitrophenolate ions to pass through the polymer chains and reach the metal surface

where the $4NP^-$ reduction occurs. Future work on the nature of ligands and catalyst stability will further elucidate these effects. Similar experiments have been performed for Au/Ag-NSs synthesized at 65 °C (Figure 3.18), and commercially bought Ag nanospheres (Figure 3.19). We note that the spectral characteristics of the Ag nanospheres do not stabilize and continues to decrease during the course of the catalysis indicating a slow degradation of the nanospheres upon removal of the citrate ligands by $NaBH_4$.

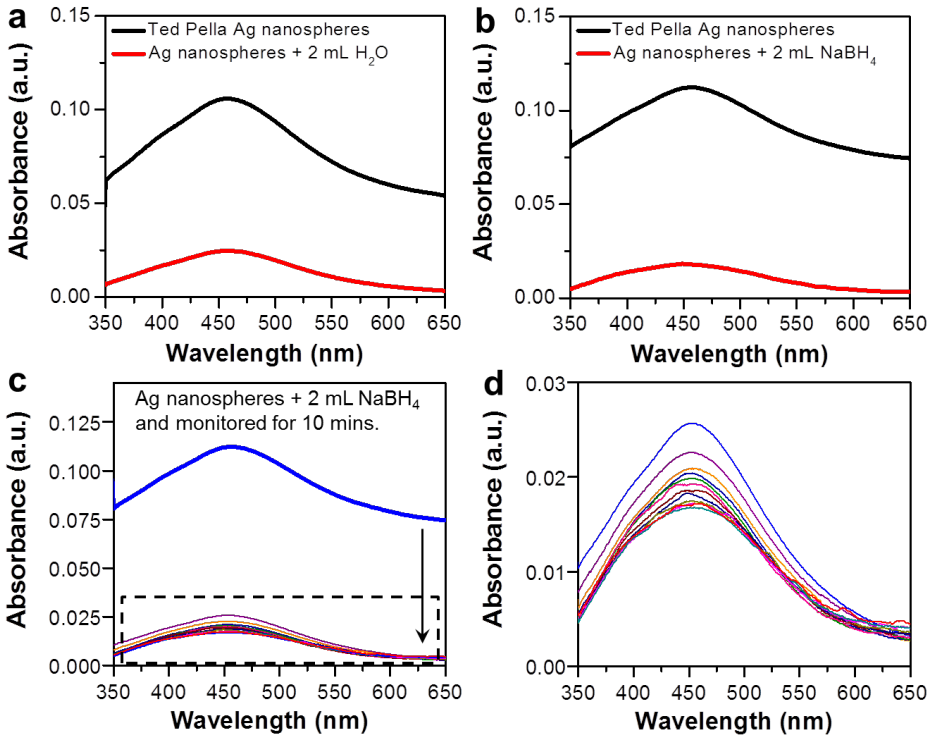

Figure 3.19: UV-vis absorption spectra of Ag nanospheres commercially purchased from Ted Pella: (a) diluted with 2 mL H_2O, (b) diluted with 2 mL $NaBH_4$, (c) diluted with 2 mL $NaBH_4$ and monitored for 10 mins, i.e. the course of the catalytic reaction, and (d) zoomed in view of the spectra shown in dashed box from (c).

The four factors discussed above: electronic effects due to presence of dual metals, the effects of the total surface area of a nanocatalyst available for catalytic reactions to occur, binding energies of different crystalline facets towards ions and molecules, and the nature of the surface ligands, collectively play a role in the superior performance of the bimetallic nanostructures in the catalytic reduction of 4-nitrophenol to 4-aminophenol. While it is difficult to separate the role played by each effect, our results suggest that the bimetallic

composition of the Au/Ag-NSs has the strongest contribution to the overall enhancement in catalytic reduction of 4-nitrophenol. The effect of composition will likely be enhanced in alloyed nanostructures where both metals are present on the surface where the catalysis occurs. Our results also suggest that the shape of the nanostructure and the corresponding crystalline facets also strongly impacts the rate of catalysis. We also note that the presence of both nanocubes and nanopyramids in the reaction mixture likely impacts the reaction kinetics of 4-NP to 4-AP. While the $\{100\}$ facets have higher catalytic rate relative to $\{111\}$ facets, nanopyramids have a $2\times$ higher surface-area-to-volume ratio relative to nanocubes. Therefore, a shape-pure reaction mixture consisting of one of the shapes may not necessarily enhance the reaction rate of 4-NP reduction. Further, while 4-NP reduction is catalyzed strongly along the $\{100\}$ facet, several other reactions demonstrate higher activity on $\{111\}$ facets, for example, preferential CO oxidation or PROX reaction.[68] This implies a shape-pure nanocatalyst solution with a single dominant crystalline facet will likely be applicable to only a few catalytic reactions. We therefore anticipate the Au/Ag-NSs synthesized in this work can be generalized to a wide-range of heterogeneous catalytic reactions where different crystalline facets influence the reaction rate. Additionally, the dual plasmon resonances at 615 nm and 535 nm will allow their use in light induced catalysis where the nanostructures can be excited at multiple resonances, allowing multiplexed catalysis.[69]

3.4 Conclusions

In conclusion, we demonstrate the morphological evolution of Au/Ag-NSs at different reaction temperatures and evaluate the role of edge morphology in controlling the catalytic rates of 4-NP to 4-AP. Due to slower growth dynamics at lower temperatures, bimetallic nanostructures are formed with rounded corners bound by the [110] crystal planes. As the temperature is increased growth along the [100] and [111] planes progresses more rapidly relative to the less reactive [110] planes eliminating the rounded corners and giving rise to Au/Ag nanostructures with sharp edges and corners. The corner morphology has a signif-

icant impact on the catalytic performance where rounded corners show a longer induction time relative to sharper corners, but comparable catalytic rates for the reduction of 4-NP to 4-AP. The commercially purchased Ag nanospheres demonstrated the slowest catalytic rate. These differences in catalysis is attributed to a combination of high surface-area-to-volume ratio, favorable crystallographic facets, electronic effects where the synergistic role of Au and Ag results in higher catalytic rates, and ligand effects where long-chain CTAC molecules present a higher diffusion barrier for 4-NP- ions to reach the surface of the nanocatalysts. We anticipate in addition to catalysis, the sharp edges and corners of Au/Ag nanostructures will also give rise to intense near-fields particularly at the dipole resonance, rendering these bimetallic nanostructures highly relevant for sensing, surface enhanced spectroscopy, and thermoplasmonic applications. Further, the dual resonances in the visible region of the spectrum also make these bimetallic nanostructures highly promising for light harvesting in solar energy conversion devices.

3.5 Methods

Au Nanocrystal Synthesis: Au nanocrystals (Au-NC) were synthesized by modifying a procedure previously described.[46, 47] All reagents were purchased from Sigma-Aldrich. Au seeds were prepared by adding 0.6 mL of freshly prepared and ice cold 10 mM $NaBH_4$ to an aqueous solution composed of 7.5 mL of 100 mM cetyltrimethylammonium bromide (CTAB), 2.75 mL milli-Q H_2O (18.2 MΩ), and 0.8 mL of 10 mM $HAuCl_4$. This solution was stirred vigorously for 1 minute and then transferred to a 35 °C water bath where it was left undisturbed for one hour. A growth solution was prepared by the sequential addition of 6.4 mL of 100 mM CTAB, 0.8 mL of 10 mM $HAuCl_4$, and 3.8 mL of 100 mM ascorbic acid to 32 mL of milli-Q H_2O. The seed solution was diluted by a factor of ten with milli-Q H_2O. The 20 μL of diluted seed solution was added to the growth solution, mixed gently by inversion, and then left undisturbed at 35 °C for 5 hours.

Au/Ag Nanostructure Synthesis: Au/Ag nanostructures (Au/Ag-NSs) were synthesized

by a seed mediated growth process. The Au-NC suspension synthesized above was centrifuged at 1100 RCF for 12 minutes (x3) and washed and soaked in 20 mM cetyltrimethylammonium chloride (CTAC) for 15 minutes. The nanocubes were then redispersed in 333 μL of milli-Q H_2O for use as precursor solution for Ag growth. Typically, 200 μL of precursor solution and 50 μL of 10 mM KBr were added to 5 mL of 20 mM CTAC and heated in a 65 °C water bath for 10 minutes before adding in 50 μL of 10 mM $AgNO_3$ and 150 μL of 100 mM ascorbic acid. The solution was mixed gently by inversion and left undisturbed at 65 °C for one hour.

Temperature Dependence: Au/Ag-NSs were synthesized following the above procedure keeping all reagent concentrations constant and varying the reaction temperature between 35-80 °C. All reactions were performed in a water bath for duration of 60-90 minutes.

Silver Concentration Variation: Au/Ag-NSs were synthesized following the above procedure keeping all other reaction parameters constant and varying [$AgNO_3$] from 20-200 μL (0.2-2 μmoles).

Change in Core Size: The Au-NC core size was varied by addition of 5, and 10 μL of diluted seed solution respectively to the nanocube growth solution (instead of the standard 20 μL seed solution described above). All other reaction parameters were kept constant, and Au/Ag-NSs synthesis was followed as described above.

Catalysis Experiments: Catalysis experiments were carried out in a quartz cuvette with a 1 cm path length. Three different catalysts were tested; Au/Ag NCs synthesized at 35 °C, Au/Ag NCs synthesized at 65 °C, and commercially purchased Ted Pella 80 nm Ag nanospheres. In a typical process, 250 μL of a 2 mM aqueous solution of 4-nitrophenol was added to 1 mL of ultrapure H_2O. Next, unwashed colloidal nanoparticle solution was added so that each reaction contained 6 μg of metal. The resulting solution was well mixed by perturbation, and then 2 mL of 60 mM freshly prepared, ice cold $NaBH_4$ was added at once. The color of the solution turned bright yellow immediately indicating the formation of nitrophenolate ions due to the alkalinity of the environment. The kinetics

of this reaction was monitored by using a Varian Cary 5000 UV-vis spectrophotometer to follow the decrease in absorption of the nitrophenolate ions at 400 nm over time. From this, the rate constant of the reaction was determined for each different catalyst.

Nanoparticle Characterization: A Varian Cary 5000 UV-vis NIR spectrophotometer (Agilent Technologies) with dual beam capability was used to measure the extinction of the Au-NC and Au/Ag-NSs solutions using a 1 cm path length cuvette. The nanoparticle size, geometry, and composition were characterized using Philips CM20T TEM at 200 keV, an Osiris TEM at 200 keV, and a Zeiss Merlin SEM (Oak Ridge National Lab). Nanoparticle samples were centrifuged at 2500 RPM for 15 minutes ($\times 2$) and washed with milli-Q water prior to SEM/TEM sample preparation.

X-ray Photoelectron Spectroscopy: X-ray photoelectron spectroscopy (XPS) data were collected using a Physical Electronics (PHI) VersaProbe 5000 equipped with a monochromatic Al $K\alpha$ x-ray source. A 100 μm diameter, 50 W x-ray beam rastered over an area of approximately 400 μm by 400 μm square was used with a takeoff angle of 45°off sample normal. Charge neutralization was accomplished using 1.1 eV electrons and 10 eV Ar^+. Survey and high-resolution spectra were taken with pass energies of 187.85 eV and 11.75 eV, respectively. All spectra were energy normalized to carbon at 284.8 eV.

Simulation Protocol: Calculations were performed on single particles in water using a total-field scattered-field (TFSF) plane wave source. The simulated Au/Ag nanocube has a 50 nm Au core and a 12.5 nm thick Ag shell, with a forward injection of the TFSF source along the y-axis. The simulated nanopyramid has a 60 nm edge length for the Au core, and a 20 nm thick Ag shell, with a backward injection of the TFSF source along the z-axis.

3.6 Bibliography

[1] C. Burda, X. B. Chen, R. Narayanan, and M. A. El-Sayed. Chemistry and properties of nanocrystals of different shapes. *Chem. Rev.*, 105(4):1025–1102, 2005.

[2] Haitao Fu, Xiaohong Yang, Xuchuan Jiang, and Aibing Yu. Bimetallic Ag-Au nanowires: Synthesis, growth mechanism, and catalytic properties. *Langmuir*, 29(23):7134–7142, 2013.

[3] Pablo Herves, Moises Perez-Lorenzo, Luis M. Liz-Marzan, Joachim Dzubiella, Yan Lu, and Matthias Ballauff. Catalysis by metallic nanoparticles in aqueous solution: model reactions. *Chem. Soc. Rev.*, 41(17):5577–5587, 2012.

[4] Kwangyeol Lee, Minsik Kim, and Heonjo Kim. Catalytic nanoparticles being facet-controlled. *J. Mater. Chem.*, 20(19):3791–3798, 2010.

[5] Chun-Ya Chiu, Pei-Ju Chung, Ka-Un Lao, Ching-Wen Liao, and Michael H. Huang. Facet-dependent catalytic activity of gold nanocubes, octahedra, and rhombic dodecahedra toward 4-nitroaniline reduction. *J. Phys. Chem. C*, 116(44):23757–23763, 2012.

[6] Moonjung Eo, Jayeon Baek, Hyeon Don Song, Suseung Lee, and Jongheop Yi. Quantification of electron transfer rates of different facets on single gold nanoparticles during catalytic reactions. *Chem. Comm.*, 49(45):5204–5206, 2013.

[7] Run Xu, Dingsheng Wang, Jiatao Zhang, and Yadong Li. Shape-dependent catalytic activity of silver nanoparticles for the oxidation of styrene. *Chem. Asian J.*, 1(6):888–893, 2006.

[8] Jianfeng Huang, Sascha Vongehr, Shaochun Tang, Haiming Lu, Jiancang Shen, and Xiangkang Meng. Ag dendrite-based Au/Ag bimetallic nanostructures with strongly enhanced catalytic activity. *Langmuir*, 25(19):11890–11896, 2009.

[9] Mohamed Mokhtar Mohamed and Merfat S. Al-Sharif. Visible light assisted reduction of 4-nitrophenol to 4-aminophenol on Ag/TiO_2 photocatalysts synthesized by hybrid templates. *Appl. Catal., B*, 142:432–441, 2013.

[10] Michael M. Nigra, Jeong-Myeong Ha, and Alexander Katz. Identification of site requirements for reduction of 4-nitrophenol using gold nanoparticle catalysts. *Catal. Sci. Tech.*, 3(11):2976–2983, 2013.

[11] M. A. Mahmoud and M. A. El-Sayed. Time dependence and signs of the shift of the surface plasmon resonance frequency in nanocages elucidate the nanocatalysis mechanism in hollow nanoparticles. *Nano Lett.*, 11(3):946–953, 2011.

[12] Pinhua Zhang, Yongming Sui, Guanjun Xiao, Yingnan Wang, Chunzhong Wang, Bingbing Liu, Guangtian Zou, and Bo Zou. Facile fabrication of faceted copper nanocrystals with high catalytic activity for p-nitrophenol reduction. *J. Mater. Chem. A*, 1(5):1632–1638, 2013.

[13] Gengtao Fu, Linfei Ding, Yu Chen, Jun Lin, Yawen Tang, and Tianhong Lu. Facile water-based synthesis and catalytic properties of platinum-gold alloy nanocubes. *CrystEngComm*, 16(9):1606–1610, 2014.

[14] Leng Leng Chng, Nandanan Erathodiyil, and Jackie Y. Ying. Nanostructured catalysts for organic transformations. *Acc. Chem. Res.*, 46(8):1825–1837, 2013.

[15] Hyunjoo Lee, Cheonghee Kim, Sungeun Yang, Joung Woo Han, and Jiyeon Kim. Shape-controlled nanocrystals for catalytic applications. *Catal. Surv. Asia*, 16(1):14–27, 2011.

[16] S. K. Ghosh, M. Mandal, S. Kundu, S. Nath, and T. Pal. Bimetallic Pt-Ni nanoparticles can catalyze reduction of aromatic nitro compounds by sodium borohydride in aqueous solution. *Appl. Catal., A*, 268(1-2):61–66, 2004.

[17] J. H. Liu, A. Q. Wang, Y. S. Chi, H. P. Lin, and C. Y. Mou. Synergistic effect in an Au-Ag alloy nanocatalyst: CO oxidation. *J. Phys. Chem. B*, 109(1):40–43, 2005.

[18] Jianfeng Huang, Sascha Vongehr, Shaochun Tang, Haiming Lu, and Xiangkang Meng. Highly catalytic Pd-Ag bimetallic dendrites. *J. Phys. Chem. C*, 114(35):15005–15010, 2010.

[19] Shaojun Guo, Sen Zhang, and Shouheng Sun. Tuning nanoparticle catalysis for the oxygen reduction reaction. *Angew. Chem. Int. Ed.*, 52(33):8526–8544, 2013.

[20] Rajib Ghosh Chaudhuri and Santanu Paria. Core/shell nanoparticles: Classes, properties, synthesis mechanisms, characterization, and applications. *Chem. Rev.*, 112(4):2373–2433, 2012.

[21] T. Shibata, B. A. Bunker, Z. Y. Zhang, D. Meisel, C. F. Vardeman, and J. D. Gezelter. Size-dependent spontaneous alloying of Au-Ag nanoparticles. *J. Am. Chem. Soc.*, 124(40):11989–11996, 2002.

[22] Jeunghoon Lee, Warefta Hasan, Christopher L. Stender, and Teri W. Odom. Pyramids: A platform for designing multifunctional plasmonic particles. *Acc. Chem. Res.*, 41(12):1762–1771, 2008.

[23] Yanyun Ma, Weiyang Li, Eun Chul Cho, Zhiyuan Li, Taekyung Yu, Jie Zeng, Zhaoxiong Xie, and Younan Xia. Au@Ag core-shell nanocubes with finely tuned and well-controlled sizes, shell thicknesses, and optical properties. *Acs Nano*, 4(11):6725–6734, 2010.

[24] Rafael Contreras-Caceres, Claudine Dawson, Petr Formanek, Dieter Fischer, Frank Simon, Andreas Janke, Petra Uhlmann, and Manfred Stamm. Polymers as templates for Au and Au@Ag bimetallic nanorods: UV-Vis and surface enhanced Raman spectroscopy. *Chem. Mater.*, 25(2):158–169, 2013.

[25] Cuncheng Li, Lin Sun, Yiqiang Sun, and Toshiharu Teranishi. One-pot controllable synthesis of Au@Ag heterogeneous nanorods with highly tunable plasmonic absorption. *Chem. Mater.*, 25(13):2580–2590, 2013.

[26] Hongjun You, Shengchun Yang, Bingjun Ding, and Hong Yang. Synthesis of colloidal metal and metal alloy nanoparticles for electrochemical energy applications. *Chem. Soc. Rev.*, 42(7):2880–2904, 2013.

[27] Shuang Wu, Andreas W. Schell, Michael Lublow, Julian Kaiser, Thomas Aichele, Stefan Schietinger, Frank Polzer, Sergei Kuehn, Xuhong Guo, Oliver Benson, Matthias Ballauff, and Yan Lu. Silica-coated Au/Ag nanorods with tunable surface plasmon bands for nanoplasmonics with single particles. *Colloid Polym. Sci.*, 291(3):585–594, 2013.

[28] Masaharu Tsuji, Ryoichi Matsuo, Peng Jiang, Nobuhiro Miyamae, Daisuke Ueyama, Michiko Nishio, Sachie Hikino, Hisayo Kumagae, Khairul Sozana Nor Kamarudin, and Xin-Ling Tang. Shape-dependent evolution of Au@Ag core-shell nanocrystals by PVP-assisted N,N-dimethylformamide reduction. *Cryst. Growth Des.*, 8(7):2528–2536, 2008.

[29] Udishnu Sanyal, Della Therese Davis, and Balaji R. Jagirdar. Bimetallic core-shell nanocomposites using weak reducing agent and their transformation to alloy nanostructures. *Dalton T.*, 42(19):7147–7157, 2013.

[30] B. Rodriguez-Gonzalez, A. Burrows, M. Watanabe, C. J. Kiely, and L. M. Liz-Marzan. Multishell bimetallic AuAg nanoparticles: synthesis, structure and optical properties. *J. Mater. Chem.*, 15(17):1755–1759, 2005.

[31] Houde She, Yuanzhi Chen, Xiaozhen Chen, Kun Zhang, Ziyuan Wang, and Dong-Liang Peng. Structure, optical and magnetic properties of Ni@Au and Au@Ni

nanoparticles synthesized via non-aqueous approaches. *J. Mater. Chem.*, 22(6):2757–2765, 2012.

[32] Wenzheng Li, Long Kuai, Qing Qin, and Baoyou Geng. Ag-Au bimetallic nanostructures: co-reduction synthesis and their component-dependent performance for enzyme-free H_2O_2 sensing. *J. Mater. Chem. A*, 1(24):7111–7117, 2013.

[33] Marie-Pier Murray-Methot, Mathieu Ratel, and Jean-Francois Masson. Optical properties of Au, Ag, and bimetallic Au on Ag nanohole arrays. *J. Phys. Chem. C*, 114(18):8268–8275, 2010.

[34] Ovidio Pena, Umapada Pal, Luis Rodriguez-Fernandez, Hector G. Silva-Pereyra, Vladimir Rodriguez-Iglesias, Juan Carlos Cheang-Wong, Jesus Arenas-Alatorre, and Alicia Oliver. Formation of Au-Ag core-shell nanostructures in silica matrix by sequential ion implantation. *J. Phys. Chem. C*, 113(6):2296–2300, 2009.

[35] Jianxiao Gong, Fei Zhou, Zhiyuan Li, and Zhiyong Tang. Synthesis of Au@Ag core-shell nanocubes containing varying shaped cores and their localized surface plasmon resonances. *Langmuir*, 28(24):8959–8964, 2012.

[36] Ming L. Tang, Na Liu, Jennifer A. Dionne, and A. Paul Alivisatos. Observations of shape-dependent hydrogen uptake trajectories from single nanocrystals. *J. Am. Chem. Soc.*, 133(34):13220–13223, 2011.

[37] Lu Chen, Long Kuai, and Baoyou Geng. Shell structure-enhanced electrocatalytic performance of Au-Pt core-shell catalyst. *CrystEngComm*, 15(11):2133–2136, 2013.

[38] Partha Pratim Patra and G. V. Pavan Kumar. Single-molecule surface-enhanced raman scattering sensitivity of Ag-core Au-shell nanoparticles: Revealed by bi-analyte method. *J. Phys. Chem. Lett.*, 4(7):1167–1171, 2013.

[39] Leslie Au, Xianmao Lu, and Younan Xia. A comparative study of galvanic replacement reactions involving Ag nanocubes and $AuCl_2^-$ or $AuCl_4$. *Adv. Mater.*, 20(13):2517–2522, 2008.

[40] Lakshminarayana Polavarapu and Luis M. Liz-Marzan. Growth and galvanic replacement of silver nanocubes in organic media. *Nanoscale*, 5(10):4355–4361, 2013.

[41] Edgar Gonzalez, Jordi Arbiol, and Victor F. Puntes. Carving at the nanoscale: Sequential galvanic exchange and kirkendall growth at room temperature. *Science*, 334(6061):1377–1380, 2011.

[42] Sara E. Skrabalak, Jingyi Chen, Yugang Sun, Xianmao Lu, Leslie Au, Claire M. Cobley, and Younan Xia. Gold nanocages: Synthesis, properties, and applications. *Acc. Chem. Res.*, 41(12):1587–1595, 2008.

[43] Sergio Gomez-Grana, Bart Goris, Thomas Altantzis, Cristina Fernandez-Lopez, Enrique Carbo-Argibay, Andres Guerrero-Martinez, Neyvis Almora-Barrios, Nuria Lopez, Isabel Pastoriza-Santos, Jory Perez-Juste, Sara Bals, Gustaaf Van Tendeloo, and Luis M. Liz-Marzan. Au@Ag nanoparticles: Halides stabilize $\{100\}$ facets. *J. Phys. Chem. Lett.*, 4(13):2209–2216, 2013.

[44] Matthew S. Shore, Junwei Wang, Aaron C. Johnston-Peck, Amy L. Oldenburg, and Joseph B. Tracy. Synthesis of Au(Core)/Ag(Shell) nanoparticles and their conversion to AuAg alloy nanoparticles. *Small*, 7(2):230–234, 2011.

[45] Shuangxi Xing, Li Huey Tan, Tao Chen, Yanhui Yang, and Hongyu Chen. Facile fabrication of triple-layer (Au@Ag)@polypyrrole core-shell and ($Au@H_2O$)@polypyrrole yolk-shell nanostructures. *Chem. Comm.*, (13):1653–1654, 2009.

[46] T. K. Sau and C. J. Murphy. Room temperature, high-yield synthesis of multiple

shapes of gold nanoparticles in aqueous solution. *J. Am. Chem. Soc.*, 126(28):8648–8649, 2004.

[47] Jian Feng Li, Xiang Dong Tian, Song Bo Li, Jason R. Anema, Zhi Lin Yang, Yong Ding, Yuan Fei Wu, Yong Ming Zeng, Qi Zhen Chen, Bin Ren, Zhong Lin Wang, and Zhong Qun Tian. Surface analysis using shell-isolated nanoparticle-enhanced Raman spectroscopy. *Nat. Protoc.*, 8(1):52–65, 2013.

[48] Huanjun Chen, Zhenhua Sun, Weihai Ni, Kat Choi Woo, Hai-Qing Lin, Lingdong Sun, Chunhua Yan, and Jianfang Wang. Plasmon coupling in clusters composed of two-dimensionally ordered gold nanocubes. *Small*, 5(18):2111–2119, 2009.

[49] Xi Wu, Tian Ming, Xin Wang, Peinan Wang, Jianfang Wang, and Jiyao Chen. High-photoluminescence-yield gold nanocubes: For cell imaging and photothermal therapy. *Acs Nano*, 4(1):113–120, 2010.

[50] William D. Michalak and Gabor A. Somorjai. Catalysis in energy generation and conversion: How insight into nanostructure, composition, and electronic structure leads to better catalysts (perspective). *Top. Catal.*, 56(18-20):1611–1622, 2013.

[51] L. F. Gou and C. J. Murphy. Fine-tuning the shape of gold nanorods. *Chem. of Mater.*, 17(14):3668–3672, 2005.

[52] M. B. Mohamed, Z. L. Wang, and M. A. El-Sayed. Temperature-dependent size-controlled nucleation and growth of gold nanoclusters. *J. Phys. Chem. A*, 103(49):10255–10259, 1999.

[53] Richard Becker, Bo Liedberg, and Per-Olov Kall. CTAB promoted synthesis of Au nanorods - temperature effects and stability considerations. *J. Colloid Interface Sci.*, 343(1):25–30, 2010.

[54] Xuemin Zhang, Junhu Zhang, Huan Wang, Yudong Hao, Xun Zhang, Tieqiang Wang, Yunan Wang, Ran Zhao, Hao Zhang, and Bai Yang. Thermal-induced surface plasmon band shift of gold nanoparticle monolayer: morphology and refractive index sensitivity. *Nanotechnology*, 21(46):465702, 2010.

[55] Wenxin Niu, Ling Zhang, and Guobao Xu. Shape-controlled synthesis of single-crystalline palladium nanocrystals. *Acs Nano*, 4(4):1987–1996, 2010.

[56] Wenxin Niu, Ling Zhang, and Guobao Xu. Seed-mediated growth of noble metal nanocrystals: crystal growth and shape control. *Nanoscale*, 5(8):3172–3181, 2013.

[57] Matthias Kahm, Guido Hasenbrink, Hella Lichtenberg-Frate, Jost Ludwig, and Maik Kschischo. grofit: Fitting biological growth curves with R. *J. Stat. Softw.*, 33(7):1–21, 2010.

[58] Vladimir V. Tatarchuk, Anastasiya P. Sergievskaya, Irina A. Druzhinina, and Vladimir I. Zaikovsky. Kinetics and mechanism of the growth of gold nanoparticles by reduction of tetrachloroauric acid by hydrazine in Triton N-42 reverse micelles. *J. Nanopart. Res.*, 13(10):4997–5007, 2011.

[59] Andrea R. Tao, Susan Habas, and Peidong Yang. Shape control of colloidal metal nanocrystals. *Small*, 4(3):310–325, 2008.

[60] Emilie Ringe, Mark R. Langille, Kwonnam Sohn, Jian Zhang, Jiaxing Huang, Chad A. Mirkin, Richard P. Van Duyne, and Laurence D. Marks. Plasmon length: A universal parameter to describe size effects in gold nanoparticles. *J. Phys. Chem. Lett.*, 3(11):1479–1483, 2012.

[61] Emilie Ringe, Jian Zhang, Mark R. Langille, Chad A. Mirkin, Laurence D. Marks, and Richard P. Van Duyne. Correlating the structure and localized surface plasmon resonance of single silver right bipyramids. *Nanotechnology*, 23(44):444005, 2012.

[62] Subhra Jana, Sujit Kumar Ghosh, Sudip Nath, Surojit Pande, Snigdhamayee Praharaj, Sudipa Panigrahi, Soumen Basu, Takeshi Endo, and Tarasankar Pal. Synthesis of silver nano shell-coated cationic polystyrene beads: A solid phase catalyst for the reduction of 4-nitrophenol. *Appl. Catal., A*, 313(1):41–48, 2006.

[63] John F. Moulder, W. F. Stickle, P. E. Sobol, and K. D. Bomben. *Handbook of X-ray photoelectron spectroscopy*. Physical Electronics, 1995.

[64] C. D. Wagner and A. Joshi. The Auger parameter, its utility and advantages - a review. *J. Electron Spectrosc. Relat. Phenom.*, 47:283–313, 1988.

[65] R. Narayanan and M. A. El-Sayed. Effect of colloidal catalysis on the nanoparticle size distribution: Dendrimer-Pd vs PVP-Pd nanoparticles catalyzing the Suzuki coupling reaction. *J. Phys. Chem. B*, 108(25):8572–8580, 2004.

[66] Jie Zeng, Qiang Zhang, Jingyi Chen, and Younan Xia. A comparison study of the catalytic properties of Au-based nanocages, nanoboxes, and nanoparticles. *Nano Lett.*, 10(1):30–35, 2010.

[67] Yu Mei, Yan Lu, Frank Polzer, Matthias Ballauff, and Markus Drechsler. Catalytic activity of palladium nanoparticles encapsulated in spherical polyelectrolyte brushes and core-shell microgels. *Chem. Mater.*, 19(5):1062–1069, 2007.

[68] Dongwei Li, Ye Zhu, Hui Wang, and Yi Ding. Nanoporous gold as an active low temperature catalyst toward CO oxidation in hydrogen-rich stream. *Sci. Rep.*, 3:03015, 2013.

[69] Shaunak Mukherjee, Florian Libisch, Nicolas Large, Oara Neumann, Lisa V. Brown, Jin Cheng, J. Britt Lassiter, Emily A. Carter, Peter Nordlander, and Naomi J. Halas. Hot electrons do the impossible: Plasmon-induced dissociation of H^-_2 on Au. *Nano Lett.*, 13(1):240–247, 2013.

CHAPTER 4

ULTRAFAST EXCITED STATE DYNAMICS IN SHAPE- AND COMPOSITION-CONTROLLED GOLD-SILVER BIMETALLIC NANOSTRUCTURES

Adapted from H. F. Zarick, A. Boulesbaa, E. M. Talbert, A. Puretzky, D. Geohegan, and R. Bardhan, *J. Phys. Chem. C*, **2017**, *121*, 4540 with permission from the American Chemical Society.

4.1 Summary

In this chapter, we have examined the ultrafast dynamics of shape- and composition-controlled bimetallic Au/Ag core/shell nanostructures with transient absorption spectroscopy (TAS) as a function of Ag layer thickness (0-15 nm) and pump excitation fluence (50-500 nJ/pulse). Our synthesis approach generated both bimetallic nanocubes and nanopyramids with distinct dipolar plasmon resonances and plasmon dephasing behavior at the resonance. Lifetimes obtained from TAS at low powers (50 nJ/pulse) demonstrated minimal dependence on the Ag layer thickness, whereas at high power (500 nJ/pulse) a rise in electron-phonon coupling lifetime (τ_1) was observed with increasing Ag shell thickness for both nanocubes and nanopyramids. This is attributable to the stronger absorption of the 400 nm pump pulse with higher Ag content, which induced higher electron temperatures. The phonon-phonon scattering lifetime (τ_2) also rises with increasing Ag layer, contributed both by the increasing size of the Au/Ag nanostructures as well as by surface chemistry effects. Further, we observed that even the thinnest, 2 nm, Ag shell strongly impacts both τ_1 and τ_2 at high power despite minimal change in overall size, indicating that the nanostructure composition also strongly impacts the thermalization temperature following absorption of 400 nm light. We also observed a shape-dependent trend at high power, where τ_2 increased for

the nanopyramids with increasing Ag shell thickness and nanostructure size, but bimetallic nanocubes demonstrated an unexpected decrease in τ_2 for the thickest, 15 nm, Ag shell. This was attributed to the larger number of corners and edges in the nanocubes relative to the nanopyramids.

4.2 Introduction

Bimetallic nanostructures, where two metals are coupled together in a core-shell architecture, are of tremendous interest since their optoelectronic properties can be manipulated by not only tuning their shape and size, but also by controlling the composition of the two metals achieved by tuning the core-shell ratio. The unique characteristics of bimetallic nanostructures have recently enabled their use in several applications including biomedicine,[1, 2, 3, 4, 5] surface-enhanced spectroscopies,[6, 7, 8, 9] and photovoltaics[10, 11, 12, 13] among others. We recently reported the synthesis and catalytic properties of bimetallic gold core/silver shell nanostructures[14] (Au/Ag NSs) and demonstrated their role in plasmonic enhancement of photocatalysis and emerging solar cells.[15, 16, 17, 18] In this work, we explore the ultrafast excited state dynamics of these Au/Ag NSs in aqueous media with transient absorption spectroscopy (TAS). TAS is a time-resolved pump-probe approach where the electron distribution of metal nanostructures is selectively excited by a femtosecond pump pulse and the resulting relaxation dynamics are monitored by a time-delayed spectrally broad probe pulse. This excitation pulse gives rise to broadening of the plasmon absorption band and, as a result, a transient photobleach (PB) band is observed in the TAS spectrum. The decay of the PB band provides characteristic relaxation times as hot electrons in metal nanostructures thermalize with the nanostructure lattice through electron-phonon interactions followed by heat release to the surrounding medium via phonon-phonon scattering.[19, 20, 21] Electron-phonon relaxation typically occurs within 1-5 ps following excitation, and phonon-phonon relaxation is known to occur in longer timescales of $>$100 ps.[22, 23, 24, 25, 26, 27] Characteristic decay times of

electron-phonon relaxation are dependent on the rise in electron temperature correlated to the power of the pump pulse and linearly increases with pump energy fluence.[28] Phonon-phonon scattering is impacted by several factors, including nanostructure size and composition, and surface chemistry.[29, 30, 31, 32, 33] TAS studies, therefore, enable us to understand the optical, optoelectronic, and optothermal behavior of metal nanostructures to ultimately enable their use in relevant technological applications.

While the ultrafast dynamics of monometallic nanostructures have been thoroughly studied in the past two decades,[19, 20, 24, 34, 35, 36, 37, 38] few reports have been devoted to bimetallic nanostructures.[25, 39, 40, 41, 42] Here we studied the excited-state relaxation dynamics of core/shell Au/Ag NSs of two different geometries, nanocubes and nanopyramids, which result from our seed-mediated synthesis approach. We examined the electron-phonon and phonon-phonon lifetime as a function of the Ag shell thickness surrounding the Au nanocrystal core, varied between 0-15 nm, and as a function of the pump energy fluence varied between 50-500 nJ/pulse. Our results demonstrate that at low laser powers size and compositional effects have minimal impact on the relaxation dynamics of Au/Ag NSs. However, at high pump power, the composition of the Au/Ag NSs controls the absorption of the 400 nm pump pulse which directly impacts the electron-phonon coupling lifetimes. The phonon-phonon scattering lifetime is influenced by the size of Au/Ag NSs as well as by the presence of surface ligands. We also observe an unexpected shape-dependent trend in the lifetimes associated with the larger number of edges and corners of the nanocubes relative to the nanopyramids. The results of this work will provide fundamental insight into the physical properties of core/shell nanostructures and guide the design of new shape-, size-, and composition-controlled bimetallic nanostructures. We expect this will ultimately enable their use in a range of photothermal and photoelectric applications where these characteristic electron-phonon and phonon-phonon interactions will improve the overall efficiency of the processes being investigated.

4.3 Results and Discussion

Bimetallic Au/Ag core/shell nanostructures (NSs) were synthesized following a seed-mediated growth process described in our previous work.[14] Au nanocrystal cores (Au NCs) of 45 ± 3 nm were synthesized in aqueous media utilizing cetyltrimethylammonium bromide (CTAB) as a stabilizing and shape-directing agent.[43] Uniform Ag shells of varying thicknesses were grown by transferring the Au cores into a growth solution containing cetyltrimethylammonium chloride (CTAC) ligands, KBr, ascorbic acid, and $AgNO_3$ as a silver source. Ag layer thickness was controlled by manipulating the Ag concentration, temperature, and reaction time, the details of which are provided in the experimental methods section. Nanostructure morphology, composition, and Ag layer thicknesses were characterized with high angle annular dark field (HAADF) STEM provided in Figure 4.1. EDS elemental mapping confirms the Ag layer thicknesses surrounding the Au NC core (Figure 4.2). The synthesis of Au NC cores (Figure 4.2a) yields a mixture of $\sim 60\%$ rounded edge nanocubes and 40% to truncated nanocubes, as determined in our previous work.[14] While the morphology of the Au/Ag NSs remains unchanged with the growth of the thin 2 nm Ag shell (Figure 4.2b, Figure 4.3), with the thicker Ag shells the morphology evolves to well-defined Au/Ag nanocubes and nanopyramids stemming from the rounded-edge, and truncated nanocubes, respectively. Additional TEM images confirming the shape and size of Au/Ag NSs are also provided (Figure 4.4). Shape heterogeneity is a consequence of most seed-mediated growth processes,[44, 45, 46, 47] and often considered undesirable. However, our recent work on the use of these bimetallic nanostructures in enhancing the efficiency of solar cells[15, 16, 17, 18] demonstrated broadband solar photon absorption and substantial increase in efficiencies in the plasmon enhanced devices as a result of the shape mixture. Therefore, in this study we examine the ultrafast dynamics of the distinct optical resonances that arises from the two geometries, nanocubes and nanopyramids, as well as study the impact of their overall composition to ultimately understand their role in improving optoelectronic devices.

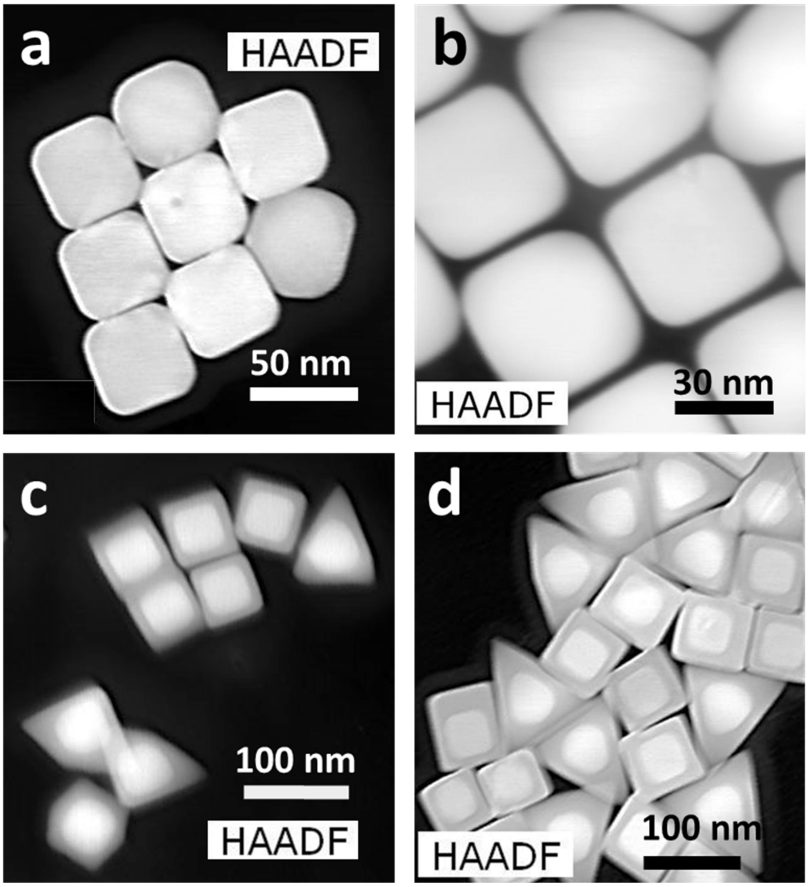

Figure 4.1: HAADF-STEM images corresponding to the EDS elemental mapping images found in Figure 4.2. Au/Ag bimetallic nanostructures containing a 45 nm Au core and (a) 0 nm Ag, (b) 2 nm Ag, (c) 8 nm Ag, and (d) 15 nm Ag shells are shown.

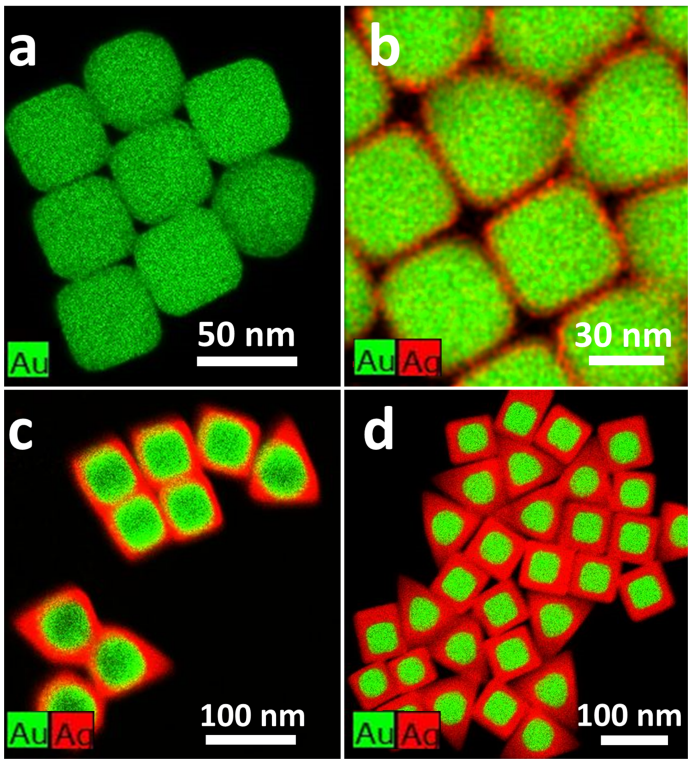

Figure 4.2: STEM and EDS elemental mapping images indicating Au (green) and Ag (red) in bimetallic nanostructures with a 45 nm Au core and (a) 0 nm Ag, (b) 2 nm Ag, (c) 8 nm Ag, and (d) 15 nm Ag shells.

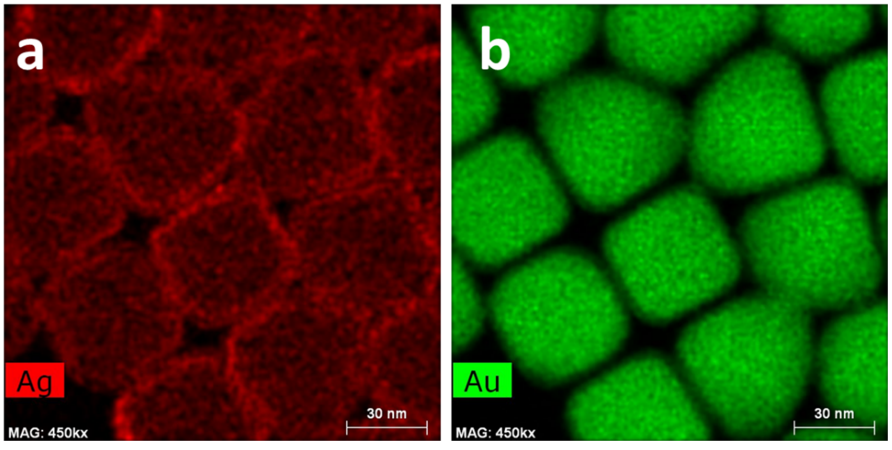

Figure 4.3: EDS elemental mapping images of 2 nm Ag Au/Ag NSs of (a) Ag and (b) Au. Individual elemental maps provided show thin but uniform silver shells encasing the Au NC cores.

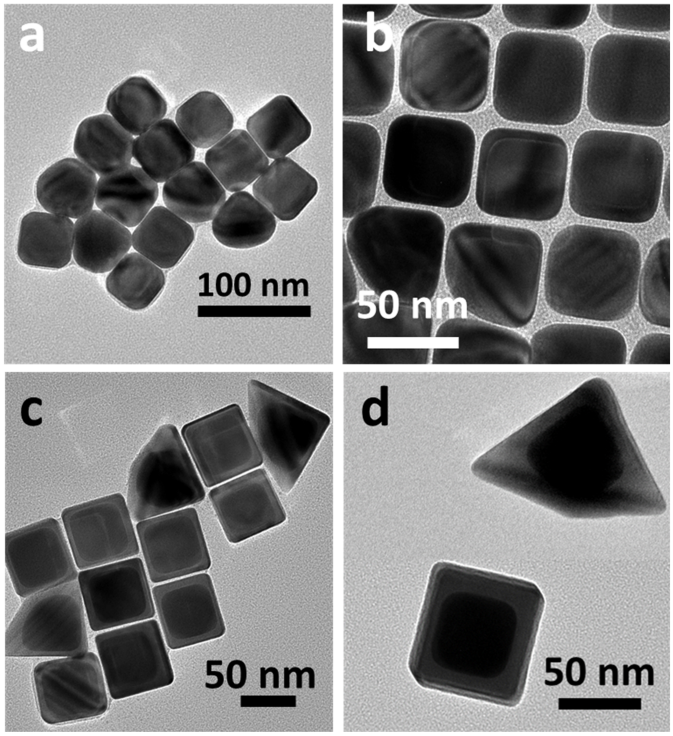

Figure 4.4: Standard TEM images of Au/Ag bimetallic nanostructures containing a 45 nm Au core and (a) 0 nm Ag, (b) 2 nm Ag, (c) 8 nm Ag, and (d) 15 nm Ag shells are shown.

The evolution of the optical properties of the Au/Ag NSs with increasing Ag layer thickness (Figure 4.5a) indicates a strong plasmon mode at ∼545 nm for the Au NC cores. While the growth of 2 nm Ag shell introduces slight broadening and blue-shift in the plasmon resonance, no additional peaks are observed due to low Ag concentration. With increasing Ag shell thickness to 8 nm, and 15 nm a second strong dipole resonance is observed at ∼620 nm corresponding to the bimetallic nanopyramids, a quadrupole mode is observed at 475 nm associated with the bimetallic nanocubes, and other higher-order modes associated with the corners of the nanopyramids/nanocubes are observed at 410 nm and 350 nm. These plasmonic modes are discussed in detail in our previous work.[14, 15] Spectral broadening and red-shift with increasing Ag shell thickness is attributable to phase retardation and radiation damping which result from increasing nanostructure size.[48, 49, 50, 51]

The corresponding normalized transient absorption (TA) spectra at 1 ps time delay,

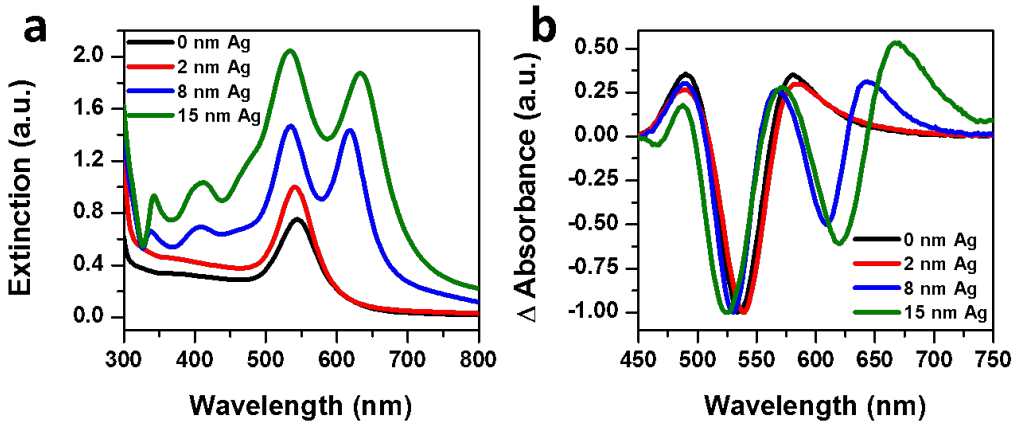

Figure 4.5: (a) Extinction spectra of Au/Ag core/shell nanostructures with varying Ag shell thicknesses, ranging from 0-15 nm. (b) Normalized transient absorption spectra at 1 ps time delay for Au NC core (0 nm Ag) and Au/Ag NSs.

near the time of maximum bleach, for all the samples are shown in Figure 4.5b. The data was normalized to the maximum bleach amplitude to enable comparison of the TA dynamics eliminating any effects from the concentration of the samples that impacts the magnitude of the peaks. We have also provided the non-normalized TAS data for each sample in Figure 4.6. The capping ligands on the nanostructures were not removed prior to the TA measurements to avoid aggregation during measurements. Any undesirable thermal effects in the aqueous medium should be minimal since low pump energy fluences were used in these studies. Samples were pumped at 400 nm and probed from 450 - 900 nm. The ultrafast TA dynamics of Au/Ag NSs evolves similar to the steady-state absorption measurements where a negative photobleaching band (PB1) centered at 530 nm is observed for the Au NC core (0 nm Ag). The laser pump at 400 nm perturbs the electron distribution in the metal nanostructures resulting in an increase in electron temperature. This broadens the plasmon band and gives rise to the photobleach at the band maximum, 530 nm, whereas absorption in the wings of the band appear as positive signals centered at 490 nm and 580 nm. The dominant PB1 feature is observable for all samples (Figure 4.5b), and shifts with the 2 nm Ag shell Au/Ag NSs due to the changes in surrounding dielectric medium, and continues to blue shift with thicker Ag shell similar to that observed in the extinction spectra

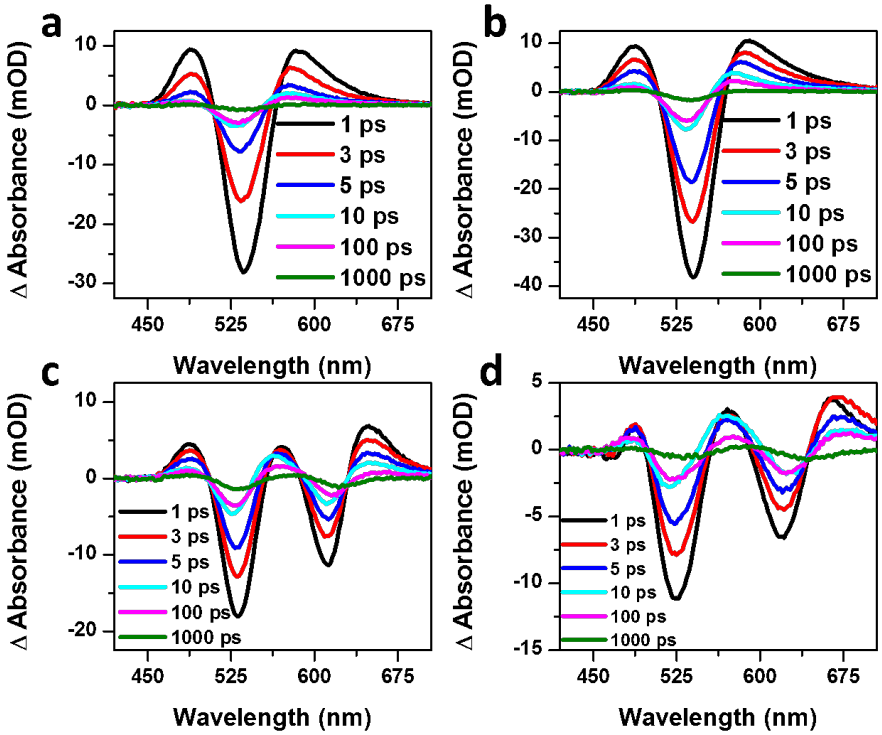

Figure 4.6: Transient absorption spectra at various time delays of solution samples of Au/Ag bimetallic nanostructures with (a) 0 nm Ag, (b) 2 nm Ag, (c) 8 nm Ag, and (d) 15 nm Ag shells around 45 nm Ag NC cores.

(Figure 4.5a). With increasing thickness of the Ag layer, the rise in electron temperature also broadens the dipolar resonance of the nanopyramids resulting in transient bleaching of the plasmon band centered at 610 nm and 625 nm for the 8 nm and 15 nm Ag layer samples, respectively. Transient absorption in the wings of this band manifests as an additional positive signal centered at 650 nm for the 8 nm Ag layer sample, and 670 nm for the 15 nm Ag layer sample.

The recovery of PB1 band, which correlates to the Au/Ag nanocubes, as a function of Ag layer thickness is shown in Figure 4.7a for low power (50 nJ/pulse) and Figure 4.7d for high power (500 nJ/pulse) measurements. Following femtosecond excitation of the bimetallic nanostructures, the electron distribution of the metal is subjected to ultra-fast changes where the incident energy is thermalized by the electrons via electron-electron scattering giving rise to a hot electron distribution around the Fermi level.[52] These hot

electrons ultimately relax back to equilibrium and thermally equilibrate with the nanocrystal lattice through electron-phonon scattering.[20, 37, 53] Subsequently, heat is released to the surrounding medium via phonon-phonon scattering, a phenomenon that has been extensively harnessed in photothermal therapies.[3, 54] Electron-phonon decay in metal nanostructures typically occur in timescales of 1-5 ps whereas phonon-phonon interactions occur in several hundred ps which is not only driven by the nanostructure size, composition, and surface chemistry, but also by the excitation energy.[21, 22, 36, 39] These characteristic timescales for the Au/Ag NSs were determined by fitting the experimental data (symbols) with a biexponential decay function (smooth lines) that yielded a fast (τ_1) and a slow (τ_2) time components at both 50 nJ/pulse (Figure 4.7b, c) and 500 nJ/pulse (Figure 4.7e, f). The electron-phonon scattering lifetimes of metal nanostructures are more accurately determined using sub-100 nJ/pulse power because low laser powers induce minimal perturbation of the electron distribution in the metal giving rise to nominal increase in electron temperature in the range of 100-200 K.[55] The electron-phonon, τ_1, (Figure 4.7b) lifetimes obtained at 50 nJ/pulse are in the 1-2 ps range and phonon-phonon, τ_2, (Figure 4.7c) lifetimes are in the 200-400 ps range consistent with that noted in the literature.[23, 25, 26, 27] Notably at 50 nJ/pulse, τ_1 increases by only 0.2 ps as a function of Ag layer thickness (Table 4.1) and no clear trends are seen in τ_2. This indicates that at low laser powers the Au/Ag NSs composition and increasing dimensions has nominal impact on the electronic lifetimes specifically in the size-regime we have probed. The decrease in τ_1 at 50 and 100 nJ/pulse (Table 4.1) observed for the 15 nm Ag shell sample is likely due to some aggregation of the nanostructures in the solution.

We further examined the electronic behavior of the Au/Ag NSs at a higher laser power (500 nJ/pulse) and observed that the electron-phonon lifetime, τ_1, (Figure 4.7e) increases with increasing Ag layer thickness in the 2-5 ps range which is simply attributable to photothermal effects in these nanostructures. With increasing Ag shell thickness their ability to absorb the 400 nm pump pulse improves due to the interband transition of Ag in the

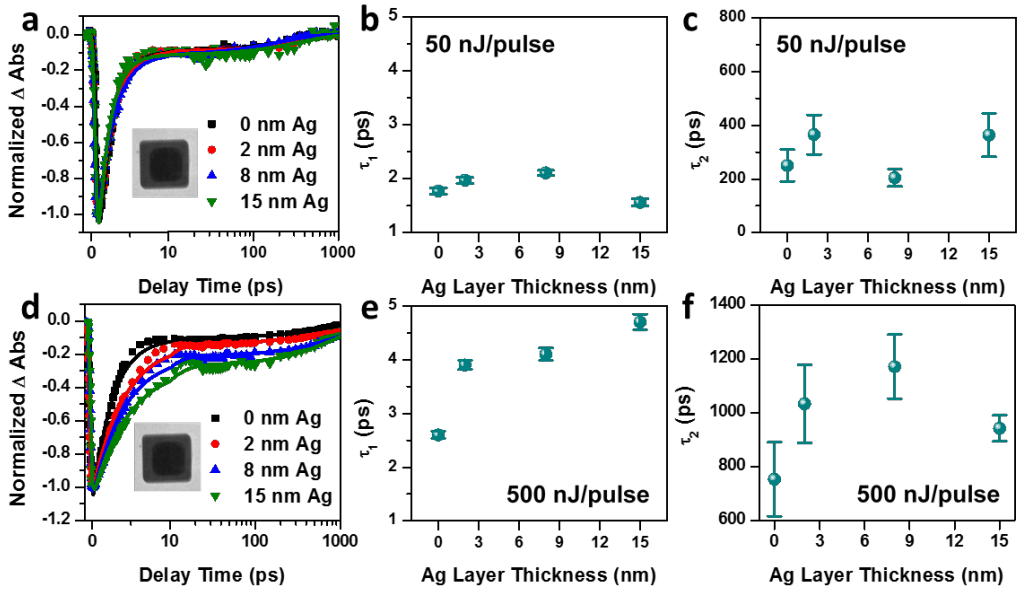

Figure 4.7: (a) Plasmon bleach recovery monitored at the maximum bleach of PB1 ($\sim$ 530 nm) after 400 nm pump for all samples types at low power excitation, 50 nJ/pulse. Kinetics are shown with experimental data (symbols) fitted with a biexponential decay function (smooth line). Corresponding fast (τ_1) and slow (τ_2) lifetimes obtained from fits in (a) are shown in (b) and (c) respectively. (d) Plasmon bleach recovery monitored at the maximum bleach of PB1 after 400 nm pump at high power excitation, 500 nJ/pulse. Corresponding fast (τ_1) and slow (τ_1) lifetimes obtained from fits in (d) are shown in (e) and (f) respectively. For (a) and (d), the early time scales are plotted linearly while later times (>10 ps) are plotted on a base-10 logarithmic scale. The TEM inset in (a) and (d) represents the nanostructure attributed to the PB1 band.

Table 4.1: The fast (electron-phonon, τ_1) and slow (phonon-phonon, τ_2) excited state decay lifetimes from the PB1 bleach centered at $\sim$ 530 nm of the Au/Ag nanocubes with varying Ag layer thickness at different excitation energies. Lifetimes were obtained by fitting time-dependent transient absorption data with a bi-exponential decay function.

	Excitation Energy			
Ag Layer Thickness	**50 nJ/pulse**	**100 nJ/pulse**	**250 nJ/pulse**	**500 nJ/pulse**
0 nm	1.77 ± 0.06 ps 250 ± 59 ps	2.23 ± 0.06 ps 279 ± 56 ps	2.01 ± 0.04 ps 757 ± 153 ps	2.63 ± 0.07 ps 752 ± 137 ps
2 nm	1.96 ± 0.05 ps 365 ± 74 ps	2.28 ± 0.05 ps 392 ± 54 ps	2.99 ± 0.07 ps 981 ± 98 ps	3.92 ± 0.09 ps 1033 ± 145 ps
8 nm	2.11 ± 0.05 ps 204 ± 32 ps	2.67 ± 0.07 ps 181 ± 29 ps	2.91 ± 0.09 ps 1173 ± 193 ps	4.08 ± 0.11 ps 1170 ± 118 ps
15 nm	1.55 ± 0.06 ps 363 ± 81 ps	1.76 ± 0.06 ps 503 ± 73 ps	3.74 ± 0.09 ps 803 ± 71 ps	4.70 ± 0.15 ps 942 ± 47 ps

UV. The absorption of the pump pulse induces an initial rise in electron temperature which increases with Ag thickness resulting in longer electron-phonon coupling lifetimes. The phonon-phonon scattering, τ_2, (Figure 4.7f) also increases with Ag layer thickness and is within 700-1200 ps range. Our observed τ_2 lifetimes at 500 nJ/pulse are higher than the time scale reported for metal nanoparticles in the 5-30 nm size[21, 22, 23, 24, 26, 37] likely contributed by the size effects of the $>$50 nm dimensions of our Au/Ag NSs, as well as contributed by surface chemistry effects. Since the mean free path of electrons in Au and Ag is $\sim$40 nm,[20, 56, 57] a larger nanostructure size would result in slower relaxation of excited electron-hole pairs and longer τ_2. Previous studies have reported similar observation where electron relaxation lifetime scales with size and decreasing surface area to volume ratio.[35, 58] Additionally the presence of surface ligands, CTAB and CTAC, also plays a strong role in the longer lifetimes. The presence of the ligands is necessary to prevent aggregation of the nanostructures during measurements. The amount of CTAB and CTAC required to keep the nanostructures in suspension in aqueous media exceeds the critical micelle concentration. This gives rise to the formation of stable bilayers of the surfactant on the surface of the nanostructures. Due to the hydrophobic nature of CTAB/CTAC direct contact between the Au/Ag NSs and the aqueous media is unlikely. Heat flux from the nanostructures to the aqueous media is slowed by resistances caused by interfacial thermal conductance between the nanostructure and the surfactant, as well as surfactant and surrounding media, which increases the lifetime.[32, 33, 59] It is also notable that both τ_1 and τ_2 are altered significantly at 500 nJ/pulse for the 2 nm Ag shell Au/Ag NSs despite minimal change in size and optical properties relative to the Au NC cores. This suggests that at higher laser powers even a thin Ag layer can sufficiently enhance absorption of excitation light at 400 nm and impact the electron-phonon and phonon-phonon lifetimes. However as shown in Figure 4.7a-c and Table 4.1 minimal change is observed in lifetimes at the lower power. This further affirms that the presence of the Ag layer impacts the absorption of the pump laser and corresponding electron temperature driven entirely by the pump fluence.

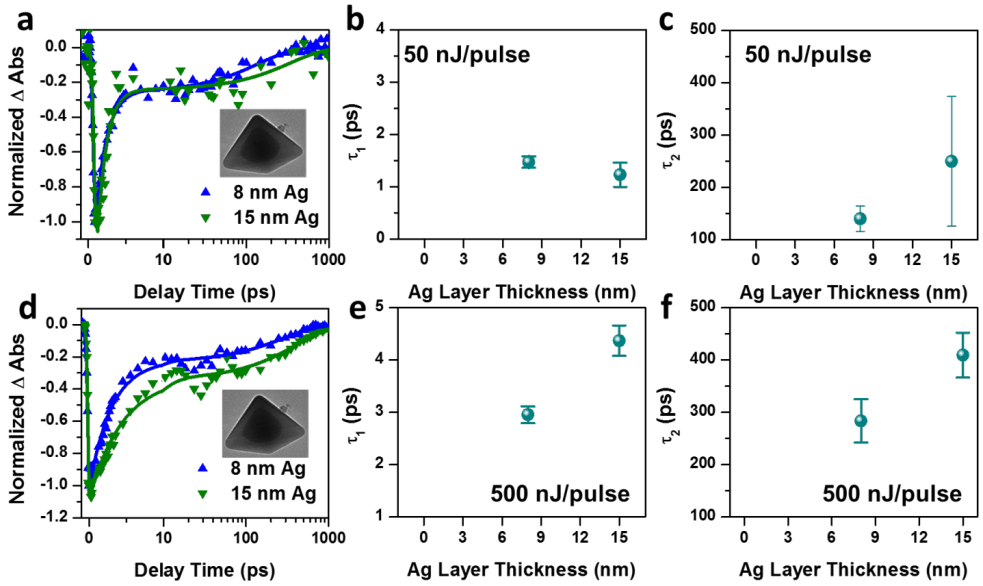

Figure 4.8: (a) Plasmon bleach recovery monitored at the maximum bleach of PB2 (∼620 nm) after 400 nm excitation for 8 nm and 15 nm Ag samples at low power excitation, 50 nJ/pulse. Corresponding fast (τ_1) and slow (τ_2) lifetimes obtained from fits in (a) are shown in (b) and (c), respectively. (d) Plasmon bleach recovery monitored at the maximum bleach of PB2 after 400 nm pump at high power excitation, 500 nJ/pulse. Corresponding fast (τ_1) and slow (τ_1) lifetimes obtained from fits in (d) are shown in (e) and (f) respectively. For (a) and (d), the early time scales are plotted linearly while later times (>10 ps) are plotted on a base-10 logarithmic scale. The TEM inset in (a) and (d) represents the nanostructure attributed to the PB2 band.

Table 4.2: The fast (electron-phonon, τ_1) and slow (phonon-phonon, τ_2) excited state decay lifetimes from the PB2 bleach centered at ∼620 nm of the Au/Ag nanocubes with varying Ag layer thickness at different excitation energies. Lifetimes were obtained by fitting time-dependent transient absorption data with a bi-exponential decay function.

	Excitation Energy			
Ag Layer Thickness	**50 nJ/pulse**	**100 nJ/pulse**	**250 nJ/pulse**	**500 nJ/pulse**
8 nm	1.47 ± 0.11 ps 139 ± 24 ps	1.96 ± 0.09 ps 172 ± 22 ps	2.20 ± 0.17 ps 296 ± 57 ps	2.98 ± 0.16 ps 283 ± 41 ps
15 nm	1.23 ± 0.23 ps 250 ± 124 ps	1.08 ± 0.20 ps 296 ± 83 ps	2.41 ± 0.19 ps 440 ± 54 ps	4.37 ± 0.29 ps 409 ± 43 ps

We also monitored the recovery of the second photobleaching band (PB2) at ∼620 nm, correlating to the plasmon relaxation of the bimetallic nanopyramids, at both 50 and 500 nJ/pulse (Figure 4.8a and d, respectively). Experimental data were fit with a biexponential decay function, and the extracted electron-phonon lifetimes (τ_1) for the 50 nJ/pulse measurements show minimal change with increasing Ag layer thickness (Figure 4.8b, c) similar to the recovery of PB1 observed for the nanocubes at low power (Figure 4.7a-c). While the phonon-phonon lifetimes (τ_2) appear to increase with increasing Ag, the low signal to noise ratio of the measurements for 15 nm Ag shell results in a large error bar (Figure 4.8c) diminishing the accuracy of the extracted time constant. Conversely, the extracted electron-phonon (τ_1) and phonon-phonon lifetimes (τ_2) at 500 nJ/pulse clearly show an increase with thicker Ag shells (Figure 4.8e, f), which is correlated to the increasing nanostructure size, surface chemistry effects, and absorption of the 400 nm pump pulse (Table 4.2). The decrease in τ_1 at 50 and 100 nJ/pulse (Table 4.2) observed for the 15 nm Ag shell nanopyramids sample is likely due to some agglomeration of the nanostructures in the solution. Further, we also observe an unexpected behavior at 500 nJ/pulse that is strongly shape-dependent. First, the phonon-phonon coupling lifetime, τ_2, for the nanopyramids is in the sub 600 ps range (Table 4.2), faster than τ_2 observed for the nanocubes (Table 4.1). This observation is correlated to the excitation of the nanostructures at 400 nm. While both nanocubes and nanopyramids have higher order modes that absorb near 400 nm, the strong dipole resonance of nanocubes at ∼530 nm is relatively closer to the 400 nm excitation than the dipolar resonance of the nanopyramids at ∼620 nm. This suggests that the nanocubes absorb more energy from the excitation pulse, resulting in a higher thermalization temperature due to an increase in heat capacity of the electron gas, and thus requiring longer dissipation times which result in longer τ_2.[24, 25] Second, at 500 nJ/pulse, τ_2 decreases for the thickest Ag shell (15 nm) Au/Ag nanocubes (Figure 4.7f) but not for the Au/Ag nanopyramids (Figure 4.8f). While more experiments will need to be done to elucidate the exact mechanism of this shape-dependent phenomenon, it may be correlated to the larger

number of edges and corners of the nanocubes relative to the nanopyramids.

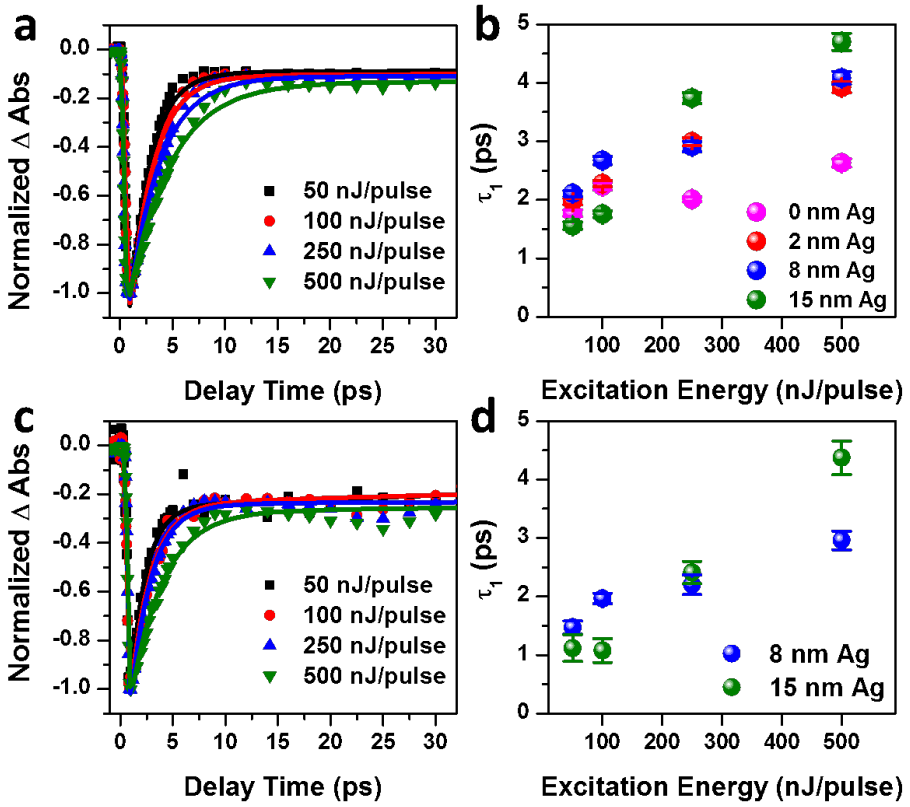

Figure 4.9: Normalized plasmon bleach recovery kinetics at (a) PB1 (∼530 nm) for 2 nm Ag shell Au/Ag NSs and (c) at PB2 (∼620 nm) for 8 nm Ag shell Au/Ag NSs at four different excitation energies. Kinetics are shown with experimental data (symbols) fitted with a biexponential decay function (smooth lines). The fast time component relating to electron-phonon interactions (τ_1) for all samples as a function of excitation energy at PB1 shown in (b), and for the 8 nm and 15 nm at PB2 is shown in (d).

To further examine the influence of excitation energy on electron dynamics of Au/Ag NSs, two additional excitation energies were probed so that samples of all Ag shell thickness were systematically studied at 50, 100, 250, and 500 nJ/pulse corresponding to pump fluences of ∼0.07, 0.14, 0.36, and 0.71 μJ/cm^2. Representative plasmon bleach recovery kinetics at 530 nm (PB1) for the 2 nm Ag shell Au/Ag NSs is shown in Figure 4.9a with increasing pump fluence. All the samples were probed at the four excitation energies and τ_1 and τ_2 were obtained from biexponential fits of the experimental data shown in Table 4.1. Note that the electron-phonon coupling times, τ_1, for all samples demonstrate a linear

dependence with increasing pump power (Figure 4.9b). Since the number of phonons in the nanocrystal is limited, higher pump powers result in longer decay lifetimes. This behavior is explained by the two temperature model which states that higher pump powers result in higher electron temperatures which gives rise to longer relaxation times due to the temperature dependence of electron heat capacity.[26, 27, 38] Note that the linear slope of thermalization lifetimes as a function of excitation energy increases with increasing Ag layer attributable to a rise in electron temperature. We also measured the photobleach recovery kinetics at 620 nm (PB2) correlating to the nanopyramids and representative spectra for the 8 nm Ag shell Au/Ag NSs is shown in Figure 4.9c. A similar trend was observed in the electron-phonon lifetime for the 8 nm and 15 nm Ag shell samples (Figure 4.9d) which suggests regardless of nanostructure shape, the thickness of the Ag layer governs the absorption of the 400 nm pump pulse, and higher the pump fluence, longer the lifetime of the Au/Ag NSs.

4.4 Conclusions

In summary, we have demonstrated the ultrafast dynamics of Au/Ag core/shell nanostructures with Ag shell thicknesses varying from 0-15 nm and the corresponding impact of shape and composition control on the electron-phonon coupling and phonon-phonon scattering lifetimes. Our synthesis resulted in both bimetallic nanocubes and nanopyramids with distinct optical properties and corresponding relaxation dynamics at the plasmon resonance. TAS measurements at low power show that both electron-phonon and phonon-phonon lifetimes have minimal dependence on the Ag layer thickness, whereas at high powers both lifetimes rise with increasing Ag shell. At high pump fluence the amount of Ag directly correlates to the absorption of the 400 nm pump laser and the rise in electron temperature, which then strongly impacts the electron-phonon coupling lifetime. The phonon-phonon scattering lifetime is affected by both the size of the Au/Ag nanostructures, which determines the timescale for heat dissipation, as well as the pres-

ence of surface ligands which controls the interfacial thermal conductance. In addition to composition-dependent trends, we also observe an unexpected shape-driven phenomenon at high power measurements. Whereas electron-phonon lifetime increased with increasing Ag shell thickness for both bimetallic nanocubes and nanopyramids, phonon-phonon lifetime decreased for the thickest Ag shell nanopyramids. We correlated this trend to the larger number of edges and corners in nanocubes relative to nanopyramids. We anticipate this fundamental study will enable deeper understanding of the ultrafast optical behavior of bimetallic shape-controlled nanostructures to ultimately allow their use in a range of applications including optoelectronics, sensing, contrast-enhanced imaging, and cancer therapeutics.

4.5 Methods

All reagents were purchased from Sigma Aldrich unless otherwise specified, and were used as received without further purification. Ultrapure water was used for nanostructure synthesis.

Au Nanocube Synthesis: All nanostructures used in this study were synthesized by following procedures described in our previous work.[14] Au nanocubes (Au NCs, 0 nm Ag) were prepared following a seed-mediated growth process. In a 20 mL vial, 7.5 mL of 100 mM cetyltrimethylammonium bromide (CTAB), 2.75 mL H_2O, and 0.25 mL of 10 mM $HAuCl_4$ were combined and equilibrated to 35 °C. An amount of 600 μL of freshly prepared, ice cold 10 mM $NaBH_4$ was injected to the mixture and stirred vigorously for 1 minute. It was then returned to the 35 °C water bath where it was left undisturbed for 1 hour to form the seeds. A growth solution was prepared by the sequential addition of 6.4 mL of 100 mM CTAB, 0.8 mL of 10 mM $HAuCl_4$, and 3.8 mL of 100 mM ascorbic acid to 32 mL of H_2O. Seeds were diluted tenfold with H_2O. An amount of 20 μL of diluted Au seeds were added to the growth solution, mixed gently by inversion, and then placed in the 35 °C water bath to react for 5 hours. Prior to Ag shell growth around the Au NC

cores, a ligand exchange was performed. CTAB-capped Au NCs were spun down in 7.5 mL aliquots at 1100 rcf for 15 minutes ($\times$3). The supernatant was removed and the Au NC pellet was washed and soaked in 3.75 mL of 20 mM cetyltrimethylammonium chloride (CTAC) for 15 minutes. After the final spin, the CTAC-capped Au NCs were re-dispersed in 500 μL of H_2O, and these were used as the final precursor for all Ag growth reactions.

Ag Shell Growth: A uniform standard silver shell (8 nm Ag) was formed by combining 400 μL of Au NC precursor with 100 μL of 10 mM KBr in 10 mL of 20 mM CTAC and placed in a 65 °C water bath. After 10 minutes, 100 μL of 10 mM $AgNO_3$ and 300 μL of 100 mM ascorbic acid were added and the concoction was mixed by inversion before being place back in the 65 °C water bath and allowed to react for 2 hours. To form the thin Ag shell (2 nm Ag), the same procedure was followed, however the reaction was slowed by using a 35 °C water bath and stopped at 2 minutes. Thick Ag shells (15 nm Ag) were grown by following the same procedure with one modification: 200 μL of 10 mM $AgNO_3$ was added to increase the amount of Ag in the reaction from 0.5 μmol to 1.0 μmol. The concentration of ascorbic acid addition was also increased to 600 μL.

Sample Preparation for TAS: Prior to transient absorption measurements, nanostructures were concentrated by centrifugation in order to achieve optimum optical density for the TAS experiments. Particles were re-dispersed in the remaining supernatant to ensure the presence of CTAC that was necessary to prevent aggregation of nanostructures during measurements.

Characterization: All optical absorbance spectra of the various nanostructures were taken using a Varian Cary 5000 UV-vis NIR spectrophotometer. Transmission electron micrographs and STEM-EDS maps were obtained using an FEI Tecnai Osiris transmission electron microscope at 200 kV.

Transient Absorption Spectroscopy: Femtosecond transient absorption measurements were conducted using a home-built pump-probe setup based on a femtosecond laser system, that utilizes seed pulses from a titanium sapphire oscillator (Micra, Coherent), amplified by

a Ti:Sapphire amplifier (Legend USP-HE, Coherent) to provide 800 nm femtosecond pulses (2.5 mJ/pulse), operating at 1 kHz repetition rate with 40 fs pulse durations. The Legend amplifier is pumped by a Nd:YLF laser (Evolution-30, Coherent). A small portion of the output of the amplifier ($\sim$4 μJ/pulse) is focused on a sapphire window (2 mm thick) to generate a white light continuum (WLC) probe (450-900 nm). To minimize temporal chirp in the spectrally broad probe, a set of parabolic mirrors was used to collimate and focus the WLC on the sample. The transmitted probe was focused onto 100 μm core fiber coupled with a spectrometer/CCD (USB2000ES, Ocean Optics). The pump pulse at 400 nm is generated by doubling $\sim$50 μJ/pulse of the 800 nm fundamental in a BBO crystal. The pump beam passes through a delay line to allow control of time-delay between the pump and the probe. In order to measure absorbance changes between every two successive laser shots, the pump beam was chopped at a frequency of 500 Hz. At the sample, the spot sizes of the pump and probe pulses were 150 μm and 50 μm, respectively. The samples were held between two quartz windows with a 200 micron spacer, and the experiments were performed without flowing. The pulse energy of the pump was varied between 50, 100, 250, and 500 nJ/pulse using a neutral density filter, corresponding to energy fluence of $\sim$0.07, 0.14, 0.36, and 0.71 μJ/cm^2, respectively.

4.6 Bibliography

[1] Mei Chen, Shaoheng Tang, Zhide Guo, Xiaoyong Wang, Shiguang Mo, Xiaoqing Huang, Gang Liu, and Nanfeng Zheng. Core-shell Pd@Au nanoplates as theranostic agents for in-vivo photoacoustic imaging, CT imaging, and photothermal therapy. *Adv. Mater.*, 26(48):8210–8216, 2014.

[2] Xiaoqing Huang, Shaoheng Tang, Biju Liu, Bin Ren, and Nanfeng Zheng. Enhancing the photothermal stability of plasmonic metal nanoplates by a core-shell architecture. *Adv. Mater.*, 23(30):3420–3425, 2011.

[3] Joseph A. Webb and Rizia Bardhan. Emerging advances in nanomedicine with engineered gold nanostructures. *Nanoscale*, 6(5):2502–2530, 2014.

[4] Ping Wu, Yang Gao, Hui Zhang, and Chenxin Cai. Aptamer-guided silver-gold bimetallic nanostructures with highly active surface-enhanced Raman scattering for specific detection and near-infrared photothermal therapy of human breast cancer cells. *Anal. Chem.*, 84(18):7692–7699, 2012.

[5] Weitai Wu, Jing Shen, Probal Banerjee, and Shuiqin Zhou. Core-shell hybrid nanogels for integration of optical temperature-sensing, targeted tumor cell imaging, and combined chemo-photothermal treatment. *Biomaterials*, 31(29):7555–7566, 2010.

[6] Rafael Contreras-Caceres, Claudine Dawson, Petr Formanek, Dieter Fischer, Frank Simon, Andreas Janke, Petra Uhlmann, and Manfred Stamm. Polymers as templates for Au and Au@Ag bimetallic nanorods: UV-Vis and surface enhanced Raman spectroscopy. *Chem. Mater.*, 25(2):158–169, 2013.

[7] Y. Cui, B. Ren, J. L. Yao, R. A. Gu, and Z. Q. Tian. Synthesis of Ag-core Au-shell bimetallic nanoparticles for immunoassay based on surface-enhanced Raman spectroscopy. *J. Phys. Chem. B*, 110(9):4002–4006, 2006.

[8] Simona E. Hunyadi and Catherine J. Murphy. Bimetallic silver-gold nanowires: fabrication and use in surface-enhanced Raman scattering. *J. Mater. Chem.*, 16(40):3929–3935, 2006.

[9] Yong Yang, Jianlin Shi, Go Kawamura, and Masayuki Nogami. Preparation of Au-Ag, Ag-Au core-shell bimetallic nanoparticles for surface-enhanced Raman scattering. *Scripta Mater.*, 58(10):862–865, 2008.

[10] Se-Woong Baek, Garam Park, Jonghyeon Noh, Changsoon Cho, Chun-Ho Lee, Min-Kyo Seo, Hyunjoon Song, and Jung-Yong Lee. Au@Ag core-shell nanocubes for efficient plasmonic light scattering effect in low bandgap organic solar cells. *Acs Nano*, 8(4):3302–3312, 2014.

[11] Hua Dong, Zhaoxin Wu, Ahmed El-Shafei, Bin Xia, Jun Xi, Shuya Ning, Bo Jiao, and Xun Hou. Ag-encapsulated Au plasmonic nanorods for enhanced dye-sensitized solar cell performance. *J. Mater. Chem. A*, 3(8):4659–4668, 2015.

[12] William R. Erwin, Holly F. Zarick, Eric M. Talbert, and Rizia Bardhan. Light trapping in mesoporous solar cells with plasmonic nanostructures. *Energy Environ. Sci.*, 9(5):1577–1601, 2016.

[13] Juyoung Yun, Sun Hye Hwang, and Jyongsik Jang. Fabrication of Au@Ag core/shell nanoparticles decorated TiO_2 hollow structure for efficient light-harvesting in dye-sensitized solar cells. *ACS Appl. Mater. Inter.*, 7(3):2055–2063, 2015.

[14] Holly F. Zarick, William R. Erwin, Jayde Aufrecht, Andrew Coppola, Bridget R. Rogers, Cary L. Pint, and Rizia Bardhan. Morphological modulation of bimetallic nanostructures for accelerated catalysis. *J. Mater. Chem. A*, 2(19):7088–7098, 2014.

[15] William R. Erwin, Andrew Coppola, Holly F. Zarick, Poorva Arora, Kevin J. Miller, and Rizia Bardhan. Plasmon enhanced water splitting mediated by hybrid bimetallic Au-Ag core-shell nanostructures. *Nanoscale*, 6(21):12626–12634, 2014.

[16] William R. Erwin, Chanse Hungerford, Holly F. Zarick, Eric M. Talbert, Poorva Arora, and Rizia Bardhan. Enhancement in organic photovoltaics controlled by the interplay between charge-transfer excitons and surface plasmons. *Acs Omega*, 1(4):722–729, 2016.

[17] Holly F. Zarick, William R. Erwin, Abdelaziz Boulesbaa, Olivia K. Hurd, Joseph A. Webb, Alexander A. Puretzky, David B. Geohegan, and Rizia Bardhan. Improving light harvesting in dye-sensitized solar cells using hybrid bimetallic nanostructures. *ACS Photonics*, 3(3):385–394, 2016.

[18] Holly F. Zarick, Abdelaziz Boulesbaa, Alexander A. Puretzky, Eric M. Talbert, Zachary R. DeBra, Naiya Soetan, David B. Geohegan, and Rizia Bardhan. Ultrafast carrier dynamics in bimetallic nanostructure-enhanced methylammonium lead bromide perovskites. *Nanoscale*, 9(4):1475–1483, 2017.

[19] J. Hodak, I. Martini, and G. V. Hartland. Ultrafast study of electron-phonon coupling in colloidal gold particles. *Chem. Phys. Lett.*, 284(1-2):135–141, 1998.

[20] S. Link, C. Burda, M. B. Mohamed, B. Nikoobakht, and M. A. El-Sayed. Femtosecond transient-absorption dynamics of colloidal gold nanorods: Shape independence of the electron-phonon relaxation time. *Phys. Rev. B*, 61(9):6086–6090, 2000.

[21] S. Link and M. A. El-Sayed. Spectral properties and relaxation dynamics of surface plasmon electronic oscillations in gold and silver nanodots and nanorods. *J. Phys. Chem. B*, 103(40):8410–8426, 1999.

[22] M. A. El-Sayed. Some interesting properties of metals confined in time and nanometer space of different shapes. *Acc. Chem. Res.*, 34(4):257–264, 2001.

[23] Y. Hamanaka, N. Hayashi, A. Nakamura, and S. Omi. Ultrafast relaxation dynamics of electrons in silver nanocrystals embedded in glass. *J. Lumin.*, 76-7:221–225, 1998.

[24] J. H. Hodak, I. Martini, and G. V. Hartland. Spectroscopy and dynamics of nanometer-sized noble metal particles. *J. Phys. Chem. B*, 102(36):6958–6967, 1998.

[25] Tony E. Karam, Holden T. Smith, and Louis H. Haber. Enhanced photothermal effects and excited-state dynamics of plasmonic size-controlled gold-silver-gold core-shell-shell nanoparticles. *J. Phys. Chem. C*, 119(32):18573–18580, 2015.

[26] S. Link, C. Burda, Z. L. Wang, and M. A. El-Sayed. Electron dynamics in gold and gold-silver alloy nanoparticles: The influence of a nonequilibrium electron distribution and the size dependence of the electron-phonon relaxation. *J. Chem. Phys.*, 111(3):1255–1264, 1999.

[27] Kuai Yu, Lakshminarayana Polavarapu, and Qing-Hua Xu. Excitation wavelength and fluence dependent femtosecond transient absorption studies on electron dynamics of gold nanorods. *J. Phys. Chem. A*, 115(16):3820–3826, 2011.

[28] Gregory V. Hartland. Optical studies of dynamics in noble metal nanostructures. *Chem. Rev.*, 111(6):3858–3887, 2011.

[29] G. V. Hartland. Measurements of the material properties of metal nanoparticles by time-resolved spectroscopy. *Phys. Chem. Chem. Phys.*, 6(23):5263–5274, 2004.

[30] M. Hu, H. Petrova, and G. V. Hartland. Investigation of the properties of gold nanoparticles in aqueous solution at extremely high lattice temperatures. *Chem. Phys. Lett.*, 391(4-6):220–225, 2004.

[31] Orla M. Wilson, Xiaoyuan Hu, David G. Cahill, and Paul V. Braun. Colloidal metal particles as probes of nanoscale thermal transport in fluids. *Phys. Rev. B*, 66(22):224301, 2002.

[32] Joshua Alper and Kimberly Hamad-Schifferli. Effect of ligands on thermal dissipation from gold nanorods. *Langmuir*, 26(6):3786–3789, 2010.

[33] Aaron J. Schmidt, Joshua D. Alper, Matteo Chiesa, Gang Chen, Sarit K. Das, and Kimberly Hamad-Schifferli. Probing the gold nanorod-ligand-solvent interface by plasmonic absorption and thermal decay. *J. Phys. Chem. C*, 112(35):13320–13323, 2008.

[34] L. Bonacina, A. Callegari, C. Bonati, F. van Mourik, and M. Chergui. Time-resolved photodynamics of triangular-shaped silver nanoplates. *Nano Lett.*, 6(1):7–10, 2006.

[35] M. Hu and G. V. Hartland. Heat dissipation forAu particles in aqueous solution: Relaxation time versus size. *J. Phys. Chem. B*, 106(28):7029–7033, 2002.

[36] S. Link and M. A. El-Sayed. Size and temperature dependence of the plasmon absorption of colloidal gold nanoparticles. *J. Phys. Chem. B*, 103(21):4212–4217, 1999.

[37] S. L. Logunov, T. S. Ahmadi, M. A. ElSayed, J. T. Khoury, and R. L. Whetten. Electron dynamics of passivated gold nanocrystals probed by subpicosecond transient absorption spectroscopy. *J. Phys. Chem. B*, 101(19):3713–3719, 1997.

[38] Damon A. Wheeler, Thomas D. Green, Haining Wang, Cristina Fernandez-Lopez, Luis Liz-Marzan, Shengli Zou, Kenneth L. Knappenberger, and Jin Z. Zhang. Optical properties and coherent vibrational oscillations of gold nanostars. *Chem. Phys. Lett.*, 543:127–132, 2012.

[39] J. H. Hodak, A. Henglein, M. Giersig, and G. V. Hartland. Laser-induced interdiffusion in AuAg core-shell nanoparticles. *J. Phys. Chem. B*, 104(49):11708–11718, 2000.

[40] Kuai Yu, Guanjun You, Lakshminarayana Polavarapu, and Qing-Hua Xu. Bimetallic Au/Ag core-shell nanorods studied by ultrafast transient absorption spectroscopy under selective excitation. *J. Phys. Chem. C*, 115(29):14000–14005, 2011.

[41] M. Broyer, E. Cottancin, J. Lerme, M. Pellarin, N. Del Fatti, F. Vallee, J. Burgin, C. Guillon, and P. Langot. Optical properties and relaxation processes at femtosecond scale of bimetallic clusters. *Faraday Discuss.*, 138:137–145, 2008.

[42] J. H. Hodak, A. Henglein, and G. V. Hartland. Tuning the spectral and temporal response in PtAu core-shell nanoparticles. *J. Chem. Phys.*, 114(6):2760–2765, 2001.

[43] Jian Feng Li, Xiang Dong Tian, Song Bo Li, Jason R. Anema, Zhi Lin Yang, Yong Ding, Yuan Fei Wu, Yong Ming Zeng, Qi Zhen Chen, Bin Ren, Zhong Lin Wang, and Zhong Qun Tian. Surface analysis using shell-isolated nanoparticle-enhanced Raman spectroscopy. *Nat. Protoc.*, 8(1):52–65, 2013.

[44] Vivek Sharma, Kyoungweon Park, and Mohan Srinivasarao. Colloidal dispersion of gold nanorods: Historical background, optical properties, seed-mediated synthesis, shape separation and self-assembly. *Mat. Sci. Eng. R-Rep.*, 65(1-3):1–38, 2009.

[45] Min Hu, Jingyi Chen, Zhi-Yuan Li, Leslie Au, Gregory V. Hartland, Xingde Li, Manuel Marquez, and Younan Xia. Gold nanostructures: engineering their plasmonic properties for biomedical applications. *Chem. Soc. Rev.*, 35(11):1084–1094, 2006.

[46] T. K. Sau and C. J. Murphy. Room temperature, high-yield synthesis of multiple shapes of gold nanoparticles in aqueous solution. *J. Am. Chem. Soc.*, 126(28):8648–8649, 2004.

[47] M. Hu, H. Petrova, X. Wang, and G. V. Hartland. Time-resolved and steady state spectroscopy of polydisperse colloidal silver nanoparticle samples. *J. Phys. Chem. B*, 109(30):14426–14432, 2005.

[48] Joseph A. Webb, William R. Erwin, Holly F. Zarick, Jayde Aufrecht, Harris W. Manning, Matthew J. Lang, Cary L. Pint, and Rizia Bardhan. Geometry-dependent plasmonic tunability and photothermal characteristics of multibranched gold nanoantennas. *J. Phys. Chem. C*, 118(7):3696–3707, 2014.

[49] Emilie Ringe, Jian Zhang, Mark R. Langille, Chad A. Mirkin, Laurence D. Marks, and Richard P. Van Duyne. Correlating the structure and localized surface plasmon resonance of single silver right bipyramids. *Nanotechnol.*, 23(44), 2012.

[50] Emilie Ringe, Mark R. Langille, Kwonnam Sohn, Jian Zhang, Jiaxing Huang, Chad A. Mirkin, Richard P. Van Duyne, and Laurence D. Marks. Plasmon length: A universal parameter to describe size effects in gold nanoparticles. *J. Phys. Chem. Lett.*, 3(11):1479–1483, 2012.

[51] C. Sonnichsen, T. Franzl, T. Wilk, G. von Plessen, J. Feldmann, O. Wilson, and P. Mulvaney. Drastic reduction of plasmon damping in gold nanorods. *Phys. Rev. Lett.*, 88(7):077402, 2002.

[52] C. Voisin, N. Del Fatti, D. Christofilos, and F. Vallee. Ultrafast electron dynamics and optical nonlinearities in metal nanoparticles. *J. Phys. Chem. B*, 105(12):2264–2280, 2001.

[53] J. Y. Bigot, V. Halte, J. C. Merle, and A. Daunois. Electron dynamics in metallic nanoparticles. *Chem. Phys.*, 251(1-3):181–203, 2000.

[54] Wenxue Chen, Ciceron Ayala-Orozco, Nrusingh C. Biswal, Carlos Perez-Torres, Marc Bartels, Rizia Bardhan, Gary Stinnet, Xian-De Liu, Baoan Ji, Amit Deorukhkar, Lisa V. Brown, Sushovan Guha, Robia G. Pautler, Sunil Krishnan, Naomi J. Halas, and Amit Joshi. Targeting pancreatic cancer with magneto-fluorescent theranostic gold nanoshells. *Nanomedicine*, 9(8):1209–1222, 2014.

[55] A. Arbouet, C. Voisin, D. Christofilos, P. Langot, N. Del Fatti, F. Vallee, J. Lerme, G. Celep, E. Cottancin, M. Gaudry, M. Pellarin, M. Broyer, M. Maillard, M. P. Pileni, and M. Treguer. Electron-phonon scattering in metal clusters. *Phys. Rev. Lett.*, 90(17):177401, 2003.

[56] Wolfgang Haiss, Nguyen T. K. Thanh, Jenny Aveyard, and David G. Fernig. Determination of size and concentration of gold nanoparticles from UV-Vis spectra. *Anal. Chem.*, 79(11):4215–4221, 2007.

[57] Fuming Wang and Nicholas A. Melosh. Plasmonic energy collection through hot carrier extraction. *Nano Lett.*, 11(12):5426–5430, 2011.

[58] M. Hu, H. Petrova, J. Y. Chen, J. M. McLellan, A. R. Siekkinen, M. Marquez, X. D. Li, Y. N. Xia, and G. V. Hartland. Ultrafast laser studies of the photothermal properties of gold nanocages. *J. Phys. Chem. B*, 110(4):1520–1524, 2006.

[59] Xuewang Wu, Yuxiang Ni, Jie Zhu, Nathan D. Burrows, Catherine J. Murphy, Traian Dumitrica, and Xiaojia Wang. Thermal transport across surfactant layers on gold nanorods in aqueous solution. *ACS Appl. Mater. Inter.*, 8(16):10581–10589, 2016.

CHAPTER 5

ENHANCED EFFICIENCY IN DYE-SENSITIZED SOLAR CELLS WITH SHAPE-CONTROLLED PLASMONIC NANOSTRUCTURES

Adapted from H. F. Zarick, O. Hurd, J. A. Webb, C. Hungerford, W. R. Erwin, and R. Bardhan, *ACS Photonics*, **2014**, *1*, 806 with permission from the American Chemical Society.

5.1 Summary

In this chapter, we demonstrate enhanced light harvesting in dye-sensitized solar cells (DSSCs) with gold nanocubes of controlled shape. Silica-coated nanocubes ($Au@SiO_2$ nanocubes) embedded in the photoanodes of DSSCs had a power conversion efficiency of 7.8% relative to 5.8% of reference (TiO_2 only) devices, resulting in a 34% improvement in DSSC performance. Photocurrent behavior and incident photon to current efficiency spectra revealed that device performance is controlled by the particle density of $Au@SiO_2$ nanocubes and monotonically decreases at very high nanocube concentration. Finite difference time domain simulations suggest that, at the 45 nm size regime, the nanocubes predominantly absorb incident light, giving rise to the lightning rod effect, which results in intense electromagnetic fields at the edges and corners. These intense fields increase the plasmonic molecular coupling, amplifying the carrier generation and DSSC efficiency.

5.2 Introduction

Dye-sensitized solar cells (DSSCs) have rapidly emerged as an appealing alternative to silicon photovoltaics due to the low processing costs and inexpensive constituent materials. Recent efforts to improve power conversion efficiencies (PCEs) have focused on the synthesis of panchromatic sensitizers, such as porphyrins, with enhanced light-harvesting

characteristics in the 600-900 nm wavelength range.[1] While effective, the overall PCE of these sensitizers is often lower than the best performing ruthenium dyes due to their reduced incident photon to current efficiency (IPCE) at shorter wavelengths. In addition to organic sensitizers, semiconductor quantum dots have also been utilized to enhance light absorption in solar cells.[2] However, new sensitizers often alter the energy band positions relative to the conduction band of TiO_2 and are incompatible with the redox potential of the electrolyte.[3, 4] Misaligned band energies result in poor charge separation and high recombination, lowering the overall device efficiency. Other strategies to augment light absorption have focused on increasing the thickness or changing the morphology of the photoanodes[5, 6] and adding scattering layers or back reflectors.[7, 8] Whereas these approaches have resulted in incremental enhancements in PCE, the higher materials and fabrication costs associated with thick film solar cells have outweighed the benefits. Alternative approaches are hence imperative to increase the overall light trapping in DSSCs and enhance the PCE without altering the material or electronic properties of sensitizers.

Metal nanostructures integrated with DSSCs can significantly amplify the light-harvesting characteristics of sensitizing molecules without affecting their chemical functionalities.[9, 10, 11, 12, 13] Following photoexcitation, metal nanostructures couple incident photons to conduction band electrons, generating surface plasmon resonances (SPRs). These SPRs give rise to light scattering into the nanoparticle far field, as well as generation of electromagnetic near fields, which decay exponentially within tens of nanometers from the particle surface.[14] By effectively manipulating these near-field and far-field properties, a range of technological applications have been realized, including chemical and biological sensing,[15] nanomedicine,[16] solar devices,[17, 18, 19] and photodetectors. The absorption and scattering efficiencies are governed by both the nanostructure size and shape. Nanostructures $>$100 nm in size primarily scatter light, whereas smaller nanostructures predominantly absorb light. Unlike spherical nanoparticles, isotropic and anisotropic plasmonic nanostructures with sharp edges and corners generate intense fields localized at the

corners and behave as nanosized light concentrators.[20, 21] Such shape-controlled nanostructures, when coupled with sensitizing molecules in a DSSC, give rise to three distinct phenomena: (*i*) nanostructures capture solar energy and scatter light, which is reabsorbed by the dye monolayer, increasing the total light harvested by the dye; (*ii*) nanostructures function as antennas, coupling the plasmonic near field to the optical absorption of the sensitizer, thereby increasing the total absorption cross-section; and (*iii*) nanostructures convert incident photons to hot electrons, which are rapidly injected into the conduction band of TiO_2, amplifying the number of carriers available for photocurrent generation.[22, 23] The strongest plasmon-molecule coupling is achieved when the absorption of the molecules overlaps with the nanostructure plasmon resonance, a phenomenon that has been actively harnessed in surface-enhanced spectroscopies.[24, 25, 26]

Whereas metal-enhanced DSSCs have largely focused on spherical nanostructures,[10, 12, 13, 27, 28, 29, 30] here we demonstrate the use of gold (Au) nanocubes of controlled geometry and dimensions to enable plasmonic enhancement of solar cells. Relative to their spherical counterparts, a cubic morphology (1) has two times higher absorption and extinction efficiency and three times higher scattering efficiency (Figure 5.1), (2) has about two times larger surface area, which suggests more dye molecules will be enhanced for a given DSSC area, and (3) facilitates a higher concentration of charges localized at the corners and edges, giving rise to larger electromagnetic fields due to the quasi-static lightning-rod effect.[21, 31, 32] These confined fields can be used as a secondary light source to promote optical interactions with vicinal molecules and materials. In this work, we have coated the Au nanocubes in a 3-5 nm uniform layer of silica ($Au@SiO_2$) and incorporated them into the photoanodes of DSSCs. We observed that 1.8 *wt.%* $Au@SiO_2$ nanocubes in photoanodes resulted in a 34% increase in the PCE of the device, and we note that device performance is driven entirely by an improvement in short-circuit current density. By varying the concentration of $Au@SiO_2$ nanocubes in DSSCs, we find a systematic dependence of nanocube *wt.%* on device efficiency. IPCE measurements demonstrate that the improve-

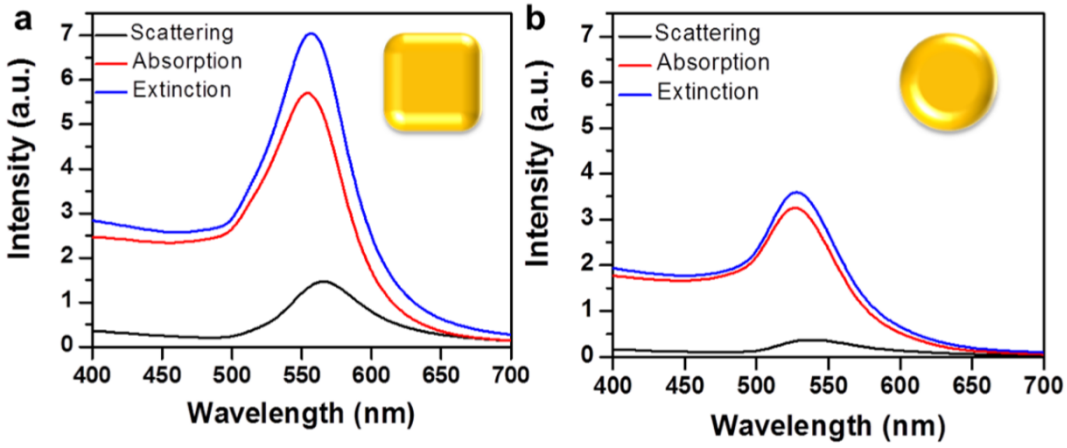

Figure 5.1: Calculated absorption, scattering, and extinction intensity in water of (a) rounded corner Au nanocubes of 45 nm edge length, and (b) Au nanospheres of 45 nm diameter using FDTD simulations. The calculations show that nanocubes have a two times higher absorption and extinction efficiency and three times higher scattering efficiency relative to nanospheres. Additionally, nanocubes also have a larger surface area compared to nanospheres. While the surface area of 45 nm nanospheres is 6361.74 nm^2, the surface area of 45 nm edge length nanocubes is 12150 nm^2. If we assume each N719 dye molecule is nominally 3 nm, then $\sim$2121 molecules will be adsorbed on each nanosphere and $\sim$4050 molecules will be adsorbed on each nanocube. Given the higher optical efficiencies and about two times larger surface area of nanocubes relative to nanospheres, DSSCs embedded with nanocubes will result in more intense light trapping, and more dye molecules will be enhanced for a given DSSC area.

ment in device performance is attributed to the enhanced light harvesting in the visible region of the spectrum due to direct coupling of Au nanocube plasmons with N719, ditetrabutylammonium *cis*-bis(isothiocyanato)bis(2,2-bipyridyl-4,4-dicarboxylato)ruthenium(II), dye molecules.

5.3 Results and Discussion

Au nanocubes of $\sim$45$\pm$3 nm edge length (Figure 5.2) were synthesized following a procedure previously described,[33] by a seed-mediated growth process with cetyltrimethylammonium bromide (CTAB) ligands as a shape-directing agent in aqueous media. We calculated the absorption and scattering efficiencies of rounded-corner nanocubes of a range of sizes (Figure 5.3). While for sizes $<$30 nm, Ohmic losses are high with very small

contribution from light scattering, for sizes $\geq$75 nm, scattering has a larger contribution relative to absorption. Based on our calculations at the 45-60 nm size range absorption to scattering ratios are optimal. The 45 nm edge length was chosen to facilitate enhanced light trapping due to large absorption cross-section at that size and also due to ease of synthesis. The CTAB-mediated growth process generates size-controlled Au nanocubes in the 15-50 nm size range but results in high degree of polydispersity with many shapes at larger sizes. It is possible 60 nm edge length nanocubes would have resulted in higher enhancements due to nearly equal contributions of absorption and scattering, however, it was difficult to synthesize this size with proper shape control. Before integrating the nanocubes in DSSC anodes, they were coated with a thin, 3-5 nm, layer of silica, generating Au@SiO_2 nanocubes (Figure 5.4a).[22] The silica layer serves several purposes. Since metals are electron scavengers, the silica spacer provides electrical isolation, minimizing recombination of electron-hole (e^-/h^+) pairs on the surface of the metal.[12] The silica layer protects the metal from the corrosive iodide/triiodide (I^-/I_3^-) liquid electrolyte. Finally, the silica layer also provides thermal stability to the nanocubes, reducing Ostwald ripening during the 500 °C annealing processes necessary for DSSC fabrication. A $\sim$3-5 nm silica layer is adequate in providing thermal and chemical stability to the nanocubes without detrimentally dampening the electromagnetic fields surrounding the nanocube surface. Thicker layers of silica ($>$10 nm) not only result in a red-shift of the plasmon resonance due to the higher refractive index of silica, but also shield the electron oscillation on the metal, causing plasmon dampening.[23] Au@SiO_2 nanocubes were integrated in DSSC photoanodes by mixing a concentrated colloidal solution with 20 nm TiO_2 nanoparticle paste to form a homogeneous mixture. The mixture was deposited on fluorine-doped tin oxide (FTO) glass substrates by doctor blading and sintered to convert the amorphous TiO_2 to its crystalline anatase phase. The nanocube-incorporated TiO_2 active layer was then sensitized with dye. FTO glass with a thin layer of Pt served as the cathode, and an I^-/I_3^- redox couple based liquid electrolyte enabled electron transport between the electrodes. A

schematic representation of the plasmon-enhanced DSSC is illustrated in Figure 5.4b. The optical characteristics of the nanocubes showed good overlap with the absorption spectrum of the N719 sensitizer (Figure 5.4c). Finite difference time domain (FDTD) simulations were performed to predict the absorption and scattering contributions of the nanocubes and overall extinction behavior. The calculated extinction spectrum (Figure 5.4c) of the nanocubes (555 nm) is slightly red-shifted from the experimental spectrum (548 nm). This shift is due to the heterogeneity in the reaction mixture attributed to the presence of both rounded-corner nanocubes and truncated nanocubes. Detailed particle distribution analysis is provided in Figure 5.5. As expected, the sub-50 nm size regime of the nanocubes results in a very low albedo, i.e., ratio of scattering to total extinction (Figure 5.4d), suggesting that nanocube-enhanced PCE of DSSCs occurs *via* near-field coupling with the dye molecules. The electromagnetic intensity profile, $\langle E^2/E_0{}^2 \rangle$, at the plasmon resonance peak of the Au nanocubes (Figure 5.4d inset) illustrates intense near fields localized at the edges and corners of the nanocubes. We note that, due to the high absorption to scattering ratio of Au@SiO_2 nanocubes, we chose to embed the nanocubes within the mesoporous TiO_2 layer of the photoanodes (Figure 5.4a) to enhance the overall optical absorption of the devices. Plasmonic nanostructures designed by lithographic approaches have been incorporated into DSSCs as back reflectors on the conductive substrate[18, 34] or on the counter electrode surface,[35] both of which enhance the overall device performance by forward light scattering with minimal contribution from near-field coupling. While effective, forward scattered light may not effectively couple with all of the sensitizer molecules within the $\sim$10 μm mesoporous layer; our strategy therefore focused on homogeneous mixing of the nanocubes within the TiO_2 layer to maximize proximity to sensitizer molecules.

To understand the mechanism of plasmonic enhancement of DSSCs, an energy diagram showing the mechanistic processes of DSSCs incorporated with nanostructured Au is demonstrated in Figure 5.6. Upon illumination, Au nanocubes preferentially absorb (with some scattering) incident light, generating confined electromagnetic fields on their surface.

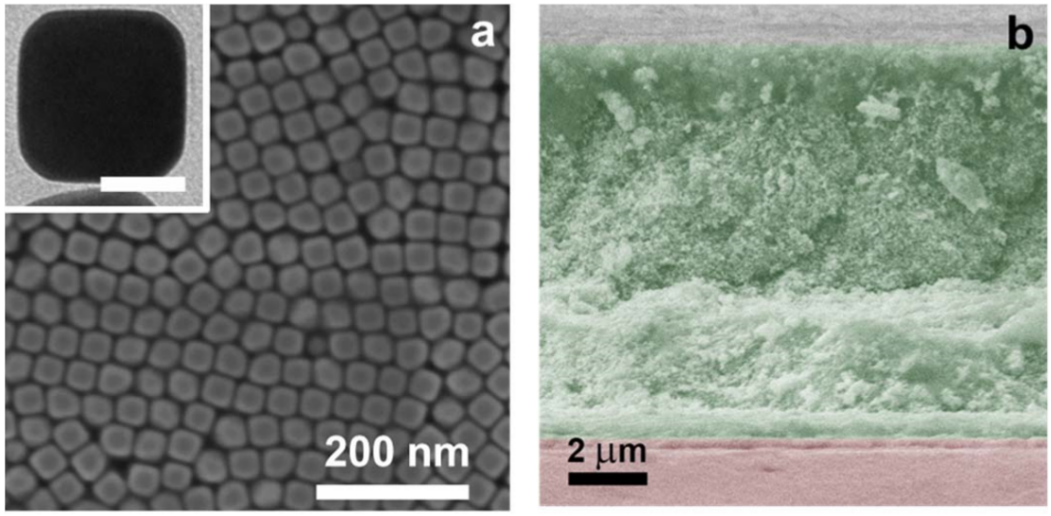

Figure 5.2: (a) SEM micrograph of as-synthesized Au nanocubes with TEM image of an individual nanocube in the inset. Scale bar is 20 nm in the inset. (b) Cross-section SEM image of DSSC showing $\sim 9 \pm 1$ μm thick dye-infiltrated mesoporous TiO_2 layer (green) on FTO-glass (red).

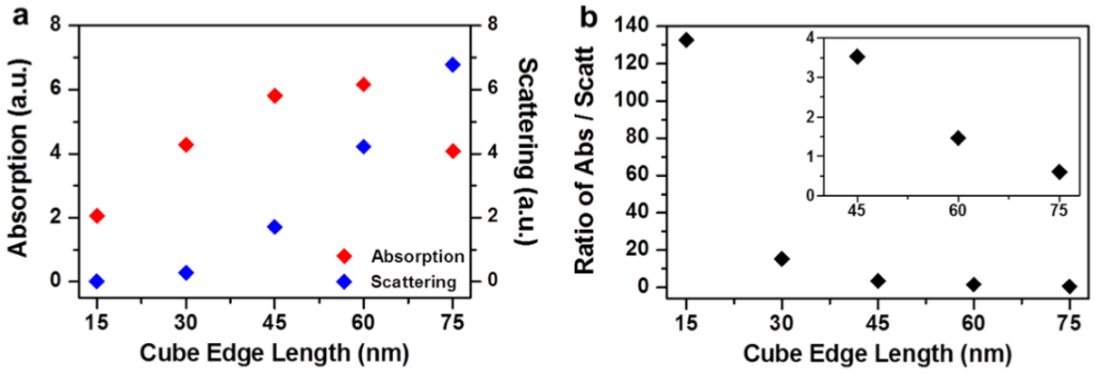

Figure 5.3: (a) Calculated absorption and scattering efficiencies of rounded-corner nanocubes of various edge lengths, and (b) ratio of absorption to scattering as a function of edge length. The inset in (b) shows a magnified view of nanocubes of 45-75 nm edge length.

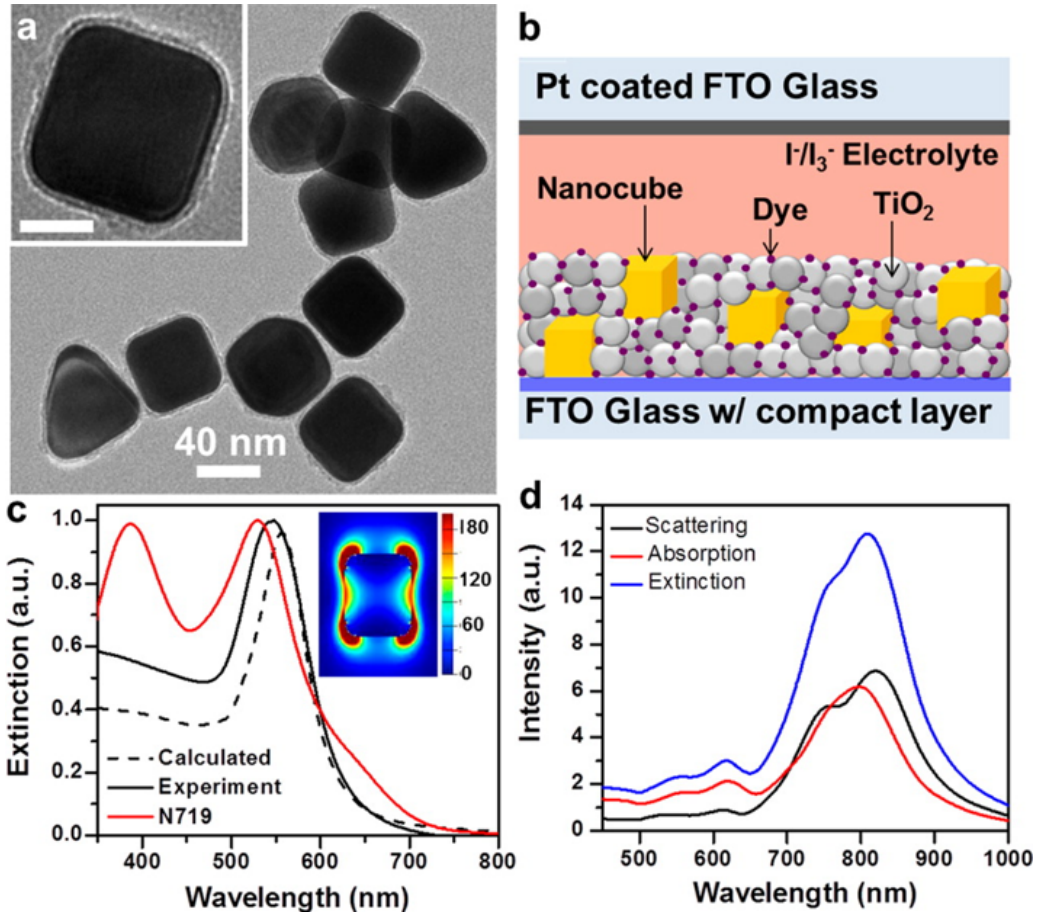

Figure 5.4: (a) Low-magnification TEM micrograph of $Au@SiO_2$ nanocubes and high-magnification image provided in the inset. The scale bar is 20 nm in the inset. (b) Schematic representation of plasmon-enhanced DSSCs showing nanocubes embedded within the N719-sensitized mesoporous TiO_2 layer with I^-/I_3^- liquid electrolyte. (c) Normalized experimental (solid black) and calculated (dashed black) extinction spectra of rounded-corner Au nanocubes in aqueous media with the electromagnetic intensity profile, $\langle E^2/{E_0}^2 \rangle$, in the inset. The absorption spectrum of N719 is also shown (red) to compare the peak position of N719 with Au nanocubes. (d) Calculated absorption, scattering, and extinction spectra of 45 nm edge length Au nanocubes in anatase TiO_2 surrounding media.

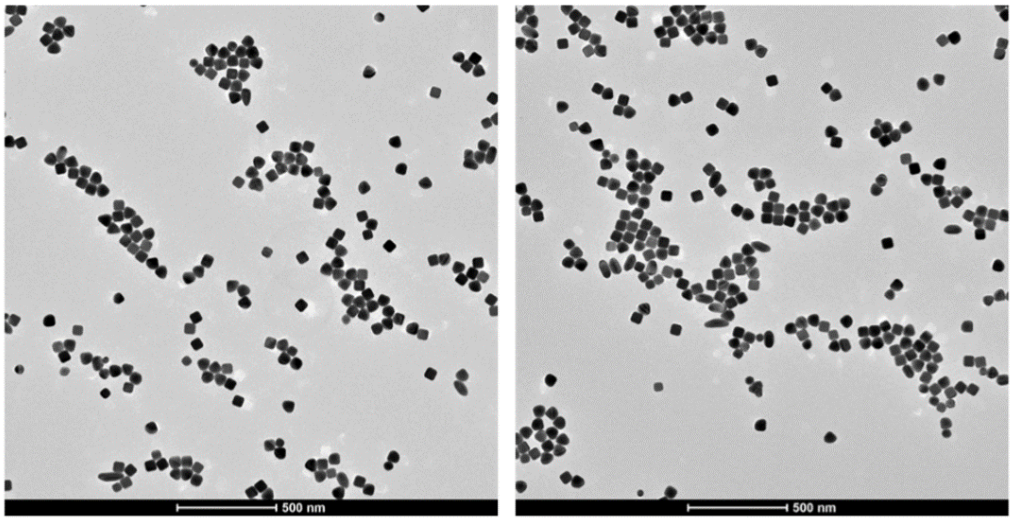

Figure 5.5: TEM images used to verify distribution of nanoparticles. 405 particles were counted, 54% are rounded-corner nanocubes, 45% are truncated nanocubes, and 1% are nanorods.

The vicinal sensitizer molecules couple with the intense plasmonic near field, using it as a secondary light source. This plasmon-molecular coupling results in enhanced light absorption by the dye molecules, augmenting the number of electron-hole pairs produced in the sensitizer. This subsequently results in a larger number of electrons transferring from the lowest unoccupied molecular orbital (LUMO) of the sensitizer to the conduction band of TiO_2. A larger carrier density increases the overall short-circuit current density of the DSSCs.

The optical absorption spectrum of the mesoporous TiO_2 sensitized with N719 is significantly enhanced with $Au@SiO_2$ nanocubes incorporated in the photoanodes (Figure 5.7a). Spectra are shown for the best performing devices containing an optimized concentration of 1.8 *wt.%* $Au@SiO_2$ nanocubes. We also show the absorbance in total percentage units in Figure 5.8 to demonstrate the amount of light absorbed in the devices. The absorption enhancement in photoanodes incorporated with nanocubes (Figure 5.7b), obtained by normalizing to a reference, shows strong improvement in light harvesting throughout the visible and near-infrared. Particularly, a three-fold enhancement in the 400-600 nm re-

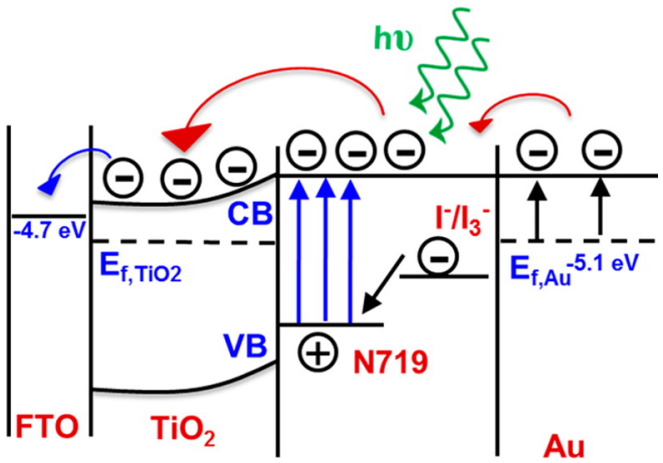

Figure 5.6: Energy diagram describing how the molecular coupling between plasmonic nanostructure and sensitizer results in enhanced absorption by N719, generating more electrons that transfer from the LUMO of the dye to the conduction band of TiO_2.

gion is attributed to dipole-dipole coupling of nanocubes and dye molecules. We also note that a 4-12 times absorption enhancement is also observable in the 600-800 nm region, attributable to a red-shift of the plasmon resonance of Au@SiO_2 nanocubes when embedded in the high refractive index ($n = 2.55$) of the TiO_2 mesoporous layer (Figure 5.4d), as well as some clustering of the nanocubes within the TiO_2 layer. In addition to the red-shift, both clustering of nanocubes and a high dielectric constant surrounding media also increase the overall light-scattering ability of the Au@SiO_2 nanocubes, improving the optical path length of the DSSCs and enhancing the device efficiency.[17] The PCEs of reference and plasmon-enhanced DSSCs of equivalent area of 0.12 cm^2 were examined under AM 1.5 illumination and received one sun (100 mW/cm^2) of power. The best performing reference and Au@SiO_2 nanocube-incorporated devices (Figure 5.7c) had PCEs of 5.8% and 7.8%, respectively, i.e., a 34% increase in PCE with plasmonic enhancement of DSSCs. IPCE measurements for these devices were performed to investigate the spectral response of DSSCs (Figure 5.7d) and to examine the light-harvesting characteristics of the plasmon-enhanced devices. A supercontinuum white light laser coupled with an acousto-optical tunable filter was used to modulate the wavelengths from 400 to 700 nm. While the shape of IPCE spectra of plasmon-enhanced and reference devices are similar,

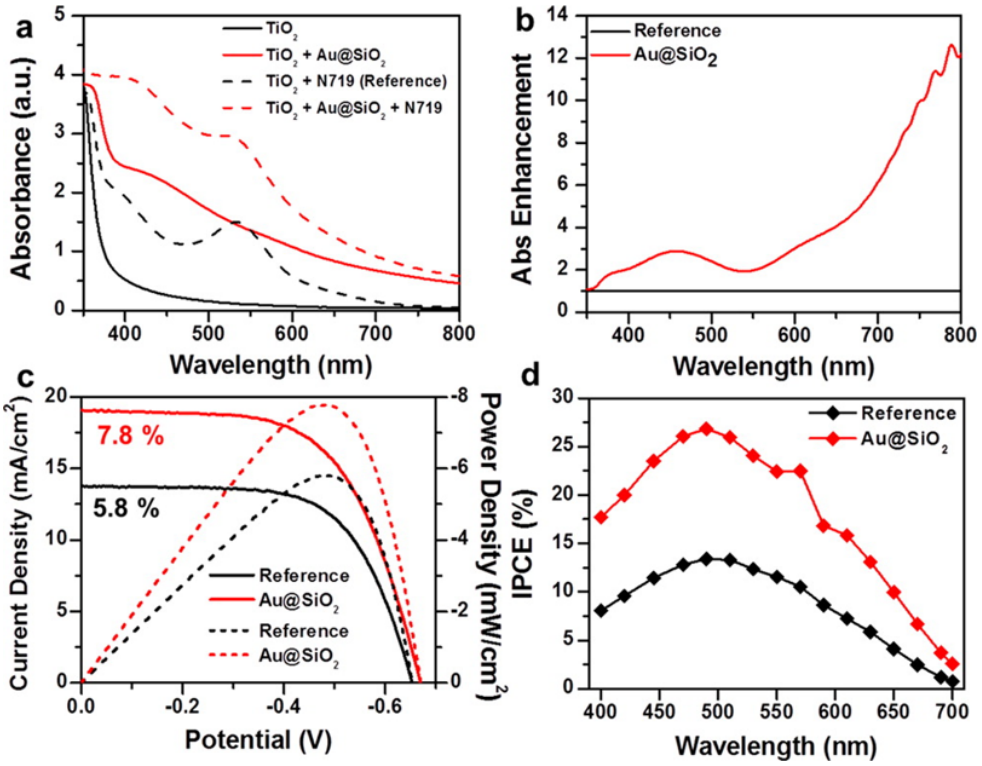

Figure 5.7: Optical absorption spectra of mesoporous TiO_2 before and after sensitizing with N719 and embedded with $Au@SiO_2$ nanocubes. The sample TiO_2 + N719 is referred to as Reference, and the sample with TiO_2 + $Au@SiO_2$ + N719 is referred to as $Au@SiO_2$ in (b), (c), and (d). (b) Absorption enhancement after embedding $Au@SiO_2$ nanocubes in the photoanode. A strong improvement in light harvesting is observed throughout the visible and near-infrared. (c) Current density (solid lines) and power density (dashed lines) curves of the DSSCs with ($Au@SiO_2$) and without (Reference) nanocubes. Corresponding incident photon to current efficiency (IPCE) curves are shown in (d). All plasmon-enhanced data are shown for the best performing devices with an optimized concentration of 1.8 *wt.%* $Au@SiO_2$ nanocubes.

the nanocube-incorporated devices showed a remarkable increase across the visible spectrum, specifically in the 450-550 nm range, overlapping with the plasmon resonance of $Au@SiO_2$ nanocubes. The IPCE spectra correspond well with the absorption spectra (Figure 5.7a), supporting that the nanocubes promote light trapping in the DSSCs. Enhancement in IPCE of nanocube-enhanced DSSCs relative to the reference is shown in Figure 5.9.

To further understand the light-harvesting capabilities of $Au@SiO_2$ nanocubes, the optimum concentration of the nanocubes was found by varying the particle density of

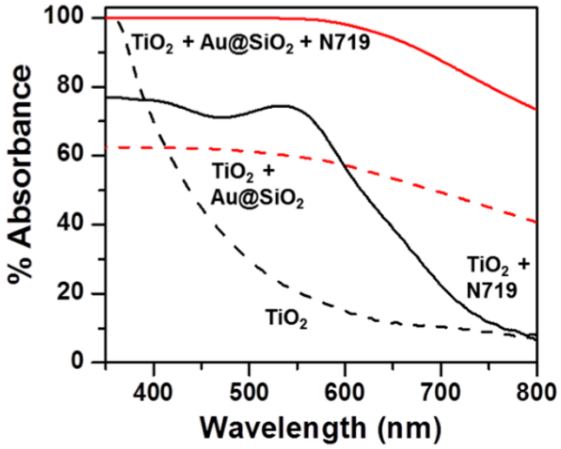

Figure 5.8: Percent absorbance of light in photoanodes with TiO_2 only (black dashed), TiO_2 sensitized with N719 (balck solid), TiO_2 with $Au@SiO_2$ nanocubes (red dashed), and TiO_2 with $Au@SiO_2$ nanocubes sensitized with N719 (red solid). The strong absorbance in the 600-800 nm spectral range of photoanodes with nanocubes is attributed to red-shift in plasmon resonances of nanocubes when embedded in the mesoporous TiO_2 film due to the high dielectric constant of anatase TiO_2. It is evident the light harvesting ability of DSSCs is significantly improved when embedded with $Au@SiO_2$ nanocubes.

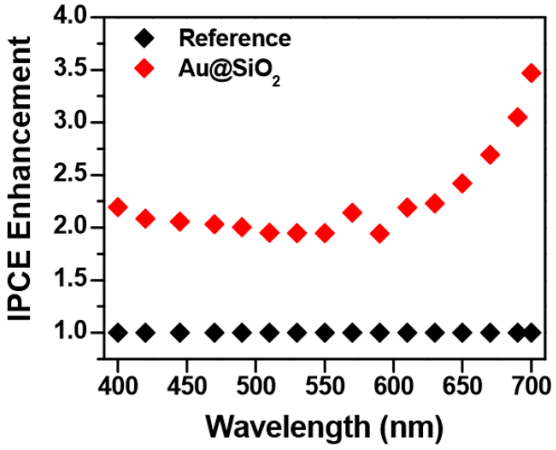

Figure 5.9: Enhancement in IPCE obtained by normalizing nanocube enhanced (1.8 *wt.%*) DSSC relative to reference DSSC. An overall increase in IPCE is observed throughout the spectral range and specifically in the near-infrared consistent with enhancement in absorption in the nearinfrared as observed in Figure 5.7b and Figure 5.11.

nanocubes from 0.6 to 4.47 *wt.%* in the TiO_2 active layer. The absorption spectra of nanocube-embedded anodes are shown in Figure 5.10a. For clarity, only selected concentrations are shown here; detailed spectra of all of the particle densities are shown in Figure 5.11. The optical absorption gradually increases across the entire visible spectrum with increasing nanocube concentration, indicating a stronger coupling between nanocube plasmons and dye molecules. At very high particle density of $Au@SiO_2$ nanocubes (>2.95 *wt.%*) in the TiO_2 active layer, we observe a strong red-shift in the optical absorption, which may be attributable to an increase in nanocube clustering at such high concentrations. The PCEs of the plasmon-enhanced DSSCs were examined under the same conditions as described above. Photocurrent spectra for select devices are shown in Figure 5.10b. IPCE measured in the 400-700 nm wavelength range (Figure 5.10c and Figure 5.12 for all concentrations) follows a similar trend to that observed in the photocurrent spectra (Figure 5.10b); IPCE is enhanced across the visible spectrum and reaches a maximum for 1.8 *wt.%* $Au@SiO_2$ nanocube concentration and then decreases with increasing concentration. The IPCE spectral characteristics correspond well to the absorbance spectra of the N719-sensitized photoanodes, and all show maximum enhancements in the 450-550 nm range, where the plasmon resonance peak of the nanocubes occurs. We note that all IPCE spectra show an enhancement relative to the reference (Figure 5.12), which suggests that even at the high particle densities of $Au@SiO_2$ nanocubes, plasmonic light trapping still occurs in these devices.

The detailed device performances of reference (nonenhanced) and plasmon-enhanced devices for all of the particle densities are shown in Figure 5.13 and also provided in Table 5.1. The open-circuit voltage (V_{oc}) and fill factor (FF) of the devices are almost equivalent (Figure 5.13a,b) with a significant increase in the short-circuit current density (J_{sc}) of the $Au@SiO_2$ nanocube-incorporated devices (Figure 5.13c). We do note that there are slight variances in V_{oc} and FF with metal weight percent, which can be attributed to batch-to-batch variations in nanocube to TiO_2 ratio in the DSSC photoanodes, environmental

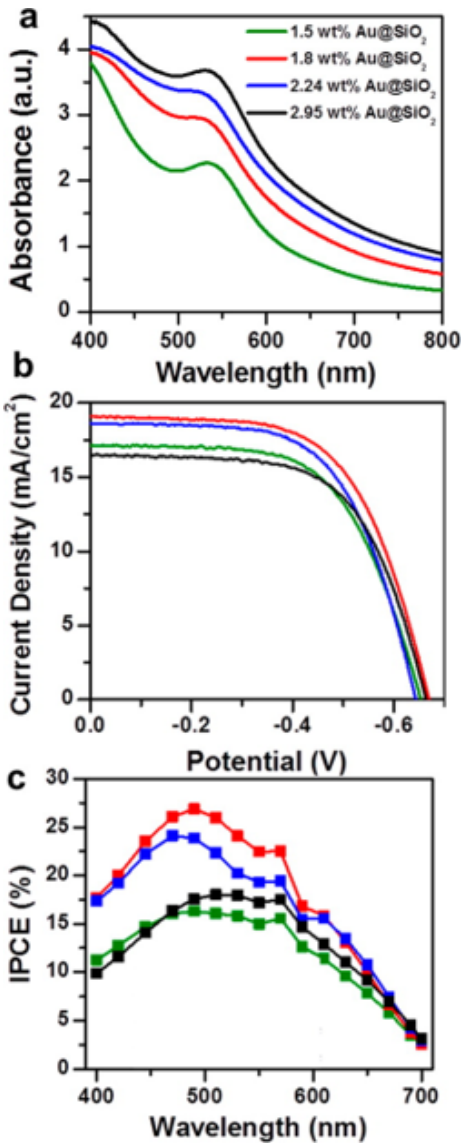

Figure 5.10: (a) Optical absorption spectra of N719-sensitized mesoporous TiO_2 with varied particle density of $Au@SiO_2$ nanocubes embedded in the photoanodes. (b) Corresponding current density spectra of the devices. (c) % IPCE of the same devices as a function of excitation wavelength.

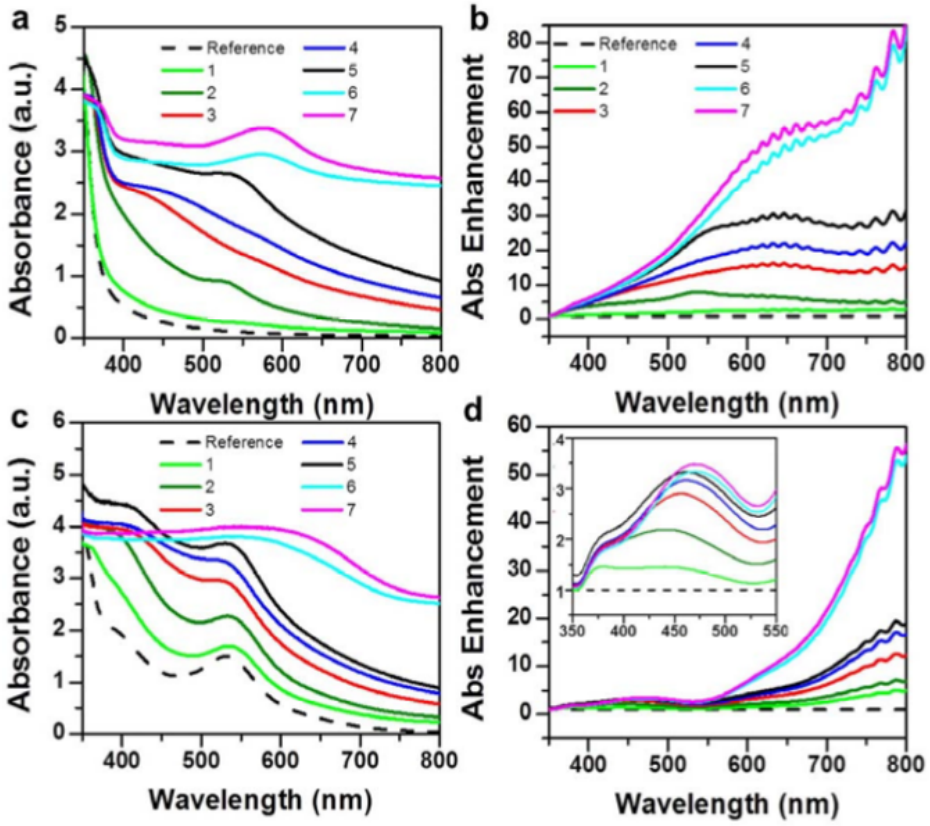

Figure 5.11: Optical absorption spectra (a,c) and absorption enhancement of DSSCs (b,d) embedded with Au@SiO_2 nanocubes relative to reference (TiO_2 only) photoanodes before (a,b) and after (c,d) sensitization with N719 dye. Absorption enhancement spectra were obtained by dividing the plasmon-enhanced spectra by the reference spectrum. A strong improvement in light harvesting is observed throughout the visible and near-infrared in the absorption enhancement spectra. Line 1 refers to 0.6 *wt.%* Au@SiO_2 nanocubes in the TiO_2 active layer, line 2 refers to 1.5 *wt.%*, line 3 refers to 1.8 *wt.%*, line 4 refers to 2.24 *wt.%*, line 5 refers to 2.95 *wt.%*, line 6 refers 3.56 *wt.%*, and line 7 refers to 4.47 *wt.%*.

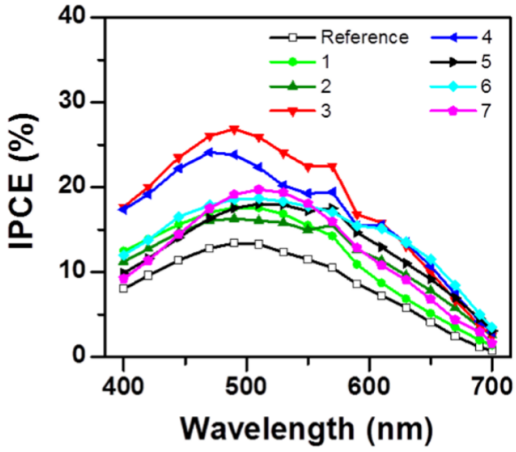

Figure 5.12: IPCE (%) spectra of the DSSCs as a function of excitation wavelength is shown for the reference (TiO_2 only) and plasmon-enhanced DSSCs. The figure is color-coordinated and the Au@SiO_2 nanocubes concentration is provided in the caption of Figure 5.11.

conditions such as humidity, or possibly some defects in the silica layer surrounding the nanocubes resulting in a reaction of the metal with the corrosive electrolyte. Since V_{oc} is highly sensitive to these parameters, a non-monotonic variance in the values is not surprising. However, we note that these parameters do not have a significant impact on the device performance because J_{sc} shows a clear trend with nanocube weight percent, and the small statistical uncertainty does not affect the overall trends in DSSC efficiency. This indicates that the observed plasmonic enhancements in DSSC efficiency are not due to any changes in the electrochemical properties, but rather due to improved light harvesting in DSSCs, resulting in an increased J_{sc}. The best efficiencies obtained for the DSSCs (Figure 5.13d) indicate that a maximum PCE of 7.8% is achieved for plasmon-enhanced DSSCs with 1.8 *wt.%* of nanocubes. We note that even at a low concentration of 0.6 *wt.%* of Au@SiO_2 nanocubes incorporated in the photoanodes, a 6.33% PCE is obtained, i.e., a 9% increase in efficiency relative to the reference device (5.8% PCE). Both best and average PCEs of plasmon-enhanced DSSCs reach a maximum at 1.8 *wt.%* of nanocubes, then monotonically decrease with further increases in concentration, and finally level off at 4.47 *wt.%* of nanocubes in the active layer. This decrease in device performance at high particle density

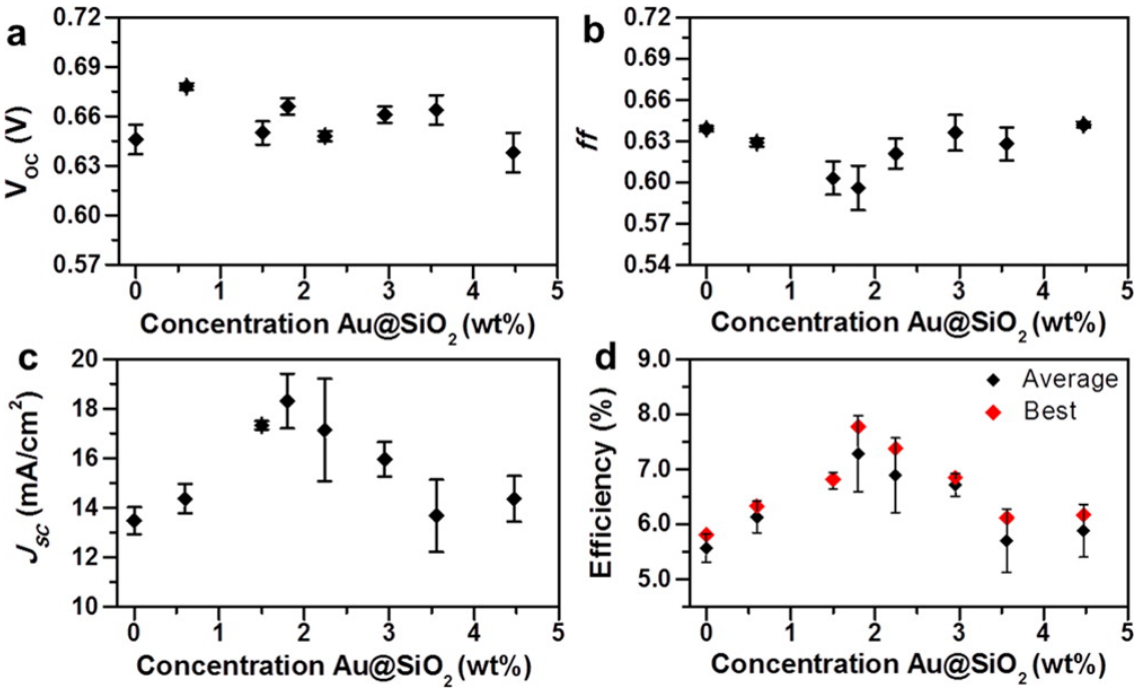

Figure 5.13: Open-circuit voltage (a), fill factor (b), short-circuit current density (c), and both average and best power conversion efficiency (d) from five devices are shown as a function of Au@SiO_2 nanocube particle density (*wt*.%). The nanocube concentration was varied between 0.6 and 4.47 *wt*.%.

of Au@SiO_2 nanocubes may be attributable to three phenomena: (*i*) the high concentration of metal increases electron-hole recombination, decreasing the number of carriers available for photocurrent generation; (*ii*) large volume of nanocubes results in the loss of absorbing dye volume; and (*iii*) the high nanocube density and interparticle interaction between adjacent nanocubes may result in light to heat conversion by electron-phonon coupling. The dissipation of this heat results in an increase in phonon density, which consequently reduces the number of carriers available for photocurrent generation, decreasing device efficiency.[13, 27] We have also provided a table (Table 5.2) with examples from the literature of other plasmon-enhanced work on DSSCs and how the efficiencies compare to our work (Table 5.2).

Table 5.1: Average values for short circuit current density (J_{sc}), open circuit voltage (V_{oc}), fill factor (FF), and efficiency (η), as well as best efficiencies for all DSSCs. A total of five devices were tested for each sample and standard deviation were used to calculate uncertainties.

Sample (Au@SiO_2 *wt.%* in TiO_2	**Average V_{oc} (V)**	**Average J_{sc} (mA/cm_2)**	**Average FF**	**Average η (%)**	**Best η (%)**
Reference	0.646 ± 0.009	13.5 ± 0.6	0.639 ± 0.002	5.6 ± 0.3	5.8
0.6 *wt.%*	0.678 ± 0.002	14.4 ± 0.6	0.629 ± 0.003	6.1 ± 0.3	6.3
1.5 *wt.%*	0.650 ± 0.007	17.3 ± 0.2	0.603 ± 0.012	6.8 ± 0.2	6.8
1.8 *wt.%*	0.666 ± 0.005	18.3 ± 1.1	0.596 ± 0.016	7.3 ± 0.7	7.8
2.24 *wt.%*	0.648 ± 0.003	17.1 ± 2.1	0.621 ± 0.011	6.9 ± 0.7	7.4
2.95 *wt.%*	0.661 ± 0.005	16.0 ± 0.7	0.636 ± 0.013	6.7 ± 0.2	6.9
3.56 *wt.%*	0.664 ± 0.009	13.7 ± 1.5	0.628 ± 0.012	5.7 ± 0.6	6.1
4.47 *wt.%*	0.638 ± 0.012	14.4 ± 0.9	0.642 ± 0.002	5.9 ± 0.5	6.2

5.4 Conclusions

In summary, we employed shape-controlled gold nanocubes coated in a thin, uniform layer of silica, Au@SiO_2 nanocubes, in the photoanodes of DSSCs and observed a 34% increase in efficiency relative to the reference (nonenhanced) devices. By varying the particle density, we observed a systematic dependence of device performance on the nanocube concentration; maximum enhancement was achieved with a 1.8 *wt.%* concentration of nanocubes. The 7.8% PCE achieved with the best performing plasmon-enhanced DSSC is attributed to a combination of intense electromagnetic fields confined at the corners and edges of the nanocubes, due to the lightning-rod effect, and nanocube scattering into the far field. Both phenomena give rise to plasmonic-molecular coupling and enhanced light absorption by the sensitizer. The enhanced light-harvesting characteristics of DSSCs integrated with nanocubes will ultimately enable the design of high-efficiency thin-film solar cells with a thickness of $<$500 nm with lower costs and better stability. The intrinsic properties of such shape-controlled metal nanostructures make them appealing for a range of optoelectronic devices beyond DSSCs, such as Si photovoltaics, organic solar cells, perovskite solar cells, and photodetectors.

Table 5.2: Survey of few examples from literature of power conversion efficiency of reference and plasmon enhanced DSSCs with metal nanostructures. Our work is shown at the end.

Nanoparticle	**Best PCE of Reference**	**Best PCE of Plasmon-Enhanced**	**% Enhancement**	**Ref.**
Ag@TiO_2 nanospheres	7.8%	9.00%	15.38%	[27]
Ag@TiO_2 hollow nanospheres	6.25%	8.13%	30.08%	[36]
Ag/TiO_2 short nanorods	7.10%	8.90%	25.35%	[37]
Au-SiO_2 nanospheres	1.70%	4.00%	135.29%	[12]
Au-Ag alloy popcorn nanoparticles	5.94%	7.85%	32.15%	[38]
Ag nanospheres	1.44%	1.96%	36.11%	[39]
Au@Ag_2S nanorods	5.8%	7.10%	22.41%	[11]
Ag nanospheres, patterned Ag/TiO_2	4.59%	5.69%	23.97%	[40]
Ag@SiO_2 nanoprisms	6.50%	8.40%	29.23%	[9]
Virus-templated Au@TiO_2nanoparticles	6.03%	8.46%	40.30%	[10]
Patterned Ag nanodomes	5.64%	5.93%	5.14%	[35]
Sandwiched TiO_2/NPs-Ag/TiO_2	1.43%	3.01%	110.49%	[34]
Au-coated counter-electrode	5.61%	6.64%	18.36%	[41]
Au nanoislands	5.31%	6.32%	19.02%	[42]
Au@SiO_2@TiO_2 nanospheres	3.07%	6.42%	109.12%	[29]
SiO_2@TiO_2@AuNP & SiO_2@AuNP@TiO_2	4.51%	5.94%	31.71%	[30]
Au@SiO_2 nanocubes	**5.80**%	**7.77**%	**33.97**%	**This work**

5.5 Methods

Au Nanocube Synthesis: Au nanocubes were synthesized by modifying a procedure previously described.[33] All reagents were purchased from Sigma-Aldrich. Au seeds were prepared by adding 0.6 mL of freshly prepared and ice cold 10 mM $NaBH_4$ to an aqueous solution composed of 7.5 mL of 100 mM CTAB, 2.75 mL milli-Q H2O (18.2 MΩ), and 0.8 mL of 10 mM $HAuCl_4$. This solution was stirred vigorously for 1 minute and then transferred to a 35 °C water bath where it was left undisturbed for one hour. A growth solution was prepared by the sequential addition of 6.4 mL of 100 mM CTAB, 0.8 mL of 10 mM $HAuCl_4$, and 3.8 mL of 100 mM ascorbic acid to 32 mL of milli-Q H_2O. The seed solution was diluted by a factor of ten with milli-Q H_2O. Then 20 μL of diluted seed solution was added to the growth solution, mixed gently by inversion, and then left undisturbed at 35 °C for 5 hours.

Silica-Coating Au Nanocubes (Au@SiO_2 Nanocubes): Au nanocubes were coated with a thin layer of silica (3-5 nm) by modifying a procedure previously described.[22] 30 mL of as-prepared Au nanocubes were first functionalized with 400 μL of 1 mM 3-aminopropyltriethoxysilane (APTES) for 15 minutes at room temperature while stirring. A 54 *wt.%* solution of sodium silicate was adjusted to pH ∼10.2 with 5 N HCl followed by injecting 700 μL into the APTES functionalized Au nanocubes. The reaction mixture was stirred for 3 minutes at room temperature and then transferred to a 50 °C oil bath and stirred for 4 hrs to form the silica shell.

Electrode Preparation: Electrodes were prepared on conductive substrates, fluorine-doped tin oxide coated on glass (FTO, MTI Corp.), that were first cleaned by sonication in a bath of 50/50 acteone/isopropanol with 1% Triton-X100 and 50/50 acetone/isopropanol for 30 minutes each. Cleaned FTO glass slides were treated with 40 mM $TiCl_4$ in water for 30 min at 70 °C and then dried in air. Reference TiO_2 anodes were prepared by doctor-blading a ∼10 μm layer of a 20 nm TiO_2 paste (Dyesol Inc., MS002010) onto the surface of the FTO using 1 layer of Scotch® tape to control the thickness, and then

fired in air at 500 °C for 30 minutes. Plasmon-enhanced anodes were prepared by first adding a washed and concentrated solution of $Au@SiO_2$ nanocubes directly into the 20 nm TiO_2 paste and mixing until homogeneous. The nanocube incorporated paste was then deposited via the doctor blade technique and fired as above. Note that the nanocubes are stable for up to four months after coating with silica; however, for best results, nanocubes were freshly prepared before each experiment and immediately coated with silica followed by incorporation in the photoanodes. We did not notice any aggregation or issues with stability of freshly prepared nanocubes. All anodes received a 40 mM $TiCl_4$ post treatment for 12 hours at 35 °C, and were then fired in air for 30 minutes at 500 °C. Finally, anodes were immersed in 0.6 mM Di-tetrabutylammonium cis-bis(isothiocyanato) bis(2,2-bipyridyl-4,4dicarboxylato)ruthenium(II) (N719 dye Sigma, 703206) in ethanol overnight inside a N_2 glove box. Platinum cathodes were prepared by drilling holes into the FTO glass before cleaning. A 25 mM H_2PtCl_6 in isopropanol solution was brushed onto clean FTO glass substrates and then fired at 450 °C for one hour.

DSSC Fabrication: The cathode and anode were heat-sealed with a ring of surlyn film (McMaster Carr, 7622A41). They were filled with I^-/I_3^- electrolyte comprised of 50 mM I_2, 500 mM LiI, and 500 mM tertbutylpyridine (TBP) in acetonitrile by injection through holes in the Pt electrode. Holes were then heat-sealed with additional surlyn.

Characterization: A Varian Cary 5000 UV-vis NIR spectrophotometer was used to measure the extinction of the Au nanocubes as well as the absorption of the TiO_2 thin film electrodes. The nanocubes were characterized using Philips CM20T TEM at 200 keV, an Osiris TEM at 200 keV, and a Zeiss Merlin SEM (Oak Ridge National Laboratory). Characterization of power conversion performance of the DSSCs was conducted with a Newport solar simulator and a potentiostat. Each cell received 1 sun (100 mW/cm^2) of power from the solar simulator at AM 1.5 and was tested in a range from -1.0 to 1.0 V at a scan rate of 50 mV/s. A cell area of 0.12 cm^2 was illuminated using a shadow mask. Incident photon conversion efficiency (IPCE) measurements were conducted with a 6 W Fianium fiber laser

supercontinuum source coupled with a Fianium acousto-optical tunable filter to filter out the desired excitation wavelength from the white light source.

Simulation Protocol: Finite difference time domain (FDTD) simulations were run with Lumerical FDTD Solutions. Calculations were performed on a single particle in water using a total-field scattered-field (TFSF) plane wave source. The simulated Au nanocube had a 45 nm edge length with a forward injection of the TFSF source along the y-axis.

5.6 Bibliography

[1] Aswani Yella, Hsuan-Wei Lee, Hoi Nok Tsao, Chenyi Yi, Aravind Kumar Chandiran, Md Khaja Nazeeruddin, Eric Wei-Guang Diau, Chen-Yu Yeh, Shaik M. Zakeeruddin, and Michael Graetzel. Porphyrin-sensitized solar cells with cobalt (II/III)-based redox electrolyte exceed 12 percent efficiency. *Science*, 334(6056):629–634, 2011.

[2] Matthew C. Beard, Joseph M. Luther, Octavi E. Semonin, and Arthur J. Nozik. Third generation photovoltaics based on multiple exciton generation in quantum confined semiconductors. *Acc. Chem. Res.*, 46(6):1252–1260, 2013.

[3] Chia-Yuan Chen, Mingkui Wang, Jheng-Ying Li, Nuttapol Pootrakulchote, Leila Alibabaei, Cevey-ha Ngoc-le, Jean-David Decoppet, Jia-Hung Tsai, Carole Graetzel, Chun-Guey Wu, Shaik M. Zakeeruddin, and Michael Graetzel. Highly efficient light-harvesting ruthenium sensitizer for thin-film dye-sensitized solar cells. *Acs Nano*, 3(10):3103–3109, 2009.

[4] Prashant V. Kamat. Boosting the efficiency of quantum dot sensitized solar cells through modulation of interfacial charge transfer. *Acc. Chem. Res.*, 45(11):1906–1915, 2012.

[5] Ki Seok Kim, Hui Song, Sang Hoon Nam, Sang-Mook Kim, Huisu Jeong, Won Bae Kim, and Gun Young Jung. Fabrication of an efficient light-scattering functionalized photoanode using periodically aligned ZnO hemisphere crystals for dye-sensitized solar cells. *Adv. Mater.*, 24(6):792–798, 2012.

[6] Xinjian Feng, Kai Zhu, Arthur J Frank, Craig A Grimes, and Thomas E Mallouk. Rapid charge transport in dyesensitized solar cells made from vertically aligned singlecrystal rutile TiO_2 nanowires. *Angew. Chem.*, 124(11):2781–2784, 2012.

[7] Poulomi Roy, Doohun Kim, Kiyoung Lee, Erdmann Spiecker, and Patrik Schmuki.

TiO_2 nanotubes and their application in dye-sensitized solar cells. *Nanoscale*, 2(1):45–59, 2010.

[8] Se-Hoon Han, Sangwook Lee, Hyunjung Shin, and Hyun Suk Jung. A quasi-inverse opal layer based on highly crystalline TiO_2 nanoparticles: A new light-scattering layer in dye-sensitized solar cells. *Adv. Energy Mater.*, 1(4):546–550, 2011.

[9] Mahesh K. Gangishetty, Kee Eun Lee, Robert W. J. Scott, and Timothy L. Kelly. Plasmonic enhancement of dye sensitized solar cells in the red-to-near-infrared region using triangular core shell $Ag@SiO_2$ nanoparticles. *Acs Appl. Mater. Interfaces*, 5(21):11044–11051, 2013.

[10] Po-Yen Chen, Xiangnan Dang, Matthew T. Klug, Jifa Qi, Noemie-Manuelle Dorval Courchesne, Fred J. Burpo, Nicholas Fang, Paula T. Hammond, and Angela M. Belcher. Versatile three-dimensional virus-based template for dye-sensitized solar cells with improved electron transport and light harvesting. *Acs Nano*, 7(8):6563–6574, 2013.

[11] Shuai Chang, Quan Li, Xudong Xiao, King Young Wong, and Tao Chen. Enhancement of low energy sunlight harvesting in dye-sensitized solar cells using plasmonic gold nanorods. *Energy Environ. Sci.*, 5(11):9444–9448, 2012.

[12] Michael D. Brown, Teeraporn Suteewong, R. Sai Santosh Kumar, Valerio D'Innocenzo, Annamaria Petrozza, Michael M. Lee, Ulrich Wiesner, and Henry J. Snaith. Plasmonic dye-sensitized solar cells using core-shell metal-insulator nanoparticles. *Nano Lett.*, 11(2):438–445, 2011.

[13] Xiangnan Dang, Jifa Qi, Matthew T. Klug, Po-Yen Chen, Dong Soo Yun, Nicholas X. Fang, Paula T. Hammond, and Angela M. Belcher. Tunable localized surface plasmon-enabled broadband light-harvesting enhancement for high-efficiency panchromatic dye-sensitized solar cells. *Nano Lett.*, 13(2):637–642, 2013.

[14] Prashant K. Jain and Mostafa A. El-Sayed. Plasmonic coupling in noble metal nanostructures. *Chem. Phys. Lett.*, 487(4-6):153–164, 2010.

[15] Joseph A. Webb and Rizia Bardhan. Emerging advances in nanomedicine with engineered gold nanostructures. *Nanoscale*, 6(5):2502–2530, 2014.

[16] Matthew D. Sonntag, Jordan M. Klingsporn, Alyssa B. Zrimsek, Bhavya Sharma, Laura K. Ruvuna, and Richard P. Van Duyne. Molecular plasmonics for nanoscale spectroscopy. *Chem. Soc. Rev.*, 43(4):1230–1247, 2014.

[17] K. R. Catchpole and A. Polman. Design principles for particle plasmon enhanced solar cells. *Appl. Phys. Lett.*, 93(19):191113, 2008.

[18] Carl Hagglund, Michael Zach, and Bengt Kasemo. Enhanced charge carrier generation in dye sensitized solar cells by nanoparticle plasmons. *Appl. Phys. Lett.*, 92(1):013113, 2008.

[19] M. Westphalen, U. Kreibig, J. Rostalski, H. Lth, and D. Meissner. Metal cluster enhanced organic solar cells. *Sol. Energy Mater. Sol. Cells*, 61(1):97–105, 2000.

[20] Joseph A. Webb, William R. Erwin, Holly F. Zarick, Jayde Aufrecht, Harris W. Manning, Matthew J. Lang, Cary L. Pint, and Rizia Bardhan. Geometry-dependent plasmonic tunability and photothermal characteristics of multibranched gold nanoantennas. *J. Phys. Chem. C*, 118(7):3696–3707, 2014.

[21] Matthew Rycenga, Xiaohu Xia, Christine H. Moran, Fei Zhou, Dong Qin, Zhi-Yuan Li, and Younan Xia. Generation of hot spots with silver nanocubes for single-molecule detection by surface-enhanced Raman scattering. *Angew. Chem., Int. Ed.*, 50(24):5473–5477, 2011.

[22] Jian Feng Li, Xiang Dong Tian, Song Bo Li, Jason R. Anema, Zhi Lin Yang, Yong Ding, Yuan Fei Wu, Yong Ming Zeng, Qi Zhen Chen, Bin Ren, Zhong Lin Wang, and

Zhong Qun Tian. Surface analysis using shell-isolated nanoparticle-enhanced raman spectroscopy. *Nat. Protoc.*, 8(1):52–65, 2013.

[23] H. Baida, P. Billaud, S. Marhaba, D. Christofilos, E. Cottancin, A. Crut, J. Lerme, P. Maioli, M. Pellarin, M. Broyer, N. Del Fatti, F. Vallee, A. Sanchez-Iglesias, I. Pastoriza-Santos, and L. M. Liz-Marzan. Quantitative determination of the size dependence of surface plasmon resonance damping in single $Ag@SiO_2$ nanoparticles. *Nano Lett.*, 9(10):3463–3469, 2009.

[24] Rizia Bardhan, Nathaniel K. Grady, and Naomi J. Halas. Nanoscale control of near-infrared fluorescence enhancement using Au nanoshells. *Small*, 4(10):1716–1722, 2008.

[25] Kyle C. Bantz, Audrey F. Meyer, Nathan J. Wittenberg, Hyungsoon Im, Ozge Kurtulus, Si Hoon Lee, Nathan C. Lindquist, Sang-Hyun Oh, and Christy L. Haynes. Recent progress in SERS biosensing. *Phys. Chem. Chem. Phys.*, 13(24):11551–11567, 2011.

[26] Louis Brus. Noble metal nanocrystals: Plasmon electron transfer photochemistry and single-molecule raman spectroscopy. *Acc. Chem. Res.*, 41(12):1742–1749, 2008.

[27] Jifa Qi, Xiangnan Dang, Paula T. Hammond, and Angela M. Belcher. Highly efficient plasmon-enhanced dye-sensitized solar cells through metal@oxide core-shell nanostructure. *Acs Nano*, 5(9):7108–7116, 2011.

[28] Rounak A. Naphade, Mukta Tathavadekar, Jyoti P. Jog, Shruti Agarkar, and Satishchandra Ogale. Plasmonic light harvesting of dye sensitized solar cells by Au-nanoparticle loaded TiO_2 nanofibers. *J. Mater. Chem. A*, 2(4):975–984, 2014.

[29] Stafford W. Sheehan, Heeso Noh, Gary W. Brudvig, Hui Cao, and Charles A. Schmuttenmaer. Plasmonic enhancement of dye-sensitized solar cells using core-shell-shell nanostructures. *J. Phys. Chem. C*, 117(2):927–934, 2013.

[30] Yoon Hee Jang, Yu Jin Jang, Saji Thomas Kochuveedu, Myunghwan Byun, Zhiqun Lin, and Dong Ha Kim. Plasmonic dye-sensitized solar cells incorporated with Au-TiO_2 nanostructures with tailored configurations. *Nanoscale*, 6(3):1823–1832, 2014.

[31] Mohamed Haggui, Montacer Dridi, Jerome Plain, Sylvie Marguet, Henri Perez, George C. Schatz, Gary P. Wiederrecht, Stephen K. Gray, and Renaud Bachelot. Spatial confinement of electromagnetic hot and cold spots in gold nanocubes. *Acs Nano*, 6(2):1299–1307, 2012.

[32] Matthew Rycenga, Moon Ho Kim, Pedro H. C. Camargo, Claire Cobley, Zhi-Yuan Li, and Younan Xia. Surface-enhanced Raman scattering: Comparison of three different molecules on single-crystal nanocubes and nanospheres of silver. *J. Phys. Chem. A*, 113(16):3932–3939, 2009.

[33] T. K. Sau and C. J. Murphy. Room temperature, high-yield synthesis of multiple shapes of gold nanoparticles in aqueous solution. *J. Am. Chem. Soc.*, 126(28):8648–8649, 2004.

[34] Su-Jien Lin, Kuang-Che Lee, Jyun-Lin Wu, and Jun-Yi Wu. Enhanced performance of dye-sensitized solar cells via plasmonic sandwiched structure. *Appl. Phys. Lett.*, 99(4):043306, 2011.

[35] I. Kang Ding, Jia Zhu, Wenshan Cai, Soo-Jin Moon, Ning Cai, Peng Wang, Shaik M. Zakeeruddin, Michael Graetzel, Mark L. Brongersma, Yi Cui, and Michael D. McGehee. Plasmonic dye-sensitized solar cells. *Adv. Energy Mater.*, 1(1):52–57, 2011.

[36] Jiang Du, Jian Qi, Dan Wang, and Zhiyong Tang. Facile synthesis of Au@TiO_2 core-shell hollow spheres for dye-sensitized solar cells with remarkably improved efficiency. *Energy Environ. Sci.*, 5(5):6914–6918, 2012.

[37] N. C. Jeong, C. Prasittichai, and J. T. Hupp. Photocurrent enhancement by surface

plasmon resonance of silver nanoparticles in highly porous dye-sensitized solar cells. *Langmuir*, 27(23):14609–14614, 2011.

[38] Q. Xu, F. Liu, Y. Liu, K. Cui, X. Feng, W. Zhang, and Y. Huang. Broadband light absorption enhancement in dye-sensitized solar cells with Au-Ag alloy popcorn nanoparticles. *Sci. Rep.*, 3:2112, 2013.

[39] Su-Jien Lin, Kuang-Che Lee, Jyun-Lin Wu, and Jun-Yi Wu. Plasmon-enhanced photocurrent in dye-sensitized solar cells. *Sol. Energy*, 86(9):2600–2605, 2012.

[40] Wei Jiang, Hongzhong Liu, Lei Yin, and Yucheng Ding. Fabrication of well-arrayed plasmonic mesoporous TiO_2/Ag films for dye-sensitized solar cells by multiple-step nanoimprint lithography. *J. Mater. Chem. A*, 1(21):6433–6440, 2013.

[41] N. Yang, Q. Yuan, J. Zhai, T. Wei, D. Wang, and L. Jiang. Enhanced light harvesting in plasmonic dye-sensitized solar cells by using a topologically ordered gold light-trapping layer. *ChemSusChem*, 5(3):572–576, 2012.

[42] Siu-Pang Ng, XiaoQing Lu, Ning Ding, Chi-Man Lawrence Wu, and Chun-Sing Lee. Plasmonic enhanced dye-sensitized solar cells with self-assembly gold-TiO_2@core-shell nanoislands. *Sol. Energy*, 99:115–125, 2014.

CHAPTER 6

IMPROVING LIGHT HARVESTING IN DYE-SENSITIZED SOLAR CELLS USING HYBRID BIMETALLIC NANOSTRUCTURES

Adapted from H. F. Zarick, W. R. Erwin, A. Boulesbaa, O. K. Hurd, J. A. Webb, A. A. Puretzky, D. B. Geohegan, and R. Bardhan, *ACS Photonics*, **2016**, *3*, 385 with permission from the American Chemical Society.

6.1 Summary

In this chapter, we investigate the impact of composition by improving light trapping in dye-sensitized solar cells (DSSCs) with hybrid bimetallic gold core/silver shell nanostructures. Silica-coated bimetallic nanostructures (Au/Ag/SiO_2 NSs) integrated in the active layer of DSSCs resulted in 7.51% power conversion eciency relative to 5.97% for reference DSSCs, giving rise to 26% enhancement in device performance. DSSC eciencies were governed by the particle density of Au/Ag/SiO_2 NSs with best performing devices utilizing only 0.44 *wt*.% of nanostructures. We performed transient absorption spectroscopy of DSSCs with variable concentrations of Au/Ag/SiO_2 NSs and observed an increase in amplitude and decrease in lifetime with increasing particle density relative to reference. We attributed this trend to plasmon resonant energy transfer and population of the singlet excited states of the sensitizer molecules at the optimum concentration of NSs promoting enhanced exciton generation and rapid charge transfer into TiO_2.

6.2 Introduction

Dye-sensitized solar cells (DSSCs), a class of mesoporous solar device, have evolved in the past two decades as an inexpensive alternative to silicon photovoltaics; however, low efficiencies of 8-10% have remained a major roadblock to commercialization in DSSCs.[1, 2,

3] Recently, metal nanostructures have emerged as a transformational approach to augment light harvesting in solar cells, giving rise to enhanced optical absorption, carrier generation, and improved efficiency.[4, 5, 6, 7, 8, 9, 10] Through small additions of metal nanostructures (<2 *wt.%*), the active material required to achieve high efficiency solar conversion can be drastically reduced,[11] enabling thin film architectures compatible with scalable manufacturing routes. Upon illumination, metal nanostructures with subwavelength dimensions couple incident photons to conduction electrons, giving rise to localized surface plasmon resonances (LSPR).[12, 13] By altering the shape, size, and composition of metal nanostructures, LSPRs can be manipulated to give rise to unique optical characteristics that can be harnessed for several technological applications from spectroscopy[14, 15, 16] to nanomedicine[17, 18, 19] to photovoltaics.[20, 21, 22]

Plasmonic enhancement in DSSCs is achieved by four possible mechanisms: (*i*) Far-field coupling of scattered light: light incident on metal nanostructures with a sufficiently high albedo (ratio of total scattered light to extinction) is scattered into the far-field, reaching distances up to $10\times$ the geometrical area[22, 23] and is ultimately reabsorbed by the sensitizer.[24, 25] In addition, nanostructures can also capture solar photons not absorbed by the sensitizer, which is achieved by tuning the plasmon resonance to wavelengths complementary to the sensitizers absorption.[26, 27] Both processes increase the total light harvested by the solar cell. (*ii*) Near-field coupling of electromagnetic fields: nanostructures function as antennas concentrating incident light on the metal surface and generating intense near-fields, which can be orders of magnitude higher than incident light. Proximal sensitizers couple with the strong near-fields, and the enhanced photon flux increases the total absorption cross-section of the solar cell. (*iii*) Plasmon resonance energy transfer (PRET): PRET is similar to Förster resonance energy transfer, where the LSPR dipole replaces the fluorescent molecule. In this nonradiative process, energy from the metal nanostructures contained in the localized plasmonic oscillations is transferred to the semiconductor or vicinal sensitizer inducing charge separation and e^-/h^+ pair generation. Unlike

the transfer of hot electrons, which depends on band alignment of semiconductor with metal Fermi level, the dipole-dipole energy transfer mechanism of PRET is not limited by band alignment and charge equilibration. PRET is also unaffected by any insulating interlayer, such as SiO_2 between the metal and semiconductor.[28, 29] (*iv*) Hot electron transfer: if a plasmon is neither scattered nor undergoes PRET, then it is absorbed by the metal and decays via energetic relaxation generating e^-/h^+ pairs. These photoexcited electrons undergo electron-electron scattering giving rise to a hot electron distribution. These energetic electrons can gain enough energy to overcome the Schottky barrier at the metal/semiconductor junction and rapidly transfer (at picosecond time scales) into the semiconductor conduction band, amplifying the number of carriers available for photocurrent generation.[23, 30, 31] Unlike PRET, any insulating spacer separating the metal and semiconductor will block hot electrons from transferring unless the spacer thickness is less than the electron tunneling barrier of the insulator ($<$3 nm for SiO_2).

While plasmonic enhancement of DSSCs has largely focused on monometallic spherical nanostructures,[32, 33, 34, 35, 36] in this study we demonstrate the use of Au/Ag/SiO_2 bimetallic core/shell/shell nanostructures with controlled morphology and composition, tailored to maximize light harvesting in DSSCs. These bimetallic nanostructures have several advantages: (*i*) they possess multipolar plasmon resonances due to the use of dual metals resulting in broadband capture of solar light specifically at longer wavelengths where the dye sensitizer has poor light absorption,[37] (*ii*) they have well-defined nonspherical geometries, which give rise to intense near-field enhancements localized at the edges and corners of the nanostructures facilitating superior light harvesting abilities, (*iii*) the use of Ag can potentially reduce Ohmic losses compared to Au alone, resulting in enhanced radiative damping and strong light scattering,[38] (*iv*) the presence of dual metals and nonspherical geomtery promotes 10$\times$ more light scattering relative to monometallic nanoparticles improving the total light absorbed in the active layer, and (*v*) they have a tunable core-shell architecture that allows modulation of optical and electronic properties with minimal

alterations of overall size.[12]

6.3 Results and Discussion

In this work we have enhanced the performance of standard DSSCs by integrating Au/Ag/SiO_2nanostructures (NSs) in the mesoporous layer. By varying the particle density, we find a systematic dependence of nanostructure concentration on device efficiency. While previous studies on plasmonic enhancement of DSSCs have utilized $\sim$0.6-3 *wt.%* of nanoparticles,[20, 36, 39, 40] here only 0.44 *wt.%* Au/Ag/SiO_2 NSs in the photoanodes resulted in a 26% enhancement in the power conversion efficiency (PCE) of the device, largely attributed to an improvement in short circuit current density. The incident photon to charge conversion efficiency (IPCE) and absorbance of the devices demonstrate that enhanced light harvesting is driven by direct coupling of nanostructure plasmons with the sensitizer, N719 (di-tetrabutylammonium *cis*-bis(isothiocyanato)bis(2,2-bipyridyl-4,4-dicarboxylato)ruthenium(II)) dye. In addition, IPCE and absorbance provide evidence for broadband light capture at wavelengths beyond 550 nm, where N719 does not absorb, attributable to the multipolar plasmon resonances of the nanostructures. We also performed pump-probe transient absorption spectroscopy (TAS) on the reference and plasmon enhanced DSSCs to understand the fundamental underpinnings of exciton generation and electron injection lifetimes in DSSCs in the presence of the nanostructures. We observed a decrease in lifetimes obtained from TAS with increasing concentration of bimetallic nanostructures in the devices, which we have attributed to a combination of enhanced exciton generation and rapid injection of electrons into the TiO_2 conduction band.

Bimetallic Au/Ag core/shell nanostructures (Au/Ag-NSs) were synthesized following our previously reported seed-mediated growth process.[41] Initially, Au nanocrystal (NC) cores of $\sim$45 nm edge length were synthesized utilizing cetyltrimethylammonium bromide (CTAB) as a shape directing agent in aqueous media. Subsequently, Au NC cores were transferred into a growth solution with cetyltrimethylammonium chloride (CTAC) ligands,

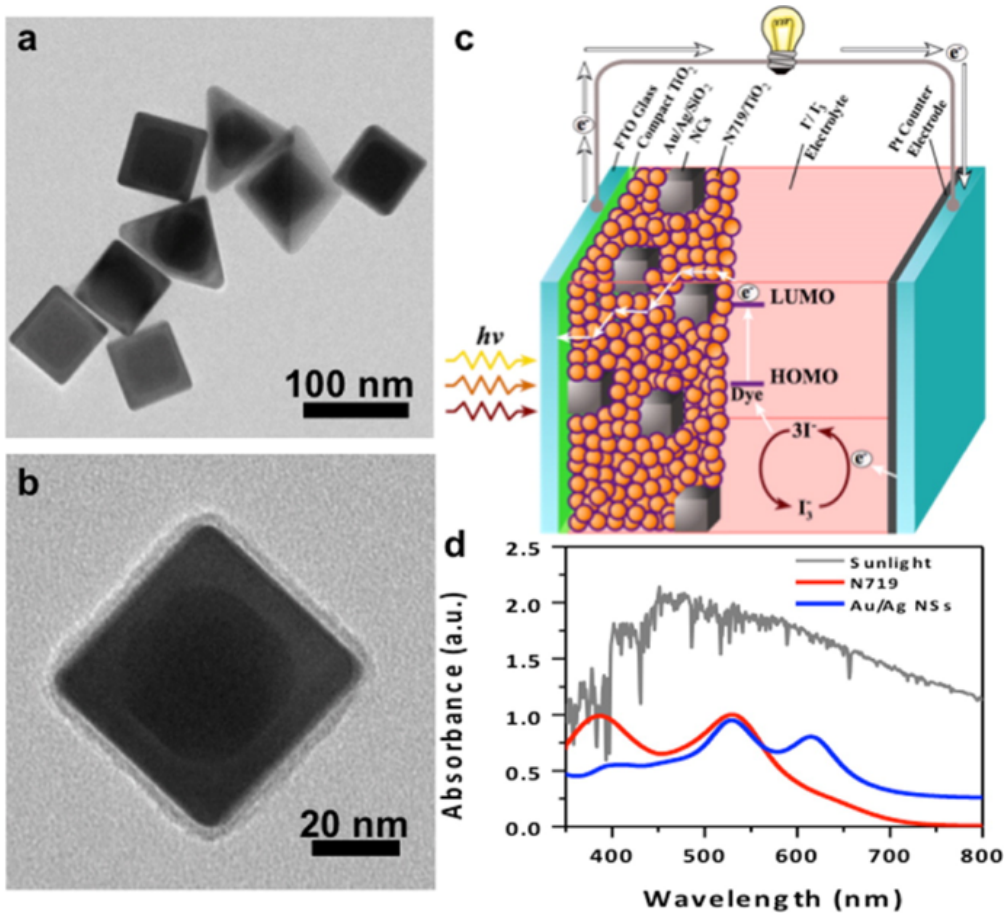

Figure 6.1: (a) Low-magnification TEM image of Au/Ag NSs and (b) high magnification image after silica coating the nanostructures. (c) Schematic of operation of plasmon-enhanced DSSCs showing bimetallic nanostructures embedded within the N719-sensitized mesoporous TiO_2 layer with an I^-/I_3^- liquid electrolyte. (d) Normalized extinction spectrum of Au/Ag NSs in aqueous media and normalized absorption spectrum of N719 compared to the solar irradiance spectrum, which has been offset for clarity, of ASTM G173-03 reference (AM 1.5).

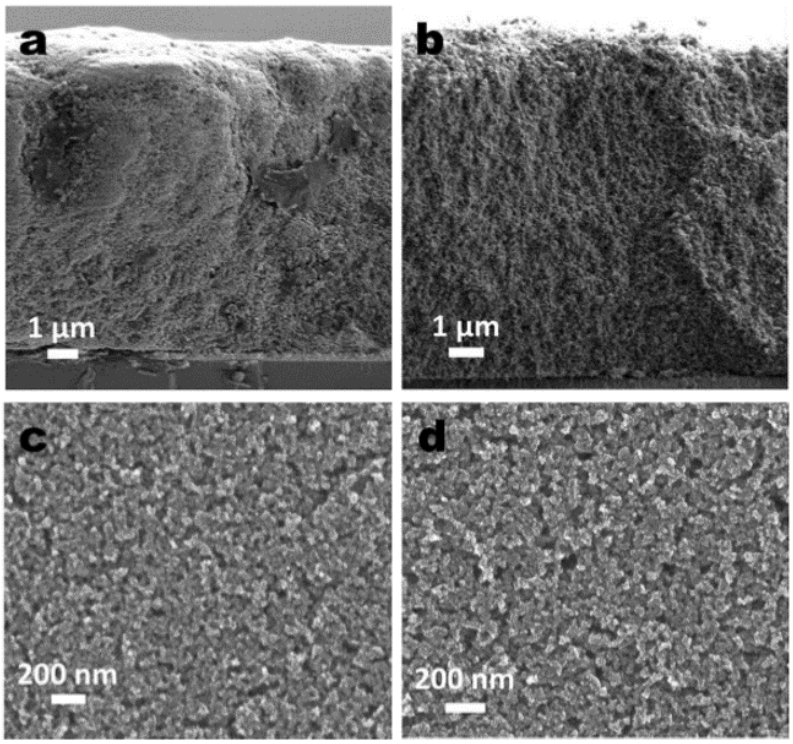

Figure 6.2: Cross-sectional SEM micrographs of $\sim$10 μm thick (a) reference TiO_2 layer and (b) TiO_2 layer containing 0.95 *wt.%* Au/Ag/SiO_2 nanostructures. Top view SEM micrographs of the corresponding (c) reference and (d) 0.95 *wt.%* Au/Ag/SiO_2 in TiO_2.

Ag^+ ions, KBr, and ascorbic acid and were reacted to form a thin Ag shell around the Au cores (Figure 6.1a). Sharp edges and corners enable strong electromagnetic fields; therefore, to promote such growth in the Ag layer, the reaction was carried out at an elevated temperature. We demonstrated in our previous work that by increasing the reaction temperature, Ag growth is preferentially accelerated along the [100] and [111] crystal planes, resulting in more defined edges and corners than those attained in the Au NC cores.[41] These shapes are governed by the shape of the Au core, where rounded-edge Au nanocubes give rise to bimetallic nanocubes and truncated Au nanocube cores generate bimetallic nanopyramids. While shape impurity is unavoidable during this seed-mediated growth process,[42, 43, 44] this mixture of shapes is advantageous in our DSSC in capturing broadband solar light, as discussed below.

Prior to incorporation into the photoanodes of the devices, the Au/Ag-NSs were coated

with a thin ($\sim$5 nm) layer of silica,[23] giving rise to Au/Ag/SiO_2 nanostructures (Figure 6.1b). The silica layer serves several purposes, including (*i*) ensuring electrical isolation to minimize electron recombination on the metal surface, (*ii*) minimizing Ostwald ripening during annealing of the photoanode at 500 °C, which is necessary to convert TiO_2 to anatase phase, (*iii*) the oxides of silica provide similar chemical functionality as the TiO_2, promoting infiltration and attachment of dye throughout the active layer, and (*iv*) providing resistance to degradation in the presence of the iodide/triiodide (I^-/I_3^-) corrosive liquid electrolyte. The $\sim$5 nm silica layer is sufficient to provide thermal and electrochemical stability[35, 45, 46] without detrimentally damping the plasmon; thicker layers of silica ($>$10 nm) shield the electron oscillation on the metal, resulting in a decrease in nanoparticle near-fields. The thin spacer layer enables enhanced near-field coupling between Au/Ag/SiO_2 NSs and N719 dye, promoting plasmon enhanced dye-excitation, which is controlled by the metal-molecule distance.[33, 47]

The silica-coated Au/Ag-NSs were purified, concentrated, and mixed with the nanocrystalline TiO_2 paste to form a homogeneous mixture before depositing on FTO glass by the doctor-blading technique, which yielded a $\sim$10 μm thick active layer (Figure 6.2). The reference and bimetallic nanostructure embedded photoanodes were sensitized with N719 dye and integrated with a counter electrode consisting of a thin layer of Pt on FTO glass. The two electrodes were heat sealed together with a low-temperature thermoplastic sealant and injected with I^-/I_3^--based liquid electrolyte. A schematic representation of DSSC architecture and device operation is depicted in Figure 6.1c. In a DSSC, upon light exposure, electrons (e^-) are excited from the HOMO to the LUMO band of the dye and are rapidly injected into the conduction band of the TiO_2, subsequently traveling through the conductive electrode via the external circuit to the counter electrode. The I^-/I_3^- redox couple promotes shuttling of e^-, reducing I_3^- to I^- at the counterelectrode. The oxidized dye then replenishes the e^- lost during photoexcitation by oxidizing I^- to I_3^-.[48] The homogeneous distribution of the Au/Ag/SiO_2 NSs throughout the mesoporous TiO_2 layer increases proximity to N719

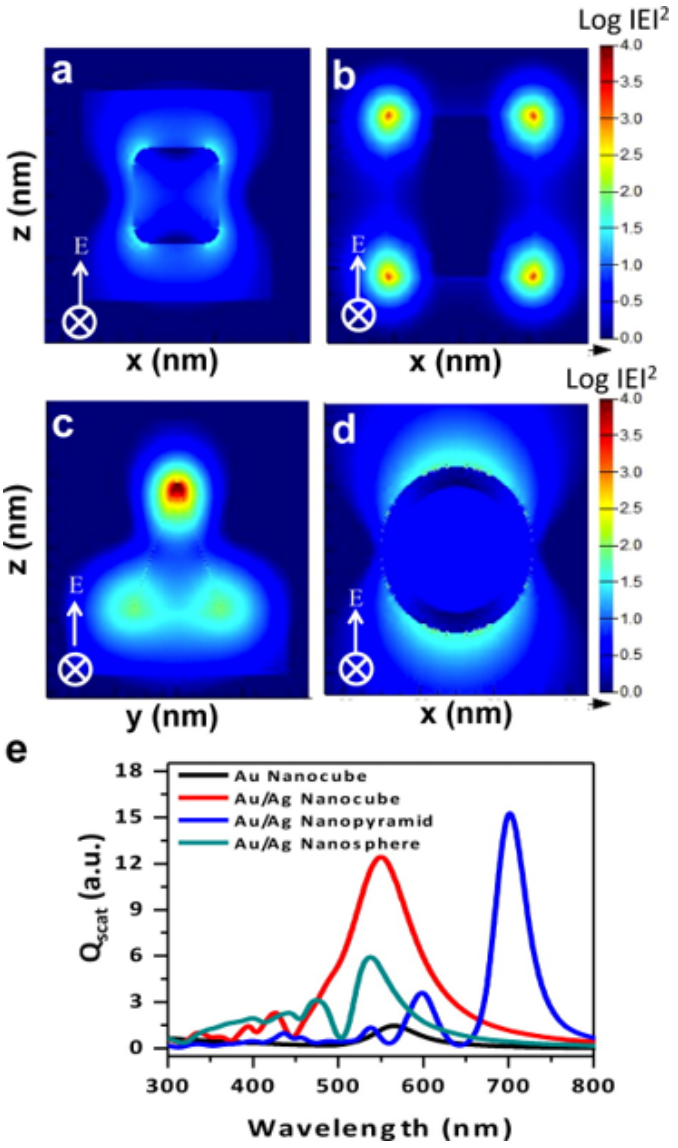

Figure 6.3: Electromagnetic intensity profiles, $\langle E^2/{E_0}^2 \rangle$ with a scale bar of $10^0 10^4$, of (a) a rounded edge Au nanocube, and bimetallic (b) nanocube, (c) nanopyramid, and (d) nanosphere simulated in aqueous media. Corresponding calculated scattering cross sections (area normalized) for all simulated nanostructures are shown in (e).

molecules, maximizing near-field coupling with the sensitizer and total light harvested in the active layer while minimizing any detrimental effects to the redox processes necessary for DSSC operation.

The multipolar plasmon resonances of Au/Ag-NSs not only have good overlap with the optical absorption of N719 centered at 390 and 530 nm, but also capture broadband solar light (Figure 6.1d). The nanostructures exhibit two dipolar resonances at $\sim$535 and 615 nm attributed to the Au/Ag nanocubes and nanopyramids, respectively, as described in our previous work.[41] The nanostructures also demonstrate a broad mode at 400 nm assigned to the interband transition of Ag and higher order modes associated with the nanocube corners.[41] The direct overlap of the plasmon resonances of Au/Ag-NSs with N719 absorption enables strong metal-molecule coupling, allowing enhanced light trapping.[49, 50] In addition, the 615 nm resonance attributed to the Au/Ag nanopyramids extends the light-harvesting ability of the plasmonic DSSCs to spectral regions where N719 does not absorb, therefore, enabling broadband solar light capture.

We performed finite difference time domain (FDTD) simulations on single particles in aqueous media to understand the advantages of bimetallic composition and nonspherical geometries. Calculated electromagnetic (EM) field intensity enhancements of a rounded-edge Au nanocube, Au/Ag nanocube, Au/Ag nanopyramid, and Au/Ag nanosphere at their LSPR frequency are shown in Figure 6.3a-d. Compared with the Au nanocube (Figure 6.3a), the Au/Ag nanocube (Figure 6.3b) has a stronger field enhancement attributable to the sharp corners of the Ag shell, presence of Ag that has low Ohmic losses and strong light scattering, and the synergistic plasmonic coupling between the Au core and its Ag shell.[41, 51, 52, 53] While Au is more electronegative than Ag, Ag has a higher electron conductivity; the synergistic combination of the two metals in a core/shell architecture improves their electronic properties. The sharp edges and corners of the Au/Ag nanocube (Figure 6.3b) and Au/Ag nanopyramid (Figure 6.3c) also give rise to an intense nanoantenna effect and a quasistatic lightning-rod effect,[12, 54, 55, 56] making these geometries

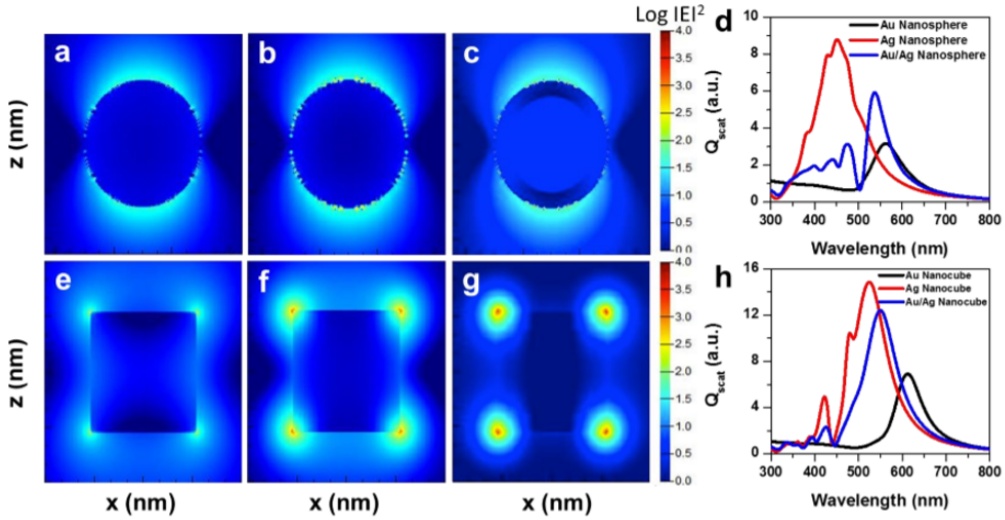

Figure 6.4: The electromagnetic intensity profiles, $\langle E^2/{E_0}^2 \rangle$, of 80 nm diameter (a) Au nanosphere, (b) Ag nanosphere, and (c) Au/Ag nanosphere simulated in aqueous media. Corresponding calculated scattering cross sections (area normalized) for all simulated nanospheres are shown in (d). The electromagnetic intensity profiles, $\langle E^2/{E_0}^2 \rangle$, of 65 nm edge length (e) Au nanocube, (f) Ag nanocube, and (g) Au/Ag nanocube simulated in aqueous media. Corresponding calculated scattering cross sections (area normalized) for all simulated nanocubes are shown in (h).

ideally suited for light concentration in DSSCs. Further, these edges also provide superior performance over bimetallic nanospheres (Figure 6.3d) in the augmentation of light harvesting capabilities of N719 sensitizer. Corresponding calculated normalized scattering cross sections (Q_{scat}) of each of these nanostructures (Figure 6.3e) demonstrate that the addition of the silver shell increases the light scattering ability of the Au/Ag nanocube to nearly 10$\times$ greater than that of the Au nanocube. In addition, the anisotropic bimetallic geometries have 2-3$\times$ higher light scattering relative to the Au/Ag nanosphere, allowing augmented light trapping via an increased optical path length.

Additional simulations that further decouple the impact of the morphology and composition can be found in Figure 6.4. These simulations compare the electromagnetic field profiles and scattering cross-sections of spherical Au, Ag, and Au/Ag nanoparticles and cubic Au, Ag, and Au/Ag nanoparticles of nearly identical volume. These calculations clearly show (*i*) cubic shapes have stronger near-fields and scattering efficiency relative to

spherical nanoparticles, and (*ii*) bimetallic composition, i.e. the addition of Ag layer on Au core, results in stronger optical properties than an Au nanoparticle of similar size and shape.

The light-harvesting capabilities of the Au/Ag/SiO_2 NSs were investigated by incorporating them into the photoanodes of DSSCs and comparing to reference devices (no plasmonic nanostructures). The particle density of incorporated nanostructures within the mesoporous TiO_2 matrix was varied between 0.22 and 0.95 *wt.%* to find the optimal range for plasmonic enhancement. The absorption spectra of the plasmon-enhanced photoanodes, when compared to the reference, shows a gradual increase across the entire visible spectrum with increasing particle density from 400-550 and >600 nm overlapping with the plasmon resonance peaks of Au/Ag/SiO_2 NSs (Figure 6.5a). By normalizing the absorbance of the plasmon-enhanced devices to the reference (0 *wt.%*), the relative enhancement in light absorption is observed in these ranges (Figure 6.6). It is also notable that, at high particle densities (>0.60 *wt.%*), light absorption rapidly increases at longer wavelengths, which may be attributable to aggregation of the nanostructures in the photoanodes, which results in the red-shift of the plasmon resonance to longer wavelengths.[11]

The power conversion efficiencies (PCEs) of reference and plasmon-enhanced DSSCs of equivalent area of 0.12 cm^2 were examined under AM 1.5 simulated solar light with each device being illuminated at 100 mW/cm^2 of power. Photocurrent spectra of the best performing DSSCs (Figure 6.5b) demonstrate that maximum plasmonic enhancement is achieved for DSSCs containing 0.44 *wt.%* Au/Ag/SiO_2 nanostructures reaching a maximum PCE of 7.51%, which is 26% higher than the 5.97% PCE achieved with the reference DSSC. The spectral responses of the DSSCs were further investigated with IPCE measurements obtained with a supercontinuum white light laser coupled with an acousto-optic tunable filter used to modulate the wavelengths from 400 to 800 nm. Similar to the trend observed in absorbance spectra, the IPCE for the plasmon enhanced devices (Figure 6.5c) show an increase in photocurrent generation throughout the visible spectrum, with

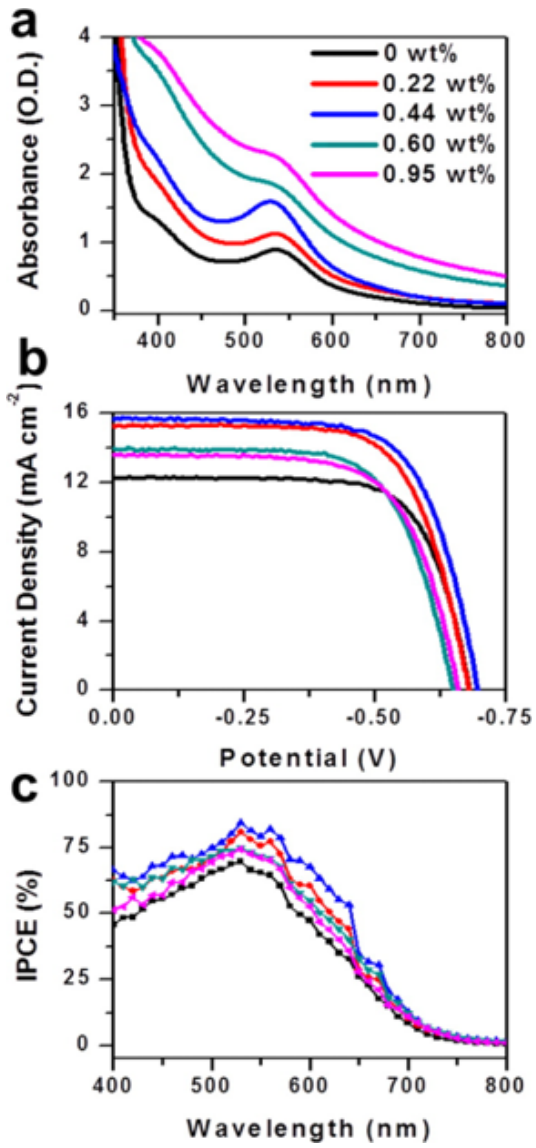

Figure 6.5: (a) Optical absorption spectra of N719-sensitized mesoporous TiO_2 with varied particle density of Au/Ag/SiO_2 nanostructures embedded in the photoanodes. (b) Corresponding current density spectra of the devices, and (c) % IPCE of the same devices as a function of excitation wavelength. Parts (a)-(c) are color coordinated with the legend provided in (a).

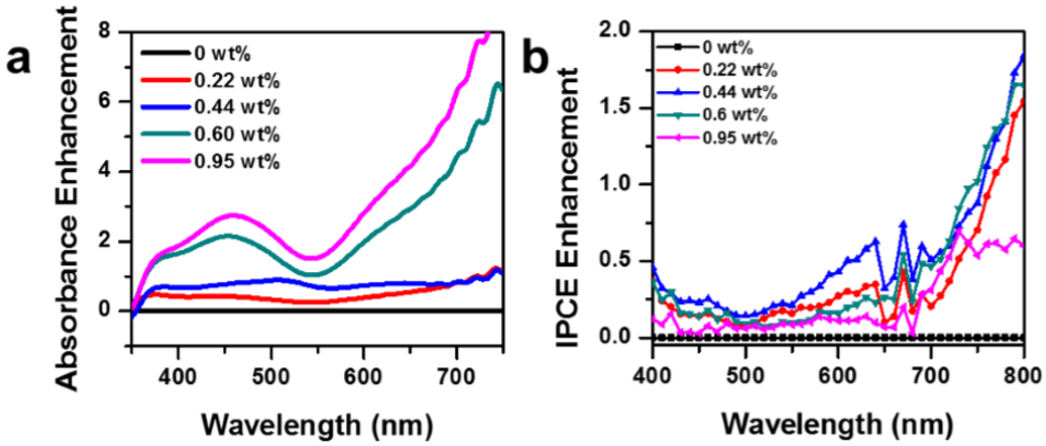

Figure 6.6: (a) Absorbance of the Au/Ag/SiO_2 photoandodes normalized to the reference to determine relative enhancement in light absorption. (b) IPCE spectra normalized to the reference to determine the IPCE enhancement.

the maximum IPCE enhancements observed for the DSSCs incorporated with 0.44 *wt.%* Au/Ag/SiO_2 NSs. Note that all plasmon-enhanced devices show an increase in photocurrent over the entire visible spectrum, corresponding well with the plasmon resonance of the nanostructures (Figure 6.1d).

The detailed device performance for both reference and nanostructure-incorporated DSSCs as a function of particle density is demonstrated in Figure 6.7, with the values shown in Table 6.1; we tested a total of five devices for each sample and used standard deviations from these devices to calculate uncertainties. The open-circuit voltages (V_{oc}) displays a slight increasing trend up to 0.44*wt.%* Au/Ag/SiO_2 NSs (Figure 6.7a), which is most likely attributed to improved charge transfer at optimal nanostructure loadings. Previous studies have performed impedance spectroscopy on plasmon-enhanced DSSC systems and reported a decrease in R_1, which is the charge transfer resistance over the conducting layer/photoanode interface and counter electrode/electrolyte interface collectively. This charge transfer resistance in the presence of metal nanoparticles is manifested in device performance, both as an increase in J_{sc} as well as V_{oc}.[57, 58] It has also been reported that at high nanoparticle loadings R_2, the charge transfer resistance at the photoanode/-electrolyte interface, increases, indicating that metal nanoparticles act as recombination

Table 6.1: Average values for open circuit voltage (V_{oc}), short circuit current density (J_{sc}), fill factor (FF), and power conversion efficiency (PCE), and best PCEs for all devices. A total of five devices were tested for each sample and standard deviations were used to calculate uncertainties.

Sample [Au/Ag/SiO_2 $wt.\%$ in TiO_2]	**Average V_{oc} [V]**	**Average J_{sc} [mA/cm_2]**	**Average FF**	**Average PCE [%]**	**Best PCE [%]**
Reference	0.635 ± 0.016	11.4 ± 0.5	0.697 ± 0.010	5.19 ± 0.45	5.97
0.22 $wt.\%$	0.680 ± 0.005	14.5 ± 0.5	0.694 ± 0.006	6.82 ± 0.23	7.15
0.44 $wt.\%$	0.695 ± 0.005	15.2 ± 0.4	0.689 ± 0.005	7.29 ± 0.17	7.51
0.60 $wt.\%$	0.650 ± 0.006	13.5 ± 0.5	0.677 ± 0.003	5.92 ± 0.27	6.12
0.95 $wt.\%$	0.648 ± 0.011	12.8 ± 0.5	0.672 ± 0.004	5.57 ± 0.28	6.04

centers. Therefore, optimizing the nanostructure concentrations in solar devices is of utmost importance.[27, 59] A slight decrease in V_{oc} is observed at higher particle densities; as the V_{oc} is determined by the energy difference between the semiconductor under illumination and the Nerst potential of the I^-/I_3^- redox couple in the electrolyte, it is likely that the presence of metal nanostructures within the TiO_2 semiconductor results in a downshift in the Fermi level.[60, 61] This downshift likely decreases the gap between the Fermi level of TiO_2 and the Nerst potential of the redox couple, which would decrease the V_{oc}.[33, 62] At low particle densities, up to 0.44 $wt.\%$ Au/Ag/SiO_2 NSs, the amount of metal present does not have appreciable effects on the Fermi level; therefore, this trend is observable when devices contain higher concentrations of Au/Ag/SiO_2 NSs. The fill factor (FF, Figure 6.7b) also has a consistent slight decrease with increasing nanostructure concentrations suggesting that, at high densities, aggregation of nanostructures may result in electron trapping within metallic junctions.

The short circuit current density (J_{sc}) and PCE of the devices (Figure 6.7c,d) show a near-identical trend where the highest J_{sc} of 15.70 mA/cm^2 and PCE of 7.51% are achieved at 0.44 $wt.\%$ of Au/Ag/SiO_2 NSs. The maximum J_{sc} observed for the best-performing, plasmon-enhanced devices is 28% higher than the J_{sc} for the best-performing reference DSSC (12.27 mA/cm^2), analogous to the maximum enhancement achieved in PCE (26%).

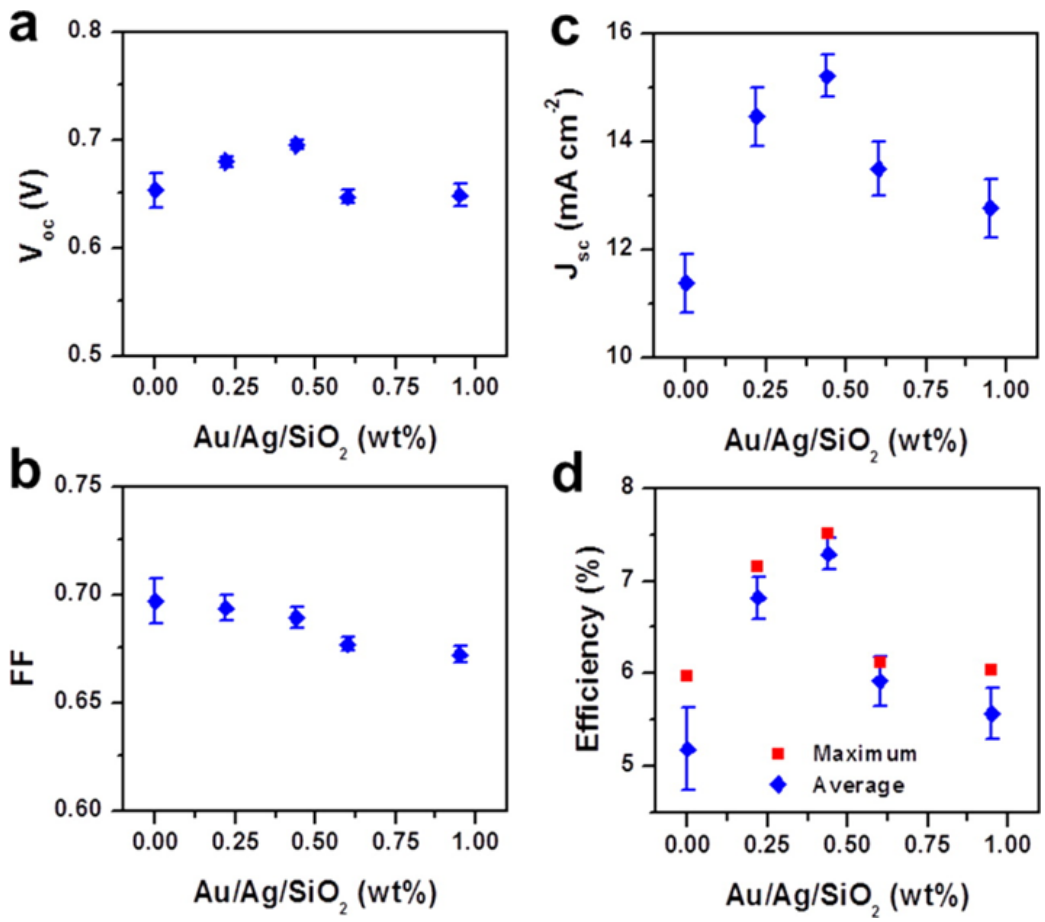

Figure 6.7: Average (a) open-circuit voltage, (b) fill factor, and (c) short circuit current density values for devices as a function of Au/Ag/SiO_2 nanostructure particle density (*wt.%*). (d) Both best and average power conversion efficiencies obtained from five devices at each concentration tested.

Since J_{sc} is reflective of the light harvesting capability of the devices, the trends in PCE and J_{sc} suggest plasmonic enhancement in DSSCs is contributed by increase in light absorption with minimal alterations in the electrochemical properties of the devices. The improved light harvesting in the nanostructure-incorporated devices can be attributed to (*i*) near-field coupling between the LSPR and adjacent sensitizer molecules, (*ii*) PRET from nanostructures to semiconductor, and (*iii*) light scattering in the nanoparticle far field, which can be trapped in the mesoporous semiconductor layer. These mechanisms are supported by the trends observed in absorption and IPCE measurements of the photoanodes. Due to the homogeneous mixing of the bimetallic nanostructures throughout the active layer (see Figure 6.2), we anticipate interparticle coupling between adjacent nanostructures may promote long-range surface plasmon polariton modes, which would also contribute to the overall enhancements. It is unlikely that hot electron transfer plays a role in our system due to the large size of the nanostructures and the $\sim$5 nm silica layer surrounding the Au/Ag-NSs. The process of hot electron generation in metal nanostructures depends on both the mean free path of electrons (λ_e) and thickness of insulating barrier between the metal and semiconductor. The λ_e in both Au and Ag is on the range of 40-50 nm;[63] as the size of both the nanocubes and the nanopyramids is $>$50 nm, fewer electrons likely travel to the metal surface due to loss of electrons by scattering. The few electrons that reach the metal/SiO_2 interface would then need to pass the insulating silica barrier. Since the electron tunneling barrier (Φ_b) of silica is $\sim$3 nm or less[64, 65, 66, 67] and the thickness of our spacer layer is $\sim$5 nm, we do not anticipate that hot electrons transfer to the sensitizer or TiO_2.

We also observed a decrease in J_{sc} and PCE at high particle densities of Au/Ag/SiO_2 NSs. This decrease in performance is a consequence of excess metal which results in (*i*) a loss of absorbing dye volume due to the large volume of nanostructures, (*ii*) aggregation of nanostructures resulting in electron trapping within junctions, and (*iii*) nanostructure aggregation, which gives rise to interparticle coupling between adjacent nanostructures that results in electron-phonon coupling and subsequent generation of heat.[11, 36, 68] These

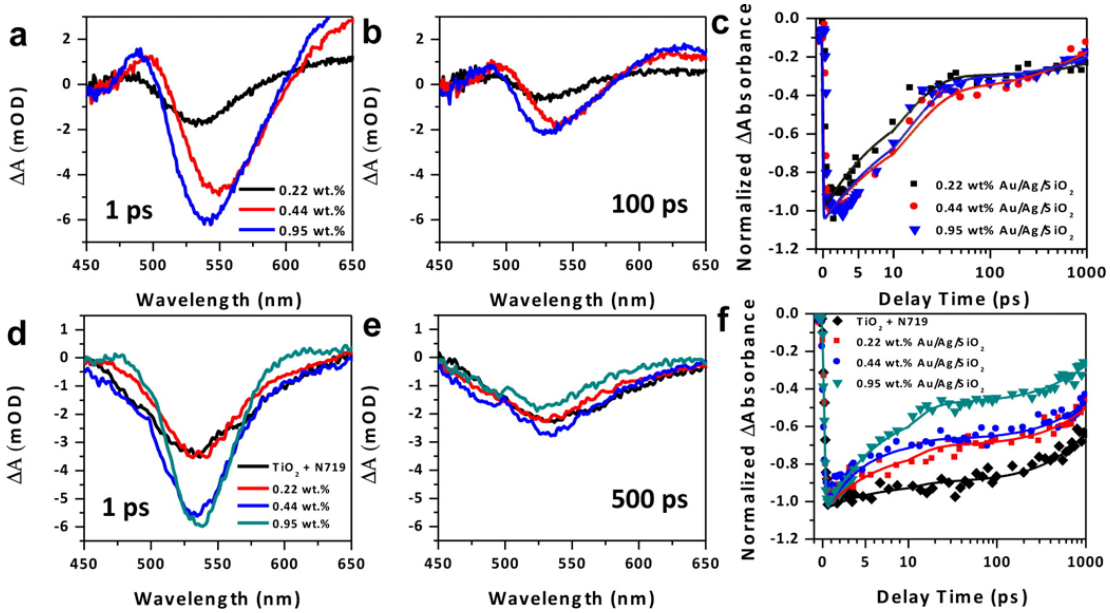

Figure 6.8: Transient absorption spectra for Au/Ag/SiO_2 + TiO_2 only samples (not sensitized with N719) at (a) 1 ps and (b) 100 ps time delays at the photobleaching state at ∼530 nm. (c) Decay kinetics at 530 nm for all samples. Transient absorption spectra for N719 sensitized reference and N719 sensitized Au/Ag/SiO_2 NSs incorporated samples at (d) 1 ps and (e) 500 ps time delays at 530 nm. (f) Decay kinetics at 530 nm for the N719 sensitized reference and N719 sensitized plasmon-enhanced samples. All decay kinetics are shown with experimental data (symbols) fitted with a biexponential decay function (smooth line). Early time scales are plotted linearly; later time scales (>10 ps) plotted on a logarithmic scale with a base of 10.

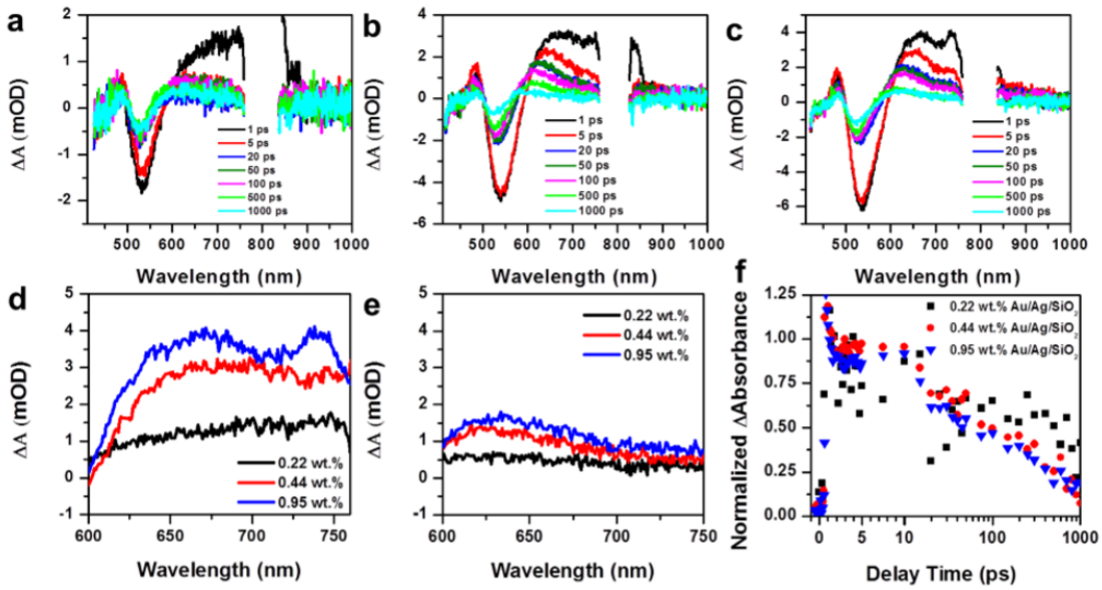

Figure 6.9: Transient absorption spectra at various time delays for Au/Ag/SiO_2 NSs incorporated in TiO_2 at (a) 0.22 *wt.%*, (b) 0.44 *wt.%*, and (c) 0.95 *wt.%*. These samples were not sensitized with N719. Transient absorption spectra at (d) 1 ps and (e) 100 ps time delay for the same samples pumped at 400 nm and probed at 650 nm which is characterized as the photoinduced absorption (PIA) band. (f) The decay kinetics at 650 nm for all samples. Due to the low amplitude of the PIA band, the kinetics data could not be fit to a decay function to obtain reasonable time constants.

detrimental processes would diminish the number of carriers available for photocurrent generation leading to decreased device performance.

To evaluate the fundamental mechanisms that drive plasmonic enhancement in DSSCs with Au/Ag/SiO_2 NSs, we performed TAS to understand dynamics of exciton generation, electron injection, and charge recombination within the mesoporous TiO_2 active layer. All samples were excited with a 400 nm pump and probed with white light continuum from 450 to 900 nm. We first examined the photoanodes in the absence of the sensitizer with the nanostructures embedded in the mesoporous TiO_2. Three different particle densities were chosen relevant to the plasmon-enhanced DSSCs tested earlier (see Figure 6.7), including 0.22, 0.44, and 0.95 *wt.%* Au/Ag/SiO_2NSs in TiO_2 (Note: DSSCs with 0.44 *wt.%* Au/Ag/SiO_2 NSs were the best performing devices). The evolution of the TA spectra of the three samples at 1 and 100 ps time delays at 530 nm (Figure 6.8a, b) clearly demon-

strate particle density dependent changes in spectral properties. The complete evolutionary spectra for the samples from 1-1000 ps time delays are provided in the Figure 6.9a-c. The spectral feature observed at 530 nm for all samples is attributable to the photobleaching (PB) state of the plasmon mode of the Au/Ag/SiO_2 NSs which corresponds well with the 530 nm plasmon resonance of the bimetallic nanostructures (Figure 6.1d). The amplitude of the PB state increases monotonically with particle density at both 1 ps (Figure 6.8a) and 100 ps (Figure 6.8b) time delays, and the spectral evolution clearly shows the relaxation of the plasmon excitation culminates within the first 100 ps followed by energy transfer into TiO_2conduction band. This is consistent with previous observation of inelastic electron-phonon scattering and subsequent energy transfer from metal nanoparticles to TiO_2 within the first 100 ps.[69] The decay kinetics of these samples were fit with a biexponential decay function (Figure 6.8c), and the corresponding amplitudes, time constants, and amplitude weighted lifetime, τ_{avg}, given by $\tau_{avg} = ((A_1 \times \tau_1 + A_2 \times \tau_2)/(A_1 + A_2))$, were derived from the fits and are shown in Table 6.2. We attribute the fast time constant (τ_1) to relaxation by means of electron-electron scattering after initial electronic excitation of nanostructures, which results in hot e^- generation, and we attribute the slow time constant (τ_2) to energy transfer to TiO_2. Since τ_1 is relatively constant for all the samples, we infer hot electrons do not transfer across the insulating silica layer of the Au/Ag/SiO_2 NSs. However, the change in τ_2 among the samples and the overall rapid decrease in τ_{avg} with increasing particle density of Au/Ag/SiO_2 NSs is direct evidence of PRET. This suggests PRET occurs from the bimetallic nanostructures to the TiO_2 conduction band across the insulating SiO_2 layer resulting from the dipole-dipole relaxation of the excited plasmons.[28, 69] We also note that energy transport between adjacent nanostructures at high concentrations is possible and has been reported previously in metal nanoparticle chains.[70, 71] However, at high concentrations, when nanostructures are touching, such long-range energy transfer will likely be a slower process relative to PRET from metal to TiO_2. Therefore, the latter mechanism will likely dominate. Further, previous studies have shown energy transfer from

Table 6.2: Amplitudes (A), time constants (τ), and amplitude-weighted lifetimes (τ_{avg}) derived from biexponential fits of the transient absorption decay function for the different samples. All samples are embedded in mesoporous TiO_2.

Sample	A_1	τ_1 [ps]	A_2	τ_2 [ps]	τ_{avg} [ps]
0.22 *wt.%* Au/Ag/SiO_2	-0.69	11.08	-0.23	2387	711
0.44 *wt.%* Au/Ag/SiO_2	-0.68	13.98	-0.30	912	291
0.95 *wt.%* Au/Ag/SiO_2	-0.74	13.86	-0.24	1553	392
TiO_2 + N719	-0.14	6.67	-0.90	2915	2523
0.22 *wt.%* Au/Ag/SiO_2 + N719	-0.34	6.67	-0.70	2928	1977
0.44 *wt.%* Au/Ag/SiO_2 + N719	-0.40	4.57	-0.67	2826	1781
0.95 *wt.%* Au/Ag/SiO_2 + N719	-0.60	6.33	-0.48	1822	815

metal to $TiO_2$when pumped at wavelengths higher than the bandgap of TiO_2 but lower or equivalent to the plasmon resonance of the metal.[72, 73] With increasing concentration of Au/Ag/SiO_2 NSs in the mesoporous TiO_2 layer, an enhancement in plasmonic excitations is anticipated, which augments the rate of energy transfer and decreases τ_{avg}. Though, a slight increase in τ_{avg} is observable for the photoanode integrated with highest particle density, 0.95 *wt.%* Au/Ag/SiO_2 NSs. This is likely attributable to aggregation of Au/Ag/SiO_2 NSs in the mesoporous TiO_2 at such high concentrations, which results in damping of the plasmon resonance giving rise to a weaker PRET mechanism, and, therefore, an increase in the corresponding τ_{avg}. In addition to the PB state, we also observe broad photoinduced absorption (PIA) band at $\sim$650 nm (Figure 6.9a-d), which rapidly decays within the first 20-100 ps (Figure 6.9d, e), corresponding well with the 615 nm plasmon resonance peak of the Au/Ag/SiO_2 NSs. The PIA band is much weaker than the PB band; therefore, meaningful lifetimes could not be derived from the biexponential fits of the evolutionary spectra of the samples (Figure 6.9f). However, a particle density dependent trend is still observable, showing evidence of PRET from the Au/Ag/SiO_2 NSs into TiO_2.

We then investigated the photoanodes sensitized with N719 dye and compared the TA evolutionary spectra of the reference and plasmon-enhanced photoanodes at 530 nm (Figure 6.8d). Due to the strong spectral overlap in the extinction of the bimetallic nanostruc-

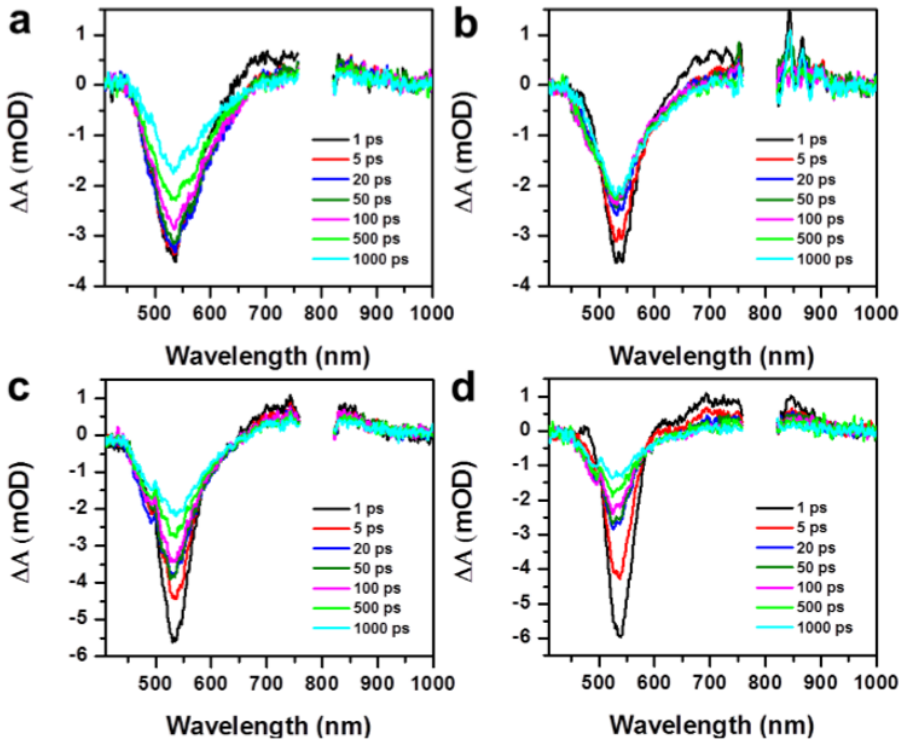

Figure 6.10: Transient absorption spectra at various time delays for samples sensitized with N719. (a) Reference, (b) 0.22 *wt*.% Au/Ag/SiO_2 NSs, (c) 0.44 *wt*.% Au/Ag/SiO_2 NSs, and (d) 0.95 *wt*.% Au/Ag/SiO_2 NSs.

tures and N719 dye (see Figure 6.1d), the plasmon-enhanced samples are expected to have contributions from both the photobleaching of the dye and relaxation of the Au/Ag/SiO_2 NSs plasmons at 530 nm. Representative TA spectra at 1 and 500 ps of reference (TiO_2 + N719) and photoanodes embedded with nanostructures sensitized with N719 are shown in Figure 6.8d,e (full spectra of each sample for a range of time delays can be found in Figure 6.10). The spectra show a clear particle density-dependent evolution and complete recovery of the photobleaching state by 500 ps in all samples. The data were fit with a biexponential decay function, and corresponding amplitudes and lifetimes were derived (Table 6.2). The fits yield a fast (τ_1) and a slow time constant (τ_2). Previous studies on N719-sensitized TiO_2 systems have demonstrated two time components; τ_1 was attributed to electron injection into the conduction band of the TiO_2 from the singlet metal to ligand charge transfer (^{1}MLCT) states and τ_2 to the triplet (^{3}MLCT) states of the excited N719 complexes.[74, 75] The decay kinetics at 530 nm of the reference and plasmon-enhanced samples (Figure 6.8f) show several noteworthy characteristics: (*i*) the amplitude of the decay kinetics is enhanced for the nanostructure embedded photoanodes relative to the reference and monotonically increases with particle density. This is likely attributable to the stronger molecular absorption coefficient of metal nanostructures, typically on the order of 10^9 to 10^10 M^{-1} cm^{-1},[35, 76] as compared to N719, which is 1.58×10^4 M^{-1} cm^{-1}.[77] This suggests that the photobleaching of the excited Au/Ag/SiO_2 NSs is anticipated to be stronger than that of the dye alone. (*ii*) The amplitude-weighted lifetime, τ_{avg}, drastically decreases with increasing particle density relative to the reference sample. This suggests bimetallic nanostructures augment light trapping in the active layer of DSSCs enhancing the e^-/h^+ pairs generated in N719, resulting in more electrons being available to rapidly transfer to the TiO_2 conduction band. Therefore, the presence of metal nanostructures leads to faster electron injection into TiO_2conduction band before recombination can occur in the bulk, resulting in shorter exciton lifetime. Decreased lifetime of photogenerated carriers in the presence of metal nanoparticles was recently reported in perovskite solar cells as

well.[78] Finally, (*iii*) for the best performing plasmonic photoanodes embedded with 0.44 *wt*.% Au/Ag/SiO_2 NSs, both the fast (τ_1) and slow time component (τ_2) are shorter relative to the reference photoanode (see Table 6.2). This is notable since the non-optimized concentrations (0.22 and 0.95 *wt*.%) only affect electron dynamics at longer time scales (τ_2). These time constants indicate, following photoexcitation and plasmon enhanced light trapping in samples, PRET occurs at time scales of several hundred picoseconds, altering τ_2 across all samples. However, at the optimum particle density of 0.44*wt*.% Au/Ag/SiO_2 NSs, a strong metal-molecule interaction occurs via both plasmonic near-field and far-field coupling which likely populates the singlet (^{1}MLCT) states of the excited N719 molecules, promoting enhanced e^-/h^+ pair generation and rapid charge transfer into TiO_2. This phenomenon decreases τ_1 from 6.67 ps in reference to 4.57 ps in Au/Ag/SiO_2 NSs embedded photoanodes. We do observe τ_{avg} for the sensitized photoanodes decreases consistently with increasing particle density, but before sensitization, τ_{avg} slightly increases for the highest particle density (0.95 *wt*.%). We anticipate this likely results from an improved charge transfer and PRET when the dye molecules surround the nanostructures; however, the exact mechanism of this observation remains unclear and further studies are underway. In an effort to further examine the role of PRET and to demonstrate that the thickness of the silica layer does have an impact on DSSCs electron dynamics, we have performed additional transient absorption studies of Au/Ag nanostructures coated with $\sim$30 nm silica layer (Figure 6.11) and integrated in the photoanode of DSSCs sensitized with N719 at the optimized particle density of 0.44 *wt*.%. PRET is strongly dependent on the near-field profile of nanostructures; at 30 nm from the surface of bimetallic nanocubes and nanopyramids, the near-field still exists but is very weak, so we do anticipate a very weak effect of PRET with the 30 nm silica coated Au/Ag nanostructures.

Decay kinetics of 30 nm SiO_2 coated samples were compared to the standard 5 nm silica coated Au/Ag nanostructures embedded in DSSC photoanodes at 0.44 *wt*.% particle density (Figure 6.12a). The data were fitted with a biexponential decay function (solid

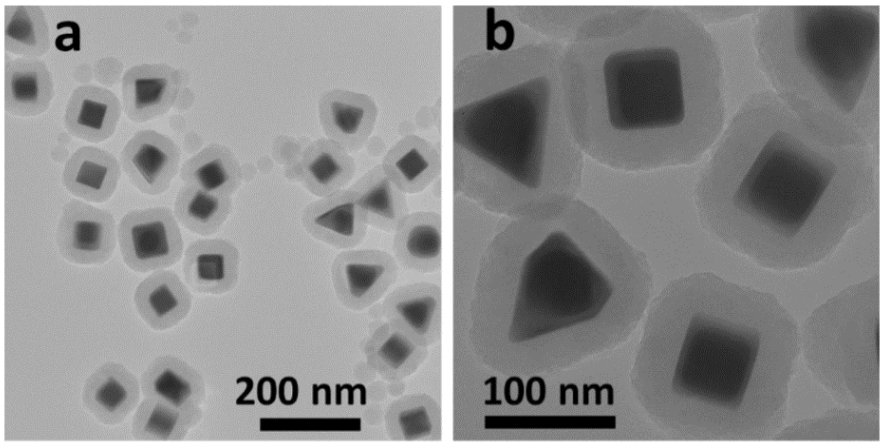

Figure 6.11: (a) Low-magnification and (b) high magnification TEM micrograph of Au/Ag nanostructures coated with a ∼30 nm layer of SiO_2 achieved with a modified Stöber process.[79]

lines in Fig. S8a) and the derived amplitudes, time constants, and average lifetimes from the fit are shown in Figure 6.12b. We observe that the fast time component, τ_1, increases in the 30 nm SiO_2 sample to 5.26 ps compared to 4.57 ps in the 5 nm SiO_2. This is nearly equivalent to τ_1 of all the samples that are shown in Table 6.2. The increase in τ_1 shows that since the near-field substantially decays off 30 nm from the metal surface, this separation distance between the dye and metal weakens the metal-molecule interaction that is observable in the case of 5 nm silica layer thickness. This weak coupling likely does not allow population of the singlet metal ligand charge transfer (^{1}MLCT) states of the excited N719 molecules, which increases τ_1 to values equivalent to the reference and non-optimized plasmonic samples.

We expected the slow time component, τ_2, of the 30 nm SiO_2 coated Au/Ag samples to increase as well due to weak PRET effects. Instead, to our surprise, a much shorter lifetime of 262 ps was observed compared to 2982 ps for the reference and 2826 ps for the 5 nm silica coated Au/Ag sample at 0.44 *wt.%* particle density. This decrease in lifetime, by nearly an order of magnitude, likely results from a high degree of e^-/h^+ pair recombination in the DSSC photoanodes. This recombination process dominates and supersedes any charge injection processes from the metal into the TiO_2. The increase in recombination

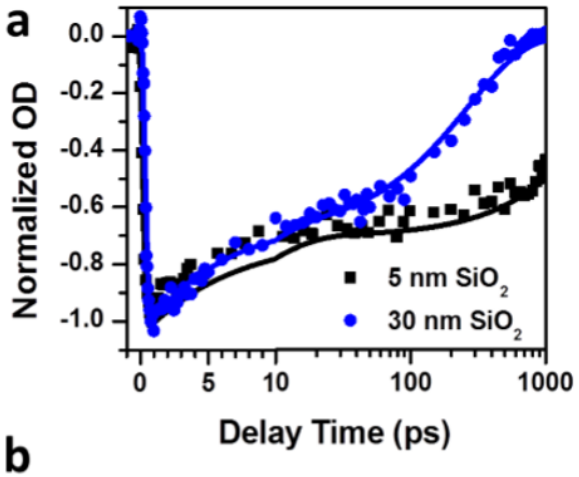

b

Sample	A_1	τ_1 [ps]	A_2	τ_2 [ps]	τ_{avg} [ps]
5 nm SiO_2 Au/Ag + TiO_2 + N719	-0.40	4.57	-0.67	2826	1781
30 nm SiO_2 Au/Ag + TiO_2 + N719	-0.34	5.26	-0.68	262	176

Figure 6.12: (a) Decay kinetics at 530 nm from transient absorption spectra of 0.44 *wt.%* Au/Ag NSs in TiO_2 and sensitized with N719 dye. Au/Ag NCs coated in 5 nm of SiO_2 and 30 nm SiO_2 are compared. Experimental data has been fit with a biexponential decay function, shown by the solid lines in part (a). Derived amplitudes (A) and time constants (τ) and calculated average lifetimes obtained from biexponential fits are listed in (b).

is attributed to the excess insulating silica that is now present in the photoanodes, which is both optically (plasmon damping, near-field decay) and electronically (recombination) detrimental. We note that the system we are studying here is highly complex and several competing processes are likely occurring, such as exciton recombination, energy transport between adjacent nanostructures, PRET from metal to TiO_2, etc. A more thorough and systematic study, including silica layer thickness dependence, would be necessary to decouple the effects and make definite conclusions.

6.4 Conclusions

In summary, we investigated the impact of shape- and composition-controlled Au/Ag/SiO_2 core/shell/shell bimetallic nanostructures on the device performance and electron dynamics of DSSCs. The best performing plasmon-enhanced DSSCs resulted in 7.51% PCE relative to 5.97% for reference DSSCs, giving rise to $\sim$26% enhancement. By varying the particle density, a systematic dependence of device performance on nanostructure concentration was observed. Maximum enhancement was achieved at 0.44 *wt.%* Au/Ag/SiO_2 NSs, which is substantially less than previously studied DSSCs integrated with monometallic nanostructures and poorly controlled shapes. Enhanced device performance was attributed to increased light harvesting enabled by the intense near-field interactions of nanostructures with N719, far-field coupling of scattered light into the active layer, and PRET from nanostructures to TiO_2. Transient absorption spectroscopy studies demonstrated a decrease in amplitude weighted lifetimes with increasing particle density, showing strong evidence of PRET. Further, unlike the unoptimized plasmonic devices (0.22 *wt.%*, 0.95 *wt.%*), which only impact the slow time constants, plasmonic DSSCs with optimized particle density of Au/Ag/SiO_2 NSs (0.44 *wt.%*) alter both the fast and slow lifetimes. We attributed this to strong metal-molecule interaction that likely populates the singlet metal ligand charge transfer states of the excited dye, augmenting e^-/h^+ pair generation and rapid charge transfer into TiO_2. We anticipate morphology-controlled bimetallic nanostructures can be ulti-

mately tailored, tuned, and targeted toward a range of optical and optoelectronic technologies beyond DSSCs.

6.5 Methods

Au Nanocrystal Synthesis: Au nanocrystals (Au NCs) were synthesized by modifying a procedure previously described.[80] All reagents were purchased from Sigma-Aldrich. Au seeds were prepared by adding 0.6 mL of freshly prepared and ice cold 10 mM $NaBH_4$ to an aqueous solution composed of 7.5 mL of 100 mM CTAB, 2.75 mL milli-Q H_2O (18.2 MΩ), and 0.8 mL of 10 mM $HAuCl_4$. This solution was stirred vigorously for 1 minute and then transferred to a 35 °C water bath where it was left undisturbed for one hour. A growth solution was prepared by adding 6.4 mL of 100 mM CTAB, 0.8 mL of 10 mM $HAuCl_4$, and 3.8 mL of 100 mM ascorbic acid sequentially to 32 mL of milli-Q H_2O. The seed solution was diluted by a factor of ten with milli-Q H_2O. Then 20 μL of diluted seed solution was added to the growth solution, mixed gently by inversion, and then left undisturbed at 35 °C for 5 hours.

Au/Ag Nanostructure Synthesis: Au/Ag nanostructures (Au/Ag NSs) were synthesized by following our previously published procedure.[41] First, 5 mLs of the Au NC suspension synthesized above was centrifuged at 1100 RCF for 15 minutes ($\times$3) and washed and soaked in 20 mM cetyltrimethylammonium chloride (CTAC) for 15 minutes. The nanocrystals were then re-dispersed in 333 μL of milli-Q H_2O for use as precursor solution for Ag growth. Typically, 200 μL of precursor solution and 50 μL of 10 mM KBr were added to 5 mL of 20 mM CTAC and heated in a 65 °C water bath for 10 minutes before adding in 50 mL of 10 μM $AgNO_3$ and 150 μL of 100 mM ascorbic acid. The solution was mixed gently by inversion and left undisturbed at 65 °C for two hours.

Silica Coating Au/Ag nanostructures (Au/Ag/SiO_2 NSs): Au/Ag nanostructures were coated with a thin layer of silica (3-5 nm) by modifying a procedure previously described.[81] 30 mL of as-prepared Au/Ag NSs were first functionalized with 400 μL of 1 mM 3-

aminopropyltrimethoxysilane (APTMS) for 15 minutes at room temperature while stirring. A 0.54 *wt.%* solution of sodium silicate was adjusted to pH ∼10.2 with 5 N HCl followed by injecting 500 μL into the APTMS functionalized Au nanocubes. The reaction mixture was stirred for 3 minutes at room temperature and then transferred to a 50 °C oil bath and stirred for 4 hours to form the silica shell.

Electrode Preparation: Electrodes were prepared on fluorine-doped tin oxide coated on glass (FTO, MTI Corp.), that were first cleaned by sonication in a bath of 2% by volume Hellmanex in water and 50/50 acetone/isopropanol for 30 minutes each. They were then plasma treated for 20 minutes immediately before use. Cleaned FTO glass slides were treated with 40 mM $TiCl_4$ in H_2O for 30 min at 70 °C, rinsed with H_2O and EtOH, and dried with nitrogen. They were then fired in air at 500 °C for 15 minutes. Reference TiO_2 anodes were prepared by doctor-blading a ∼10 μm layer of a 20 nm TiO_2 paste (Dyesol Inc., MS002010) onto the surface of the FTO using 1 layer of Scotch® tape to control the thickness, and then fired in air at 500 °C. Plasmon-enhanced anodes were prepared by first adding a washed and concentrated solution of $Au/Ag/SiO_2$ nanostructures directly into the 20 nm TiO_2 paste and mixing until homogeneous. The nanostructure-incorporated paste was then deposited via the doctor blade technique and fired as above. All anodes received a 40 mM $TiCl_4$ post-treatment for 30 mins at 70 °C, were rinsed with H_2O and EtOH, and were then fired in air for 15 minutes at 500 °C. Finally, anodes were immersed in 0.6 mM Di-tetrabutylammonium *cis*-bis(isothiocyanato) bis(2,2-bipyridyl-4,4dicarboxylato) ruthenium(II) (N719 dye Sigma, 703206) in ethanol overnight inside a N_2 glove box. Platinum cathodes were prepared by drilling two holes into the FTO glass prior to cleaning. A 25 mM H_2PtCl_6 in isopropanol solution was brushed onto clean FTO glass substrates and then fired at 450 °C for one hour.

DSSC Fabrication: The cathode and anode were heat-sealed with a ring of 50 μm thick, low temperature thermoplastic sealant (Dyesol, 7622A41). They were filled with an I^-/I_3^- based electrolyte comprised of 50 mM I_2, 100 mM LiI, 600 mM 1-hexyl-2,3-

dimethylimadizolium iodide, and 500 mM tertbuylpyridine (TBP) in acetonitrile by injection through holes in the Pt electrode. Holes were then closed with additional sealant.

Characterization: A Varian Cary 5000 UV-vis NIR spectrophotometer was used to measure the extinction of the Au/Ag NSs as well as the absorption of the TiO_2 thin film electrodes. The nanostructures were characterized using an Osiris TEM at 200 keV. Characterization of power conversion performance of the DSSCs was conducted with a Newport solar simulator and a Metrohm potentiostat. Each cell received 1 sun (100 mW/cm^2) of power from the solar simulator at AM 1.5 and was tested in a range from -1.0 to 1.0 V at a scan rate of 50 mV/s. A cell area of 0.12 cm^2 was illuminated using a shadow mask. Incident photon conversion efficiency (IPCE) measurements were conducted with a 6 W Fianium fiber laser supercontinuum source coupled with a Fianium acousto-optic tunable filter to filter out the desired excitation wavelength from the white light source.

Ultrafast Pump-Probe spectroscopy: Femtosecond transient absorption measurements are conducted using a home-built pump-probe setup based on a femtosecond laser system, that utilizes seed pulses from a titanium sapphire oscillator (Micra, Coherent), amplified by a Ti:Sapphire amplifier (Legend USP-HE, Coherent) to provide 800 nm femtosecond pulses (2.5 mJ/pulse), operating at 1 kHz repetition rate with 40 fs pulse durations. The Legend amplifier is pumped by a Nd:YLF laser (Evolution-30, Coherent). A small portion of the output of the amplifier ($\sim$4 μJ/pulse) is focused on a sapphire window (2 mm thick) to generate a white light continuum (WLC) probe (450-900 nm). To minimize temporal chirp in the spectrally broad probe, a set of parabolic mirrors is used to collimate and focus the WLC on the sample. The transmitted probe is focused onto 100 μm core fiber coupled with a spectrometer/CCD (USB2000ES, Ocean Optics). The pump pulse at 400 nm is generated by doubling $\sim$50 μJ/pulse of the 800 nm fundamental in a BBO crystal. The pump beam passes through a delay line to allow control of time-delay between the pump and the probe. In order to measure absorbance changes between every two successive laser shots, the pump beam was chopped at a frequency of 500 Hz. At the sample, the spot sizes

of the pump and probe pulses were 100 μm and 50 μm, respectively. The pump fluence at the sample was $\sim$ 5 μJ/cm^2.

Simulation Protocol: Finite difference time domain (FDTD) simulations were run with Lumerical FDTD Solutions. Calculations were performed on a single particle in water using a total-field scattered-field (TFSF) plane wave source. The simulated rounded edge Au nanocube has a 45 nm edge length with a forward injection of the TFSF source along the y-axis. The simulated Au/Ag nanocube has a 45 nm rounded edge Au core and a 10 nm thick Ag shell, with a forward injection of the TFSF source along the y-axis. The simulated nanopyramid has a 60 nm edge length for the Au core, and a 20 nm thick Ag shell, with a forward injection of the TFSF source along the x-axis. The simulated nanosphere has a 60 nm diameter on the Au core with a 10 nm thick Ag shell, with a forward injection of the TFSF source along the y-axis. All simulations used perfectly matched layer (PML) boundary conditions.

6.6 Bibliography

[1] Wu-Qiang Wu, Yang-Fan Xu, Cheng-Yong Su, and Dai-Bin Kuang. Ultra-long anatase TiO_2 nanowire arrays with multi-layered configuration on FTO glass for high-efficiency dye-sensitized solar cells. *Energy Environ. Sci.*, 7(2):644–649, 2014.

[2] George Y. Margulis, M. Greyson Christoforo, David Lam, Zach M. Beiley, Andrea R. Bowring, Colin D. Bailie, Alberto Salleo, and Michael D. McGehee. Spray deposition of silver nanowire electrodes for semitransparent solid-state dye-sensitized solar cells. *Adv. Energy Mater.*, 3(12):1657–1663, 2013.

[3] William R. Erwin, Landon Oakes, Shahana Chatterjee, Holly F. Zarick, Cary L. Pint, and Rizia Bardhan. Engineered porous silicon counter electrodes for high efficiency dye-sensitized solar cells. *ACS Appl. Mater. Interfaces*, 6(12):9904–9910, 2014.

[4] Yin-Cheng Yen, Po-Hung Chen, Jing-Zhi Chen, Jau-An Chen, and Kuan-Jiuh Lin. Plasmon-induced efficiency enhancement on dye-sensitized solar cell by a 3D TNW-AuNP layer. *ACS Appl. Mater. Interfaces*, 7(3):1892–1898, 2015.

[5] Joshua D. Winans, Chanse Hungerford, Krishanu Shome, Lewis J. Rothberg, and Philippe M. Fauchet. Plasmonic effects in ultrathin amorphous silicon solar cells: performance improvements with Ag nanoparticles on the front, the back, and both. *Opt. Express*, 23(3):A92–A105, 2015.

[6] Wei E. I. Sha, Xuanhua Li, and Wallace C. H. Choy. Breaking the space charge limit in organic solar cells by a novel plasmonic-electrical concept. *Sci. Rep.*, 4, 2014.

[7] Duck Hyun Lee, Jae Young Kwon, Stephen Maldonado, Anish Tuteja, and Akram Boukai. Extreme light absorption by multiple plasmonic layers on upgraded metallurgical grade silicon solar cells. *Nano Lett.*, 14(4):1961–1967, 2014.

[8] I. Kang Ding, Jia Zhu, Wenshan Cai, Soo-Jin Moon, Ning Cai, Peng Wang, Shaik M. Zakeeruddin, Michael Graetzel, Mark L. Brongersma, Yi Cui, and Michael D. McGehee. Plasmonic dye-sensitized solar cells. *Adv. Energy Mater.*, 1(1):52–57, 2011.

[9] Bo Ding, Bong Jae Lee, Mengjin Yang, Hyun Suk Jung, and Jung-Kun Lee. Surface-plasmon assisted energy conversion in dye-sensitized solar cells. *Adv. Energy Mater.*, 1(3):415–421, 2011.

[10] Se-Woong Baek, Garam Park, Jonghyeon Noh, Changsoon Cho, Chun-Ho Lee, Min-Kyo Seo, Hyunjoon Song, and Jung-Yong Lee. Au@Ag core-shell nanocubes for efficient plasmonic light scattering effect in low bandgap organic solar cells. *ACS Nano*, 8(4):3302–3312, 2014.

[11] Holly F. Zarick, Olivia Hurd, Joseph A. Webb, Chanse Hungerford, William R. Erwin, and Rizia Bardhan. Enhanced efficiency in dye-sensitized solar cells with shape-controlled plasmonic nanostructures. *ACS Photonics*, 1(9):806–811, 2014.

[12] Joseph A. Webb, William R. Erwin, Holly F. Zarick, Jayde Aufrecht, Harris W. Manning, Matthew J. Lang, Cary L. Pint, and Rizia Bardhan. Geometry-dependent plasmonic tunability and photothermal characteristics of multibranched gold nanoantennas. *J. Phys. Chem. C*, 118(7):3696–3707, 2014.

[13] Suljo Linic, Umar Aslam, Calvin Boerigter, and Matthew Morabito. Photochemical transformations on plasmonic metal nanoparticles. *Nat. Mater.*, 14(6):567–576, 2015.

[14] Matthew D. Sonntag, Jordan M. Klingsporn, Alyssa B. Zrimsek, Bhavya Sharma, Laura K. Ruvuna, and Richard P. Van Duyne. Molecular plasmonics for nanoscale spectroscopy. *Chem. Soc. Rev.*, 43(4):1230–1247, 2014.

[15] Ronen Adato and Hatice Altug. In-situ ultra-sensitive infrared absorption spectroscopy of biomolecule interactions in real time with plasmonic nanoantennas. *Nat. Commun.*, 4:2154, 2013.

[16] Joseph A. Webb, Jayde Aufrecht, Chanse Hungerford, and Rizia Bardhan. Ultrasensitive analyte detection with plasmonic paper dipsticks and swabs integrated with branched nanoantennas. *J. Mater. Chem. C*, 2(48):10446–10454, 2014.

[17] Joseph A. Webb and Rizia Bardhan. Emerging advances in nanomedicine with engineered gold nanostructures. *Nanoscale*, 6(5):2502–2530, 2014.

[18] Naveen Gandra, Christopher Portz, Saide Z. Nergiz, Andrew Fales, Tuan Vo-Dinh, and Srikanth Singamaneni. Inherently stealthy and highly tumor-selective gold nanoraspberries for photothermal cancer therapy. *Sci. Rep.*, 5, 2015.

[19] Rinat Meir, Katerina Shamalov, Oshra Betzer, Menachem Motiei, Miryam Horovitz-Fried, Ronen Yehuda, Aron Popovtzer, Rachela Popovtzer, and Cyrille J. Cohen. Nanomedicine for cancer immunotherapy: Tracking cancer-specific T-cells in vivo with gold nanoparticles and CT imaging. *ACS Nano*, 9(6):6363–6372, 2015.

[20] Qi Xu, Fang Liu, Yuxiang Liu, Kaiyu Cui, Xue Feng, Wei Zhang, and Yidong Huang. Broadband light absorption enhancement in dye-sensitized solar cells with Au-Ag alloy popcorn nanoparticles. *Sci. Rep.*, 3, 2013.

[21] Carl Hagglund, Michael Zach, and Bengt Kasemo. Enhanced charge carrier generation in dye sensitized solar cells by nanoparticle plasmons. *Appl. Phys. Lett.*, 92(1):013113, 2008.

[22] Harry A. Atwater and Albert Polman. Plasmonics for improved photovoltaic devices. *Nat. Mater.*, 9(3):205–213, 2010.

[23] Shaunak Mukherjee, Florian Libisch, Nicolas Large, Oara Neumann, Lisa V. Brown, Jin Cheng, J. Britt Lassiter, Emily A. Carter, Peter Nordlander, and Naomi J. Halas. Hot electrons do the impossible: Plasmon-induced dissociation of H^-_2 on Au. *Nano Lett.*, 13(1):240–247, 2013.

[24] M. Claire van Lare and Albert Polman. Optimized scattering power spectral density of photovoltaic light-trapping patterns. *ACS Photonics*, 2(7):822–831, 2015.

[25] Na Zhou, Vanesa Lopez-Puente, Qing Wang, Lakshminarayana Polavarapu, Isabel Pastoriza-Santos, and Qing-Hua Xu. Plasmon-enhanced light harvesting: applications in enhanced photocatalysis, photodynamic therapy and photovoltaics. *RSC Adv.*, 5(37):29076–29097, 2015.

[26] Mahesh K. Gangishetty, Kee Eun Lee, Robert W. J. Scott, and Timothy L. Kelly. Plasmonic enhancement of dye sensitized solar cells in the red-to-near-infrared region using triangular core shell $Ag@SiO_2$ nanoparticles. *ACS Appl. Mater. Interfaces*, 5(21):11044–11051, 2013.

[27] Shuai Chang, Quan Li, Xudong Xiao, King Young Wong, and Tao Chen. Enhancement of low energy sunlight harvesting in dye-sensitized solar cells using plasmonic gold nanorods. *Energy Environ. Sci.*, 5(11):9444–9448, 2012.

[28] Scott K. Cushing, Jiangtian Li, Fanke Meng, Tess R. Senty, Savan Suri, Mingjia Zhi, Ming Li, Alan D. Bristow, and Nianqiang Wu. Photocatalytic activity enhanced by plasmonic resonant energy transfer from metal to semiconductor. *J. Am. Chem. Soc.*, 134(36):15033–15041, 2012.

[29] Scott K. Cushing, Jiangtian Li, Joeseph Bright, Brandon T. Yost, Peng Zheng, Alan D. Bristow, and Nianqiang Wu. Controlling plasmon-induced resonance energy transfer and hot electron injection processes in metal$@TiO_2$ core-shell nanoparticles. *J. Phys. Chem. C*, 119(28):16239–16244, 2015.

[30] P. James Schuck. Nanoimaging hot electrons go through the barrier. *Nat. Nanotechnol.*, 8(11):799–800, 2013.

[31] Fuming Wang and Nicholas A. Melosh. Power-independent wavelength determina-

tion by hot carrier collection in metal-insulatormetal devices. *Nat. Commun.*, 4:1711, 2013.

[32] Stafford W. Sheehan, Heeso Noh, Gary W. Brudvig, Hui Cao, and Charles A. Schmuttenmaer. Plasmonic enhancement of dye-sensitized solar cells using core-shell-shell nanostructures. *J. Phys. Chem. C*, 117(2):927–934, 2013.

[33] Yoon Hee Jang, Yu Jin Jang, Saji Thomas Kochuveedu, Myunghwan Byun, Zhiqun Lin, and Dong Ha Kim. Plasmonic dye-sensitized solar cells incorporated with Au-TiO_2 nanostructures with tailored configurations. *Nanoscale*, 6(3):1823–1832, 2014.

[34] Xiangnan Dang, Jifa Qi, Matthew T. Klug, Po-Yen Chen, Dong Soo Yun, Nicholas X. Fang, Paula T. Hammond, and Angela M. Belcher. Tunable localized surface plasmon-enabled broadband light-harvesting enhancement for high-efficiency panchromatic dye-sensitized solar cells. *Nano Lett.*, 13(2):637–642, 2013.

[35] Michael D. Brown, Teeraporn Suteewong, R. Sai Santosh Kumar, Valerio D'Innocenzo, Annamaria Petrozza, Michael M. Lee, Ulrich Wiesner, and Henry J. Snaith. Plasmonic dye-sensitized solar cells using core-shell metal-insulator nanoparticles. *Nano Lett.*, 11(2):438–445, 2011.

[36] Jifa Qi, Xiangnan Dang, Paula T. Hammond, and Angela M. Belcher. Highly efficient plasmon-enhanced dye-sensitized solar cells through metal@oxide core-shell nanostructure. *ACS Nano*, 5(9):7108–7116, 2011.

[37] Naomi J. Halas, Surbhi Lal, Wei-Shun Chang, Stephan Link, and Peter Nordlander. Plasmons in strongly coupled metallic nanostructures. *Chem. Rev.*, 111(6):3913–3961, 2011.

[38] N. K. Grady, N. J. Halas, and P. Nordlander. Influence of dielectric function properties on the optical response of plasmon resonant metallic nanoparticles. *Chem. Phys. Lett.*, 399(1-3):167–171, 2004.

[39] Qi Xu, Fang Liu, Yuxiang Liu, Weisi Meng, Kaiyu Cui, Xue Feng, Wei Zhang, and Yidong Huang. Aluminum plasmonic nanoparticles enhanced dye sensitized solar cells. *Opt. Express*, 22(5):A301–A310, 2014.

[40] Lihua Bai, Meiya Li, Kaimo Guo, Mengdai Luoshan, Hadja Fatima Mehnane, Ling Pei, Muchen Pan, Lei Liao, and Xingzhong Zhao. Plasmonic enhancement of the performance of dye-sensitized solar cell by core-shell AuNRs@SiO_2 in composite photoanode. *J. Power Sources*, 272:1100–1105, 2014.

[41] Holly F. Zarick, William R. Erwin, Jayde Aufrecht, Andrew Coppola, Bridget R. Rogers, Cary L. Pint, and Rizia Bardhan. Morphological modulation of bimetallic nanostructures for accelerated catalysis. *J. Mater. Chem. A*, 2(19):7088–7098, 2014.

[42] Min Hu, Jingyi Chen, Zhi-Yuan Li, Leslie Au, Gregory V. Hartland, Xingde Li, Manuel Marquez, and Younan Xia. Gold nanostructures: engineering their plasmonic properties for biomedical applications. *Chem. Soc. Rev.*, 35(11):1084–1094, 2006.

[43] M. Hu, H. Petrova, X. Wang, and G. V. Hartland. Time-resolved and steady state spectroscopy of polydisperse colloidal silver nanoparticle samples. *J. Phys. Chem. B*, 109(30):14426–14432, 2005.

[44] Vivek Sharma, Kyoungweon Park, and Mohan Srinivasarao. Colloidal dispersion of gold nanorods: Historical background, optical properties, seed-mediated synthesis, shape separation and self-assembly. *Mater. Sci. Eng., R*, 65(1-3):1–38, 2009.

[45] Bjorn Torngren, Kenta Akitsu, Anne Ylinen, Simon Sanden, Hua Jiang, Janne Ruokolainen, Makoto Komatsu, Tomofumi Hamamura, Jotaro Nakazaki, Takaya Kubo, Hiroshi Segawa, Ronald Osterbacka, and Jan-Henrik Smatt. Investigation of plasmonic gold-silica core-shell nanoparticle stability in dye-sensitized solar cell applications. *J. Colloid Interface Sci.*, 427:54–61, 2014.

[46] Gede Widia Pratama Adhyaksa, Se-Woong Baek, Ga In Lee, Dong Ki Lee, Jung-Yong Lee, and Jeung Ku Kang. Coupled near- and far-field scattering in silver nanoparticles for high-efficiency, stable, and thin plasmonic dye-sensitized solar cells. *ChemSusChem*, 7(9):2461–2468, 2014.

[47] Stacey D. Standridge, George C. Schatz, and Joseph T. Hupp. Distance dependence of plasmon-enhanced photocurrent in dye-sensitized solar cells. *J. Am. Chem. Soc.*, 131(24):8407–8409, 2009.

[48] G. Paruthimal Kalaignan and Yong Soo Kang. A review on mass transport in dye-sensitized nanocrystalline solar cells. *J. Photochem. Photobiol., C*, 7(1):17–22, 2006.

[49] Heykel Aouani, Oussama Mahboub, Eloise Devaux, Herve Rigneault, Thomas W. Ebbesen, and Jerome Wenger. Plasmonic antennas for directional sorting of fluorescence emission. *Nano Lett.*, 11(6):2400–2406, 2011.

[50] Rizia Bardhan, Nathaniel K. Grady, Joseph R. Cole, Amit Joshi, and Naomi J. Halas. Fluorescence enhancement by Au nanostructures: Nanoshells and nanorods. *ACS Nano*, 3(3):744–752, 2009.

[51] Hua Dong, Zhaoxin Wu, Ahmed El-Shafei, Bin Xia, Jun Xi, Shuya Ning, Bo Jiao, and Xun Hou. Ag-encapsulated au plasmonic nanorods for enhanced dye-sensitized solar cell performance. *J. Mater. Chem. A*, 3(8):4659–4668, 2015.

[52] J. H. Liu, A. Q. Wang, Y. S. Chi, H. P. Lin, and C. Y. Mou. Synergistic effect in an Au-Ag alloy nanocatalyst: CO oxidation. *J. Phys. Chem. C*, 109(1):40–43, 2005.

[53] Lakshminarayana Polavarapu, Stefanos Mourdikoudis, Isabel Pastoriza-Santos, and Jorge Perez-Juste. Nanocrystal engineering of noble metals and metal chalcogenides: controlling the morphology, composition and crystallinity. *Cryst. Eng. Comm.*, 17(20):3727–3762, 2015.

[54] Mohamed Haggui, Montacer Dridi, Jerome Plain, Sylvie Marguet, Henri Perez, George C. Schatz, Gary P. Wiederrecht, Stephen K. Gray, and Renaud Bachelot. Spatial confinement of electromagnetic hot and cold spots in gold nanocubes. *ACS Nano*, 6(2):1299–1307, 2012.

[55] Matthew Rycenga, Moon Ho Kim, Pedro H. C. Camargo, Claire Cobley, Zhi-Yuan Li, and Younan Xia. Surface-enhanced raman scattering: Comparison of three different molecules on single-crystal nanocubes and nanospheres of silver. *J. Phys. Chem. A*, 113(16):3932–3939, 2009.

[56] Matthew Rycenga, Xiaohu Xia, Christine H. Moran, Fei Zhou, Dong Qin, Zhi-Yuan Li, and Younan Xia. Generation of hot spots with silver nanocubes for single-molecule detection by surface-enhanced raman scattering. *Angew. Chem. Int. Ed.*, 50(24):5473–5477, 2011.

[57] Subas Muduli, Onkar Game, Vivek Dhas, K. Vijayamohanan, K. A. Bogle, N. Valanoor, and Satishchandra B. Ogale. TiO_2-Au plasmonic nanocomposite for enhanced dye-sensitized solar cell (DSSC) performance. *Sol. Energy*, 86(5):1428–1434, 2012.

[58] Yumin Liu, Haowei Zhai, Feng Guo, Niu Huang, Weiwei Sun, Chenghao Bu, Tao Peng, Jikang Yuan, and Xingzhong Zhao. Synergistic effect of surface plasmon resonance and constructed hierarchical TiO_2 spheres for dye-sensitized solar cells. *Nanoscale*, 4(21):6863–6869, 2012.

[59] Kaimo Guo, Meiya Li, Xiaoli Fang, Xiaolian Liu, Bobby Sebo, Yongdan Zhu, Zhongqiang Hu, and Xingzhong Zhao. Preparation and enhanced properties of dye-sensitized solar cells by surface plasmon resonance of Ag nanoparticles in nanocomposite photoanode. *J. Power Sources*, 230:155–160, 2013.

[60] P. Naresh Kumar, Melepurath Deepa, and Avanish Kumar Srivastava. Ag plasmonic

nanostructures and a novel gel electrolyte in a high efficiency TiO_2/CdS solar cell. *Phys. Chem. Chem. Phys.*, 17(15):10040–10052, 2015.

[61] P. Naresh Kumar, Melepurath Deepa, and Partha Ghosal. Low-cost copper nanostructures impart high efficiencies to quantum dot solar cells. *ACS Appl. Mater. Interfaces*, 7(24):13303–13313, 2015.

[62] Jiang Du, Jian Qi, Dan Wang, and Zhiyong Tang. Facile synthesis of Au@TiO_2 core-shell hollow spheres for dye-sensitized solar cells with remarkably improved efficiency. *Energy Environ. Sci.*, 5(5):6914–6918, 2012.

[63] S. Link and M. A. El-Sayed. Shape and size dependence of radiative, non-radiative and photothermal properties of gold nanocrystals. *Int. Rev. Phys. Chem.*, 19(3):409–453, 2000.

[64] B. E. Deal, E. H. Snow, and C. A. Mead. Barrier energies in metal-silicon dioxide-silicon structures. *J. Phys. Chem. Solids*, 27(11-1):1873–1879, 1966.

[65] W. C. Lee and C. M. Hu. Modeling CMOS tunneling currents through ultrathin gate oxide due to conduction- and valence-band electron and hole tunneling. *IEEE Trans. Electron Devices*, 48(7):1366–1373, 2001.

[66] Chu-Hsuan Lin and Chee Wee Liu. Metal-insulator-semiconductor photodetectors. *Sensors*, 10(10):8797–8826, 2010.

[67] Z. A. Weinberg and A. Hartstein. Photon assisted tunneling from aluminum into silicon dioxide. *Solid State Commun.*, 20(3):179–182, 1976.

[68] Hyun-Young Kim and Jung Sang Suh. Panchromatic quasi-monolayer of Ag nanoparticles for high-efficiency dye-sensitized solar cells. *RSC Adv.*, 5(74):59895–59902, 2015.

[69] Luchao Du, Akihiro Furube, Kazuhiro Yamamoto, Kohjiro Hara, Ryuzi Katoh, and M. Tachiya. Plasmon-induced charge separation and recombination dynamics in gold-TiO_2 nanoparticle systems: Dependence on TiO_2 particle size. *J. Phys. Chem. C*, 113(16):6454–6462, 2009.

[70] Britain Willingham and Stephan Link. Energy transport in metal nanoparticle chains via sub-radiant plasmon modes. *Opt. Express*, 19(7):6450–6461, 2011.

[71] Jr. Solis, David, Britain Willingham, Scott L. Nauert, Liane S. Slaughter, Jana Olson, Pattanawit Swanglap, Aniruddha Paul, Wei-Shun Chang, and Stephan Link. Electromagnetic energy transport in nanoparticle chains via dark plasmon modes. *Nano Lett.*, 12(3):1349–1353, 2012.

[72] Luchao Du, Akihiro Furube, Kohjiro Hara, Ryuzi Katoh, and Masanori Tachiya. Ultrafast plasmon induced electron injection mechanism in gold-TiO_2 nanoparticle system. *J. Photochem. Photobiol., C*, 15:21–30, 2013.

[73] Akihiro Furube, Luchao Du, Kohjiro Hara, Ryuzi Katoh, and Masanori Tachiya. Ultrafast plasmon-induced electron transfer from gold nanodots into TiO_2 nanoparticles. *J. Am. Chem. Soc.*, 129(48):14852–14853, 2007.

[74] Li-Hong Yu, Jing-Yu Xi, Kin Cheung Lo, Lucy Jane Antrobus, David Lee Phillips, and Wai Kin Chan. Transient absorption of N719 and its electron transfer kinetics on ZnO nanoparticles surface. *J. Inorg. Organomet. Polym.*, 25(1):169–175, 2015.

[75] Hung-Yu Hsu, Chi-Wen Cheng, Wei-Kai Huang, Yuan-Pern Lee, and Eric Wei-Guang Diau. Femtosecond infrared transient absorption dynamics of benzimidazole-based ruthenium complexes on TiO_2 films for dye-sensitized solar cells. *J. Phys. Chem. C*, 118(30):16904–16911, 2014.

[76] Eun Chul Cho, Chulhong Kim, Fei Zhou, Claire M. Cobley, Kwang Hyun Song, Jingyi Chen, Zhi-Yuhan Li, Lihong V. Wang, and Younan Xia. Measuring the optical

absorption cross sections of Au-Ag nanocages and Au nanorods by photoacoustic imaging. *J. Phys. Chem. C*, 113(21):9023–9028, 2009.

[77] Fantai Kong, Songyuan Dai, and Kongjia Wang. Purification of bipyridyl ruthenium dye and its application in dye-sensitized solar cells. *Plasma Sci. Tech.*, 8(5):531–534, 2006.

[78] Zelin Lu, Xujie Pan, Yingzhuang Ma, Yu Li, Lingling Zheng, Danfei Zhang, Qi Xu, Zhijian Chen, Shufeng Wang, Bo Qu, Fang Liu, Yidong Huang, Lixin Xiao, and Qihuang Gong. Plasmonic-enhanced perovskite solar cells using alloy popcorn nanoparticles. *RSC Adv.*, 5(15):11175–11179, 2015.

[79] M. P. Brandon, D. M. Ledwith, and J. M. Kelly. Preparation of saline-stable, silica-coated triangular silver nanoplates of use for optical sensing. *J. Colloid Interface Sci.*, 415:77–84, 2014.

[80] T. K. Sau and C. J. Murphy. Room temperature, high-yield synthesis of multiple shapes of gold nanoparticles in aqueous solution. *J. Am. Chem. Soc.*, 126(28):8648–8649, 2004.

[81] Jian Feng Li, Xiang Dong Tian, Song Bo Li, Jason R. Anema, Zhi Lin Yang, Yong Ding, Yuan Fei Wu, Yong Ming Zeng, Qi Zhen Chen, Bin Ren, Zhong Lin Wang, and Zhong Qun Tian. Surface analysis using shell-isolated nanoparticle-enhanced raman spectroscopy. *Nat. Protoc.*, 8(1):52–65, 2013.

CHAPTER 7

ULTRAFAST CARRIER DYNAMICS IN BIMETALLIC NANOSTRUCTURES-ENHANCED METHYLAMMONIUM LEAD BROMIDE PEROVSKITES

Adapted from H. F. Zarick, A. Boulesbaa, A. A. Puretzky, E. M. Talbert, Z. R. DeBra, N. Soetan, D. B. Geohegan, and R. Bardhan, *Nanoscale*, **2017**, *9*, 1475 with permission from the Royal Society of Chemistry.

7.1 Summary

In this chapter, we examine the impact of hybrid bimetallic Au/Ag core/shell nanostructures on the carrier dynamics of methylammonium lead tribromide ($MAPbBr_3$) mesoporous perovskite solar cells (PSCs). Plasmon-enhanced PSCs incorporated with Au/Ag nanostructures demonstrated improved light harvesting and increased power conversion efficiency by 26% relative to reference devices. Two complementary spectral techniques, transient absorption spectroscopy (TAS) and time-resolved photoluminescence (trPL), were employed to gain a mechanistic understanding of plasmonic enhancement processes. TAS revealed a decrease in the photobleach formation time, which suggests that the nanostructures improve hot carrier thermalization to an equilibrium distribution, relieving hot phonon bottleneck in $MAPbBr_3$ perovskites. TAS also showed a decrease in carrier decay lifetimes, indicating that nanostructures enhance photoinduced carrier generation and promote efficient electron injection into TiO_2 prior to bulk recombination. Furthermore, nanostructure-incorporated perovskite films demonstrated quenching in steady-state PL and decreases in trPL carrier lifetimes, providing further evidence of improved carrier injection in plasmon-enhanced mesoporous PSCs.

7.2 Introduction

An unprecedented rise in efficiency has been observed in methylammonium lead trihalide ($MAPbX_3$, X = I, Cl, Br) perovskite solar cells (PSCs) from 3.8% in 2009 to >20% in early 2016.[1, 2, 3, 4, 5] The inexpensive materials and low cost of solution-based processing[6] make this class of perovskites amenable to scalable manufacturing and has the potential to be a serious contender for utility-scale solar power. $MAPbI_3$-based PSCs have been a primary focus due to their near-complete visible light absorption in films <1 μm and their fast charge extraction rates.[7, 8] However, the poor stability of $MAPbI_3$ and rapid degradation in humidity has remained a major obstacle for commercialization,[9, 10] necessitating complex encapsulation techniques.[11] $MAPbBr_3$ is a promising alternative to $MAPbI_3$ with a large 2.2 eV bandgap, which gives rise to a high open circuit voltage (V_{oc}) ~1.2-1.5 V)[12, 13] and makes it an ideal material for tandem devices. Their long exciton diffusion length (>1.2 μm) enables good charge transport in devices.[14] In addition, $MAPbBr_3$ demonstrates higher stability towards air and moisture due to its stable cubic phase and low ionic mobility relative to the pseudocubic $MAPbI_3$, in which inherent lattice strain provides an avenue for increased diffusion.[11, 14, 15, 16] However, a relatively large exciton binding energy, E_B, (76 meV) and poor light absorption beyond its band edge at 550 nm has limited the efficiencies for $MAPbBr_3$ solar cells.[11, 15, 17, 18]

Metal nanostructures provide an effective route to improve light harvesting in solar cells, enhance optical absorption, and increase carrier generation, resulting in higher efficiency.[19] The localized surface plasmon resonances (LSPRs) supported by metal nanostructures simultaneously give rise to intense electromagnetic near-fields and light scattering in the far fields,[20] which have been harnessed to enhance the performance of both planar[21, 22, 23] and mesoporous solar cells.[24, 25, 26, 27, 28] Recent work on plasmon-enhanced PSCs has suggested that in addition to improved scattering and near field coupling, metal nanostructures also reduce the exciton binding energy (E_B) and enable better charge separation.[29, 30, 31, 32] Highly polarizable metal nanostructures have also been shown to favor radiative

decay processes, increasing the optical path length of incident photons by the reabsorption of emitted radiation within the perovskite absorber layer.[33] Additionally, by controlling the position and polarization of metal nanostructures, the resulting LSPR modes can couple with the perovskite and give rise to strong light-matter interactions at the metal/perovskite interface.[34] In the previous chapter, we demonstrated the use of bimetallic gold/silver core/shell nanostructures (Au/Ag NSs) for enhancing the performance of organic photovoltaics[23] as well as dye-sensitized solar cells.[24] Here we investigate the interactions of Au/Ag NSs with $MAPbBr_3$ perovskites in the mesoporous device architecture. The engineered shape and controlled composition of the Au/Ag NSs gives rise to panchromatic light absorption, and their sharp edges and corners result in intense electric fields attributable to the quasistatic lightning-rod effect.[35, 36, 37, 38] These spectral characteristics of Au/Ag NSs result in broadband light absorption above the band edge of $MAPbBr_3$, a phenomenon useful for device performance. We integrated Au/Ag NSs within the mesoporous TiO_2 layer of $MAPbBr_3$ PSCs, examined the device performance, and correlated these trends with the carrier dynamics of $MAPbBr_3$ with both transient absorption spectroscopy (TAS) and time-resolved photoluminescence (trPL). Our results demonstrate that carrier lifetimes significantly decrease for both TAS and trPL in the presence of the bimetallic nanostructures. The enhancements observed in the presence of Au/Ag NSs in both photocurrent and incident photon to charge conversion efficiency (IPCE) of $MAPbBr_3$ PSCs correlate well with the decrease in carrier lifetimes. We attributed these effects in carrier dynamics to enhanced photoinduced charge generation and rapid electron injection into TiO_2 in the presence of the plasmonic nanostructures, as well as reduced recombination and improvement in hot carrier thermalization in the perovskite.

7.3 Results and Discussion

The $MAPbBr_3$ PSCs were fabricated by infiltrating the perovskite within a $\sim$500 nm mesoporous titania (mp-TiO_2) layer following a modified two-step sequential deposition

process (see Methods for details).[39] The mp-TiO_2 provides an ideal scaffold for perovskite crystal growth and for embedding the bimetallic nanostructures, and provides a pathway for selective charge collection.[40, 41] The incorporated Au/Ag NSs were synthesized following a seed-mediated growth method described in our previous work.[42] The NSs were coated with a conformal $\sim$5 nm layer of silica (silica-coated Au/Ag NSs, Figure 7.1c), then homogeneously mixed throughout the mesoporous TiO_2 layer (Figure 7.1a) allowing close proximity of the NSs to the $MAPbBr_3$crystals to enable plasmonic enhancement. The silica minimizes charge recombination at the perovskite/nanoparticle interface by prohibiting direct conduction of plasmon electrons into the perovskite. It also prevents Ostwald ripening during the high temperature TiO_2 annealing processes, and avoids degradation of the NSs by the halide ions in the perovskite.[24, 25, 33] The color-enhanced cross-sectional SEM image shown in Figure 7.1b depicts the relative morphology and layer thicknesses of the $MAPbBr_3$ PSCs. The representative TEM images of Au/Ag NSs shown in Figure 7.1c (silica-coated) illustrate the two distinct geometries that form during synthesis, nanocubes and nanopyramids, with distinct plasmon resonances centered at 540 nm and 615 nm correlating with the two geometries, respectively (Figure 7.1d). The two absorbance peaks of the mixed NSs promote light scattering above the bandgap of $MAPbBr_3$ as well as provide complementary broadband absorption spanning the entire visible spectrum.

The light harvesting ability of the Au/Ag NSs within the $MAPbBr_3$ PSCs was probed by comparing the absorbances of reference, $MAPbBr_3$-sensitized TiO_2 films without nanostructures, to TiO_2/$MAPbBr_3$ mesoporous films containing two different densities of silica-coated Au/Ag NSs, 0.5 *wt.%* and 1.0 *wt.%* (Figure 7.2a). An increase in absorbance was observed with the increasing nanostructure density in the 410-540 nm spectral range where the plasmon resonances of the bimetallic nanostructures overlap with the absorption of the $MAPbBr_3$ perovskite. This indicates enhanced radiative light trapping in the photoactive layer as a result of the Au/Ag NSs. While changes in absorbance above

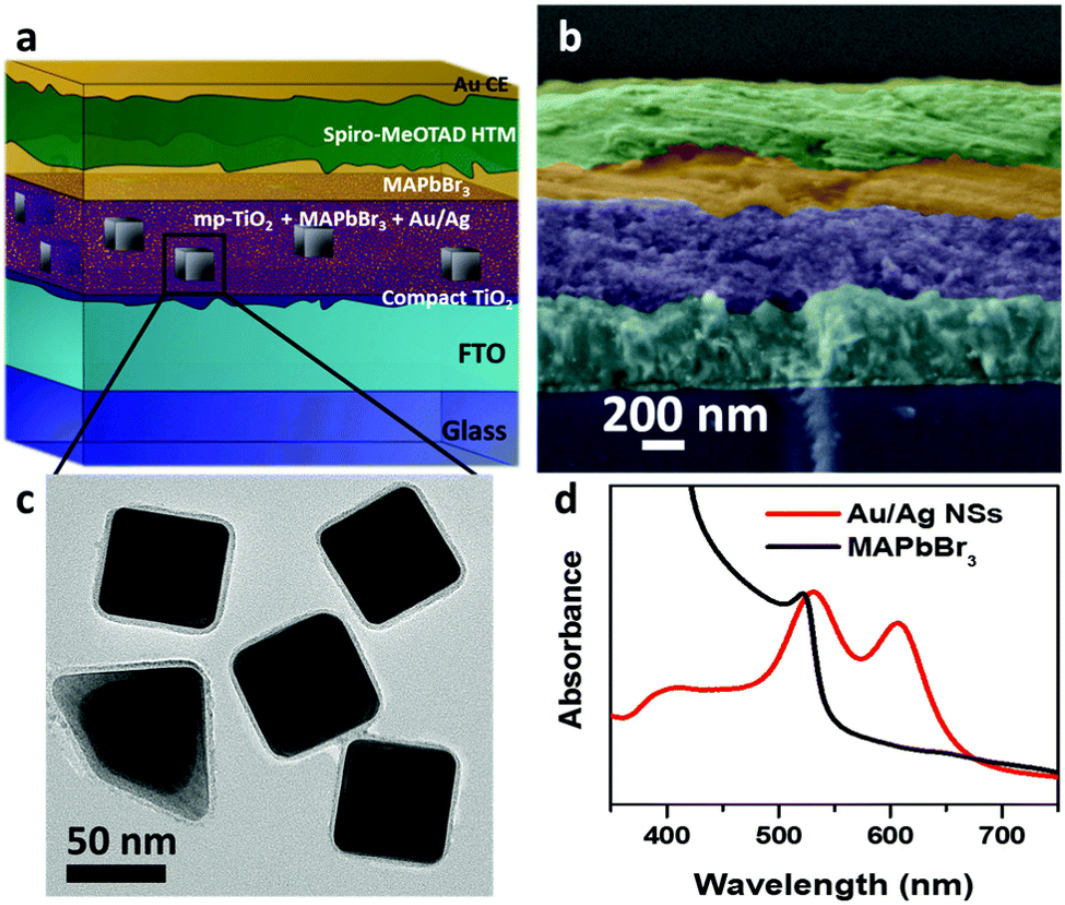

Figure 7.1: (a) Schematic representation of a $MAPbBr_3$ perovskite solar cell integrated with bimetallic Au/Ag nanostructures. The nanostructures are not shown to scale in the mesoporous TiO_2 layer. A cross-sectional SEM image of a representative reference device with an Au counter electrode (CE) is shown in (b). Coloring of the layers has been added for clarity. (c) TEM image of the bimetallic nanostructures coated with a conformal $\sim$5 nm layer of silica. The normalized absorption spectrum of $MAPbBr_3$-sensitized TiO_2 films compared to the normalized extinction spectrum of the Au/Ag NSs is shown in (d); spectra are normalized to the peaks at 530 and 535 nm, respectively.

550 nm are subtle, detailed analysis of relative absorbance enhancement (Figure 7.3a) demonstrates that Au/Ag NSs promote broadband light absorption complementary to where $MAPbBr_3$absorbs light. The absorption enhancement we observed experimentally in our work is comparable to the theoretical enhancements predicted for perovskite active layers embedded with plasmonic metal nanoparticles.[43] However enhancement in solar cells is driven by several different factors that collectively determine the external quantum efficiency and ultimately influences the total power conversion efficiency. These include the photon absorption efficiency (η_{abs}) which is the ratio of absorbed light to incident light, the exciton dissociation efficiency (η_{diss}) which is the ratio of photoexcited excitons that are converted to free carriers, the charge carrier transport efficiency (η_{ct}) which is the ratio of the generated free carriers that reach the electrode prior to recombination, and charge collection efficiency (η_{coll}), the ratio of carriers that are collected after the final interface between the active layer and the electrodes.[23] The contribution from each of these factors was examined by evaluating the device efficiencies. We investigated the device performance of the PSCs by comparing the power conversion efficiencies (PCE's) of full reference $MAPbBr_3$ PSCs with the plasmon-enhanced devices containing both 0.5 and 1.0 $wt.\%$ silica-coated Au/Ag NSs (Figure 7.2b). Average values and standard deviation for PCE were calculated from $\sim$10 devices for each reference, 0.5 $wt.\%$ Au/Ag, and 1.0 $wt.\%$ Au/Ag-incorporated devices. A steady increase in PCE is observed for both 0.5 and 1.0 $wt.\%$ silica-coated Au/Ag NS incorporations, with the best PCEs measured at 4.5% and 4.9% respectively, compared to the reference devices of 3.9% efficiency. The device parameters, Figure 7.4, show that the measured 26% increase in efficiency with Au/Ag nanostructures is not only attributed to an increase in the short circuit current density, J_{sc}, correlated with η_{abs} and η_{diss}, but also the fill factor (FF) and open circuit voltage (V_{oc}) correlated with η_{ct} and η_{coll}. This suggests that the nanostructures improve light harvesting in the devices, as well as increase charge transfer and reduce carrier recombination. However further improvements in η_{abs}, η_{diss}, η_{ct}, and η_{coll} collectively could potentially

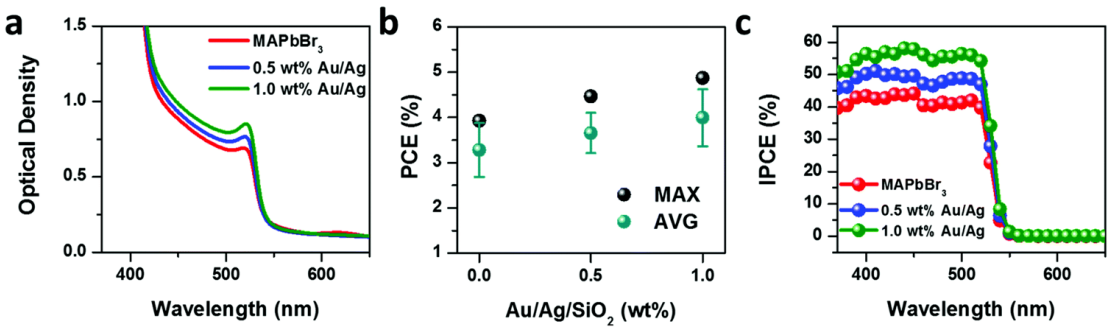

Figure 7.2: (a) Optical absorption spectra of mesoporous TiO_2 infiltrated with $MAPbBr_3$ and integrated with varying concentrations of silica-coated Au/Ag nanostructures. (b) The best and average power conversion efficiencies of devices as a function of varying concentrations of Au/Ag nanostructures (*wt.%*). Error was calculated from standard deviations of $\sim$10 devices tested at each concentration. (c) IPCE of the same devices as a function of excitation wavelength.

result in higher overall efficiencies in both reference and plasmonic devices.

While several studies have focused on plasmonic enhancement of PSCs,[29, 30, 32, 33, 44, 45, 46, 47] the carrier dynamics in metal nanostructure-incorporated PSCs remain poorly understood. Here we have employed a combination of TAS and trPL to understand the carrier dynamics in $MAPbBr_3$ reference films (non-enhanced) and investigate the impact on the exciton generation and charge recombination in $MAPbBr_3$ in the presence of Au/Ag NSs. TAS studies were performed on films of $MAPbBr_3$-infiltrated in the mp-TiO_2 layer with a compact-TiO_2 electron acceptor layer (without SpiroMeOTAD). The samples were pumped at 400 nm to fill the perovskite conduction band, and the resulting absorption dynamics were probed with a white light continuum from 450 to 600 nm. The TA spectra of mp-TiO_2/$MAPbBr_3$ (Figure 7.5a) show a ground state bleaching signal at 530 nm near the band edge of $MAPbBr_3$ as the valence band electrons are excited to the conduction band by the pump pulse.[48] A weak photoinduced absorption (PIA) signal at 490 nm is also observed, which is a result of stimulated absorption above the saturated conduction band states.[49] Our TA evolutionary spectra are in good agreement with those reported in the literature for $MAPbBr_3$.[50, 51] The normalized decay of the PIA band at 490 nm (Figure 7.5b) and dynamics of the photobleach (PB) at 530 nm (Figure 7.5c) were fit with a triex-

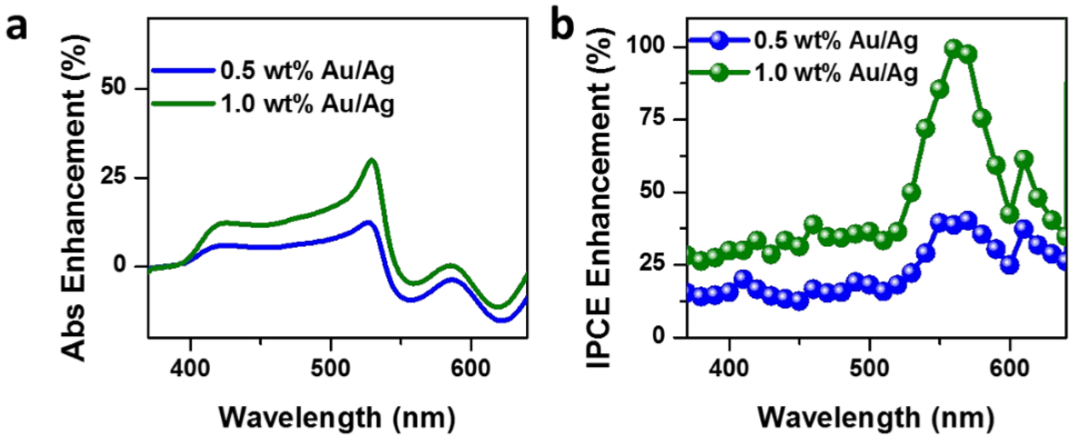

Figure 7.3: Enhancement in (a) absorbance and (b) IPCE in 0.5 *wt*.% and 1.0 *wt*.% devices compared to reference spectra.

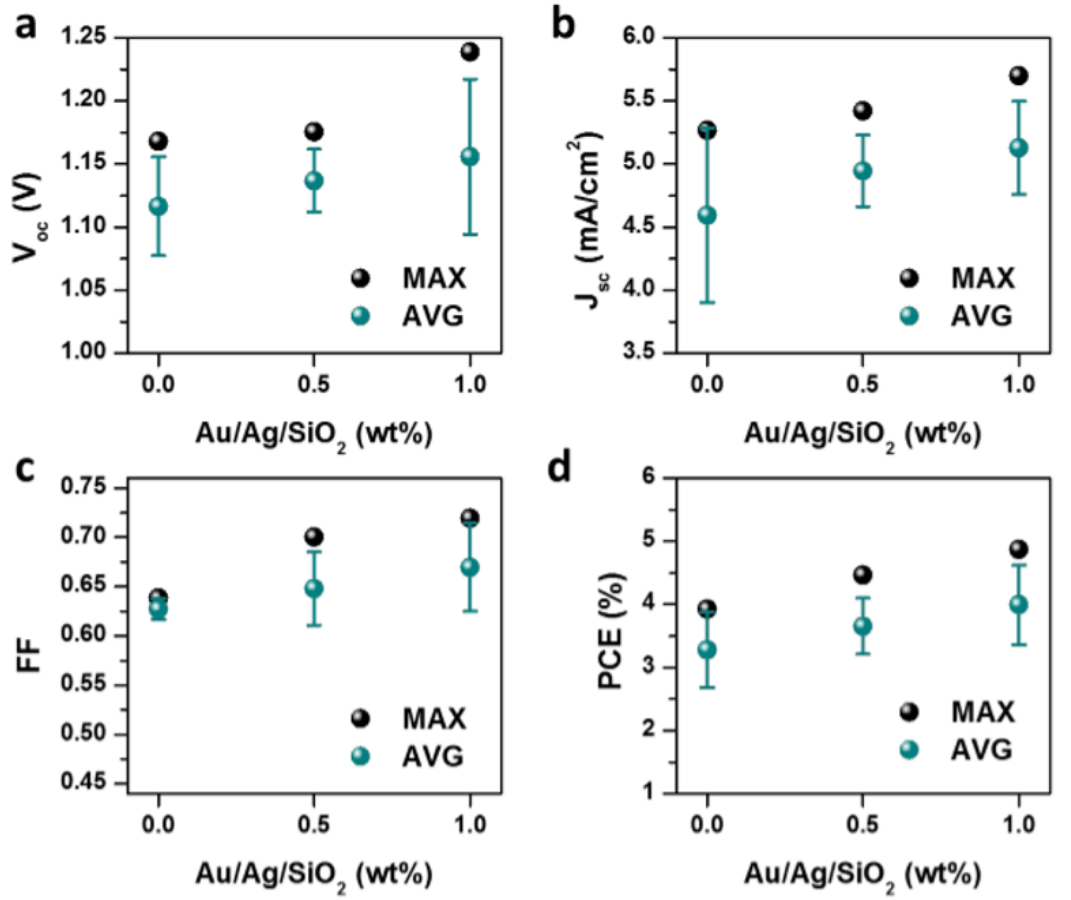

Figure 7.4: Average and best (a) open-circuit voltage, (b) fill factor, (c) short circuit current density, and (d) power conversion efficiency values for devices as a function of Au/Ag nanostructure particle density (*wt*.%). Error calculated from standard deviations calculated over a range of $\sim$10 devices tested at each concentration.

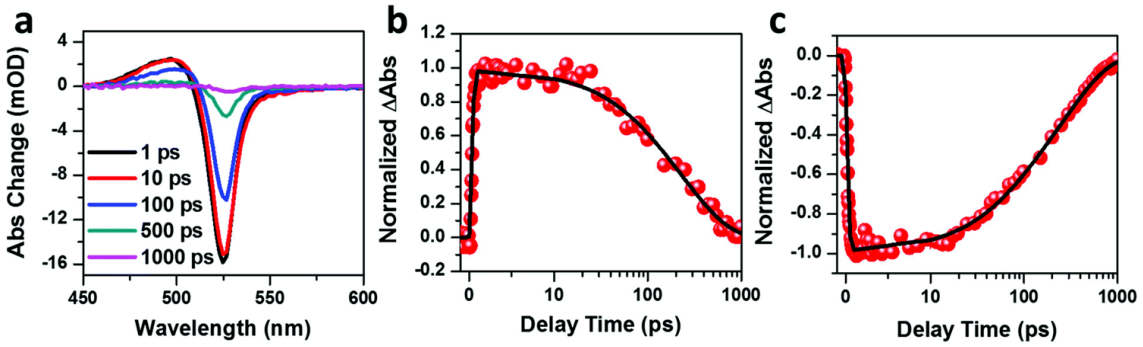

Figure 7.5: (a) Transient absorption spectra at various time delays of a mesoporous TiO_2 film infiltrated with $MAPbBr_3$. Decay kinetics at 490 nm and 530 nm are shown in (b) and (c), respectively, with the experimental data (symbols) fitted with a triexponential decay function (smooth lines). Early time scales are plotted linearly; later time scales (>10 ps) plotted on a base-10 logarithmic scale.

Table 7.1: Amplitudes (A), time constants (τ), and amplitude-weighted lifetimes (τ_{avg}) derived from triexponential fits of the transient absorption for the different samples at the photobleach band located at 530 nm

Sample	τ_R **[ps]**	A_1	τ_1 **[ps]**	A_2	τ_2 **[ps]**	τ_{avg} **[ps]**
$MAPbBr_3$	0.20±0.02	-0.23±0.06	57±16	-0.76±0.06	312±21	253
0.5 *wt.%* Au/Ag	0.09±0.03	-0.29±0.06	39±10	-0.64±0.07	225±20	167
1.0 *wt.%* Au/Ag	0.15±0.01	-0.44±0.01	25±2	-0.55±0.01	168±6	104

ponential function yielding both a fast (τ_1) and a slow (τ_2) decay component as well as an initial rise time (τ_R) related to PIA/PB band formation. The amplitudes (A), time constants (τ), and amplitude-weighted carrier lifetimes derived from the fits are listed in Table 7.1 (530 nm PB dynamics) and Table 7.2 (490 nm PIA dynamics). The bleach formation kinetics in $MAPbBr_3$ result from the relaxation of hot electron-hole pairs from the high excited states to quasi-thermal equilibrium states, which gives rise to state-filling of the conduction band, a phenomenon contributed by longitudinal optical phonon scattering.[51, 52] The decay kinetics result from the relaxation of the conduction band population by recombination and charge transfer to TiO_2. Here τ_1 is attributed to phonon scattering and trap-assisted recombination, and τ_2 is contributed by electron injection into the TiO_2.[8, 51]

To understand the effect of plasmonic nanostructures on the carrier dynamics of $MAPbBr_3$-infiltrated mp-TiO_2 films, the TA evolutionary spectra were recorded with 0.5 *wt.%* and 1.0

wt.% Au/Ag NSs (Figure 7.6a and b). Whereas the peak positions of the PB state of the Au/Ag NS-incorporated samples are comparable to that of the reference (Figure 7.5), the bandwidth of the PB increases with the increasing particle density of NSs. The broadening of the PB state may be attributed to a more rapid band filling in the nanostructure-incorporated films relative to the reference films. Sharma *et al.* observed a similar phenomenon in $MAPbBr_3$ thin films with increasing pump energy fluence as higher carrier densities result in a saturation of conduction band levels near the bandgap.[50] This is also supported in our data from the decreasing maximum bleach amplitude with the increasing particle density (Figure 7.5a and 7.6a,b), as more rapid thermalization would lead to less optimization of energy states. It is also possible, however, that the broadening may be attributed to the formation of trap states. In the TA spectra of perovskites, trap states are characterized by a weak bleach absorption with a broad distribution that decays red-shifted, or below the energy, of the optical band gap of the perovskite.[53] These traps states have longer decay times than the PB state and are populated by the relaxation of hot carriers and can result in the blocking of weakly allowed transitions during excitation.[54] While the weak sub-bandgap bleach of the 1.0 *wt.%* sample identifies some trap-state filling, the peak broadening more strongly indicates an increased rate of electron-phonon coupling. The enhanced PCE of devices (Figure 7.2) at these concentrations supports this hypothesis as the collection of free carriers is enhanced. Trapped excitons have higher exciton binding energies E_B,[54] decreasing the probability of exciton dissociation and increasing the probability of recombination, manifesting as decreased efficiency in the solar cells. Since plasmonic nanoparticles have been reported to lower the E_B (or induce resonant energy transfer to enable exciton dissociation),[30, 31, 32] the observed increases in photocurrent for plasmon-enhanced PSCs likely stem from a combination of electromagnetic effects and reduced E_B.

The recoveries of the PB at 530 nm were normalized and fit with a triexponential decay function for all samples (Figure 7.6d); the amplitudes and lifetimes derived from the fits

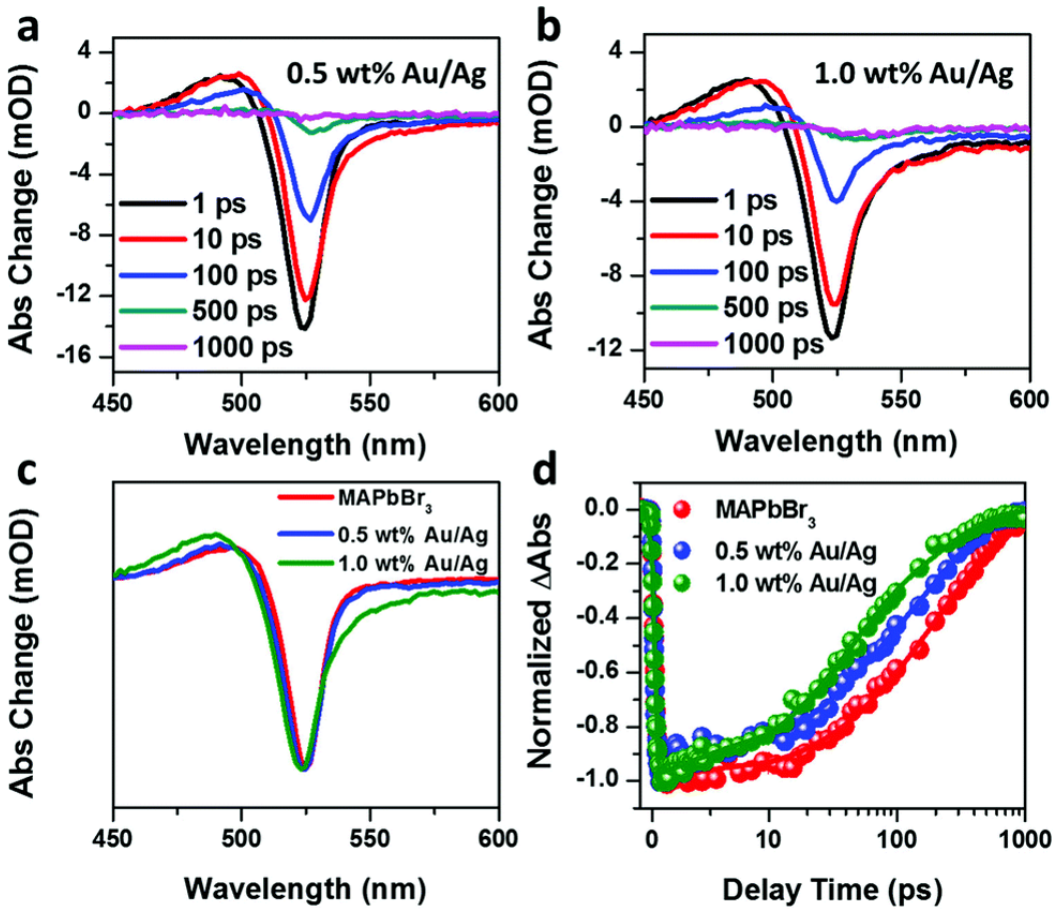

Figure 7.6: Transient absorption spectra at various time delays of mesoporous TiO_2/$MAPbBr_3$ and those containing 0.5 *wt.%* (a) and 1.0 *wt.%* (b) of silica-coated Au/Ag NSs. Normalized TA spectra at the maximum bleach peak ($\sim$1 ps time delay) comparing the reference and the Au/Ag NS-enhanced samples are shown in (c). (d) Decay kinetics at 530 nm for the reference and Au/Ag NS-incorporated samples. Decay kinetics are shown with the experimental data (symbols) fitted with a triexponential decay function (smooth lines). Early time scales are plotted linearly; later time scales ($>$10 ps) plotted on a base-10 logarithmic scale.

Table 7.2: Amplitudes (A), time constants (τ), and amplitude weighted lifetimes (τ_{avg}) derived from biexponential fits of the transient absorption for the different samples at the photoinduced absorption band located at 490 nm.

Sample	A_1	τ_1 **[ps]**	A_2	τ_2 **[ps]**	τ_{avg} **[ps]**
$MAPbBr_3$	0.20	77.20	0.78	294.45	249.25
0.5 *wt*.% Au/Ag/SiO_2	0.28	97.54	0.67	228.02	189.47
1.0 *wt*.% Au/Ag/SiO_2	0.76	75.33	0.23	513.13	176.61

are shown in Table 7.1. The amplitudes and lifetimes derived from fitting of the carrier dynamics at 490 nm are provided in Table 7.2. We first compared the bleach formation time, τ_R, between the reference and the plasmon-enhanced samples, which has been attributed to the thermalization of hot carriers after photoexcitation.[55, 56] During thermalization in $MAPbBr_3$, optical hot phonons are generated by the coupling of phonons with hot electrons that subsequently slows the cooling of carriers and increases the τ_R.[51] In $MAPbI_3$ systems, this phenomenon has been termed the hot phonon bottleneck effect.[57, 58] As seen in Table 7.1, both plasmon-enhanced samples, containing 0.5 and 1.0 *wt*.% silica-coated Au/Ag NSs, exhibit faster thermalization times compared to the reference $MAPbBr_3$. This faster τ_R lifetime likely results from plasmon-phonon coupling between the nanostructures and the perovskite which limits the coupling of phonons with hot electrons and relieves the hot phonon bottleneck. Plasmon-phonon coupling has been studied extensively in various metal-semiconductor systems.[59, 60, 61, 62, 63] In our nanostructure/$MAPbBr_3$ system, relief of this hot phonon bottleneck should also aid in phonon propagation within the active layer, reflected as a decrease in the longer (τ_2) calculated lifetimes (Table 7.1). It is noteworthy that relative to the reference $MAPbBr_3$ (0.2 ps), the τ_R of 0.5 *wt*.% Au/Ag NSs (0.09 ps) is more reduced than that of the τ_R of 1.0 *wt*.% Au/Ag NSs (0.15 ps). This indicates that plasmon-phonon coupling is very sensitive to the nanostructure density; at a 1.0 *wt*.% concentration, the sample may have a higher degree of particle aggregation where interparticle coupling likely supersedes plasmon-phonon coupling and results in less relief of the phonon bottleneck.

The amplitude-weighted lifetimes, τ_{avg}, of the PB recovery kinetics at 530 nm significantly decrease with the increasing particle density, from 253 ps for the reference $MAPbBr_3$ to 167 ps and 104 ps for the 0.5 *wt.%* and 1.0 *wt.%* Au/Ag NSs. A systematic decrease in τ_1 and τ_2 is observed as well. This suggests that the bimetallic nanostructures amplify light trapping in the $MAPbBr_3$ active layer of PSCs, by both near field coupling of the nanostructures with $MAPbBr_3$ as well as far field coupling of scattered light into the active layer.[64, 65, 66, 67, 68] The perovskite crystals are exposed to an increased photon flux generated by the intense near fields localized at the sharp edges and corners of vicinal Au/Ag NSs, giving rise to higher carrier densities. The elevated carrier densities are expected to weaken trap-assisted recombination, specifically when the density of charge carriers far exceeds that of the trap states, resulting in shorter carrier lifetimes.[69] Further the ideal size of these bimetallic nanostructures and the presence of the Ag layer amplify their ability to scatter light, facilitating enhanced light harvesting and the light is reemitted by the $MAPbBr_3$ active layer, which improves the optical path length. The enhanced light trapping, in conjunction with improved phonon propagation from relief of the hot phonon bottleneck *via* plasmon-phonon coupling, enhance the number of free carries generated, which results in more electrons being available to efficiently transfer to the TiO_2 conduction band. This implies that the presence of metal nanostructures leads to faster electron injection into TiO_2, suppressing the recombination in the bulk and resulting in a shorter carrier lifetime as reflected in the TAS results.

To further understand the role of Au/Ag NSs on the carrier dynamics of the $MAPbBr_3$ films, we supplemented our proposed mechanisms by measuring the steady-state PL and trPL of the reference and plasmon-enhanced films. The $MAPbBr_3$ reference films exhibited a narrow photoluminescence peak centered around the bandgap (Figure 7.7a) of $MAPbBr_3$ analogous to that demonstrated in the literature.[70, 71] In the presence of the nanostructures, a significant reduction in the PL intensity is observed; where the PL is quenched by $\sim$32% and $\sim$65% with 0.5 *wt.%* and 1.0 *wt.%* silica-coated Au/Ag NSs, respectively.

Table 7.3: Amplitudes (A), time constants (τ), and amplitude-weighted lifetimes (τ_{avg}) derived from biexponential fits of trPL transients of each sample.

Sample	A_1	τ_1 **[ns]**	A_2	τ_2 **[ns]**	τ_{avg} **[ns]**
$MAPbBr_3$	0.57±0.01	1.18±0.02	0.4±0.01	5.25±0.05	2.84
0.5 *wt.*% Au/Ag	0.49±0.00	0.31±0.01	0.64±0.00	2.05±0.01	1.30
1.0 *wt.*% Au/Ag	0.77±0.04	0.21±0.01	0.27±0.03	0.79±0.2	0.36

This quenching in steady-state PL indicates that non-radiative decay pathways are favored with the increasing nanostructure density, which decreases exciton decay by recombination and suppression of PL.[33, 72] Our result suggests that the presence of the nanostructures promotes more efficient charge carrier extraction at $MAPbBr_3$ and mp-TiO_2 interfaces, attributable to the intense electric fields generated by the nanostructures.[29, 73] Furthermore, the enhanced non-radiative decay pathways in the presence of the nanostructures also facilitate below band gap energy transfer into the nearby semiconductor, specifically plasmon resonant energy transfer (PRET). PRET, which has been extensively studied in a range of solar energy conversion systems,[19] occurs when the energy localized in plasmon oscillations around the nanostructure is transferred to surrounding semiconductor and induces charge separation and carrier generation.[19, 74, 75] PRET does not involve direct electron injection into the semiconductor and is not limited by band alignment or the presence of thin insulating interlayers; therefore the quenching in steady-state PL may reflect resonant energy transfer from the dipole-dipole relaxation of excited plasmons in the nanostructures into both the mp-$TiO_2$and $MAPbBr_3$ crystals. In addition to PRET, hot electron transfer (HET) is another non-radiative enhancement mechanism that occurs when plasmons decay *via* energetic relaxation and create hot electron/hole pairs.[76, 77] These hot electrons can gain enough energy to overcome the Schottky barrier at metal/semiconductor interfaces and inject directly into the semiconductor conduction band.[19] However, we do not anticipate any HET in our system due to the presence of $\sim$5 nm silica insulating layer coating the nanostructures (Figure 7.1c); since the electron tunneling barrier of silica is $<$3 nm,[78, 79, 80] this will prohibit HET from the nanostructures to the perovskite.

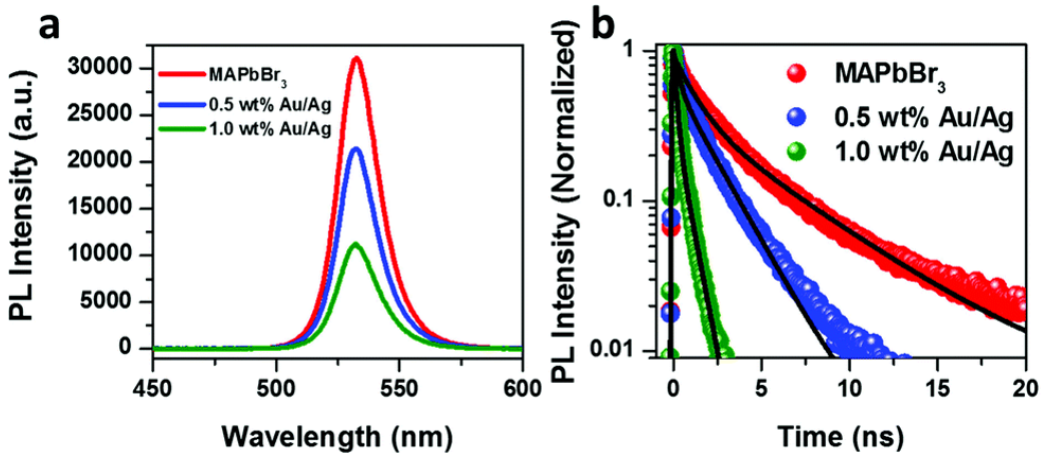

Figure 7.7: (a) Steady-state photoluminescence spectra of mesoporous TiO_2 films infiltrated with $MAPbBr_3$ and different concentrations of silica-coated Au/Ag NSs. (b) The corresponding photoluminescence decay plots of the same samples with 400 nm excitation. Experimental data in (b) are denoted by symbols and have been fitted with a biexponential decay function (black lines).

The trends in steady-state PL follow the PL decay observed with room temperature trPL measurements of the reference $MAPbBr_3$ and nanostructure-incorporated films (Figure 7.7b). Carrier lifetimes, shown in Table 7.3, were obtained by fitting the experimental data with a biexponential decay function. The average PL lifetime, τ_{avg}, of the reference films decreased from 2.84 ns to 1.3 ns for the 0.5 *wt.%* Au/Ag NSs and 0.36 ns for the 1.0 *wt.%* Au/Ag. The reduced PL lifetimes correspond well with the quenching in steady-state PL of $MAPbBr_3$ in the presence of bimetallic nanostructures, which supports our earlier hypothesis of rapid charge transfer and reduced recombination at the plasmon/perovskite interface, enhancing carrier extraction from the $MAPbBr_3$ to TiO_2. Furthermore, plasmonic nanostructures also decrease the exciton binding energy (E_B) of perovskites; in our system the reduced E_B of $MAPbBr_3$ by bimetallic nanostructures would also manifest as suppressed PL if charge transfer is promoted into the mp-TiO_2 prior to exciton recombination in the bulk. While the exact mechanism that decreases the E_B of perovskites in the presence of plasmonic nanostructures is not fully understood, it opens up an exciting avenue for $MAPbBr_3$-based devices, whose enhanced environmental stability relative to

$MAPbI_3$ is offset in part by its higher E_B. Overall, quenching of the steady-state PL and decreases in trPL carrier lifetimes translate well to the increased efficiencies observed for the nanostructure-incorporated PSCs (Figure 7.2 and 7.4).[44]

7.4 Conclusions

In summary, we boosted the efficiency of $MAPbBr_3$-based PSCs by incorporating silica-coated Au/Ag bimetallic nanostructures into the mesoporous TiO_2 active layer. The increased light harvesting in the devices as determined by absorbance and IPCE measurements in conjunction with improvements in J_{sc}, V_{oc}, and FF for plasmon-enhanced samples demonstrate strong coupling between Au/Ag NSs and the $MAPbBr_3$-inflitrated TiO_2 active layer. Our results indicate enhanced carrier generation with decreased recombination in the perovskite in the presence of the nanostructures. The decreased carrier lifetimes obtained from both TAS and trPL measurements and the quenching observed in ssPL further support our hypothesis. Lifetimes obtained from photobleach formation and recovery in transient absorption spectra suggest that the presence of the nanostructures coupled with the $MAPbBr_3$ improves the hot carrier thermalization to an equilibrium distribution *via* plasmon-phonon coupling. Decreases in lifetimes correlating with electron injection suggest that the presence of Au/Ag NS enhances photoinduced carrier generation as a result of both strong near field and far field coupling of light, promoting efficient electron injection into TiO_2prior to bulk recombination. Quenching of steady state PL and decreases in carrier lifetimes obtained from trPL, attributed in part to PRET effects and reduction in E_B, provide further evidence to the improved carrier injection in plasmon-enhanced mesoporous perovskites. We envision that these bimetallic nanostructures can be straightforwardly translated to other perovskite systems to enhance the efficiencies not only of solar devices, but also of photodetectors and lasers.

7.5 Methods

All reagents were purchased from Sigma Aldrich unless otherwise specified and were used as received without further purification. All the H_2O used for substrate preparation and nanostructure synthesis was ultrapure H_2O (18.2 MΩ) obtained from a Milli-Q Direct-Q 3UV system. All work done under an inert atmosphere was conducted in a nitrogen filled MBraun LabStar glovebox (<0.5 ppm O_2).

Au/Ag Nanostructure Synthesis: Au/Ag nanostructures were synthesized following a procedure described in our previous work.[42] Au nanocube cores were prepared following a seed-mediated growth method in which Au seeds were formed by adding 600 μL of ice cold, freshly prepared 10 mM $NaBH_4$ to a solution containing 7.5 mL of 100 mM CTAB, 2.75 mL H_2O, and 0.8 mL of 10 mM $HAuCl_4$. The solution was stirred vigorously for 1 minute before being transferred to a 35 °C water bath where it was left to stay for one hour. The seeds were then diluted by a factor of 10 with water before being added to a growth solution composed of 6.4 mL of 100 mM CTAB, 0.8 mL of 10 mM $HAuCl_4$, and 3.8 mL of 100 mM ascorbic acid that were added sequentially to 32 mL of ultrapure H_2O. Post-Au seed addition, the mixture was mixed by gentle inversion, and then left to react undisturbed for 5 hours in a 35 °C water bath. A ligand exchange was performed on the Au NC cores before Ag layer growth was performed: Au NCs were centrifuged at 1100 RCF for 15 minutes in 7.5 mL aliquots, the supernatant was removed, and the particles were washed and soaked in 3.75 mL of 20 mM CTAC for 15 minutes. This was repeated for a total of 3 spins and two 15 minute soaks. The final CTAC-capped Au NC pellet was redispersed in 500 μL of water to make the final precursor solution for Au growth. Typically, 400 μL of the Au NC precursor was added to 10 mL of 20 mM CTAC along with 100 μL of 10 mM KBr. This was mixed by inversion and heated in a 65 °C water bath for 10 minutes before adding into 100 μL of 10 mM $AgNO_3$ and 300 μL of 100 mM ascorbic acid, mixing again by inversion, and placing it back in the 65 °C water bath for two hours.

Silica-Coating of Au/Ag Nanostructures: Au/Ag NSs were capped with a thin $\sim$4 nm

layer of silica by modifying a previously described procedure.[81] In a 50 mL round bottom flask, 30 mL of as-prepared Au/Ag NSs were first functionalized with 400 μL of a freshly prepared 1 mM 3-aminopropyltrimethoxysilane (APTMS) solution for 15 minutes at room temperature while stirring at $\sim$500 RPM. A 0.54 *wt.%* solution of sodium silicate was adjusted to pH $\sim$10.2 with 5 N HCl followed by injecting 500 μL into the APTMS-functionalized Au nanocubes. The reaction mixture was stirred for 3 minutes at room temperature and then transferred to a 50 °C oil bath and stirred for 4.5 hours to form the uniform silica shell. The reaction was quenched by placing the coated nanostructures in the fridge overnight. The particles were then centrifuged at 900 RCF ($\times$2) and washed once with water prior to imaging and device incorporation.

Perovskite Layer Fabrication: $MAPbBr_3$-sensitized layers were deposited on either glass for TAS and PL testing or FTO-glass for full device characterization, including JV and IPCE testing. Glass and FTO-glass substrates were cleaned by sonication for 30 min in a 2 *vol.%* solution of Hellmanex in H_2O, rinsed first with H_2O and then IPA, and then sonicated for an additional 15 minutes in a 1 : 1 v/v mixture of IPA/acetone. The substrates were then rinsed with IPA, dried with N_2, and plasma treated for 15 minutes immediately before use. A $\sim$50 nm layer of compact TiO_2 was deposited on the substrates by hydrolyzing 40 mM $TiCl_4$ at 70 °C. The substrates were removed from the $TiCl_4$ bath after one hour, rinsed with H_2O and EtOH, dried with N_2, and then annealed at 500 °C for 15 minutes. Mesoporous TiO_2 was deposited by spin coating a diluted solution of 18NRT Dyesol paste (1 : 2 : 1 by weight of EtOH : α -terpineol : Dyesol) at 2500 RPM for 60 seconds, dried on a 100 °C hot plate, and then sintered at 500 °C for 30 minutes. Plasmon-enhanced samples were prepared in the same manner; however, washed and concentrated pellets of silica-coated Au/Ag NSs were added directly to the diluted Dyesol paste to the desired concentrations and mixed until homogeneous before spin coating. All mesoporous layers received a 40 mM $TiCl_4$ post-treatment at 70 °C for 30 minutes, were rinsed with H_2O and EtOH, dried with N_2, and fired in air at 500 °C for 15 minutes. At this point, all meso-

porous TiO_2 substrates were transferred into an inert environment. $MAPbBr_3$ films were then prepared following a modified two-step sequential deposition process.[39] First, a 1 M solution of $PbBr_2$ in DMF was stirred on a 75 °C hot plate for 20 minutes and filtered with a 0.45 μm PTFE filter immediately before use. TiO_2 substrates were heated to 75 °C prior to spin-coating 200 μL of the filtered $PbBr_2$ solution at 2500 RPM for 60 seconds followed by a 30 minute annealing at 75 °C. Once cooled post-annealing, the substrates were dipped in IPA for 1-2 s before being placed in a heated (50 °C) solution consisting of 15 mg/mL MABr (Dyesol) in IPA for 10 minutes, rinsed with IPA, and annealed again at 75 °C for 30 minutes.

PSC Fabrication: Full devices were fabricated on FTO-sensitized substrates following a typical fabrication process.[82] An HTM was prepared by the addition of 72.3 mg of SpiroMeOTAD (2,2',7,7'-tetrakis(*N,N*-di-*p*-methoxyphenyl amine)-9,9'-spirobifluorene, EMD), 29 μL of 4-*tert*-butylpyridine, 18 μL of a 520 mg/mL LiTFSI (lithium bis(trifluoromethylsulphonyl)imide) in acetonitrile solution, and 29 μL of a 300 mg/mL tris(2-(1*H*-pyrazol-1-yl)-4-*tert*-butyl-pyridine)cobalt(III) bis(trifluoromethylsulphonyl)imide (Lumtec) in acetonitrile solution to 1 mL chlorobenzene.[82] 100 μL of the HTM solution was then deposited on top of $MAPbBr_3$-sensitized TiO_2 films at 3000 RPM for 30 s. The samples were left overnight in darkness and dry air before 80 nm Au contacts were deposited *via* thermal evaporation in 8 mm diameter circles utilizing shadow masks in an Angstrom Amod system.

Materials Characterization: All optical absorbance spectra were taken using a Varian Cary 5000 UV-vis NIR spectrophotometer. Scanning and transmission electron microscopy were conducted with a Zeiss Merlin and an FEI Tecnai Osiris, respectively. Characterization of power conversion performance of full device PSCs was conducted with a Newport solar simulator and a Metrohm potentiostat. Each cell received 1 sun (100 mW/cm^2) of power from the solar simulator at AM 1.5 over equivalent areas of 0.081 cm^2 and was tested at a scan rate of 50 mV/s. An average of 10 devices were tested for each sample

type. Incident photon conversion efficiency (IPCE) measurements were conducted with a 6 W Fianium fiber laser supercontinuum source coupled with a Fianium acousto-optic tunable filter to filter out the desired excitation wavelength from the white light source.

Transient Absorption Measurements: Femtosecond transient absorption measurements were conducted using a home-built pump-probe setup based on a femtosecond laser system that utilizes seed pulses from a titanium sapphire oscillator (Micra, Coherent), amplified by a Ti:Sapphire amplifier (Legend USP-HE, Coherent) to provide 800 nm femtosecond pulses (2.5 mJ per pulse) operating at a 1 kHz repetition rate with $\sim$45 fs pulse durations. The Legend amplifier is pumped by using a Nd:YLF laser (Evolution-30, Coherent). A small portion of the output of the amplifier ($\sim$4 μJ per pulse) is focused on a sapphire window (2 mm thick) to generate a white light continuum (WLC) probe (450-900 nm). To minimize temporal chirp in the spectrally broad WLC probe, a set of parabolic mirrors was used to collimate and focus the WLC on the sample. The transmitted probe was focused onto 100 μm core fiber coupled with a spectrometer/CCD (USB2000ES, Ocean Optics). The pump pulse at 400 nm is generated by doubling $\sim$50 μJ per pulse of the 800 nm fundamental in a BBO crystal. The pump beam passes through a delay-line to allow control of time-delay between the pump and the probe. In order to measure the absorbance changes between every two successive laser shots, the pump beam was chopped at a frequency of 500 Hz. At the sample, the spot sizes of the pump and probe pulses were 100 μm and 50 μm, respectively. The pump energy fluence at the sample was $\sim$5 μJ/cm^2.

Photoluminescence Measurements: The photoluminescence (PL) spectra were recorded using a spectrometer (Acton SP2300) equipped with a CCD (Princeton Instruments, Pixis 256), which was coupled to a microscope. The time-resolved PL spectra were recorded by using a time correlated single photon counting (TCSPC) module (Horiba Scientific with Picosecond Photon Detection Module, PPD-850 and Fluorohub model: Horiba JY IBH). The PPD-850 was mounted to a second port of the same spectrometer. $MAPbBr_3$-sensitized TiO_2 films, with and without Au/Ag NSs, were excited at 400 nm using a second harmonic

signal of a Ti:sapphire laser (Coherent, Mira 900, 5 ps pulse length, 76 MHz repetition rate). To match TCSPC requirements, the laser repetition rate was reduced to $\sim$5 kHz using a pulse picker (Coherent). The output from the pulse picker was frequency doubled using an ultrafast harmonic generator (Coherent 5-050) and directed into a microscope to illuminate the films through a 100$\times$ microscope objective (beam spot size $\sim$1 μm). All films were initially exposed to 400 nm light for $\sim$20 min in order to stabilize the samples.

7.6 Bibliography

[1] Martin A. Green, Keith Emery, Yoshihiro Hishikawa, Wilhelm Warta, and Ewan D. Dunlop. Solar cell efficiency tables (version 47). *Prog. Photov.*, 24(1):3–11, 2016.

[2] Akihiro Kojima, Kenjiro Teshima, Yasuo Shirai, and Tsutomu Miyasaka. Organometal halide perovskites as visible-light sensitizers for photovoltaic cells. *J. Am. Chem. Soc.*, 131(17):6050–6051, 2009.

[3] Michael M. Lee, Joel Teuscher, Tsutomu Miyasaka, Takurou N. Murakami, and Henry J. Snaith. Efficient hybrid solar cells based on meso-superstructured organometal halide perovskites. *Science*, 338(6107):643–647, 2012.

[4] Hui-Seon Kim, Chang-Ryul Lee, Jeong-Hyeok Im, Ki-Beom Lee, Thomas Moehl, Arianna Marchioro, Soo-Jin Moon, Robin Humphry-Baker, Jun-Ho Yum, Jacques E. Moser, Michael Graetzel, and Nam-Gyu Park. Lead iodide perovskite sensitized all-solid-state submicron thin film mesoscopic solar cell with efficiency exceeding 9%. *Sci. Rep.*, 2:00591, 2012.

[5] Chuantian Zuo, Henk J. Bolink, Hongwei Han, Jinsong Huang, David Cahen, and Liming Ding. Advances in perovskite solar cells. *Adv. Sci.*, 3(7):1500324, 2016.

[6] Yu Tong, Eva Bladt, Meltem F. Aygueler, Aurora Manzi, Karolina Z. Milowska, Verena A. Hintermayr, Pablo Docampo, Sara Bals, Alexander S. Urban, Lakshminarayana Polavarapu, and Jochen Feldmann. Highly luminescent cesium lead halide perovskite nanocrystals with tunable composition and thickness by ultrasonication. *Angew. Chem. Int. Ed.*, 55(44):13887–13892, 2016.

[7] Samuel D. Stranks, Giles E. Eperon, Giulia Grancini, Christopher Menelaou, Marcelo J. P. Alcocer, Tomas Leijtens, Laura M. Herz, Annamaria Petrozza, and Henry J. Snaith. Electron-hole diffusion lengths exceeding 1 micrometer in an organometal trihalide perovskite absorber. *Science*, 342(6156):341–344, 2013.

[8] Guichuan Xing, Nripan Mathews, Shuangyong Sun, Swee Sien Lim, Yeng Ming Lam, Michael Graetzel, Subodh Mhaisalkar, and Tze Chien Sum. Long-range balanced electron- and hole-transport lengths in organic-inorganic CH3NH3PbI3. *Science*, 342(6156):344–347, 2013.

[9] Yu Han, Steffen Meyer, Yasmina Dkhissi, Karl Weber, Jennifer M. Pringle, Udo Bach, Leone Spiccia, and Yi-Bing Cheng. Degradation observations of encapsulated planar CH3NH3PbI3 perovskite solar cells at high temperatures and humidity. *J. Mater. Chem. A*, 3(15):8139–8147, 2015.

[10] Jinli Yang, Braden D. Siempelkamp, Dianyi Liu, and Timothy L. Kelly. Investigation of CH3NH3PbI3 degradation rates and mechanisms in controlled humidity environments using in situ techniques. *ACS Nano*, 9(2):1955–1963, 2015.

[11] Jun Hong Noh, Sang Hyuk Im, Jin Hyuck Heo, Tarak N. Mandal, and Sang Il Seok. Chemical management for colorful, efficient, and stable inorganic-organic hybrid nanostructured solar cells. *Nano Lett.*, 13(4):1764–1769, 2013.

[12] Xiaojia Zheng, Bo Chen, Congcong Wu, and Shashank Priya. Room temperature fabrication of CH3NH3PbBr3 by anti-solvent assisted crystallization approach for perovskite solar cells with fast response and small J-V hysteresis. *Nano Energy*, 17:269–278, 2015.

[13] Chuantian Zuo and Liming Ding. Modified pedot layer makes a 1.52 V V_{oc} for perovskite/PCBM solar cells. *Adv. Energy Mater.*, 7(2):1601193, 2017.

[14] Nir Kedem, Thomas M. Brenner, Michael Kulbak, Norbert Schaefer, Sergiu Levcenko, Igal Levine, Daniel Abou-Ras, Gary Hodes, and David Cahen. Light-induced increase of electron diffusion length in a p-n junction type CH3NH3PbBr3 perovskite solar cell. *J. Phys. Chem. Lett.*, 6(13):2469–2476, 2015.

[15] Rui Sheng, Anita Ho-Baillie, Shujuan Huang, Sheng Chen, Xiaoming Wen, Xiaojing Hao, and Martin A. Green. Methylammonium lead bromide perovskite-based solar cells by vapor-assisted deposition. *J. Phys. Chem. C*, 119(7):3545–3549, 2015.

[16] Eric M. Talbert, Holly F. Zarick, Noah J. Orfield, Wei Li, William R. Erwin, Zachary R. DeBra, Kemar R. Reid, Christopher P. McDonald, James R. McBride, Jason Valentine, Sandra J. Rosenthal, and Rizia Bardhan. Interplay of structural and compositional effects on carrier recombination in mixed-halide perovskites. *RSC Adv.*, 6(90):86947–86954, 2016.

[17] Eran Edri, Saar Kirmayer, David Cahen, and Gary Hodes. High open-circuit voltage solar cells based on organic-inorganic lead bromide perovskite. *J. Phys. Chem. Lett.*, 4(6):897–902, 2013.

[18] Jin Hyuck Heo, Dae Ho Song, and Sang Hyuk Im. Planar CH3NH3PbBr3 hybrid solar cells with 10.4% power conversion efficiency, fabricated by controlled crystallization in the spin-coating process. *Adv. Mater.*, 26(48):8179–8183, 2014.

[19] William R. Erwin, Holly F. Zarick, Eric M. Talbert, and Rizia Bardhan. Light trapping in mesoporous solar cells with plasmonic nanostructures. *Energy Environ. Sci.*, 9(5):1577–1601, 2016.

[20] Joseph A. Webb, William R. Erwin, Holly F. Zarick, Jayde Aufrecht, Harris W. Manning, Matthew J. Lang, Cary L. Pint, and Rizia Bardhan. Geometry-dependent plasmonic tunability and photothermal characteristics of multibranched gold nanoantennas. *J. Phys. Chem. C*, 118(7):3696–3707, 2014.

[21] Fang-Chung Chen, Jyh-Lih Wu, Chia-Ling Lee, Yi Hong, Chun-Hong Kuo, and Michael H. Huang. Plasmonic-enhanced polymer photovoltaic devices incorporating solution-processable metal nanoparticles. *Appl. Phys. Lett.*, 95(1):013305, 2009.

[22] Abhishek P. Kulkarni, Kevin M. Noone, Keiko Munechika, Samuel R. Guyer, and David S. Ginger. Plasmon-enhanced charge carrier generation in organic photovoltaic films using silver nanoprisms. *Nano Lett.*, 10(4):1501–1505, 2010.

[23] William R. Erwin, Chanse Hungerford, Holly F. Zarick, Eric M. Talbert, Poorva Arora, and Rizia Bardhan. Enhancement in organic photovoltaics controlled by the interplay between charge-transfer excitons and surface plasmons. *ACS Omega*, 1(4):722–729, 2016.

[24] Holly F. Zarick, William R. Erwin, Abdelaziz Boulesbaa, Olivia K. Hurd, Joseph A. Webb, Alexander A. Puretzky, David B. Geohegan, and Rizia Bardhan. Improving light harvesting in dye-sensitized solar cells using hybrid bimetallic nanostructures. *ACS Photonics*, 3(3):385–394, 2016.

[25] Holly F. Zarick, Olivia Hurd, Joseph A. Webb, Chanse Hungerford, William R. Erwin, and Rizia Bardhan. Enhanced efficiency in dye-sensitized solar cells with shape-controlled plasmonic nanostructures. *ACS Photonics*, 1(9):806–811, 2014.

[26] Jifa Qi, Xiangnan Dang, Paula T. Hammond, and Angela M. Belcher. Highly efficient plasmon-enhanced dye-sensitized solar cells through metal@oxide core-shell nanostructure. *ACS Nano*, 5(9):7108–7116, 2011.

[27] Michael D. Brown, Teeraporn Suteewong, R. Sai Santosh Kumar, Valerio D'Innocenzo, Annamaria Petrozza, Michael M. Lee, Ulrich Wiesner, and Henry J. Snaith. Plasmonic dye-sensitized solar cells using core-shell metal-insulator nanoparticles. *Nano Lett.*, 11(2):438–445, 2011.

[28] Shuai Chang, Quan Li, Xudong Xiao, King Young Wong, and Tao Chen. Enhancement of low energy sunlight harvesting in dye-sensitized solar cells using plasmonic gold nanorods. *Energy Environ. Sci.*, 5(11):9444–9448, 2012.

[29] Zelin Lu, Xujie Pan, Yingzhuang Ma, Yu Li, Lingling Zheng, Danfei Zhang, Qi Xu, Zhijian Chen, Shufeng Wang, Bo Qu, Fang Liu, Yidong Huang, Lixin Xiao, and Qihuang Gong. Plasmonic-enhanced perovskite solar cells using alloy popcorn nanoparticles. *RSC Adv.*, 5(15):11175–11179, 2015.

[30] Wei Zhang, Michael Saliba, Samuel D. Stranks, Yao Sun, Xian Shi, Ulrich Wiesner, and Henry J. Snaith. Enhancement of perovskite-based solar cells employing core-shell metal nanoparticles. *Nano Lett.*, 13(9):4505–4510, 2013.

[31] Haejun Yu, Jongmin Roh, Juyoung Yun, and Jyongsik Jang. Synergistic effects of three-dimensional orchid-like TiO_2 nanowire networks and plasmonic nanoparticles for highly efficient mesoscopic perovskite solar cells. *J. Mater. Chem. A*, 4(19):7322–7329, 2016.

[32] S. Carretero-Palacios, M. E. Calvo, and H. Miguez. Absorption enhancement in organic-inorganic halide perovskite films with embedded plasmonic gold nanoparticles. *J. Phys. Chem. C*, 119(32):18635–18640, 2015.

[33] Michael Saliba, Wei Zhang, Victor M. Burlakov, Samuel D. Stranks, Yao Sun, James M. Ball, Michael B. Johnston, Alain Goriely, Ulrich Wiesner, and Henry J. Snaith. Plasmonic-induced photon recycling in metal halide perovskite solar cells. *Adv. Funct. Mater.*, 25(31):5038–5046, 2015.

[34] Wendy Niu, Lindsey A. Ibbotson, David Leipold, Erich Runge, G. Vijaya Prakash, and Jeremy J. Baumberg. Image excitons and plasmon-exciton strong coupling in two-dimensional perovskite semiconductors. *Phys. Rev. B*, 91(16):161303, 2015.

[35] C. Burda, X. B. Chen, R. Narayanan, and M. A. El-Sayed. Chemistry and properties of nanocrystals of different shapes. *Chem. Rev.*, 105(4):1025–1102, 2005.

[36] K. L. Kelly, E. Coronado, L. L. Zhao, and G. C. Schatz. The optical properties of

metal nanoparticles: The influence of size, shape, and dielectric environment. *J. Phys. Chem. B*, 107(3):668–677, 2003.

[37] Jon A. Schuller, Edward S. Barnard, Wenshan Cai, Young Chul Jun, Justin S. White, and Mark L. Brongersma. Plasmonics for extreme light concentration and manipulation. *Nat. Mater.*, 9(3):193–204, 2010.

[38] S. Link and M. A. El-Sayed. Shape and size dependence of radiative, non-radiative and photothermal properties of gold nanocrystals. *Int. Rev. Phys. Chem.*, 19(3):409–453, 2000.

[39] Michael Kulbak, David Cahen, and Gary Hodes. How important is the organic part of lead halide perovskite photovoltaic cells? efficient $CsPbBr_3$ cells. *J. Phys. Chem. Lett.*, 6(13):2452–2456, 2015.

[40] Chih-Chun Chung, Chang Soo Lee, Efat Jokar, Jong Hak Kim, and Eric Wei-Guang Diau. Well-organized mesoporous TiO_2 photoanode by using amphiphilic graft copolymer for efficient perovskite solar cells. *J. Phys. Chem. C*, 120(18):9619–9627, 2016.

[41] Teddy Salim, Shuangyong Sun, Yuichiro Abe, Anurag Krishna, Andrew C. Grimsdale, and Yeng Ming Lam. Perovskite-based solar cells: impact of morphology and device architecture on device performance. *J. Mater. Chem. A*, 3(17):8943–8969, 2015.

[42] Holly F. Zarick, William R. Erwin, Jayde Aufrecht, Andrew Coppola, Bridget R. Rogers, Cary L. Pint, and Rizia Bardhan. Morphological modulation of bimetallic nanostructures for accelerated catalysis. *J. Mater. Chem. A*, 2(19):7088–7098, 2014.

[43] S. Carretero-Palacios, A. Jimenez-Solano, and H. Miguez. Plasmonic nanoparticles as light-harvesting enhancers in perovskite solar cells: A user's guide. *ACS Energy Lett.*, 1(1):323–331, 2016.

[44] Jin Cui, Cheng Chen, Junbo Han, Kun Cao, Wenjun Zhang, Yan Shen, and Mingkui Wang. Surface plasmon resonance effect in inverted perovskite solar cells. *Adv. Sci.*, 3(3):1500312, 2016.

[45] Boyuan Cai, Yong Peng, Yi-Bing Cheng, and Min Gu. 4-fold photocurrent enhancement in ultrathin nanoplasmonic perovskite solar cells. *Opt. Express*, 23(24):A1700–A1706, 2015.

[46] Sawanta S. Mali, Chang Su Shim, Hyungjin Kim, Pramod S. Patil, and Chang Kook Hong. In situ processed gold nanoparticle-embedded TiO_2 nanofibers enabling plasmonic perovskite solar cells to exceed 14% conversion efficiency. *Nanoscale*, 8(5):2664–2677, 2016.

[47] Runsheng Wu, Bingchu Yang, Chujun Zhang, Yulan Huang, Yanxia Cui, Peng Liu, Conghua Zhou, Yuying Hao, Yongli Gao, and Junliang Yang. Prominent efficiency enhancement in perovskite solar cells employing silica-coated gold nanorods. *J. Phys. Chem. C*, 120(13):6996–7004, 2016.

[48] Yaxin Zhai, Chuan Xiang Sheng, Chuang Zhang, and Zeev Valy Vardeny. Ultrafast spectroscopy of photoexcitations in organometal trihalide perovskites. *Adv. Funct. Mater.*, 26(10):1617–1627, 2016.

[49] Tze Chien Sum, Nripan Mathews, Guichuan Xing, Swee Sien Lim, Wee Kiang Chong, David Giovanni, and Herlina Arianita Dewi. Spectral features and charge dynamics of lead halide perovskites: Origins and interpretations. *Acc. Chem. Res.*, 49(2):294–302, 2016.

[50] Vinay Sharma, Sigalit Aharon, Itay Gdor, Chunfan Yang, Lioz Etgar, and Sanford Ruhman. New insights into exciton binding and relaxation from high time resolution ultrafast spectroscopy of CH(3)NH(3)Pbl(3) and CH3NH3PbBr3 films. *J. Mater. Chem. A*, 4(9):3546–3553, 2016.

[51] Xiaofan Deng, Xiaoming Wen, Shujuan Huang, Rui Sheng, Takaaki Harada, Tak W. Kee, Martin Green, and Anita Ho-Baillie. Ultrafast carrier dynamics in methylammonium lead bromide perovskite. *J. Phys. Chem. C*, 120(5):2542–2547, 2016.

[52] Lili Wang, Christopher McCleese, Anton Kovalsky, Yixin Zhao, and Clemens Burda. Femtosecond time-resolved transient absorption spectroscopy of CH3NH3PbI3 perovskite films: Evidence for passivation effect of PbI_2. *J. Am. Chem. Soc.*, 136(35):12205–12208, 2014.

[53] Jr. Ponseca, Carlito S., Yuxi Tian, Villy Sundstrom, and Ivan G. Scheblykin. Excited state and charge-carrier dynamics in perovskite solar cell materials. *Nanotechnology*, 27(8):082001, 2016.

[54] Xiaoxi Wu, M. Tuan Trinh, Daniel Niesner, Haiming Zhu, Zachariah Norman, Jonathan S. Owen, Omer Yaffe, Bryan J. Kudisch, and X. Y. Zhu. Trap states in lead iodide perovskites. *J. Am. Chem. Soc.*, 137(5):2089–2096, 2015.

[55] Hung-Yu Hsu, Chi-Yung Wang, Amir Fathi, Jia-Wei Shiu, Chih-Chun Chung, Po-Shen Shen, Tzung-Fang Guo, Peter Chen, Yuan-Pern Lee, and Eric Wei-Guang Diau. Femtosecond excitonic relaxation dynamics of perovskite on mesoporous films of Al_2O_3 and NiO nanoparticles. *Angew. Chem. Int. Ed.*, 53(35):9339–9342, 2014.

[56] Tze Chien Sum and Nripan Mathews. Advancements in perovskite solar cells: photophysics behind the photovoltaics. *Energy Environ. Sci.*, 7(8):2518–2534, 2014.

[57] Michael B. Price, Justinas Butkus, Tom C. Jellicoe, Aditya Sadhanala, Anouk Briane, Jonathan E. Halpert, Katharina Broch, Justin M. Hodgkiss, Richard H. Friend, and Felix Deschler. Hot-carrier cooling and photoinduced refractive index changes in organic-inorganic lead halide perovskites. *Nature Commun.*, 6:8420, 2015.

[58] Ye Yang, David P. Ostrowski, Ryan M. France, Kai Zhu, Jao van de Lagemaat,

Joseph M. Luther, and Matthew C. Beard. Observation of a hot-phonon bottleneck in lead-iodide perovskites. *Nat. Photon.*, 10(1):53–59, 2016.

[59] S. Dassarma, J. K. Jain, and R. Jalabert. Theory of hot-electron energy-loss in polar semiconductors - role of plasmon-phonon coupling. *Phys. Rev. B*, 37(11):6290–6296, 1988.

[60] E. H. Hwang, Rajdeep Sensarma, and S. Das Sarma. Plasmon-phonon coupling in graphene. *Phys. Rev. B*, 82(19):195406, 2010.

[61] A. A. Kukharskii. Plasmon-phonon coupling in GaAs. *Solid State Commun.*, 13(11):1761–1765, 1973.

[62] Weiwei Zhao, Qisheng Wu, Qi Hao, Jinlan Wang, Mei Li, Yan Zhang, Kedong Bi, Yunfei Chen, and Zhenhua Ni. Plasmon-phonon coupling in monolayer WS_2. *Appl. Phys. Lett.*, 108(13):131903, 2016.

[63] Xiaolong Zhu, Weihua Wang, Wei Yan, Martin B. Larsen, Peter Boggild, Thomas Garm Pedersen, Sanshui Xiao, Jian Zi, and N. Asger Mortensen. Plasmon-phonon coupling in large-area graphene dot and antidot arrays fabricated by nanosphere lithography. *Nano Lett.*, 14(5):2907–2913, 2014.

[64] Kyeong-Seok Lee and Mostafa A. El-Sayed. Gold and silver nanoparticles in sensing and imaging: Sensitivity of plasmon response to size, shape, and metal composition. *J. Phys. Chem. B*, 110(39):19220–19225, 2006.

[65] N. K. Grady, N. J. Halas, and P. Nordlander. Influence of dielectric function properties on the optical response of plasmon resonant metallic nanoparticles. *Chem. Phys. Lett.*, 399(1-3):167–171, 2004.

[66] P. B. Johnson and R. W. Christy. Optical constants of noble metals. *Phys. Rev. B*, 6(12):4370–4379, 1972.

[67] Kathryn M. Mayer and Jason H. Hafner. Localized surface plasmon resonance sensors. *Chem. Rev.*, 111(6):3828–3857, 2011.

[68] J. M. Pitarke, V. M. Silkin, E. V. Chulkov, and P. M. Echenique. Theory of surface plasmons and surface-plasmon polaritons. *Rep. Prog. Phys.*, 70(1):1–87, 2007.

[69] Zhen-Yu Zhang, Hai-Yu Wang, Yan-Xia Zhang, Ya-Wei Hao, Chun Sun, Yu Zhang, Bing-Rong Gao, Qi-Dai Chen, and Hong-Bo Sun. The role of trap-assisted recombination in luminescent properties of organometal halide CH3NH3PbBr3 perovskite films and quantum dots. *Sci. Rep.*, 6:27286, 2016.

[70] Dong Shi, Valerio Adinolfi, Riccardo Comin, Mingjian Yuan, Erkki Alarousu, Andrei Buin, Yin Chen, Sjoerd Hoogland, Alexander Rothenberger, Khabiboulakh Katsiev, Yaroslav Losovyj, Xin Zhang, Peter A. Dowben, Omar F. Mohammed, Edward H. Sargent, and Osman M. Bakr. Low trap-state density and long carrier diffusion in organolead trihalide perovskite single crystals. *Science*, 347(6221):519–522, 2015.

[71] Verena A. Hintermayr, Alexander F. Richter, Florian Ehrat, Markus Doeblinger, Willem Vanderlinden, Jasmina A. Sichert, Yu Tong, Lakshminarayana Polavarapu, Jochen Feldmann, and Alexander S. Urban. Tuning the optical properties of perovskite nanoplatelets through composition and thickness by ligand-assisted exfoliation. *Adv. Mater.*, 28(43):9478–9485, 2016.

[72] Jun Dai, Hongge Zheng, Can Zhu, Junfeng Lu, and Chunxiang Xu. Comparative investigation on temperature-dependent photoluminescence of CH3NH3PbBr3 and CH(NH2)(2)PbBr3 microstructures. *J. Mater. Chem. C*, 4(20):4408–4413, 2016.

[73] Zhen Li, Pablo P. Boix, Guichuan Xing, Kunwu Fu, Sneha A. Kulkarni, Sudip K. Batabyal, Wenjing Xu, Anyuan Cao, Tze Chien Sum, Nripan Mathews, and Lydia Helena Wong. Carbon nanotubes as an efficient hole collector for high voltage

methylammonium lead bromide perovskite solar cells. *Nanoscale*, 8(12):6352–6360, 2016.

[74] Jiangtian Li, Scott K. Cushing, Fanke Meng, Tess R. Senty, Alan D. Bristow, and Nianqiang Wu. Plasmon-induced resonance energy transfer for solar energy conversion. *Nat. Photon.*, 9(9):601–607, 2015.

[75] Fan Nan, Si-Jing Ding, Liang Ma, Zi-Qiang Cheng, Yu-Ting Zhong, Ya-Fang Zhang, Yun-Hang Qiu, Xiaoguang Li, Li Zhou, and Qu-Quan Wang. Plasmon resonance energy transfer and plexcitonic solar cell. *Nanoscale*, 8(32):15071–15078, 2016.

[76] Fatih B. Atar, Enes Battal, Levent E. Aygun, Bihter Daglar, Mehmet Bayindir, and Ali K. Okyay. Plasmonically enhanced hot electron based photovoltaic device. *Opt. Express*, 21(6):7196–7201, 2013.

[77] Cesar Clavero. Plasmon-induced hot-electron generation at nanoparticle/metal-oxide interfaces for photovoltaic and photocatalytic devices. *Nat. Photon.*, 8(2):95–103, 2014.

[78] B. E. Deal, E. H. Snow, and C. A. Mead. Barrier energies in metal-silicon dioxide-silicon structures. *J. Phys. Chem. Solids*, 27(11-1):1873–1879, 1966.

[79] Chu-Hsuan Lin and Chee Wee Liu. Metal-insulator-semiconductor photodetectors. *Sensors*, 10(10):8797–8826, 2010.

[80] Z. A. Weinberg and A. Hartstein. Photon assisted tunneling from aluminum into silicon dioxide. *Solid State Commun.*, 20(3):179–182, 1976.

[81] William R. Erwin, Andrew Coppola, Holly F. Zarick, Poorva Arora, Kevin J. Miller, and Rizia Bardhan. Plasmon enhanced water splitting mediated by hybrid bimetallic Au-Ag core-shell nanostructures. *Nanoscale*, 6(21):12626–12634, 2014.

[82] Julian Burschka, Norman Pellet, Soo-Jin Moon, Robin Humphry-Baker, Peng Gao, Mohammad K. Nazeeruddin, and Michael Graetzel. Sequential deposition as a route to high-performance perovskite-sensitized solar cells. *Nature*, 499(7458):316–319, 2013.

CHAPTER 8

BROMINE SUBSTITUTION IMPROVES EXCITED-STATE DYNAMICS IN MESOPOROUS MIXED HALIDE PEROVSKITE FILMS

Adapted from E. M. Talbert,*H. F. Zarick,* A. Boulesbaa, N. Soetan, A. A. Puretzky, D. B. Geohegan, and R. Bardhan, *Nanoscale*, **2017**, *x*, xxx with permission from the Royal Society of Chemistry.

8.1 Summary

In this chapter, we explore improvements in carrier dynamics and stability in mesoporous organometal halide perovskite solar cells beyond efficiency improvement via plasmonics. Ultrafast transient absorption spectroscopy (TAS) is utilized to examine the excited-state dynamics in methylammonium lead iodide/bromide ($MAPb(I_{1-x}Br_x)_3$) perovskites as a function of bromide content. TAS spectral behavior reveals characteristic lifetimes for thermalization, recombination, and charge carrier injection of $MAPb(I_{1-x}Br_x)_3$ from x = 0 to 0.3 infiltrated in mesoporous titania films. Carrier recombination and charge injection lifetimes demonstrated a discernable increase with Br content likely because high carrier populations are supported by the higher density of vacant electronic states in mixed-halide perovskites due to the increased capacity of the conduction band. However, we observe for the first time that carrier thermalization lifetimes significantly decrease with increasing Br, similar to the results obtained in the previous chapter where thermalization lifetimes decreased with the presence of plasmonic nanostructures. This suggests that the shift in crystal structure from tetragonal towards pseudocubic accelerates carrier cooling, resulting in the relief of the hot phonon bottleneck. Furthermore, the stabilized $MAPb(I_{1-x}Br_x)_3$ samples exhibit a lower Burstein-Moss shift of 0.07-0.08 eV compared to pure $MAPbI_3$ (0.12 eV). Our results provide evidence that Br inclusion contributes to a broadening of the

parabolic conduction band and to improvement in electron-phonon coupling and phonon propagation in the lattice.

8.2 Introduction

Photovoltaic devices designed with organic-inorganic halide perovskites have recently attained power conversion efficiencies (PCEs) reaching 22%,[1, 2, 3] demonstrating the promise of these low-cost materials for commercial viability and application in utility scale power. In this family of materials, methylammonium lead triiodide ($MAPbI_3$) perovskites have shown extraordinary performance due to their long range ambipolar diffusion lengths, large absorption coefficients, low exciton binding energies, and favorable band energetics.[4, 5, 6] However, the rapid degradation of $MAPbI_3$ in ambient air and moisture has resulted in poor long-term stability and undesirable hysteresis.[7, 8] Several approaches have been adopted to surmount the stability issues, including device encapsulation with hydrophobic polymers and inorganic oxides[9, 10] as well as engineering the charge transport layers to be water-resistant.[11, 12] Alternatively, controllable substitution of $MAPbI_3$ perovskite with Br ions not only provides a straightforward and effective route to improve their moisture stability, but also enables tunable optical band gaps with minimal impact on the overall light absorption that can be controlled by Br ionic content.[13] The enhanced stability of mixed halide $MAPb(I_{1-x}Br_x)_3$ perovskites results from the smaller ionic radius of Br ions that shifts the lattice structure from tetragonal to pseudocubic and reduces the lattice parameter, restricting the diffusion of water into methylammonium vacancies.[14] The inclusion of Br ions has also shown to promote linear charge transport, giving rise to increased exciton diffusion lengths as well as reduced carrier recombination.[15, 16, 17] Relative to their pure iodide counterparts, the increased band gap of $MAPb(I_{1-x}Br_x)_3$perovskites also results in higher open circuit voltages in the range of 1-1.5 V.[18, 19] Therefore, by controllably infusing Br into the triiodide perovskite, moisture stability can be improved while preserving high photovoltaic performance.[20]

Recent work on mixed halide perovskites has focused on their synthesis and measurements of crystallization kinetics,[21, 22] band gap engineering of their optical properties,[23] increasing their environmental stability,[20, 24, 25] and correlating their structural and luminescent properties.[26, 27, 28] Despite this extensive work, the impact of halide composition on carrier thermalization and transport is not fully understood. While time-resolved photoluminescence (tr-PL) spectroscopy has been employed to study these fundamental parameters, tr-PL characterizes emissive states and cannot probe dark (non-emissive) states, which play a critical role in the light absorption properties of perovskites. Further, tr-PL also cannot resolve sub-picosecond carrier processes occurring in perovskites due to detection speed limitations. On the other hand, ultrafast pump-probe transient absorption spectroscopy (TAS) can reveal high resolution spectral and temporal behavior of photogenerated species and resolve the time scales of various excited state processes, and has been utilized to study perovskites extensively.[29, 30, 31, 32] Whereas time-resolved studies of carrier relaxation dynamics in pristine perovskite films (or those paired with a non-interacting scaffold) have already been reported,[32, 33, 34, 35] this study particularly probes mixed halide perovskites infiltrated in mesoporous TiO_2 films. We employed TAS to understand the impact of halide composition on the timescales of carrier thermalization, carrier recombination, and charge injection at the perovskite/TiO_2 interface in MAPb$(I_{1-x}Br_x)_3$perovskite/TiO_2 films. Our motivation to study perovskite/TiO_2 films stems from examining the literature where some of the most promising high efficiency devices are achieved with perovskites infiltrated in mesoporous TiO_2 scaffolds.[36, 37, 38] Therefore, probing the fundamental mechanisms in this system is highly relevant to understanding the driving forces in high performing solar devices. Our TAS results from mesoporous mixed halide perovskites show that carrier cooling and relaxation dynamics within a mesoporous TiO_2 architecture are favorably affected by bromide inclusion. We demonstrate for the first time that the TAS bleach formation kinetics, attributed to hot carrier thermalization, are accelerated with increasing Br content, indicating relief of the hot

phonon bottleneck. Conversely, the bleach relaxation, modeled by two characteristic lifetimes representing Auger recombination and charge injection to TiO_2, slows with increasing Br composition. Finally, the Burstein-Moss shift, which describes energetics within the conduction band and is evaluated from the position of the bleach feature, decreases with the addition of Br as the capacity of the conduction band increases. Our work provides a mechanistic understanding of the carrier accumulation and carrier decay processes in mixed halide perovskites within a mesoporous TiO_2 architecture.

8.3 Results and Discussion

The $MAPb(I_{1-x}Br_x)_3$ perovskite films were synthesized by varying the I/Br ratios in a mixed halide precursor solution (Table 8.1) and infiltrating the perovskites in a 100 nm mesoporous TiO_2 layer with an additional 100 nm perovskite overlayer. The mp-TiO_2 layer provides a scaffold for formation of the perovskite crystals, allows a precise way to control perovskite thickness, and provides an electron acceptor for carrier injection from the perovskites following optical excitation. The I/Br ratio was controlled by the relative concentrations of the MAI/MABr soak solution for PbI_2-infiltrated mp-TiO_2 substrates as detailed in the Experimental Section and Table 8.1, and the exact Br content was further confirmed via XRD and UV-vis absorption measurements. Investigation of Br substitution was capped at x = 0.3, as previous studies have found that any improvements in optoelectronic properties of $MAPb(I_{1-x}Br_x)_3$ are negated past 30% Br inclusion as light absorption decreases sharply.[39, 40] Additionally, in our experiments, we found that with Br compositions higher than x = 0.3, the average grain size increased at the expense of complete coverage and contact with the mp-TiO_2 scaffold. While the thickness of both layers is significantly lower than that used in typical perovskite solar cells,[41, 42] these thicknesses were chosen to achieve relatively consistent optical density (OD $\sim$1.0-1.25 at 400 nm) between samples, providing ample transmittance for TAS measurements even at near-complete perovskite coverage. A representative top-view and cross-sectional view of

Table 8.1: The following amounts of MAI and MABr were added to 7 mL IPA to generate the stochiometric ratios necessary for the desired Br content.

Br Content (x)	**MAI** (mg)	**MABr** (mg)
0	105	0
0.1	84	15
0.2	70	24
0.3	59	33

$MAPbI_3$ perovskite film are shown in Figure 8.1a and 8.1b, respectively. Top-view SEMs of all other Br content samples are shown in Figure 8.2, verifying that grain structure and coverage are sufficiently similar across all Br compositions.

While the grain structure in the different $MAPb(I_{1-x}Br_x)_3$ samples is similar across all Br compositions, the lattice microstructure differs due to the size difference between I and Br ions. As I ions are displaced by smaller Br ions, the lattice parameter decreases as the lattice shifts from a tetragonal structure toward a pseudocubic geometry, evidenced by the (110) peak shift toward 2θ =15°with increasing Br in normalized XRD spectra (Figure 8.1c). The peak shifts align with those observed in literature for $MAPb(I_{1-x}Br_x)_3$,[28, 43] confirming the presence of $MAPb(I_{1-x}Br_x)_3$ at the desired Br compositions. The absence of impurity peaks in full XRD spectra (Figure 8.3) further confirms the purity of the perovskite phase and minimal unreacted PbX_2 present in any sample. Moreover, the average crystallite diameter, calculated from the (110) peak width using the Scherrer equation, is relatively constant for all Br compositions (Figure 8.4). The pure $MAPbI_3$ (0% Br) sample shows slightly elevated microstructure size compared to bromide-containing perovskite films, indicating that there is some compositional heterogeneity within mixed-halide perovskite grains. However, based on the steepness of the absorbance band edge (Figure 8.1d), we conclude that this compositional heterogeneity arises from a natural dispersion of I and Br ions during the two-step perovskite synthesis. In addition to the crystallographic and topographic characterization of the perovskites, we have also probed the optical properties of the mixed-halide perovskite films. Prior to analysis of transient absorption spectra, it

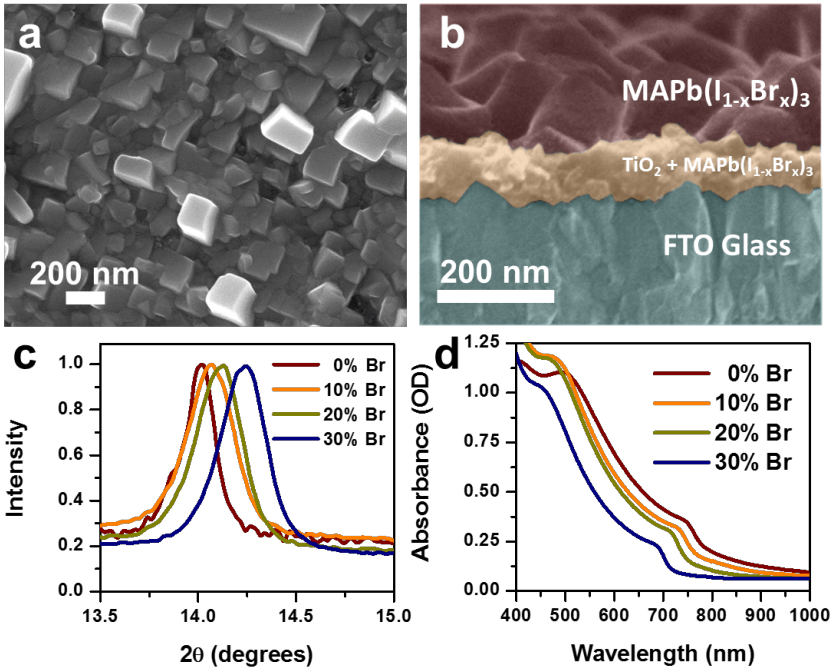

Figure 8.1: Representative top view (a) and cross-sectional (b) SEM of a 100 nm mesoporous-TiO_2 layer infiltrated with $MAPb(I_{1-x}Br_x)_3$. Shown here is x = 0 Br incorporation for both (a) and (b). (c) Glancing angle XRD peaks normalized to the (110) plane for $MAPb(I_{1-x}Br_x)_3$ mesoporous film samples with increasing Br content. (d) Optical absorbance spectra of all four samples.

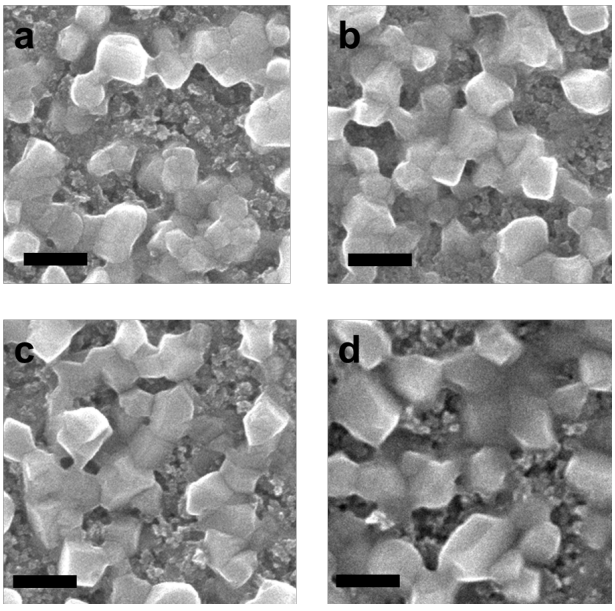

Figure 8.2: SEM micrographs of $MAPb(I_{1-x}Br_x)_3$ show that grain morphology is consistent across Br compositions. Top views of perovskite films deposited with x = 0, 0.1, 0.2, and 0.3 are shown in (a), (b), (c), and (d), respectively. All scale bars are 200 nm.

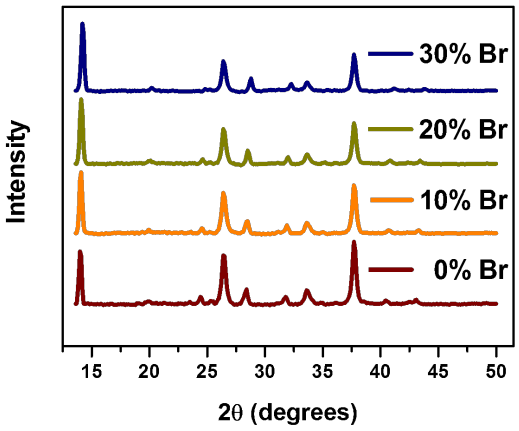

Figure 8.3: Full glancing angle XRD spectra for all samples, depicting the characteristic peaks of $MAPb(I_{1-x}Br_x)_3$ perovskite and anatase TiO_2.

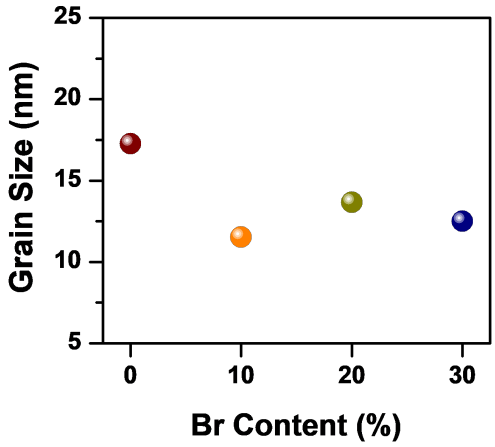

Figure 8.4: Average crystallite diameter calculated from the Scherrer equation. The crystallite diameter is relatively consistent across all Br compositions.

is essential to understand the optical behavior of perovskites, as the excited-state deviations revealed by TAS highlight excitonic features present in the absorbance spectra of the $MAPb(I_{1-x}Br_x)_3$ films. The absorbance spectra shown in Figure 8.1d demonstrate similar optical density for all Br compositions and a predictable blue shift of the absorptive band edge with increasing Br content.[44, 45]

TAS measurements were recorded at a time delay after an excitation pulse saturates the perovskite conduction band, and show the absolute deviation in absorbance from the ground-state absorbance spectra. The TAS spectra for all samples at a time-delay of 3 ps af-

ter excitation is shown in Figure 8.5a when photobleach (PB) and photoinduced absorption (PIA) features are near their maximum. The broad PIA between 500-600 nm represents increased photoexcitation at off-peak wavelengths due to conduction band saturation.[46, 47] The PIA has also recently been linked to refractive index changes induced by the free carrier population, as photoexcited states in all semiconductors result in variations in the dielectric function.[47] There are two distinct photobleaches, PB1 at $\sim$700 nm and PB2 at $\sim$500 nm, which have been described by a dual valence and common conduction band model for $MAPbI_3$. This two valence band model was first proposed by Xing *et al.* as a possible route for the formation of the two photobleach states.[48] These photobleaches represent blocked optical transitions from the two valence bands excited to the conduction band by the pump pulse.[46, 47, 49, 50] The optical transitions behind these features are depicted schematically in Figure 8.5c, where the PB1 band reflects the transition from VB1 to CB, and PB2 reflects the transition from VB2 to CB. The intensity of PB2 has been attributed to both the presence of PbI_2 impurity and to charge injection into TiO_2.[47, 49] Because the PB2 is primarily dependent on impurity presence rather than on bulk phase charge transport, our work focuses on the dynamics of the PB1 photobleach.

Following the ultrafast excitation of perovskites, carrier thermalization results in accumulation of the carrier population at near-band-gap energies (Figure 8.5c). Carriers naturally thermalize to the minimum band energy, which is bounded by a characteristic parabolic band shape, before recombining. However, since the density of states in the conduction band is finite, thermalized carriers adopt a Fermi-Dirac distribution above the parabolic boundary. After the 400 nm pump pulse creates a nonequilibrium distribution of excited electrons in the conduction band, electron-phonon coupling cools the carriers to a stable energy distribution within a couple of picoseconds. This distribution follows the parabolic band shape that is centered slightly above the absorption band edge due to the Burstein-Moss effect. The Burstein-Moss model of electronic band filling takes into account the broadening of the PB1 band, which is indicative of charge carrier accumulation

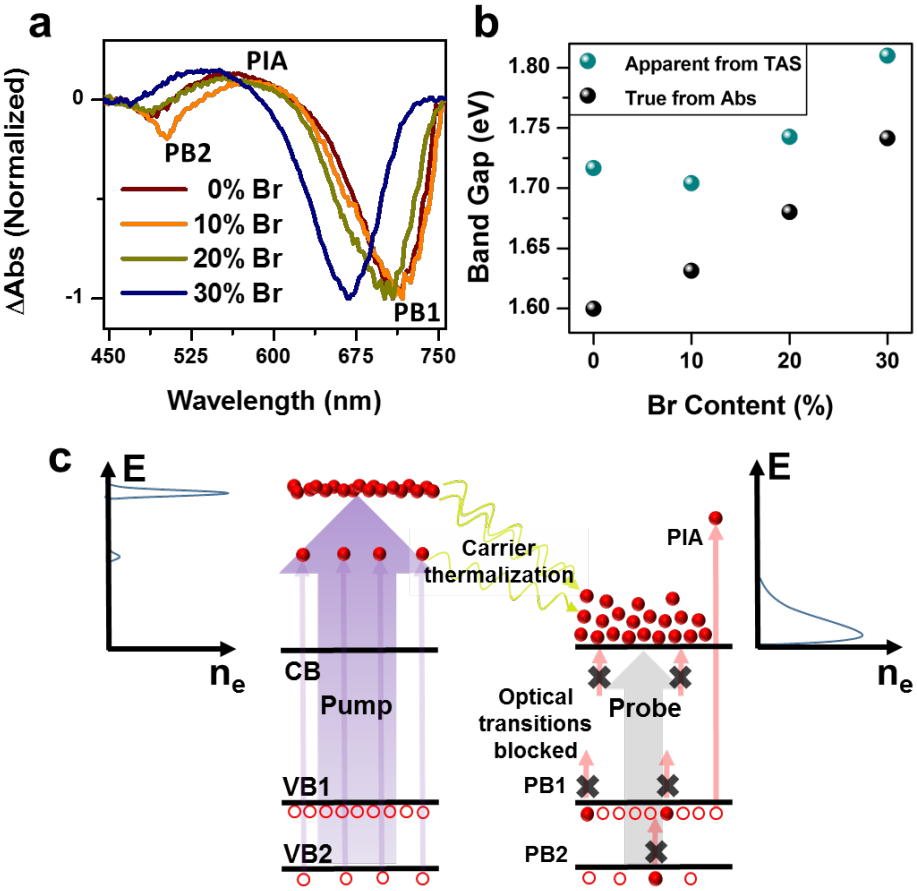

Figure 8.5: (a) Transient absorption spectra for all samples showing two distinct photobleaches near 700 nm and 500 nm corresponding to PB1 and PB2, respectively, and a broadband photoinduced absorption (PIA) in between. Spectra are normalized at the maximum peak of PB1 (∼3 ps time delay). (b) Bandgaps calculated from absorbance band edges and transient absorption evolution of PB1, separated by the Burstein-Moss shift. (c) Energy diagram of excited-state processes initiated in TAS, where n_e is the number of conduction band electrons and E is energy above the bandgap. A 400 nm laser pumps electrons (solid circles) into the conduction band (CB), leaving holes (hollow circles) in the valence bands (VB). Carriers thermalize to a quasi-equilibrium distribution, where the optical transitions of a white-light probe are either bleached (PB) or enhanced (PIA) depending on photon energy.

and correlates the change in optical bandgap to the charge density raised to the power of 2/3.[46, 51] Since excitation into the conduction band is blocked by the equilibrium distribution of filled electronic states, a photobleach is observed in the white-light continuum probe corresponding to the band gap energies with reference to the valence band. The apparent band gap for the blocked optical transitions in TAS is calculated from the centroid of the integrated TAS spectra[46, 47] and compared to the band gap from absorption in Figure 8.5b. The difference between the bandgaps as evaluated from TAS and absorption measurements represents the Burstein-Moss shift. The mixed halide samples (10-30% Br) show a consistent Burstein-Moss shift around 0.07-0.08 eV, but the pure iodide sample has a much higher Burstein-Moss shift of 0.12 eV. Based on the evolutionary spectra of all samples (Figure 8.6-8.9) we do not anticipate that a significant portion of the bleach feature is cut off by the low-pass filter; therefore, the bleach centroid position adequately represents the mean energy of the carrier population for all samples. More importantly, the measured conductivity of pure $MAPbI_3$ perovskite has been reported to be lower than that of bromide-containing perovskites,[26, 52] which suggests that parabolic conduction bands of $MAPbI_3$ have lower density of vacant electronic states available for free carriers. Thus, the energy distribution of fully pumped $MAPbI_3$ samples is shifted higher above the band gap. This is further explained below in the discussion of bleach formation lifetimes, which are markedly longer for the thermalization of carriers in $MAPbI_3$ than in $MAPb(I_{1-x}Br_x)_3$.

Carrier cooling can be tracked by the PB1 formation in TAS, which occurs within the first 2 ps after photoexcitation as shown in Figure 8.10a. The lifetimes for bleach formation, τ_0, are obtained from an exponential fit with positive amplitude, and a standard pulse width of 0.1 ps is fixed to account for the laser attenuation at early times. To understand the impact of the pump power on the thermalization lifetimes of the Br substituted mixed-halide perovskite samples, power dependent measurements were conducted between 20 and 80 μJ/pulse. The thermalization lifetime increases (i.e. the carrier cooling rate decreases) with rising pump fluence for all $MAPb(I_{1-x}Br_x)_3$ samples, as shown in

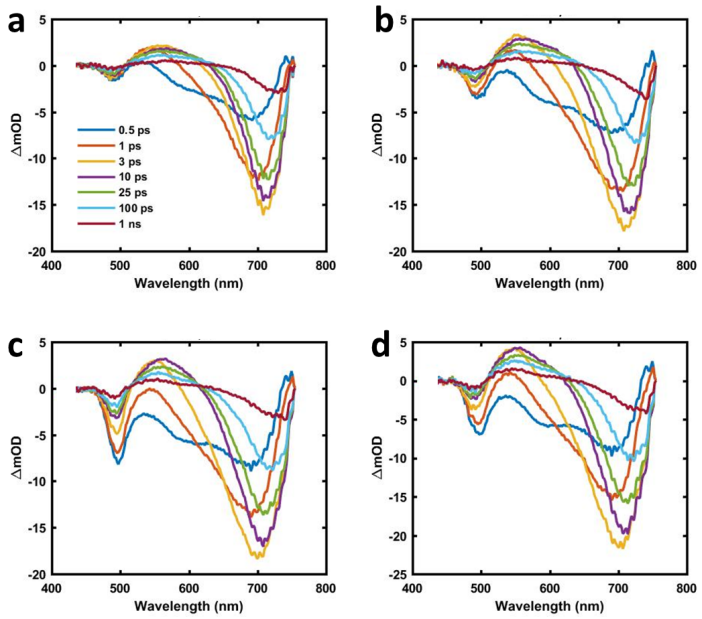

Figure 8.6: Transient absorption spectra at various time delays of a mesoporous TiO_2 film infiltrated with $MAPb(I_{1-x}Br_x)_3$ with x=0 at various excitation fluences, (a) 20 μJ/pulse, (b) 40 μJ/pulse, (c) 60 μJ/pulse, and (d) 80 μJ/pulse.

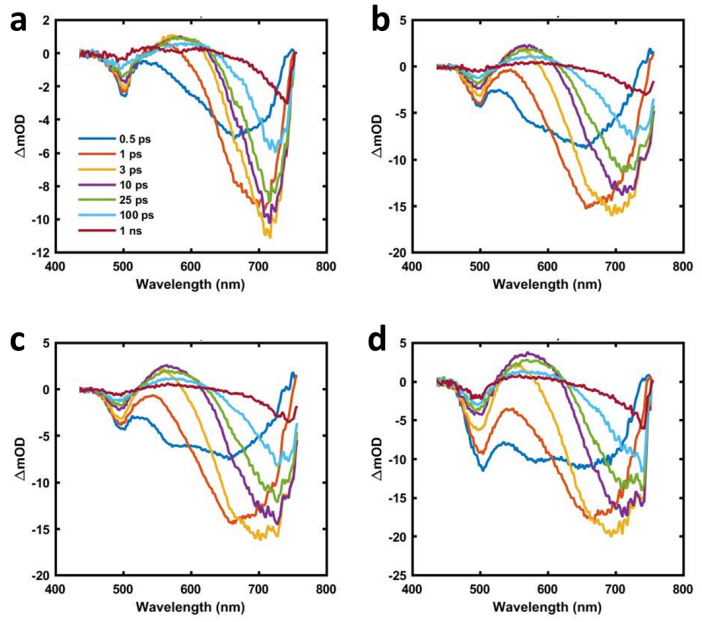

Figure 8.7: Transient absorption spectra at various time delays of a mesoporous TiO_2 film infiltrated with $MAPb(I_{1-x}Br_x)_3$ with x=0.1 at various excitation fluences, (a) 20 μJ/pulse, (b) 40 μJ/pulse, (c) 60 μJ/pulse, and (d) 80 μJ/pulse.

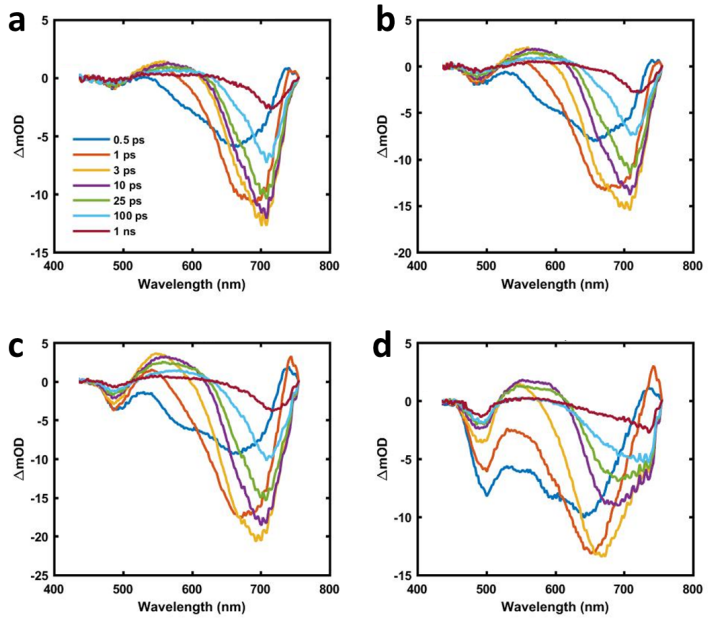

Figure 8.8: Transient absorption spectra at various time delays of a mesoporous TiO_2 film infiltrated with $MAPb(I_{1-x}Br_x)_3$ with x=0.2 at various excitation fluences, (a) 20 μJ/pulse, (b) 40 μJ/pulse, (c) 60 μJ/pulse, and (d) 80 μJ/pulse.

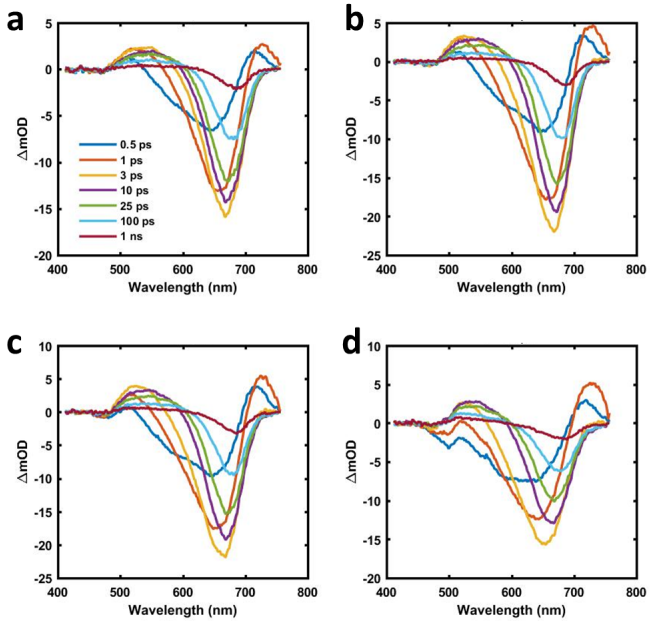

Figure 8.9: Transient absorption spectra at various time delays of a mesoporous TiO_2 film infiltrated with $MAPb(I_{1-x}Br_x)_3$ with x=0.3 at various excitation fluences, (a) 20 μJ/pulse, (b) 40 μJ/pulse, (c) 60 μJ/pulse, and (d) 80 μJ/pulse.

Figure 8.10b. With increasing pump fluence, the number of absorbed photons increases as well, resulting in high occupancy of energy levels nearest the band edge. The abundance of hot carriers, as well as the limit of phonon-electron coupling, inhibits the relaxation of carriers from the initial excited state to the conduction band edge, resulting in an enhanced hot carrier population.[53] This impediment to the carrier cooling in perovskites is a phenomenon described as the hot-phonon bottleneck effect.[54, 55, 56] The clear trends observed in carrier thermalization with pump power indicates that hot phonon bottleneck is observable in the pure iodide and mixed halide perovskite mesoporous films. Whereas phonon bottleneck is strongest in the $MAPbI_3$ sample indicating a long-lived population of hot carriers, with increasing Br substitution in the perovskite lattice the phonon bottleneck effect slightly diminishes. This observation is clearly indicated in Figure 8.10c (also can be found in Table 8.2 for all excitation fluences) showing that carrier thermalization rates become more rapid with increasing bromide composition. Our results therefore suggest that the hot phonon bottleneck is being relieved with bromine substitution, reducing the number of hot carriers with increasing Br content. Cooling of hot carriers in semiconductors dissipates the excess absorbed optical energy as lattice heat, comprising 50% of energy losses in traditional solar devices.[57] Therefore, the faster carrier thermalization in Br-substituted perovskites likely assists with device cooling and improves device longevity. However, in high power optoelectronics such as lasing and photodetection where a high population of hot carriers is useful, the pure iodide perovskite will be more desirable. The trends in Figure 8.10c also illustrate that the most substantial decrease in τ_0 occurs between 0% and 10% Br, which further suggests that even low concentrations of Br improve electron-phonon coupling within the mixed lattice of $MAPb(I_{1-x}Br_x)_3$. The mechanism of this stability arises from the local crystalline geometry around Br ions. Since the $MAPbBr_3$ perovskite adopts a nearly perfect cubic lattice,[58, 59] the Pb centers in the PbX_6 octahedra will align linearly across the Br ions. This localized alignment is expected to promote phonon propagation as well as electron-phonon coupling.[60] As the Br concentration is

Table 8.2: Premature recombination lifetimes (τ_1) and charge injection lifetimes (τ_2) and corresponding amplitudes (A) derived from triexponential fits of transient absorption photobleach recoveries of $MAPb(I_{1-x}Br_x)_3$-infiltrated mesoporous-TiO_2 films as a function of Br content and excitation energy. R squared values to check for goodness of fit are provided as well.

Br Content (%)	**Excitation Energy** ($\mu J/pulse$)	A_1	τ_1 (ps)	A_2	τ_2 (ps)	R^2
0	20	0.52	32.6	0.36	786	0.992
	40	0.58	20.0	0.35	473	0.991
	60	0.56	15.6	0.36	378	0.982
	80	0.63	15.1	0.34	390	0.986
10	20	0.43	17.9	0.39	574	0.984
	40	0.55	12.6	0.36	421	0.987
	60	0.65	15.4	0.37	416	0.994
	80	0.66	13.8	0.36	755	0.992
20	20	0.47	27.4	0.43	536	0.992
	40	0.55	21.4	0.36	457	0.986
	60	0.53	19.2	0.35	415	0.988
	80	0.67	13.5	0.30	372	0.982
30	20	0.51	28.4	0.34	614	0.987
	40	0.54	21.6	0.31	569	0.987
	60	0.56	19.8	0.30	498	0.986
	80	0.61	14.2	0.29	380	0.977

further increased, the electron-phonon coupling improves incrementally as more PbX_6 octahedra are linearly aligned. Beyond improved charge transport,[27, 61] the presence of Br ions in $MAPb(I_{1-x}Br_x)_3$ perovskites modifies the conduction band structure to enable faster carrier thermalization and phonon diffusion.[62, 63]

The PB1 decay was also studied by fitting integrated peaks to two distinct decay exponents, a fast (τ_1) and slow (τ_2) component, from a biexponential fit (Figure 8.11a). Here, τ_1 is attributed to both charge carrier trapping at perovskite grain boundaries or defect sites and Auger recombination. The relatively high pump fluence (60 μJ/pulse) indicates that the carrier density is high enough that Auger recombination likely dominates τ_1. This correlates well to previous findings by Xing *et al.*[48] suggesting the high absorption coefficient and long carrier diffusion lengths in organolead perovskites necessitates the use

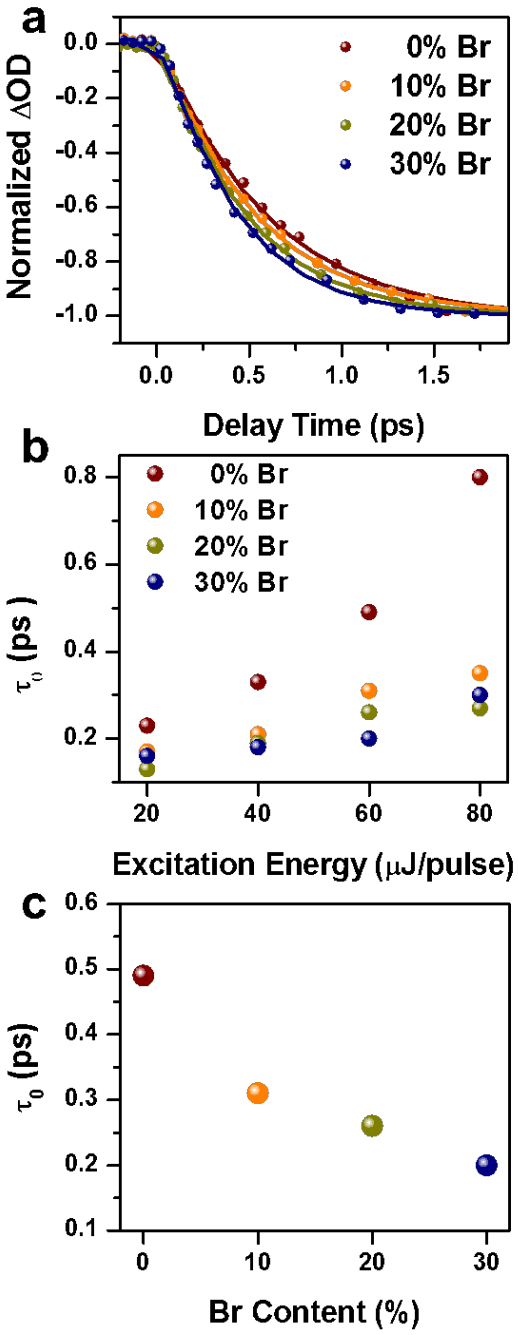

Figure 8.10: (a) Early time scales of TAS dynamics showing bleach formation dynamics of PB1 as a function of Br content. Experimental data (symbols) shown with an exponential fit (smooth lines) as described in the experimental methods. Thermalization lifetimes, τ_0, extracted from exponential fits of the samples are given as a function of excitation fluence in (b) and a function of Br content (c). The excitation fluence for the data shown in (a) and (c) was 60 μJ/pulse.

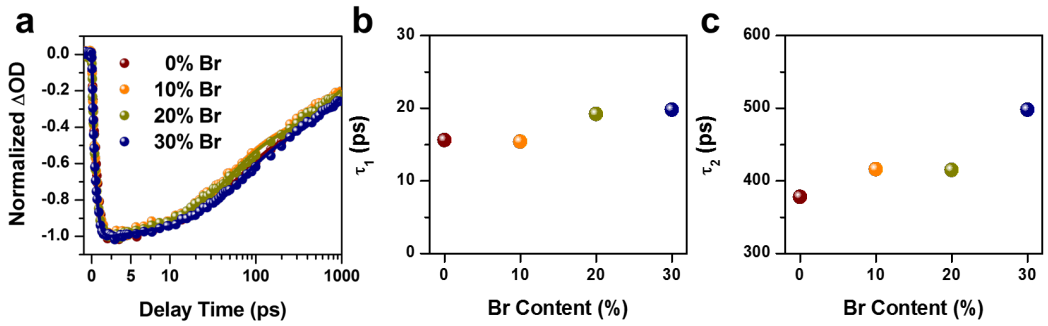

Figure 8.11: (a) Full dynamics of integrated PB1 intensity (symbols) fit with a biexponential decay function (line). (b) Premature recombination lifetimes, τ_1, measured at the pump fluence of 60 μJ/pulse and (c) charge injection lifetimes, τ_2, extracted from the exponential fits suggest that bromide content has a limited effect on recombination mechanisms in thin mesoporous films.

of low pump fluence to minimize energy losses by Auger recombination. Table 8.2 illustrates both a decrease in τ_1 as well as an increase in amplitude (A_1) with increasing pump fluence, indicating increased dominance of Auger recombination over trap-assisted recombination at high laser power.[40, 64, 65] The time constants for carrier recombination shows a small increase for Br>10% (Figure 8.11b). While in thin films of pure MA-Pb halides without a mesoporous scaffold, an increase in Auger recombination rate has been observed in $MAPbBr_3$ attributed to their higher exciton binding energy relative to $MAPbI_3$,[66] we observe only a weak increase in the Auger-dominated τ_1 with increasing Br content in $MAPb(I_{1-x}Br_x)_3/TiO_2$ films within the x = 0 to 0.3 studied here. This observation is expected because high carrier populations are supported by the higher density of vacant electronic states in Br-containing perovskites due to the increased capacity of the conduction band.[26, 52] The slow decay component, τ_2, represents charge injection from the perovskite to the mesoporous TiO_2 substrate that occurs on a time scale of hundreds of picoseconds.[31, 67] We observe a gradual increase in the charge injection time constant with increasing Br content (Figure 8.11c), which is expected due to the marginally close energy alignment between the conduction band of TiO_2 and the pure triiodide perovskite ($\sim$0.1 eV). Park *et al.* have shown that for Br compositions up to 30% the conduction

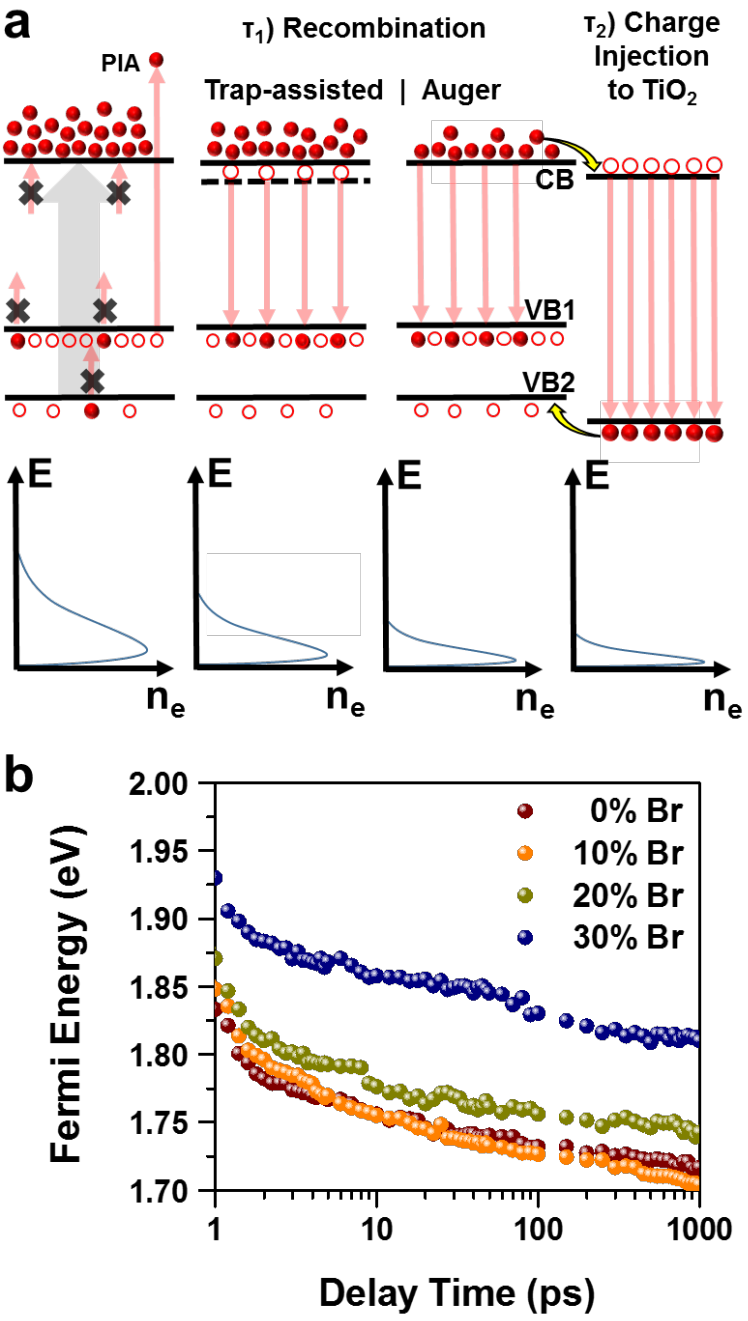

Figure 8.12: (a) Energy diagram illustrating decay processes for photogenerated carriers. Photoexcitation of perovskites pumps electrons from valence bands (VB) into the conduction band (CB). Carriers decay by either injecting into TiO_2 or relaxing via trap-assisted (one-body) or Auger (multi-body) recombination mechanisms. (b) The Fermi energy of excited carriers, calculated from the centroid of integrated PB1 features, decreases as the carrier population relaxes over time.

band increases by ∼0.05 eV; this small increase is likely responsible for delaying charge injection as bromide composition increases.[27] We note that while time-resolved photoluminescence can probe mechanisms that occur at nanosecond timescales, such as recombination within isolated bulk perovskites,[18, 20, 67] the sub-picosecond resolution of TAS is ideal for studying rapid processes, including thermalization and carrier trapping within mesoporous films.

The progression of the carrier recombination processes also impacts the energy distribution of the excited-state carriers,[68] as schematically depicted in Figure 8.12a. Auger and trap-assisted recombination, correlating to time constant τ_1, contribute to about half of the observed excited state decay. The majority of the remaining amplitude decays by the slower time constant, τ_2, represented by carrier injection from the perovskite to TiO_2. The Fermi energy of excited carriers, calculated from the integrated PB1 peak position, is tracked over time in Figure 8.12b to show the regression of mean carrier energy toward the Burstein-Moss limit. The sharp decline in Fermi energy at early timescales is a remnant of carrier thermalization, stabilizing around 3 ps when conduction electrons have relaxed to thermal equilibrium. The Fermi energy then continues to decline gradually as the carrier population is depleted. The slope of the decrease in Fermi energy shows very small variations between samples since τ_1 shows a weak variation across bromide compositions. However, the Fermi energy of pure $MAPbI_3$ approaches an apparent minimum consistent with the hypothesis that narrow-banded $MAPbI_3$ perovskites exhibit a greater Burstein-Moss shift than the mixed-halide $MAPb(I_{1-x}Br_x)_3$ samples.

8.4 Conclusions

In summary, we utilized TAS to probe the excited-state dynamics of $MAPb(I_{1-x}Br_x)_3$ mixed halide perovskites in a thin mp-TiO_2 film geometry. The TAS dynamics were well fit by a multi-exponential fit representing lifetimes for sub-picosecond thermalization, picosecond carrier trapping and recombination, and sub-nanosecond charge injection

to TiO_2, respectively. The measurements reveal that both Auger-dominated carrier recombination and charge injection lifetimes show weak increase with rising bromide compositions between 0-30%. However, carrier thermalization rapidly improves by substituting Br in $MAPbI_3$, which we conclude enhances the electron-phonon coupling in the perovskite lattice. The observed faster carrier thermalization in Br-containing perovskite samples is attributable to relief of the hot-phonon bottleneck and to the broadening of the parabolic conduction band with Br inclusion. This indicates that as low as 10% Br substitution in $MAPbI_3$ perovskites not only increases the stability of conduction band to energetic perturbations but also promotes efficient heat dissipation from the active layer with minimal impact on light absorption.[62] The fundamental insight gained from this work will not only enhance the understanding of the ultrafast carrier processes in organic-inorganic perovskites, but can also be applied to more complex systems such as such as interfaces of perovskites with other semiconductors or metal nanostructures.[69, 70]

8.5 Methods

All reagents, unless otherwise specified, were purchased from Sigma Aldrich and used as received without further purification. All H_2O used for substrate preparation was ultrapure H_2O (18.2 MΩ) obtained from a Milli-Q Direct-Q 3UV system. All work done under inert atmosphere was conducted in an MBraun LabStar glovebox filled with nitrogen ($<$0.5 ppm O_2).

Precursor Synthesis: Methylammonium bromide (MABr) and methylammonium iodide (MAI) were synthesized according to previously reported procedures.[71, 72] Separately, 32.3 mL of hydroiodic acid (37 *wt.*% in H_2O) was combined with 30 mL of methylamine (40% in methanol, TCI) and 44 mL of hydrobromic acid was combined with 27.8 mL of methylamine to produce MAI and MABr, respectively. Both were reacted at 0 °C for two hours under stirring using an ice bath. After two hours, the solutions were evaporated at 55 °C using a rotovap. The precipitates were each washed at least 3$\times$ with diethyl ether

and then collected using vacuum filtration. Finally, the crystals were dried in a vacuum oven at 60 °C for 24 hours before use.

Perovskite Layer Fabrication: Mesoporous-TiO_2 layers infiltrated with $MAPb(I_{1-x}Br_x)_3$ were fabricated on either 1 squares of Pilkington TEC 15 FTO glass for imaging characterizations or microscope glass for optoelectronic and XRD characterizations. Glass and FTO-glass substrates were cleaned by sonication for 30 min in a 2 *vol.%* solution of Hellmanex in H_2O, rinsed with H_2O and IPA, sonicated for an additional 15 minutes in a 1:1 v/v mixture of IPA/acetone, rinsed with IPA, dried with N_2, and finally plasma treated for 15 minutes immediately before use. A $\sim$50 nm layer of compact TiO_2 was deposited on the substrates by hydrolyzing 40 mM $TiCl_4$ at 70 °C for 60 minutes. After substrates were removed from the $TiCl_4$ bath, they were rinsed with H_2O and EtOH, dried with N_2, and then annealed at 100 °C for 10 minutes and 500 °C for 15 minutes. A $\sim$100 nm mesoporous TiO_2 layer was deposited by spin coating 250 μL of a diluted 18NRT Dyesol paste solution (3:6:1 by weight of EtOH:α- terpineol:Dyesol) at 500 RPM for 5 s and 6000 RPM for 40 seconds, dried on a 100 °C hot plate, and then sintered at 500 °C for 30 minutes. Once cooled, the mesoporous layers received a 40 mM $TiCl_4$ post-treatment for 30 minutes at 70 °C, were rinsed with H_2O and EtOH, dried with N_2, and fired in air at 500 °C for 15 minutes. $MAPb(I_{1-x}Br_x)_3$was deposited on the mesoporous scaffold by modifying a two-step sequential deposition process previously described.[73] Substrates were transferred into an inert atmosphere environment. A 100 mg/mL solution of PbI_2 in N,N-dimethylformamide was stirred vigorously for 1 hour at 70 °C to dissolve before use. 200 μL was deposited onto each substrate and left to sit for $\sim$5 s to ensure that the solution was infiltrated throughout the full thickness of the mp-TiO_2 before spin coating at 500 RPM for 5 s and 6000 RPM for 40 s, followed by a 30 minute annealing at 70 °C. Once cooled post-annealing, substrates were dipped in IPA for 1-2 s before being placed in a bath containing the appropriate stoichiometric ratios of MAI and MABr in IPA, each on the range of $\sim$15 mg/mL, for 1 minute with swirling, rinsed thoroughly with IPA, and annealed again at 75

°C for 30 minutes.

Materials Characterization: All optical absorbance spectra were taken using a Varian Cary 5000 UV-vis NIR spectrophotometer. Bandgaps were estimated using Tauc plots, extrapolating the tangent to the steepest point of the absorbance band edge to where it crosses the baseline absorbance level and using the following relation: $E_g = hc/\lambda_{Tauc}$. Scanning electron micrographs were taken with a Zeiss Merlin at 10 kV accelerating voltage. Glancing angle X-ray diffraction spectra were obtained with a Scintag XGEN4000 x-ray diffractometer with CuK_α at wavelength λ = 0.154 nm, and analysis is focused on the 2θ = 15°peak because of its indication of offset from cubic crystallinity. Grain size was estimated using the Scherrer equation with K = 1:

$$d = \frac{K\lambda}{FWHM * cos\theta} \tag{1}$$

Transient Absorption Measurements: Femtosecond transient absorption measurements were conducted using a home-built pump-probe setup based on a femtosecond laser system, that utilizes seed pulses from a titanium sapphire oscillator (Micra, Coherent), amplified by a Ti:Sapphire amplifier (Legend USP-HE, Coherent) to provide 800 nm femtosecond pulses (2.5 mJ/pulse), operating at 1 kHz repetition rate with ∼45 fs pulse durations. The Legend amplifier is pumped by a Nd:YLF laser (Evolution-30, Coherent). A small portion of the output of the amplifier (∼4 μJ/pulse) is focused on a sapphire window (2 mm thick) to generate a white light continuum (WLC) probe (450-900 nm). To minimize temporal chirp in the spectrally broad WLC probe, a set of parabolic mirrors was used to collimate and focus the WLC on the sample. The transmitted probe was focused onto 100 μm core fiber coupled with a spectrometer/CCD (USB2000ES, Ocean Optics). The pump pulse at 400 nm is generated by doubling ∼50 μJ/pulse of the 800 nm fundamental in a BBO crystal. The pump beam passes through a delay-line to allow control of time-delay between the pump and the probe. In order to measure absorbance changes between every two successive laser shots, the pump beam was chopped at a frequency of 500 Hz. At the sample, the

spot sizes of the pump and probe pulses were 100 μm and 50 μm, respectively. The pulse energy of the pump was varied between 20, 40, 60, and 80 μJ/pulse using a variable neutral density filter, corresponding to energy fluences at the sample of $\sim$28.4, 56.8, 85.2, and 113.6 μJ/cm^2. Amplitudes and lifetimes were extracted by fitting the integrated PB1 peak intensity to a convolution of the excitation Gaussian pulse to the following multiexponential function which contains a positive exponential component for extracting bleach formation, and two negative components to describe the bleach recovery:

$$\Delta OD = A_0 e^{-t/\tau_0} - A_1 e^{-t/\tau_1} - A_2 e^{-t/\tau_2} \tag{2}$$

To account for temporal chirp, the absolute times of measurement data were adjusted by wavelength based on the earliest observed response time. Peaks were integrated from the time-adjusted data set, and the normalized peak areas were fit over time to obtain kinetic parameters. The centroid of the peak areas was tracked as the Fermi energy of conduction band electrons. Residuals were calculated to check for goodness of fit; corresponding R-squared values can be found in Table 8.2. All R-squared values are in the range of $\sim$0.98 and above, which shows good reliability.

8.6 Bibliography

[1] Nam-Gyu Park, Michael Grtzel, Tsutomu Miyasaka, Kai Zhu, and Keith Emery. Towards stable and commercially available perovskite solar cells. *Nat. Energy*, 1:16152, 2016.

[2] Lahoucine Atourki, Erika Vega, Bernab Mar, Miguel Mollar, Hassan Ait Ahsaine, Khalid Bouabid, and Ahmed Ihlal. Role of the chemical substitution on the structural and luminescence properties of the mixed halide perovskite thin $MAPbI_{3-x}Br_x$ ($0 \leq x \geq 1$) films. *Appl. Surf. Sci.*, 371:112–117, 2016.

[3] Martin A. Green, Keith Emery, Yoshihiro Hishikawa, Wilhelm Warta, and Ewan D. Dunlop. Solar cell efficiency tables (version 48). *Prog. Photovoltaics*, 24:905–913, 2016.

[4] Luis M. Pazos-Outn, Monika Szumilo, Robin Lamboll, Johannes M. Richter, Micaela Crespo-Quesada, Mojtaba Abdi-Jalebi, Harry J. Beeson, Milan Vruini, Mejd Alsari, Henry J. Snaith, Bruno Ehrler, Richard H. Friend, and Felix Deschler. Photon recycling in lead iodide perovskite solar cells. *Science*, 351:1430–1433, 2016.

[5] Tomas Leijtens, Giles E. Eperon, Alex J. Barker, Giulia Grancini, Wei Zhang, James M. Ball, Ajay Ram Srimath Kandada, Henry J. Snaith, and Annamaria Petrozza. Carrier trapping and recombination: The role of defect physics in enhancing the open circuit voltage of metal halide perovskite solar cells. *Energy Environ. Sci.*, 9:3472–3481, 2016.

[6] S. Kazim, M. K. Nazeeruddin, M. Gratzel, and S. Ahmad. Perovskite as light harvester: A game changer in photovoltaics. *Angew. Chem. Int. Ed.*, 53:2812–2824, 2014.

[7] Daniel Bryant, Nicholas Aristidou, Sebastian Pont, Irene Sanchez-Molina, Thana Chotchunangatchaval, Scot Wheeler, James R. Durrantab, and Saif A. Haque. Light

and oxygen induced degradation limits the operational stability of methylammonium lead triiodide perovskite solar cells. *Energy Environ. Sci.*, 9:1655–1660, 2016.

[8] Yaoguang Rong, Linfeng Liu, Anyi Mei, Xiong Li, and Hongwei Han. Beyond efficiency: the challenge of stability in mesoscopic perovskite solar cells. *Adv. Energy Mater.*, 5:1501066, 2015.

[9] Jingbi You, LeiMeng, Tze-Bin Song, Tzung-Fang Guo, Yang (Michael) Yang, Wei-Hsuan Chang, Ziruo Hong, Huajun Chen, Huanping Zhou, Qi Chen, Yongsheng Liu, Nicholas De Marco, and Yang Yang. Improved air stability of perovskite solar cells via solution-processed metal oxide transport layers. *Nat. Nanotechnol.*, 11:75–81, 2015.

[10] I. Hwang, I. Jeong, J. Lee, M. J. Ko, and K. Yong. Enhancing stability of perovskite solar cells to moisture by the facile hydrophobic passivation. *ACS Appl. Mater. Interfaces*, 7:17330–17336, 2015.

[11] S. N. Habisreutinger, T. Leijtens, G. E. Eperon, S. D. Stranks, R. J. Nicholas, and H. J. Snaith. Carbon nanotube/polymer composites as a highly stable hole collection layer in perovskite solar cells. *Nano Lett.*, 14:5561–5568, 2014.

[12] J. H. Kim, P. W. Liang, S. T. Williams, N. Cho, C. C. Chueh, M. S. Glaz, D. S. Ginger, and A. K. Jen. High-performance and environmentally stable planar heterojunction perovskite solar cells based on a solution-processed copper-doped nickel oxide hole-transporting layer. *Adv. Mater.*, 27:695–701, 2015.

[13] Sneha A. Kulkarni, Tom Baikie, Pablo P. Boix, Natalia Yantara, Nripan Mathews, and Subodh Mhaisalkar. Band-gap tuning of lead halide perovskites using a sequential deposition process. *J. Mater. Chem. A*, 2:9221–9225, 2014.

[14] T. G. Kim, S. W. Seo, H. Kwon, J. Hahn, and J. W. Kim. Influence of halide precursor

type and its composition on the electronic properties of vacuum deposited perovskite films. *Phys. Chem. Chem. Phys.*, 17:24342–24348, 2015.

[15] Jin Liu and Oleg V. Prezhdo. Chlorine doping reduces electronhole recombination in lead iodide perovskites: Time-domain ab initio analysis. *J. Phys. Chem. Lett.*, 6:4463–4469, 2015.

[16] B. Suarez, V. Gonzalez-Pedro, T. S. Ripolles, R. S. Sanchez, L. Otero, and I. Mora-Sero. Recombination study of combined halides (Cl, Br, I) perovskite solar cells. *J. Phys. Chem. Lett.*, 5:1628–1635, 2014.

[17] J. H. Heo and S. H. Im. Highly reproducible, efficient hysteresis-less $CH_3NH3PbI_{3-x}Cl_x$ planar hybrid solar cells without requiring heat-treatment. *Nanoscale*, 8:2554–2560, 2016.

[18] Y. Zhou, F. Wang, H.-H. Fang, M. A. Loi, F.-Y. Xie, Ni Zhao, and Ching-Ping Wong. Distribution of bromine in mixed iodidebromide organolead perovskites and its impact on photovoltaic performance. *J. Mater. Chem. A*, 4:16191–16197, 2016.

[19] Y.-C. Hsiao, T. Wu, M. Li, Q. Liu, W. Qin, and B. Hu. Fundamental physics behind high-efficiency organo-metal halide perovskite solar cells. *J. Mater. Chem. A*, 3:15372–15385, 2015.

[20] Weidong Zhu, Chunxiong Bao, Faming Li, Tao Yu, Hao Gao, Yong Yi, Jie Yang, Gao Fu, Xiaoxin Zhou, and Zhigang Zou. A halide exchange engineering for $CH_3NH_3PbI_{3-x}Br_x$ perovskite solar cells with high performance and stability. *Nano Energy*, 19:17–26, 2016.

[21] D. Bae, A. Palmstrom, K. Roelofs, B. Mei, I. Chorkendorff, S. F. Bent, and P. C. Vesborg. Tailoring mixed-halide, wide-gap perovskites via multistep conversion process. *ACS Appl. Mater. Interfaces*, 8(23):14301–14306, 2016.

[22] B. Yang, J. Keum, O. S. Ovchinnikova, A. Belianinov, S. Chen, M. H. Du, I. N. Ivanov, C. M. Rouleau, D. B. Geohegan, and K. Xiao. Deciphering halogen competition in organometallic halide perovskite growth. *J. Am. Chem. Soc.*, 138(15):5028–5035, 2016.

[23] D. M. Jang, K. Park, D. H. Kim, J. Park, F. Shojaei, H. S. Kang, J. P. Ahn, J. W. Lee, and J. K. Song. Reversible halide exchange reaction of organometal trihalide perovskite colloidal nanocrystals for full-range band gap tuning. *Nano Lett.*, 15:5191–5199, 2015.

[24] Z. Wang, D. P. McMeekin, N. Sakai, S. van Reenen, K. Wojciechowski, J. B. Patel, M. B. Johnston, and H. J. Snaith. Efficient and air-stable mixed-cation lead mixed-halide perovskite solar cells with n-doped organic electron extraction layers. *Adv. Mater.*, 29:1604186, 2017.

[25] S. Dastidar, D. A. Egger, L. Z. Tan, S. B. Cromer, A. D. Dillon, S. Liu, L. Kronik, A. M. Rappe, and A. T. Fafarman. High chloride doping levels stabilize the perovskite phase of cesium lead iodide. *Nano Lett.*, 16:3563–3570, 2016.

[26] E. T. Hoke, E. R. Slotcavage, D. J. Dohner, A. R. Bowring, H. I. Karunadasa, and M. D. McGehee. Reversible photo-induced trap formation in mixed-halide hybrid perovskites for photovoltaics. *Chem. Sci.*, 6:613–617, 2015.

[27] B.-w. Park, B. Philippe, S. M. Jain, X. Zhang, T. Edvinsson, H. Rensmo, B. Zietz, and G. Boschloo. Chemical engineering of methylammonium lead iodide/bromide perovskites: Tuning of optoelectronic properties and photovoltaic performance. *J. Mater. Chem. A*, 3:21760–21771, 2015.

[28] C. M. Sutter-Fella, Y. Li, M. Amani, 3rd Ager, J. W., F. M. Toma, E. Yablonovitch, I. D. Sharp, and A. Javey. High photoluminescence quantum yield in band gap tunable bromide containing mixed halide perovskites. *Nano Lett.*, 16:800–806, 2016.

[29] Angela Y. Chang, Yi-Ju Cho, Kuan-Chen Chen, Chang-Wen Chen, Alper Kinaci, Benjamin T. Diroll, Michael J. Wagner, Maria K. Y. Chan, Hao-Wu Lin, and Richard D. Schaller. Slow organic-to-inorganic sub-lattice thermalization in methylammonium lead halide perovskites observed by ultrafast photoluminescence. *Adv. Energy Mater.*, 6(15):1600422, 2016.

[30] H. Wang, L. Valkunas, T. Cao, L. Whittaker-Brooks, and G. R. Fleming. Coulomb screening and coherent phonon in methylammonium lead iodide perovskites. *J. Phys. Chem. Lett.*, 7:3284–3289, 2016.

[31] L. Wang, C. McCleese, A. Kovalsky, Y. Zhao, and C. Burda. Femtosecond time-resolved transient absorption spectroscopy of $CH_3NH_3PbI_3$ perovskite films: Evidence for passivation effect of PbI_2. *J. Am. Chem. Soc.*, 136:12205–12208, 2014.

[32] Seog Joon Yoon, Sergiu Draguta, Joseph S. Manser, Onise Sharia, William F. Schneider, Masaru Kuno, and Prashant V. Kamat. Tracking iodide and bromide ion segregation in mixed halide lead perovskites during photoirradiation. *ACS Energy Lett.*, 1:290–296, 2016.

[33] Waqaas Rehman, David P. McMeekin, Jay B. Patel, Rebecca L. Milot, Michael B. Johnston, Henry J. Snaith, and Laura M. Herz. Photovoltaic mixed-cation lead mixed-halide perovskites: Links between crystallinity, photo-stability and electronic properties. *Energy Environ. Sci.*, 10(1):361–369, 2017.

[34] W. Rehman, R. L. Milot, G. E. Eperon, C. Wehrenfennig, J. L. Boland, H. J. Snaith, M. B. Johnston, and L. M. Herz. Charge-carrier dynamics and mobilities in formamidinium lead mixed-halide perovskites. *Adv. Mater.*, 27(48):7938–7944, 2015.

[35] S. J. Yoon, K. G. Stamplecoskie, and P. V. Kamat. How lead halide complex chemistry dictates the composition of mixed halide perovskites. *J. Phys. Chem. Lett.*, 7(7):1368–1373, 2016.

[36] N. Marinova, S. Valero, and J. L. Delgado. Organic and perovskite solar cells: Working principles, materials and interfaces. *J. Colloid Interface Sci.*, 488:373–389, 2017.

[37] Yantao Shi, Yujin Xing, Yu Li, Qingshun Dong, Kai Wang, Yi Du, Xiaogong Bai, Shufeng Wang, Zhijian Chen, and Tingli Ma. $CH_3NH_3PbI_3$ and $CH_3NH_3PbI_{3x}Cl_x$ in planar or mesoporous perovskite solar cells: Comprehensive insight into the dependence of performance on architecture. *J. Phys. Chem. C*, 119(28):15868–15873, 2015.

[38] Zhi Guo, Yan Wan, Mengjin Yang, Jordan Snaider, Kai Zhu, and Libai Huang. Long-range hot-carrier transport in hybrid perovskites visualized by ultrafast microscopy. *Science*, 356(6333):59–62, 2017.

[39] J. H. Noh, S. H. Im, J. H. Heo, T. N. Mandal, and S. I. Seok. Chemical management for colorful, efficient, and stable inorganic-organic hybrid nanostructured solar cells. *Nano Lett.*, 13:1764–1769, 2013.

[40] L. Gil-Escrig, A. Miquel-Sempere, M. Sessolo, and H. J. Bolink. Mixed iodide-bromide methylammonium lead perovskite-based diodes for light emission and photovoltaics. *J. Phys. Chem. Lett.*, 6(18):3743–8, 2015.

[41] Nam-Gyu Park. Organometal perovskite light absorbers toward a 20% efficiency low-cost solid-state mesoscopic solar cell. *J. Phys. Chem. Lett.*, 4:2423–2429, 2013.

[42] S. D. Stranks and H. J. Snaith. Metal-halide perovskites for photovoltaic and light-emitting devices. *Nat. Nanotechnol.*, 10:391–402, 2015.

[43] Ralf G. Niemann, Athanassios G. Kontos, Dimitrios Palles, Efstratios I. Kamitsos, Andreas Kaltzoglou, Federico Brivio, Polycarpos Falaras, and Petra J. Cameron. Halogen effects on ordering and bonding of $CH_3NH_3^+$in $CH_3NH_3PbX_3$(X = Cl, Br, I) hybrid perovskites: A vibrational spectroscopic study. *J. Phys. Chem. C*, 120:2509–2519, 2016.

[44] V. A. Hintermayr, A. F. Richter, F. Ehrat, M. Doblinger, W. Vanderlinden, J. A. Sichert, Y. Tong, L. Polavarapu, J. Feldmann, and A. S. Urban. Tuning the optical properties of perovskite nanoplatelets through composition and thickness by ligand-assisted exfoliation. *Adv. Mater.*, 28(43):9478–9485, 2016.

[45] Y. Tong, E. Bladt, M. F. Ayguler, A. Manzi, K. Z. Milowska, V. A. Hintermayr, P. Docampo, S. Bals, A. S. Urban, L. Polavarapu, and J. Feldmann. Highly luminescent cesium lead halide perovskite nanocrystals with tunable composition and thickness by ultrasonication. *Angew. Chem. Int. Ed.*, 55:13887–13892, 2016.

[46] P. Piatkowski, Boiko Cohen, F. J. Ramos, M. Di Nunzio, M. K. Nazeeruddin, M. Gratzel, S. Ahmad, and A. Douhal. Direct monitoring of ultrafast electron and hole dynamics in perovskite solar cells. *Phys. Chem. Chem. Phys.*, 17:14674–14684, 2015.

[47] Tze Chien Sum, Nripan Mathews, Guichuan Xing, Swee Sien Lim, Wee Kiang Chong, David Giovanni, and Herlina Arianita Dewi. Spectral features and charge dynamics of lead halide perovskites: Origins and interpretations. *Accounts Chem. Res.*, 49:294–302, 2016.

[48] G. Xing, Nripan Mathews, Shuangyong Sun, Swee Sien Lim, Yeng Ming Lam, Michael Grtzel, Subodh Mhaisalkar, and Tze Chien Sum. Long-range balanced electron- and hole-transport lengths in organic-inorganic $CH_3NH_3PbI_3$. *Science*, 342(6156):344–347, 2013.

[49] S. S. Lim, W. K. Chong, A. Solanki, H. A. Dewi, S. Mhaisalkar, N. Mathews, and T. C. Sum. Modulating carrier dynamics through perovskite film engineering. *Phys. Chem. Chem. Phys.*, 18:27119–27123, 2016.

[50] J. S. Manser, J. A. Christians, and P. V. Kamat. Intriguing optoelectronic properties of metal halide perovskites. *Chem. Rev.*, 116:12956–13008, 2016.

[51] Joseph S. Manser and Prashant V. Kamat. Band filling with free charge carriers in organometal halide perovskites. *Nat. Photonics*, 8:737–743, 2014.

[52] G. R. Berdiyorov, F. El-Mellouhi, M. E. Madjet, F. H. Alharbi, F. M. Peeters, and S. Kais. Effect of halide-mixing on the electronic transport properties of organometallic perovskites. *Sol. Energ. Mat. Sol. C.*, 148:2–10, 2016.

[53] Elinore M. L. D. de Jong, Genki Yamashita, Leyre Gomez, Masaaki Ashida, Yasufumi Fujiwara, and Tom Gregorkiewicz. Multiexciton lifetime in all-inorganic $CsPbBr_3$ perovskite nanocrystals. *J. Phys. Chem. C*, 121(3):1941–1947, 2017.

[54] M. Li, S. Bhaumik, T. W. Goh, M. S. Kumar, N. Yantara, M. Gratzel, S. Mhaisalkar, N. Mathews, and T. C. Sum. Slow cooling and highly efficient extraction of hot carriers in colloidal perovskite nanocrystals. *Nat. Commun.*, 8:14350, 2017.

[55] M. B. Price, J. Butkus, T. C. Jellicoe, A. Sadhanala, A. Briane, J. E. Halpert, K. Broch, J. M. Hodgkiss, R. H. Friend, and F. Deschler. Hot-carrier cooling and photoinduced refractive index changes in organic-inorganic head halide perovskites. *Nat. Commun.*, 6:9420, 2015.

[56] J. Yang, X. Wen, H. Xia, R. Sheng, Q. Ma, J. Kim, P. Tapping, T. Harada, T. W. Kee, F. Huang, Y. B. Cheng, M. Green, A. Ho-Baillie, S. Huang, S. Shrestha, R. Patterson, and G. Conibeer. Acoustic-optical phonon up-conversion and hot-phonon bottleneck in lead-halide perovskites. *Nat. Commun.*, 8:14120, 2017.

[57] A. P. Kirk and M. V. Fischetti. Fundamental limitations of hot-carrier solar cells. *Phys. Rev. B*, 86(16):165206, 2012.

[58] C. C. Stoumpos, C. D. Malliakas, and M. G. Kanatzidis. Semiconducting tin and lead iodide perovskites with organic cations: Phase transitions, high mobilities, and near-infrared photoluminescent properties. *Inorg. Chem.*, 52:9019–9038, 2013.

[59] J. Su, D. P. Chen, and C. T. Lin. Growth of large $CH_3NH_3PbX_3$ (X=I, Br) single crystals in solution. *J. of Cryst. Growth*, 422:75–79, 2015.

[60] A. D. Wright, C. Verdi, R. L. Milot, G. E. Eperon, M. A. Perez-Osorio, H. J. Snaith, F. Giustino, M. B. Johnston, and L. M. Herz. Electron-phonon coupling in hybrid lead halide perovskites. *Nat. Commun.*, 7:11755, 2016.

[61] E. M. Talbert, H. F. Zarick, N. J. Orfield, Wei Li, W. R. Erwin, Z. R. DeBra, K. R. Reid, C. P. McDonald, J. R. McBride, J. Valentine, S. J. Rosenthal, and R. Bardhan. Interplay of structural and compositional effects on carrier recombination in mixed-halide perovskites. *RSC Adv.*, 6:86947–86954, 2016.

[62] Mohamed El-Amine Madjet, Alexey V. Akimov, Fadwa El-Mellouhi, Golibjon R. Berdiyorov, Sahel Ashhab, Nouar Tabeta, and Sabre Kaisac. Enhancing the carrier thermalization time in organometallic perovskites by halide mixing. *Phys. Chem. Chem. Phys.*, 18:5219–5231, 2016.

[63] Daniel J. Slotcavage, Hemamala I. Karunadasa, and Michael D. McGehee. Light-induced phase segregation in halide-perovskite absorbers. *ACS Energy Lett.*, 1:1199–1205, 2016.

[64] Xiaofan Deng, Xiaoming Wen, Shujuan Huang, Rui Sheng, Takaaki Harada, Tak W. Kee, Martin Green, and Anita Ho-Baillie. Ultrafast carrier dynamics in methylammonium lead bromide perovskite. *J. Phys. Chem. C*, 120:2542–2547, 2016.

[65] Tze Chien Sum and Nripan Mathews. Advancements in perovskite solar cells: Photophysics behind the photovoltaics. *Energy Environ. Sci.*, 7:2518–2534, 2014.

[66] Ye Yang, Mengjin Yang, Zhen Li, Ryan Crisp, Kai Zhu, and Matthew C. Beard. Comparison of recombination dynamics in $CH_3NH_3PbBr_3$ and $CH_3NH_3PbI_3$ perovskite films: Influence of exciton binding energy. *J. Phys. Chem. Lett.*, 6(23):4688–4692, 2015.

[67] Z. Zhu, J. Ma, Z. Wang, C. Mu, Z. Fan, L. Du, Y. Bai, L. Fan, H. Yan, D. L. Phillips, and S. Yang. Efficiency enhancement of perovskite solar cells through fast electron extraction: the role of graphene quantum dots. *J. Am. Chem. Soc.*, 136:3760–3763, 2014.

[68] Lydia H. Manger, Matthew B. Rowley, Yongping Fu, Alexander K. Foote, Morgan T. Rea, Sharla L. Wood, Song Jin, John C. Wright, and Randall H. Goldsmith. Global analysis of perovskite photophysics reveals importance of geminate pathways. *J. Phys. Chem. C*, 121:1062–1071, 2017.

[69] W. R. Erwin, H. F. Zarick, E. M. Talbert, and R. Bardhan. Light trapping in mesoporous solar cells with plasmonic nanostructures. *Energy Environ. Sci.*, 9:1577–1601, 2016.

[70] H. F. Zarick, A. Boulesbaa, A. A. Puretzky, E. M. Talbert, Z. R. DeBra, N. Soetan, D. B. Geohegan, and R. Bardhan. Ultrafast carrier dynamics in bimetallic nanostructure-enhanced methylammonium lead bromide perovskites. *Nanoscale*, 9:1475–1483, 2017.

[71] E. Edri, S. Kirmayer, M. Kulbak, G. Hodes, and D. Cahen. Chloride inclusion and hole transport material doping to improve methyl ammonium lead bromide perovskite-based high open-circuit voltage solar cells. *J. Phys. Chem. Lett.*, 5:429–433, 2014.

[72] L. Etgar, P. Gao, Z. Xue, Q. Peng, A. K. Chandiran, B. Liu, M. K. Nazeeruddin, and M. Gratzel. Mesoscopic $CH_3NH_3PbI_3/TiO_2$ heterojunction solar cells. *J. Am. Chem. Soc.*, 134:17396–17399, 2012.

[73] Julian Burschka, Norman Pellet, Soo-Jin Moon, Robin Humphry-Baker, Peng Gao, Mohammad K. Nazeeruddin, and Michael Grtzel. Sequential deposition as a route to high-performance perovskite-sensitized solar cells. *Nature*, 499:316–319, 2013.

CHAPTER 9

SUMMARY AND OUTLOOK

In this work, we investigated the use of shape- and composition-controlled bimetallic nanostructures to enhance the light harvesting capability and improve the power conversion efficiency in two different 3rd generation mesoscopic solar cells, dye-sensitized and organolead trihalide perovskite sensitized solar cells. We then utilized two complimentary time resolved spectroscopic techniques to further investigate the plasmonic enhancement mechanisms driving the improved light conversion efficiency.

To accomplish this, we first synthesized Au/Ag core/shell bimetallic nanostructures with cubic and pyramidal shape. The overall goal in synthesizing these structures was to tune nanoparticles with properties we felt to be ideal for plasmonic enhancement: broadband absorption from the dual metal presence, Ag outerlayer to reduce Ohmic losses and increase light scattering efficiency, and sharp edges and corners from the cubic and pyramidal geometries to enhance the strength of electromagnetic near-field generation. By tuning the synthesis parameters, we found that temperature controlled the morphological evolution of the structures; if the thermal energy in the reaction system was too low (35°C) then nanostructures with rounded corners and edges formed, and if it was too high (80°C), then polydispersity was intensified prompting the growth of high aspect ratio nanorods. A median temperature of 65°C was found to be most appropriate for forming sharp-edged nanostructures with minimal rod formation.

Before incorporating our structures into devices, we first probed their excited state properties as a function of Ag layer thickness (0-15 nm) in solution using transient absorption spectroscopy. Low powered TAS measurements revealed minimal dependence on Ag layer thickness, however high powered measurements revealed composition and shape dependent trends. At high power, Ag presence (even at the thinnest, 2 nm layer) controls and en-

hances the absorption of the 400 nm pump pulse leading to enhanced electron-phonon and phonon-phonon excited state decay lifetimes as Ag layer was increased. We also observed enhanced phonon-phonon lifetimes in the nanocubes with increased Ag layer thickness as opposed to the nanopyramids, which we attributed to the increased amount of edges and corners in the nanocubes vs the nanopyramids.

We attempted to decouple the impact of shape and composition effects on the plasmonic enhancement ability of the nanostructures in DSSCs by looking at both Au nanocube-enahnced and Au/Ag nanostructure-enhanced DSSC systems. When incorporating Au NCs, we observed a systematic dependence of device performance on Au nanocube concentration. At an optimized density of 1.8 *wt*.% of Au NCs incorporated, we were able to achieve a 34% increase in device performance compared to a reference, non-enhanced device. We then compared these results to devices incorporating Au/Ag bimetallic nanostructures. We observed a similar concentration dependent trend and were able to achieve a power conversion efficiency enhancement of 26% at the optimized particle density of 0.44 *wt*.%. While greater enhancements were not achieved compared to Au NCs as expected, it is interesting to note that similar enhancements were achieved using $4\times$ less the amount of nanoparticle density with the bimetallic nanostructures compared their monometallic counterparts. TAS measurements elucidated the density-dependent impact of the Au/Ag NSs on carrier dynamics in these devices and provided strong evidence of plasmon-resonant energy transfer in this system.

Moving forward, we then investigated the impact of AuAg bimetallic nanostructures on the performance and carrier dynamics in $MAPbBr_3$ devices. An unoptimized concentration of 1.0 *wt*.% incorporation of Au/Ag NSs also resulted in a 26% increase in power conversion efficiency compared to a reference, non-enhanced device. We used both time-resolved photoluminescence (trPL) and TAS to investigated the impact of these structures on carrier dynamics and to further investigate the plasmonic enhancement mechanisms at play. Most interestingly, we observed a decrease in the photobleach formation time, which

suggests that the presence of the nanostructures improves hot carrier thermalization to an equilibrium distribution and thus helps relieve the hot-phonon bottleneck in organolead halide perovskties. The presence of the nanostructures also increased the carrier decay lifetimes, observed in both TAS and trPL, suggesting enhanced rate of carrier generation that promoted more efficient charge injection into the TiO_2 scaffold.

Finally, we discovered another scheme for reducing the thermalization lifetime and relieving the hot-phonon bottleneck in organolead trihalide perovskite via controlled substitution of I with Br. Transient absorption measurements of mixed halide perovskites with 0 to 30% substation of I with Br showed little dependence of halide content on carrier recombination and injection lifetimes, however displayed significant decreases in the carrier thermalization lifetime with increasing Br content. This suggests that the shift in crystal structure from tetragonal to pseudo cubic as Br is added to the lattice improves carrier cooling, which also aides in the relief of the hot phonon bottleneck, decreasing energy losses in the devices to heat generation.

In summary, this work provides key insights into the mechanisms which enable plasmon enhancement of 3rd generation mesoscopic solar devices. Plasmonic enhancement has been applied to a wide variety of solar cell systems, from silicon-based to organic photovoltaics, and muc hprogress has been made in the eld in the last decade. Here we have investigated and elucidated mechanisms and schemes for improving light capture and carrier dynamics using both plasmonic nanostructures and halide substitution. Our work has demonstrated that despite being a universal enhancement tool, different mechanisms of enhancements can be exploited depending on the device architecture and nature of the sensitzer. DSSCs primarily benet from radiative enhancement both in the near-eld and far-eld, as well as PRET, resulting in increased photocurrent. In PSCs, plasmon-enhanced light harvesting gives rise to a modest increase in photocurrent, by both enhancing optical absorption and decreasing exciton binding energy. Understanding and considering these mechanisms and their interactions in various environments enables powerful future

optimization potential. There remains signicant opportunity to probe the impact and mechanisms of hybrid bimetallic nanostructures with other sensitizers, architectures, and solar cell types; this includes mixed halide perovskites, planar devices, and in solar devices such as quantum dot solar cells, amorphous silicon PVs, and cadmium telluride thin lm PVs.

While perovskites have already created a paradigm shift in photovoltaic technology, we anticipate that in the next decade new perovskite materials will be discovered and new PV architectures will be realized for further advances in efciency and ultimately in commercial feasibility. In particular, whereas Pb-based perovskites have thus far achieved unprecedented efciencies, the high toxicity of lead is a primary concern to the environment and to human health as even low exposure levels are associated with signicant health impairments. Concerns with Pb toxicity has also hindered the wide-scale implementation of Pb-based perovskites, and much focus has been placed on developing perovskite materials with either reduced or eliminated Pb content. We hope that information gleaned about bimetallic nanostructures on the impact of plasmonic enhancement mechanisms can further tailor their use in future devices employing these new perovskite materials and optimized cell architectures.

Additionally, we envision that the information we have learned in particular about the importance of morphology control can aid in the development of new plasmonic materials that can be used to enhance to performance of a range of optical and electronic devices. This includes devices beyond photovoltaics, such as next generation energy conversion systems like semiconductor-based photoelectrochemical fuel cells. Further, besides solution synthesized nanostructures and traditional incorporation methods, LSPRs may also be engineered into the cathode of PSCs, which is typically Au or Ag, by nanostructuring the electrode with top-down approaches to ultimately enable long-range surface plasmon polariton modes to couple to the optical resonances of the perovskites. Ultimately, we hope that our studies and forthcoming investigations will help push towards a future that utilizes clean and renewable energy sources.